Subgrain-size piezometry as a tool for measuring stress in polymineralic rocks

by Catherine R.M. Goddard

University College

Submitted for the degree of Doctor of Philosophy
at the Department of Earth Sciences, Oxford University
Trinity 2021

Supervised by
Lars H.Hansen, David Wallis, and Kathryn M. Kumamoto

Declaration

I declare that I composed and wrote this thesis and that none of the work has been submitted for any other degree or professional qualification. I confirm that the work of this thesis is my own except where explicitly stated.

The work in Chapter 2 forms a jointly authored publication. My contributions to this publication have been explicitly indicated in the signed authorship statement at the end of that chapter.

The indefinite closure of the Oxford scanning electron microscope laboratory in March 2020 due to the global COVID-19 pandemic greatly impacted the data collection for a number of chapters. Half of the EBSD data I was due to collect for Chapter 3 and all the data from Chapter 4 were collected at my direction by Lars Hansen at the University of Minnesota. Half of the EBSD data from Chapter 5 were collected at my direction by Markus Ohl at Utrecht University.

The processing of raw D-DIA data in Chapter 3 made use of unpublished codes written for that experimental set up by Kathryn Kumamoto.

This piece of work is dedicated to Marie-Louise Fages and Ronald Goddard both of whom had a deep love of learning and life. Though our time together on this Earth was short the memories and stories passed onto me of them both have greatly influenced my life.

"Art is never finished, only abandoned" - Leonardo Da Vinci

Acknowledgements

While this list of acknowledgements may seem excessively long, and even a little self-indulgent, I believe it simply reflects how fortunate I am to have been helped by so many people over the last five years. Most importantly, I would like to thank my supervisors: Lars Hansen, Dave Wallis, and Katie Kumamoto. I am in the privileged position of being in all three cases their first PhD student; a fact I feel has significantly played to my advantage.

Given my oftentimes pessimistic outlook, it may surprise Lars to know that actually I feel extremely lucky to have been part of his research group. He has enabled me to complete everything on my 'PhD wish list', while patiently giving feedback, help and support along the way. While it goes without saying that his insights and encouragement have drastically improved this thesis, he is also always happy to offer his two cents on life's other problems.

Despite our group constant musing over 'Where's Wallis?' it is fair to say that Dave has managed to be as present as an external supervisor as he was during his postdoc year in Oxford. There is something about Dave's demeanour, or maybe it's his never-failing enthusiasm for science, that always managed to help me remember that everything would turn out okay. His in-depth knowledge of micromechanics, along with his willingness to give extensive and detailed feedback has greatly increased the quality of my writing as well as my science.

Last but not least, Katie, who somewhat rescued me when Lars left for America. Extremely knowledgeable and generous with her time, Katie has been invaluable in the last couple of years of my PhD and a great confidante. Somehow, she managed to perfectly know when I needed tough love, and when I needed a beer. The emotional support she has offered me, this year in particular, has been a life saver.

Overall, I feel extremely lucky to have worked with such an incredible team and, despite all three of them moving countries to get away from me, I hope they have had fun too.

Throughout the last five years I have met and worked with amazing groups of people. Thanks to Michael Sipp and Caleb Holyoke III for entrusting me with their samples and for their useful feedback on my paper. The Rock Rheology group in Minnesota were always happy to lend a helping hand. Thanks to Edith Martel and the Northwest Territories Geological Survey for their expertise, loan of equipment, and rescue helicopter during my trip to the Great Slave Lake. My fieldwork was also greatly improved by Brendan Dyck who not only made a fantastic fish curry but was useful when it came to metamorphic rocks. My own knowledge of metamorphic rocks was greatly improved by the wisdom of Dave Waters, who patiently looked through my thin sections with me. My PhD project would not have been completed without the help of Markus Ohl at Utrecht University, who stepped in to collect EBSD maps of the remaining samples when the SEM lab closed indefinitely in Oxford due to COVID. Thanks to 'Team Beam' for making experiments so much fun at the Argonne National Laboratory, particularly Tom Breithaupt and Chris Thom for a combination of scientific aid and evenings spent in the pub.

There are a huge number of people that keep the cogs turning at an institution such as Oxford. Three members of staff I feel went above and beyond: Victoria Forth, who was always there to help navigate the never-ending red-tape, Phil Gopon, who was always there to help when the SEM didn't work, and Jon Wells, who made hundreds of thin sections for me at short notice. I also wish to thank Jessica Hawthorne who, when all my supervisors left Oxford, agreed to take on the boring job of the admin role of a supervisor.

My time in Oxford has been all the richer for the friends I've made along the way. Work was greatly improved by sharing Office 20.15 with Sean, Vicky, Ronnie, and Anna. Ronnie and Anna in particular have been there for the emotional highs and lows that come form embarking on a PhD and I can't thank them enough, especially for never getting angry when I stole their snacks ... which happened a lot.

I owe my sanity to the Oxford University Swimming Club, and specifically to Anna White and Ada Taggart. Through the last three years they have never failed to make me laugh and always kept me thinking positively. Living with Danielle was another highlight. After three years of looking after each other she will forever feel more like family. Thanks to Becca and Caleb, who have fed me, housed me, and just generally always been there for me.

I am extremely thankful to Dan Spencer for lending an ear to my rants and agreeing to take me on as an additional housemate in my 'final' year. Or, I guess, more accurately I'm thankful to the random person who threw a rock through his previous house's window, giving him the extra incentive to move. To Leo, Oli, Bernd, and Nik, thanks for agreeing to live with a stranger and for giving me a friendly, fun, environment for my last year in Oxford. It's safe to say that when they signed up to live with me, they weren't expecting months of incarceration. Though obviously a period of life I would never choose to re-live I will still be able to look back on those lock down nights of board games, movies, and quirky beers as a great deal of fun.

Few other than my boyfriend, Ed, have truly witnessed the all-consuming nature of my PhD in the last year. I feel extremely thankful for his understanding and patience with me, especially over the final few months, and also his ability to always make me laugh.

When I first got accepted by Oxford, I was crashing at Anna Twomlow's house. She handed me a note for my journey home that included a statement I have held on to for the whole of my time here—*you are so much more than a PhD*. In the same way getting to the end of this project was so much more than just doing a PhD. They say that it takes a village to raise a child a sentiment that rings true when I consider the community of people outside of Oxford who have helped me get to this point in my life. From Duncan Erratt, who bought me my first hammer, to the 'Geology Girls' who lovingly(?) mocked my enthusiasm at Durham. From my Godmother, Pamela Big, who has been there for me my whole life, offering guidance and telling me when my plans are utter madness, too my grandmother, Jenny Goddard, who has offered me guidance and comfort despite the risk it might trigger post-traumatic stress from when my dad wrote up. For all the cards, the support, the phone calls, and texts, from people over the years. To Katie Mackay for her prayers. To Matt, for putting up with rocks being dragged across his ceiling in the small hours of the morning. To Morgan for feigning interest. To Sam for his stress-relief suggestions of meditation and self-help books that I always ignored. To Joanna, for sending me the largest bag of nuts I have ever seen to snack on while I wrote up. To Kate and Annie, just because. I love you all. And of course, to Twomlow, for being there for every high and low of not only my project but my life.

Finally, it is necessary to acknowledge my parents—Nick and Marie-Christine Goddard—though to merely acknowledge them seems so inadequate. I would never have been in a position to undertake a PhD, let along complete one, if they had not instilled in me the belief that if you work hard, and are resilient, even if you do not achieve your exact goal, you can walk away head held high. Through the years they have picked me up every time that I felt low or inadequate. My dad has proofread nearly every piece of work I've ever written. My mum has tried her utmost to understand and navigate not only my work-related mood swings but the world of academia. They taught me to love learning and to never feel limited by my gender. Most importantly I owe them thanks for teaching me that there are far more important things in life than success and intelligence. Mum, Dad, I also dedicate this piece of work to you — as everything I am stems from you both.

Contents

List of Figures

List of Tables

List of symbols and abbreviations

Symbols

T: temperature

T_{m}: solidus temperature of a material

T_0: temperature at which thermal expansion coefficients were calculated

ΔT: change in temperature

ΔV: volume change of a reaction

P: pressure

Q: activation enthalpy

R: gas constant (8.3145 J/K)

r: radius of Paterson test piece

di_{full}: diameter of Paterson test piece

di: distance between the centre of the top and bottom faces of a cylinder

d: grain size

p: grain-size exponent

d_{s}: subgrain size

λ: mean line-intercept length between subgrain boundaries

λ_{gs}: mean line-intercept length between grain boundaries

λ_{best}: the value of λ associated with the smallest step size and largest map area

$\frac{\lambda}{\lambda_{\mathrm{best}}}$: intercept variation factor

$\frac{\lambda_{\mathrm{best}}}{step\ size}$: pixel per intercept

L: dislocation spacing

ρ: dislocation density

ρ_{t}: total dislocation density

k: dislocation-density exponent

σ_1: principal stress axis

σ: von Mises equivalent stress /differential stress

σ_{agg}: bulk stress

σ_{w}: stress experienced by a weak phase in an aggregate

σ_{s}: stress experienced by a strong phase in an aggregate

σ_0: empirical stress constant

n: stress exponent

$\dot{\varepsilon}$: strain rate

ε_{M}: elastic strain of apparatus

ε_{E}: elastic strain of sample

ε_{P}: plastic strain of sample

μ: shear modulus

G_{R}: X-ray shear modulus

k: Young's modulus of apparatus

M: Young's modulus of sample

K_0: bulk modulus

K'_{T}: temperature derivative of the bulk modulus

K'_{P}: pressure derivative of the bulk modulus

ν: Poisson's ratio

b: Burgers vector

V: unit-cell volume

V_0: unit-cell volume at ambient temperature and pressure

d_{v}: d-spacing measured from the detector at the vertical azimuth

d_{h}: d-spacing measured from the detector at the horizontal azimuth

ϕ: phase proportion

f_{px}: volume fraction of orthopyroxene

Ψ: azimuth to the horizontal incident beam

2θ: Bragg's angle

$a_{\mathrm{TiO_2}}$: activity of $\mathrm{TiO_2}$ in a system

X_{Ti} : ppm of Ti by weight

$X_{\mathrm{Ti}}^{\mathrm{Qz}}$: concentration of Ti (ppm by weight) in quartz

$X_{\mathrm{TiO_2}}^{\mathrm{Qz}}$: mole fraction of $\mathrm{TiO_2}$ in quartz

X_{An}: Ca/(Ca+Na) where Ca and Na are in a.p.f.u.

X_{Mg}: Mg/(Mg+$\mathrm{Fe^{2+}}$) where Mg and Fe are in a.p.f.u.

X_A^B: a.p.f.u. of A in cation sight B

Abbreviations

Ab: albite

An: anorthite

And: andesine

Ano: anorthoclase

a.p.f.u.: atoms per formula unit

BDT: brittle-ductile transition

BLG: bulging recrystalisation

BPT: brittle-plastic transition

Chl: chlorite

CPO: crystal preferred orientation

DisGBS: dislocation-accommodated grain-boundary sliding

EBSD: electron backscatter diffraction

EBSP: electron backscatter pattern

En: enstatite

EPMA: electron probe micro-analyser

Fo: forsterite

GBM: grain boundary migration

GSLsz: Great Slave Lake shear zone

HR-EBSD: high-angular resolution EBSD

Hst: hastingite

Ilm: ilmenite

Kfs: potassium feldspar

LBF: load-bearing framework

LTP: low-temperature plasticity

MSA: molten salt assembly

MUD: multiples of uniform distribution

Ol: olivine

Opx: orthopyroxene

Or: orthoclase

Py: pyrite

Qz: quartz

Rt: rutile

SEM: scanning electron microscopy

SGR: subgrain rotation recrystallisation

Spn: sphene (titanite)

SSA: solid salt assembly

TEM: transmission electron microscopy

TMZ: Taltson Magmatic Zone

TTZ: Thelon Tectonic Zone

Zrn: zircon

Abstract

We present a new subgrain-size piezometer calibrated using electron backscatter diffraction data from experimentally deformed quartz and olivine. Subgrain size is found to be inversely proportional to the applied stress. We tested a variety of different critical misorientations to define a subgrain boundary and concluded that a 1- or 2-degree threshold provides the optimum piezometric relationship.

The efficacy of subgrains to record the stress within individual phases in a polymineralic rock was tested using mixtures of olivine and orthopyroxene in a Deformation-DIA apparatus situated on a synchrotron X-ray beamline. For samples with grain sizes large enough to contain subgrains, piezometric measurements in olivine within the original calibration range displayed a good agreement with stresses measured through X-ray diffraction. Results indicated that a fine grain size severely limits the application of subgrain-size piezometry. For orthopyroxene, subgrains were too sparse to conclusively state whether the Goddard et al. (2020) piezometer can be applied to this mineral. Comparison of stresses measured through X-ray diffraction in each phase indicated that orthopyroxene supported a greater proportion of the load than olivine.

To explore stress partitioning further, we deformed olivine-orthopyroxene mixtures of various phase proportions in a gas-medium apparatus. The sample with intermediate composition was found to be weaker than would be expected simply from the grain-size sensitivity of traditional deformation mechanisms. Results from subgrain-size piezometry indicated that orthopyroxene is solely responsible for the weakening.

We apply the subgrain-size piezometer to quartz in polymineralic aggregates from the Great Slave Lake shear zone. To calculate the depth associated with each stress measurement, we conducted geothermometry. These stress measurements from subgrains are higher than those measured in other equivalent shear zones using grain-size piezometry, suggesting that the two microstructural features might record different portions of the deformation history.

Long Abstract

Quantifying the stress supported by the lithosphere is important for our understanding of a variety of different geological phenomena. While the strength of the brittle portion of the crust can be measured directly or calculated from the magnitude of seismic events, estimates for the strength of the ductile lower-crust rely on measuring microstructural features for which there is a known relationship with stress—an approach known as paleopiezometry and herein referred to simply as 'piezometry'. The most commonly applied piezometer is based on the recrystallised grain-size, which is inversely proportional to the von Mises equivalent stress, herein referred to simply as 'stress'. However, grain-size piezometers can only be applied to rocks consisting of a single mineral as secondary phases 'pin' grain boundaries, thus inhibiting grain growth. As most rocks are polymineralic, this constraint drastically limits the application of grain-size piezometers to relatively few natural settings.

The size of subgrains, which are intragranular features and therefore hypothesised to be unaffected by the presence of secondary phases, also has an inverse relationship with stress. Unfortunately, estimates of subgrain size differ significantly depending on the measurement method used, and therefore, piezometers must be individually calibrated for each method. Existing subgrain-size piezometers are based on calibrations using optical or transmission electron microscopy. However, there has previously been no calibration for subgrain sizes measured with electron backscatter diffraction (EBSD), a now common method of characterising deformed rocks.

We present a new subgrain-size piezometer calibrated using EBSD from experimentally deformed olivine and quartz samples. The mean line-intercept length, which is equivalent to the subgrain-boundary spacing and thus proportional to the subgrain size, is found to be inversely proportional to the stress. We explored subgrain boundaries defined by a range of critical misorientation angles and concluded that low misorientations, of 1 or 2 degrees, provide the best piezometric calibrations. To test the accuracy of EBSD for such small misorientation angles, we implemented high-angular resolution EBSD (HR-EBSD). Subgrain sizes measured by HR-EBSD and standard EBSD differ slightly, but the differences in the resulting piezometric relationships are minimal.

We tested the application of the newly-derived subgrain-size piezometer to polymineralic rocks using a Deformation-DIA apparatus at synchrotron X-ray beamline 6-BM-B at the Advanced Photon Source, at the Argonne National Laboratory, Illinois. This experimental set up allows the unique possibility of measuring the average stress within each phase in an aggregate through X-ray diffraction. This *in-situ* stress was then compared to the stress inferred from subgrain-size piezometry on each phase. Experiments were conducted on olivine and orthopyroxene mixtures stacked against a dunite load cell at temperatures of 800°–1250°C and pressures of 2.1–8.3 GPa. The choice of olivine as a control was based on it having previously been used to calibrate the subgrain-size piezometer.

Grain-size was found to limit the application of the subgrain-size piezometer, with many samples containing grains significantly smaller than the subgrain-size predicted by the piezometer at the final stress. Subgrain structure was also lacking in orthopyroxene within mixtures that had experienced low strain. For samples in which sufficient intragranular structure did develop, stresses measured in olivine through X-ray diffraction and subgrain-size piezometry had a strong correlation in both monomineralic and polymineralic rocks within the calibrated stress range of the piezometer. For orthopyroxene, insufficient substructure existed to be confident in the application of the subgrain-size piezometry to this mineral.

The stress measurements in olivine and orthopyroxene from X-ray diffraction were used to explore the uniformity of stress within an aggregate. Stresses were found to be higher on average in the orthopyroxene phase, with the magnitude of this difference reducing with decreasing pressure. Although subgrain-size piezometry is a useful tool for exploring the stress state for individual phases in an aggregate, it is clear that extrapolating these stresses to the bulk stress experienced by the sample is more complicated.

To explore further how the stress within individual phases in an aggregate relates to its bulk stress, we applied subgrain-size piezometry to olivine and orthopyroxene mixes with orthopyroxene volume fractions of 0.20, 0.40, 0.70, and 0.93. Experiments were conducted in a servo-controlled internally heated Paterson apparatus at constant displacement rate, 300 MPa, and 1250°C. While end-member samples exhibited a similar strength, the sample with an intermediate composition (a pyroxene fraction of 0.4) exhibited anomalous weakening, which could not be explained by the grain-size sensitivity of common deformation

mechanisms. Insight from subgrain-size piezometry indicates that weakening was solely in the orthopyroxene, which is proposed to be deforming by interface-reaction-controlled diffusion creep. This weakening effect has not been observed in previous experiments made from high-purity, synthetic rocks. We propose that the weakening in our sample is linked to the presence of impurities, such as calcium, that are segregated at phase boundaries and enhance the reaction at and/or diffusivity along the phase boundaries.

Finally, we apply the subgrain-size piezometer to the Early Proterozoic Great Slave Lake shear zone (GSLsz) in Canada. As this strike-slip shear zone remained active during its exhumation, this field site offers the opportunity to quantify the stress at various depths within the ductile continental crust. Subgrain-size piezometry was applied to quartz within polymineralic aggregates from metamorphic facies ranging from granulite to greenschist. To calculate the associated depth, we measured the temperatures using a combination of different geothermometers as well as quartz microstructures. In all instances, temperatures calculated through amphibole-plagioclase thermometry far exceeded those indicated by the quartz microstructures, implying they recorded instead the peak temperature experienced by the rock. Temperatures from Ti-in-quartz thermometry were found to be the most consistent with the temperatures indicated by the quartz microstructures.

Comparison of the strength profile measured from subgrain-size piezometry to previous profiles measured through grain-size piezometry indicated that stresses in the GSLsz were higher than seen elsewhere in other natural rocks. This result can be explained either by anomalously high temperatures at the GSLsz, or with grain-size piezometry and subgrain-size piezometry recording different parts of the stress evolution. Alternatively, the stress measured in quartz within polymineralic regions could only represent part of the total applied stress. If so, subgrain-size piezometry on multiple phases would be required before meaningful comparisons with grain-size piezometry could be made.

1 Introduction

1.1 The strength of the lithosphere

Understanding the spatial and temporal heterogeneity in the strength of the crust and mantle is essential to obtain constraints on (1) the mechanical state of Earth's lithosphere (e.g., Kohlstedt & Weathers, 1980), (2) strain localisation at plate boundaries (e.g., Boutonnet et al., 2013), and (3) the redistribution of stress within and between fault zones over the earthquake cycle (e.g., Campbell & Menegon, 2019). Assuming that the lithosphere cannot be stronger than the rocks from which it is made, it's can be probed through deformation experiments on minerals thought to be representative of lithospheric rocks.

Modes of deformation in the lithosphere can be broken down into two end-member categories: brittle and ductile. In the upper crust, deformation is commonly brittle in nature and is controlled by either the fracture strength or the frictional strength of the rock (e.g., Kirby, 1983). In experimental studies on pre-fractured, natural rocks at low temperatures and effective pressures, the stress required to initiate frictional sliding is smaller than that required for fracture (Paterson & Wong, 2005). Therefore, in pervasively fractured rocks in the upper lithosphere, the strength of a rock is limited by its frictional resistance.

The transition from brittle to ductile behaviour (the brittle-ductile transition, BDT) is the result of a change in failure mode from localised faulting to distributed shear (Kohlstedt et al., 1995). With increased temperature, a change in deformation mode also occurs, which is termed the brittle-plastic transition (BPT). This BPT is approximately controlled by the condition of $T \leq \frac{1}{2}\, T_{\mathrm{M}}$, where T is the temperature and T_{M} is the solidus temperature of the relevant material (Ranalli, 1997). As different minerals have different T_{M}, the BPT of polymineralic crust is likely to be distributed over some depth interval.

The lower crust typically deforms by ductile deformation due to increased temperatures and pressures. Ductile rocks are commonly described by experimentally-derived flow laws that take the form

$$\dot{\varepsilon} = A\sigma^{n} d^{-p} \exp\left(\frac{-Q}{RT}\right), \tag{1.1}$$

where $\dot{\varepsilon}$ is strain rate, A is a material-dependent constant, σ is differential stress, n is the stress exponent, d is grain size, p is the grain-size exponent, Q is the activation enthalpy,

and R is the gas constant. These parameters are empirically determined through experiments investigating specific deformation mechanisms, which include dislocation creep, diffusion creep, low-temperature plasticity (LTP), and dislocation-accommodated grain-boundary sliding (DisGBS). As the strength of material obeying Eq.1.1 decreases with increasing temperature, and therefore depth, the maximum strength of the lithosphere is expected to occur at the BPT (e.g., Sibson, 1982; Küster & Stöckhert, 1999; Kirby & Kronenberg, 1987).

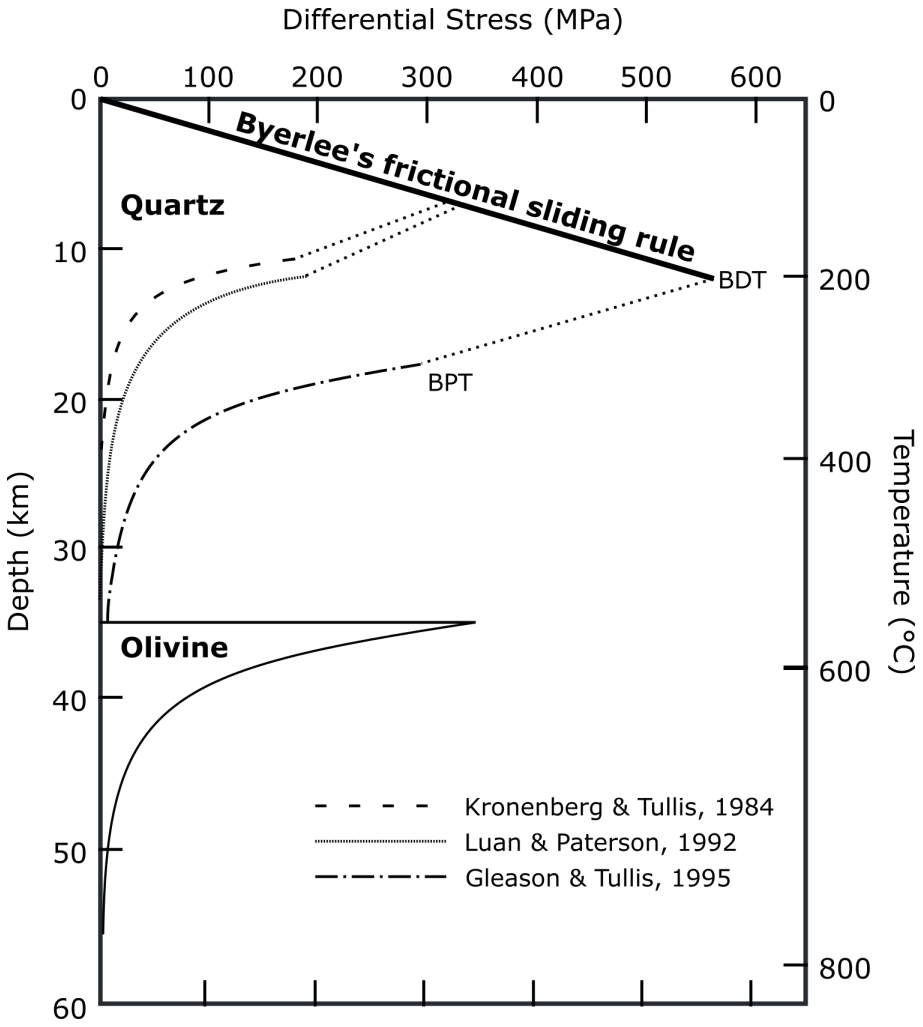

Figure 1.1: (left): Experimentally predicted strength envelope of the wet continental lithosphere after Kohlstedt et al. (Figure 9b, 1995). Differential stresses are calculated from flow laws based on a constant strain rate of 10^{-15} s^{-1}. Flow laws for wet quartzites are from Kronenberg and Tullis (1984), Luan and Paterson (1992), and Gleason and Tullis (1995). The flow law for olivine is from Chopra and Paterson (1984). Strength profiles were calculated based on a geothermal gradient estimated from a surface heat flow of 60 mW m^{-1} (Chapman, 1986). The upper limit of the BDT and the lower limit of the BPT are joined by a dotted line.

By constraining the deformation behaviour of rocks experimentally, profiles of lithospheric strength can be constructed (e.g., Figure 1.1). In the brittle regime, these strength-depth profiles can be tested by comparison to direct measurements of stress from boreholes (e.g., Zoback et al., 1993; Scholz, 2000; Boese et al., 2012) and from earthquake focal mechanisms (e.g., Zoback & Zoback, 2002; Muluneh et al., 2018). In the ductile regime, however, direct measurements of stress are not possible, and instead, stress must be inferred using microstructures in exhumed rocks that have a known relationship with stress—a technique known as paleopiezometry, often shortened simply to piezometry. As the seismogenic parts of major faults zones may contribute little to lithospheric strength (Behr & Platt, 2014), a greater understanding of the strength supported by the load-bearing ductile middle crust is fundamental to our understanding of geological phenomena.

1.2 Piezometry in natural lower-crustal rocks

The most common piezometers for measuring stress in geologic materials are based on dislocation density, recrystallised grain size, or subgrain size. Each type of piezometer is summarised briefly below.

1.2.1 Dislocation density piezometry

A dislocation is a linear defect in a crystalline lattice. The motion of dislocations as a result of the applied stress represents a fundamental mechanism of plastic deformation (Taylor, 1934; Rodriguez, 1996; De Bresser, 1996). Each dislocation elastically strains the crystal lattice and thus has an associated local stress field (Hull & Bacon, 2001, page 63). As the density of dislocations increases, dislocations increasingly interact via their stress fields. Therefore, during plastic deformation, the applied stress is inversely proportional to the dislocation spacing (L). For a simple arrangement of dislocations, L^{-1} can be replaced with $\sqrt{\rho}$, where ρ is the dislocation density (Kohlstedt & Weathers, 1980). This relationship can be more specifically stated as

$$\sigma = \alpha \mu b \rho_t^{0.5}, \tag{1.2}$$

where b is the Burgers vector, μ is the shear modulus, α is a constant depending on the type of dislocation, and ρ_t is the total dislocation density (Taylor, 1934; Kohlstedt & Weathers, 1980). The relationship between applied stress and dislocation density is independent of

strain rate and strain and is only weakly dependent on temperature and pressure through the shear modulus (De Bresser, 1996; Kohlstedt & Weathers, 1980). Empirical relationships between dislocation density and applied stress from numerous experiments on minerals (e.g., McCormick, 1977; De Bresser, 1996; Bai & Kohlstedt, 1992) reveal a deviation of the dislocation-density exponent (k) from 0.5. Twiss (1986) reevaluated previous quantitative data on the relationship between differential stress and the dislocation structure and redefined Eq.1.2 to be written with respect to the differential stress and an empirical stress constant (σ_0), concluding that the sensitivity of the dislocation density to differential stress decreases with decreasing stress. Thus, Eq.1.2 is modified to become:

$$\sigma = \alpha \mu b \rho_t^k - \sigma_0. \tag{1.3}$$

One alternative explanation for the discrepancy in dislocation-density exponent is that the theoretical dislocation-density equation, Eq.1.2, is not dependent on the dimensions of the crystalline volume, that is on the grain size. De Bresser (1996) found $k = 0.5$ if the empirical stress constant was replaced by a grain-size dependent factor.

The application of dislocation-density piezometers to both natural and experimental samples is hampered by the ease with which the dislocation density can be modified after the deformation of interest. Strains as small as 2% can be sufficient to form a new steady-state density (De Bresser, 1996). As the dislocation density is the most easily altered microstructural parameter (Kohlstedt & Weathers, 1980), there are very few examples of the application of dislocation-density piezometers to natural shear zones as they may represent late-stage overprinted deformation (e.g., Kenkmann & Dresen, 2002). In addition, measuring dislocation densities requires either transmission electron microscopy (TEM), which can only be conducted on very small, and therefore potentially unrepresentative areas (Ord & Christie, 1984), or by using decoration techniques, whereby dislocations are 'decorated' by either the introduction of a precipitate along them (Kohlstedt et al., 1976) or through chemical etching (e.g., Wegner & Christie, 1983). Despite enabling the analysis of larger areas, the decoration technique may favourably identify dislocations in a particular orientation relative to the free surface (Durham et al., 1977). Also, the introduction of a precipitate along dislocations can only be used on iron-rich minerals (Kohlstedt et al., 1976).

1.2.2 Grain-size piezometry

Grain boundaries are made up of individually indistinguishable dislocations, which occurs when the spacing between dislocations is comparable to their Burgers vector (Karato, 2012, page 243). The misorientation angle of a grain boundary is defined as the minimum rotation that is needed to bring two lattices separated by that boundary into coincidence (Kassner, 2015, page 28). The critical misorientation angle, that is the lowest angle where dislocations in a boundary are indistingishable, is between 10° and 15° (Trimby et al., 1998; Karato, 2012, page 243), but angles of $\geq 20°$ have also been described (Heinemann et al., 2005).

The presence of grain boundaries increases the internal energy of a crystal (Read & Shockley, 1950). Therefore, at low stresses and small grain size, there will be a thermodynamic driving force to reduce the grain-boundary energy by eliminating grain boundaries through grain growth (Karato, 2012, page 236). Thus in static conditions, there is no 'upper limit' to the grain size, which will increase at a rate controlled by time and temperature (Karato, 2012, page 240).

In the instance where a differential stress is applied to a crystalline aggregate, the grain size will be limited as a result of the applied stress field (Karato, 2012, page 240). The process of changing the shape, size, or orientation of a grain via the stress induced movement of dislocations is referred to as dynamic recrystallisation (Poirier & Guillopé, 1979). Different methods of dynamic recrystallisation are associated with different models that relate the stress experienced by a rock to a unique grain size. One method of recrystallisation is subgrain rotation recrystallisation (SGR), in which dislocations of the same type and sign will align to form subgrain boundaries to reduce the long-range interactions of the stress fields of individual dislocations (Hull & Bacon, 2001, p. 174). As deformation progresses, dislocations climb into subgrain boundaries until their density is so great that it is no longer possible to distinguish individual dislocations and planar structures become grain boundaries. In this instance, the grain size is modelled to be controlled by the dynamic balance between the rate of grain growth and the rate of grain-size reduction through SGR. (Karato, 2012, page 243).

An alternative method of dynamic recrystallisation occurs through grain-boundary migration (GBM) as a result of heterogeneity in the dislocation density, with boundaries migrating towards grains with higher dislocations densities (Karato, 2012, page 243). GBM models suggest the grain size is related to a dynamic balance between the rate of grain growth by grain-boundary migration and the rate of grain-size reduction through the nucleation of new grains (Derby & Ashby, 1987; Shimizu, 1998; Austin & Evans, 2007).

One model, unrelated to the recrystallisation mechanism, was suggested by De Brasser et al. (1998), which proposes that grain size is controlled by the balance of grain size reduction and grain growth and occurs on the boundary between two deformation mechanisms—dislocation creep and diffusion creep.

In each model, the size of recrystallised grains formed during dislocation-mediated deformation exhibits an inverse relationship with stress, which can be approximately described by the equation

$$d = B\sigma^{-M}. \tag{1.4}$$

where σ is the steady-state flow stress, d is the grain size, and B and M are constants.

Current grain-size piezometers for various minerals are plotted in Figure 1.2. Calibrations differ slightly, even for studies conducted on the same mineral, but are more consistent when normalised by the Burgers vector and shear modulus of each mineral (Figure 1.2b). A number of possible explanations exist for the discrepancies among different studies. First, grain-size piezometers have most commonly been based on grain sizes measured by visible-light microscopy (e.g., Karato et al., 1980; Mercier et al., 1977; Stipp & Tullis, 2003; Van der Wal et al., 1993). Newer methods for grain-size analysis are now available, including computer integrated polarisation (Heilbronner & Tullis, 2002, 2006) and electron backscatter diffraction (EBSD) (Cross et al., 2017). Measurements of grain size differ significantly among these three methods (Cross et al., 2017; Hansen et al., 2011), and therefore it is necessary to use a piezometer calibrated with the same measurement technique as that being applied to the natural rocks. Second, how the grain size is defined can also result in differing calibrations. Most commonly, measurements of grain size are based on either the mean line-intercept length or the area-equivalent diameter. In the former, the chord lengths between boundaries defined by a minimum misorientation angle are measured along

sets of lines (Humphreys, 2001). In the latter, the grain size is taken as the diameter of a circle with the equivalent area of the grain (Humphreys, 2001). Converting between these two measurement methods to compare analyses is not trivial, especially in cases where a stereological correction has been applied (De Bresser et al., 2002). Third, different piezometric relationships may arise as a result of the mechanism of recrystallisation (e.g., Rutter, 1995; Stipp & Tullis, 2003). Finally, different minerals may have fundamentally different piezometric relationships.

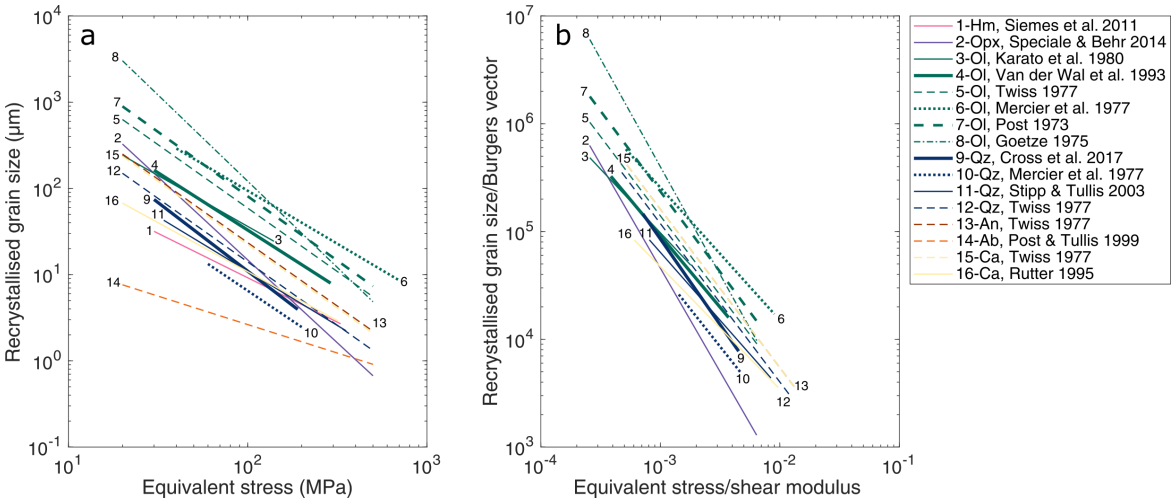

Figure 1.2: (a) Existing grain-size piezometers for geological minerals. (b) Piezometers presented in (a), with stress and grain size normalised by mineral specific shear modulus and main Burgers vectors, respectively. The shear moduli (GPa) are: Qz, 42; Ol, 77.8; Opx, 78.1, Ca, 33; and An, 38. The Burgers vectors (Å) are: Qz, 5.1; Ol, 5.0; Opx, 5.2; Ca, 8.08; and An, 7.0. Lines of the same colour represent the same mineral. The most commonly used piezometers for quartz (Cross et al., 2017) and olivine (Van der Wal et al., 1993) are plotted in bold. If possible, the piezometers are plotted spanning the stress range within which they were calibrated. Otherwise the piezometers were given the arbitrary stress range of 20–500 MPa. The Twiss (1977) piezometers are based on a normalised relationship in (a) and therefore are just rearranged to be plotted in (b)

All the piezometers presented in Figure 1.2a are sufficiently independent of temperature and pressure that the effects of these variables can be neglected in practical applications. Piezometers calibrated with normalised parameters do allow a slight temperature and pressure dependence to be accounted for through their influence on the shear modulus and lattice spacing (Twiss, 1977). However, some studies, such as TerHeege et al. (2005) for halite or Ross et al. (1980) for olivine, have found evidence for a temperature dependence of the recrystallized grain size beyond the effect on the moduli.

An alternative to piezometry, also based on grain size, which includes a temperature dependence, is the paleowattmeter (Austin & Evans, 2007). According to this approach, the average size of recrystallised grains will reach steady state when grain growth and grain-size reduction processes balance. Thus the grain size will depend on temperature if grain growth and grain-size reduction have different kinetics. The paleowattmeter is in good agreement with experimental studies on olivine, quartz, and calcite and in natural rocks gives stresses that are more consistent with flow laws than those from traditional grain-size piezometers, potentially due to the inclusion of a temperature dependance (Austin & Evans, 2007).

Despite the variability among grain-size piezometric calibrations presented in the literature (Figure 1.2), traditional grain-size piezometry has been used to measure the steady-state stresses associated with ductile shear zones in the lithosphere (e.g., Campbell & Menegon, 2019; Kohlstedt & Weathers, 1980; Küster & Stöckhert, 1999; Wex et al., 2019; White, 1979; White et al., 1985). A compilation of stress and depth measurements by Behr and Platt (2014) matches the broad shape of the experimentally-derived rheological profile presented in Figure 1.1 and suggests that the greatest stresses are supported just below the BDT (Figure 1.3).

In all cases, the data from Behr and Platt's (2014) compilation presented in Figure 1.3 were calculated based on the assumption that deformation was occurring by steady-state creep, during which the microstructure and viscosity are invariant with strain, rather than transient creep involving evolution in microstructure and viscosity. Both laboratory experiments and field work have explored the question of whether or not microstructures, especially grain-size, deviate from piezometric relationships when a material is subjected to deformation histories involving changes in stress. High-strain experiments by White et al. (1985) on magnesium, a metal with a hexagonal crystal structure often used as an analog for quartz, found that grain sizes in a localised fine-grained shear zone remained in equilibrium with the initial peak stress under which it formed despite subsequent deformation at lower stresses. However, early load-relaxation experiments by Ross et al. (1980) found that the grain size was instead in equilibrium with the final (lowest) stress experienced by the sample. More recently, Kidder et al. (2016) experimentally investigated the stability of grain size in quartz undergoing non-steady state ductile deformation. Results from their study were in accordance with those of Ross et al. (1980), indicating that the grain size represents the

last increments of stress despite abrupt increases and decreases in stress during deformation. However, during a single relaxation experiment, where stress was lowered to near isostatic conditions the grain size was much larger than would be expected from the piezometer relationship applied to the final stress.

Further research has focused on the application of grain-size piezometers to measure transient stresses in natural crustal rock (Küster & Stöckhert, 1999; Campbell & Menegon, 2019). Grain-size piezometry on eclogitic micaschists and metagranites from the Seisa Zone of the Western Alps measured significantly higher stresses than expected, 300 ± 100 MPa at depths of 16–20 km (Küster & Stöckhert, 1999). Low finite strains in these western alpine rocks suggests that these high-stress episodes must have been transient, and that grain-size piezometry is measuring fault-induced coseismic stress (Küster & Stöckhert, 1999). In addition, recent work by Campbell and Menegon (2019) on dry lower-crustal rocks from the pseudotachylyte-bearing mylonitic shear zones in the eastern Nusfjord region, Lofoten,

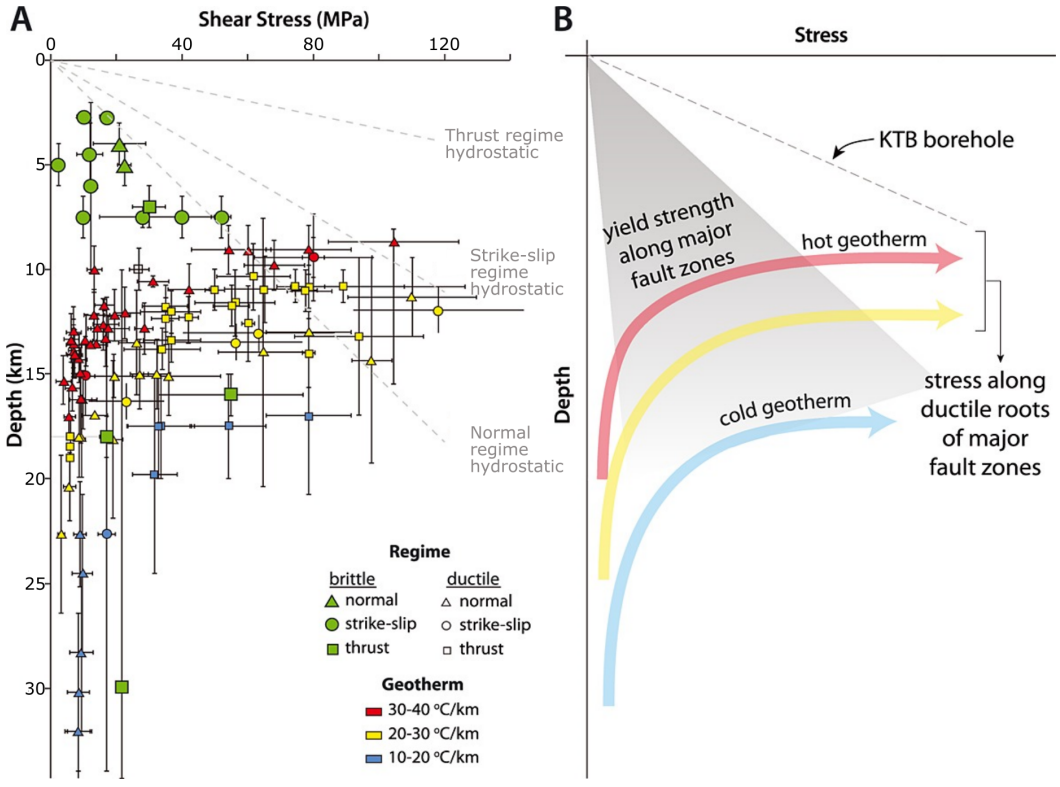

Figure 1.3: (A) Stress-depth data from grain-size piezometry along major ductile shear zones and from shear stress estimates along major faults and intact rocks within the brittle field. Image taken from Behr and Platt (Figure 1, 2014), see article for full details and for data sources. Error bars represent combined uncertainties on estimates of pressure, temperature, and grain size. Shear stress as a function of depth as predicted by Byerlee's law for normal, thrust, and strike-slip faults are also plotted for comparison. (B) Schematic of A with an indication of the relative strength of intact crust based on stress estimates from the KTB borehole (Zoback & Harjes, 1997).

Norway, used grain-size piezometry to infer elevated stresses (98 ± 18 MPa) and strain rates within mylonitised pseudotachylytes, thought to be associated with rapid post-seismic creep in the lower crust.

While previous studies have mostly focused on whether grain-size evolution can measure abrupt changes in stress, the effects of gradual changes in stress due to exhumation were explored by Soleymani et al. (2020). The authors conducted shear experiments on quartz, during which stress was increasing as a result of cooling from 900° to 800°C, at rates of 2°–10°C/h. In this experimental suite, grain size was nearly twice as large as predicted from the grain-size piezometer, indicating that even small changes of temperature slow microstructural evolution and prevent grain size from maintaining the piezometric stress. As such, stress estimates based on the grain sizes of rocks that have been exhumed through the BDT are likely to be underestimates and a function of the stress during the entire deformation (Soleymani et al., 2020).

Despite being the most commonly applied piezometers, two limitations of grain-size piezometers still inhibit their application to natural rocks. First, most experimentally calibrated grain-size piezometers are based on experiments conducted in pure shear, which may not be directly applicable to shear zones. For instance, one set of experiments on albite revealed that grain sizes of samples deformed in both general and pure shear follow the same piezometric relationship (A. Post & Tullis, 1999). However, experiments by Heilbronner and Kilian (2017) on quartz indicated that grain sizes of samples deformed in general shear exhibit a different relationship with stress than those deformed in pure shear. Second, grain-size piezometers are only applicable to monophase aggregates because secondary minerals may modify grain-size evolution by limiting grain-boundary mobility and thus inhibiting grain growth. This effect is referred to as 'pinning' (Evans et al., 2001; Hiraga et al., 2010; Smith, 1948; Tasaka, Zimmerman, Kohlstedt, Stünitz, & Heilbronner, 2017). As most natural rocks contain significant fractions of more than one mineral, and those minerals are typically well mixed in rocks deformed to high strains (e.g., Bystricky et al., 2006; Mehl & Hirth, 2008), pinning severely limits the applicability of grain-size piezometers. Piezometers are thus spatially limited to monophase zones that are then extrapolated to be representative of the stress experienced by the entire rock (e.g., Wex et al., 2019; Gerald et al., 2006; Lusk et al., 2020).

1.2.3 Subgrain-size piezometry

Subgrains are intragranular structures enclosed by low-angle grain boundaries that can be modelled as arrays of dislocations (Karato, 2012, page 94). Such arrays are low-energy configurations of dislocations and therefore form to reduce the energy of a crystalline structure that contains dislocations (Kassner, 2015, page 28). Similar to grain size, the total strain energy of dislocations in a subgrain boundary must be less than or equal to the total energy of the steady-state density of dislocations that are present in the subgrains (Twiss, 1977). There must be a unique subgrain size at which these two energies are equal, which in turn must be related to a unique stress through the relationship between dislocation density and stress (Twiss, 1977).

The inverse relationship between the spacing of subgrain boundaries and the differential stress (e.g., Servi et al., 1952), which takes the same general form as Eq. 1.4, is well established for quartz (Mercier et al., 1977) and olivine (Durham et al., 1977; Goetze, 1975; Karato et al., 1980; Mercier et al., 1977; Raleigh & Kirby, 1970; Toriumi, 1979). A theoretical subgrain-size piezometer applicable to all minerals has previously also been proposed (Twiss, 1977), in which

$$\log\left(\frac{\sigma}{\Gamma}\right) = 0.91 - \log\left(\frac{d_\mathrm{s}}{b}\right), \tag{1.5}$$

where $\Gamma = \frac{\mu}{1-\nu}$, d_s is the subgrain size, ν is the Poisson ratio, and b is the Burgers vector. Being intragranular structures, the size of a subgrain is predicted to be unaffected by the presence of a secondary phase (Hansen & Warren, 2015; White, 1979). Subgrain size has been demonstrated to be more resistant than grain size to annealing (Qin et al., 2003), and under stress, the subgrain size has also been found to reach steady state at a faster rate (Carter et al., 1982).

The subgrain sizes used to calibrate the piezometric relationships presented in Figure 1.4, have either been measured by TEM (e.g., Durham et al., 1977) or by visible-light microscopy via the application of a suitable etching reagent (Karato et al., 1980; Mercier et al., 1977; Toriumi, 1979). However, TEM can only record subgrain sizes that are the same order of magnitude as the field of view, which tends to limit subgrain diameters to $<$ 10 µm (Ord & Christie, 1984). As such, measurements of subgrain size can vary significantly depending on the measurement technique. For example, subgrain sizes of mylonitic quartzites

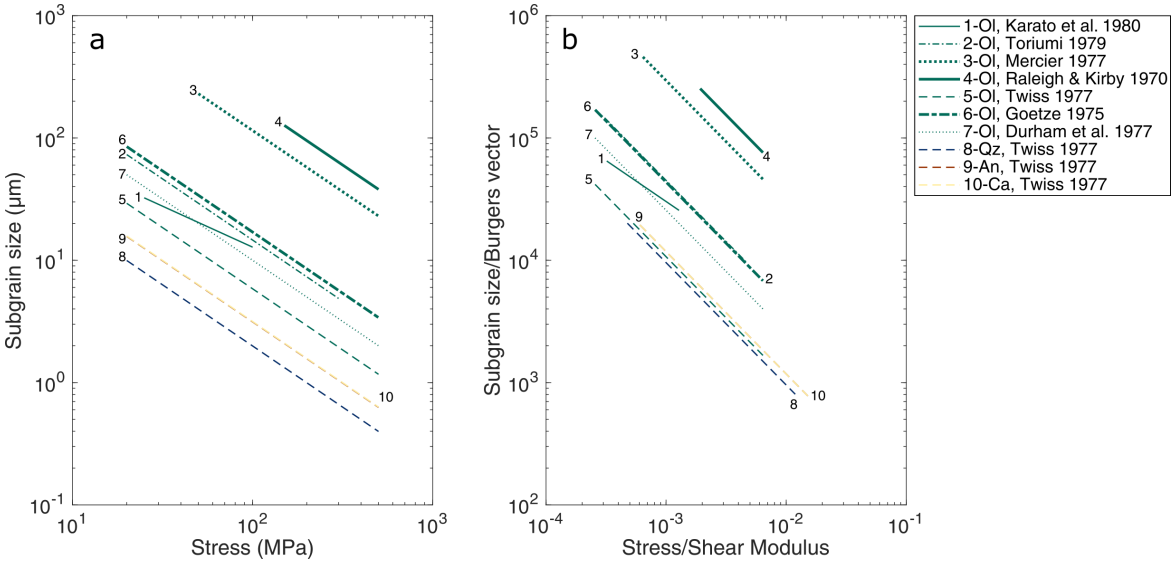

Figure 1.4: (a) Existing subgrain-size piezometers for geological minerals. (b) Piezometers presented in (a), normalised by the shear modulus and Burgers vector of each mineral. The shear moduli and Burgers vectors used for normalisation are the same as in Figure 1.2. Lines of the same colour represent the same mineral. If possible, the piezometers are plotted spanning the stress range within which they were calibrated. Otherwise the piezometers were given the arbitrary stress range of 20–500 MPa.

of the Moine Thrust zone, Assynt, Scotland, measured by visible-light microscopy of etched surfaces yield stresses of approximately 10 MPa, whereas those measured by TEM correspond to stresses of 50–80 MPa (Ord & Christie, 1984). The difficulty in measuring subgrain size both accurately and consistently is one reason for the range of calibrations presented in Figure 1.4 as well as for a relatively few examples of the application of subgrain-size piezometry to natural rocks.

The definition of a subgrain boundary has varied between different subgrain-size piezometry studies. Typically, subgrain size varies depending on the critical misorientation angle used to define the boundaries (Trimby et al., 1998; Valcke, 2008). This variation has been referred to as the 'hierarchy principle', whereby subgrains defined by larger critical misorientation angles are on average bigger. This subgrain hierarchy is found to be more significant in relict grains than in newly recrystallised 'matrix' grains (Figure 1.5).

Experimental work by Ross et al., (1980) divided subgrains into those in newly recrystallised grains (neoblasts) and those in relict grains (porphyroclasts). Subgrains in different grains were found to represent different stages in the deformation history of the rock with subgrains within neoblasts (relatively strain-free grains) recording the lowest stresses and subgrains within paleoblasts (old, strained grains) recording the maximum stress felt by

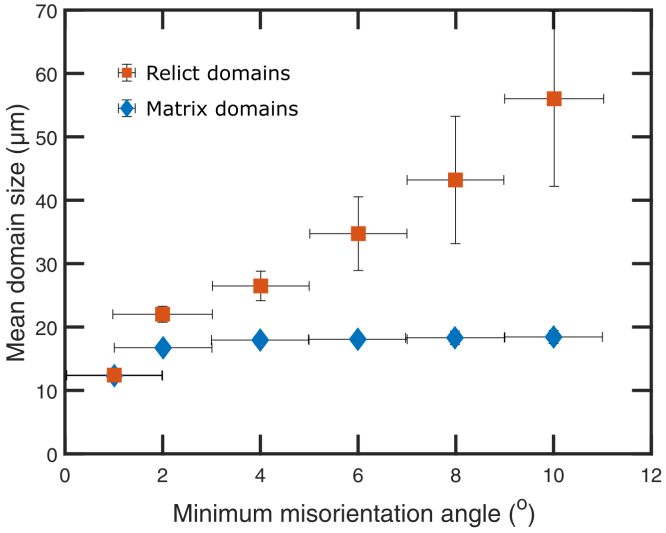

Figure 1.5: The mean domain size in low-strain quartz plotted against the minimum misorientation angle (°) used to define a boundary for relict (a.k.a. core) and matrix domains. Error bars indicate 95% confidence levels. Reproduced from Figure 6 of Trimby et al. (1998).

the sample.

Various studies have also separated subgrains based on whether they are themselves 'mantle' subgrains, which are located close to the grain boundaries and contain no internal distortion of the crystal lattice, or 'core' subgrains, which are located in the centre of old grains and contain low-angled ($< 1°$) internal structures (Figure 1.6). In a study of quartz mylonites from the Moine Thrust Zone, Scotland, the size of core subgrains was consistent with stresses estimated by grain-size piezometry (White, 1979). The size of mantle subgrains, on the other hand, gave higher stresses interpreted to be the result of elevated local stresses at grain boundaries caused by the interference of adjacent grains (White, 1979).

Valcke et al. (2007) further explored the concept of different subdivisions of subgrains by treating the relationships between stress and core and mantle subgrains separately. The sizes of core subgrains were found to decrease slightly with increasing stress but were also influenced by grain size and temperature. The size of mantle subgrain sizes were also found to decrease with increasing stress, but the stress sensitivity was related to the angle used as the critical misorientation angle, with a greater stress sensitivity at higher angles (Valcke, 2008).

The lack of consistency among subgrain-size piezometers calibrated for a single mineral, and between different minerals when normalised by the shear modulus and the Burgers vector (Figure 1.4), suggest that the lack of a criterion for identifying and measuring subgrains in these calibrations could be significant. The water content, temperature,

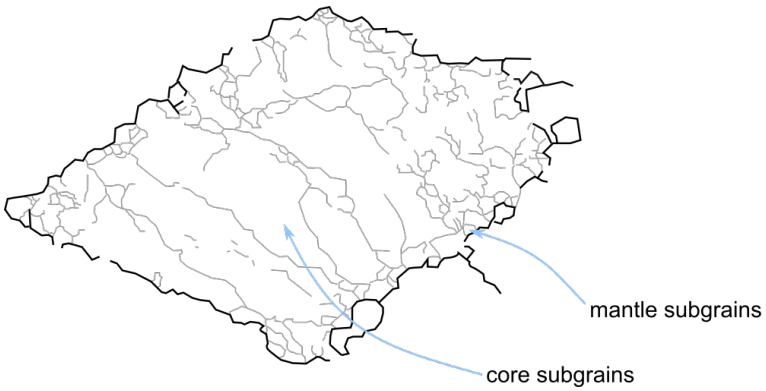

Figure 1.6: Schematic illustrations of core and mantle subgrains. Grain boundaries, with misorientations of > 10°, are shown in black and subgrain boundaries, with misorientations of > 1° are shown in grey. Modified from Figure 3.9 from Valcke (2008).

history of strain hardening, and grain size of the starting material have all also been proposed to influence the subgrain structure (Valcke et al., 2006) and thus the relationship between subgrain size and stress. As such, there is considerable scope for improvements in the accuracy and sophistication of subgrain-size piezometry.

1.3 Focus of this study

Measuring the strength of the plastically deforming lithosphere using grain-size piezometry is limited to areas that consist only of a single mineral. Subgrains present an opportunity to measure stress in polymineralic rocks. However, the lack of consensus on which boundary misorientation angles to include, and which types (i.e., core, mantle, neoblast, porphyroclast) of subgrain boundaries should be used in any calibration, has limited the application of existing subgrain-size piezometers to natural rocks. Nonetheless, the development of EBSD has enabled the rapid measurement of subgrain sizes (e.g., Ambrose et al., 2018; Hansen & Warren, 2015; Valcke et al., 2006) and presents an opportunity to re-explore the use of subgrain-size piezometry in rock deformation. In addition, the applicability of subgrain-size piezometry to polymineralic rocks has not been explored in detail, especially in relation to how the stresses supported by individual phases relate to the bulk stress supported by the rock.

This thesis examines the use of subgrain-size piezometry on experimentally and naturally deformed polymineralic rocks. First, a new subgrain-size piezometer is calibrated for EBSD using experiments on quartz and olivine. Second, the hypothesis that subgrains are unaffected by the presence of secondary phases is explored by comparing *in-situ* stress measurements collected by X-ray diffraction with *ex-situ* stress estimates from subgrain-size piezometry. Third, the subgrain-size piezometer is used to explore stress partitioning

between olivine and orthopyroxene in harzburgites of varying composition. Finally, this subgrain-size piezometer is applied to mylonites from the Great Slave Lake Shear zone, Northwest Territories, Canada, to provide new constraints on the strength of lower-crustal rocks.

2 A subgrain-size piezometer calibrated for EBSD

This chaper is published in Geophysical Research Letters,

DOI: **https://doi.org/10.1029/2020GL090056**

Authors: R.M. Goddard, L.N. Hansen, D. Wallis, M. Stipp, C.W. Holyoke III, K.M. Kumamoto, & D.L. Kohlstedt

Abstract

We calibrate a subgrain-size piezometer using electron backscatter diffraction (EBSD) data collected from experimentally deformed samples of olivine and quartz. Systematic analyses of angular and spatial resolution test the suitability of each dataset for inclusion in calibration of the subgrain-size piezometer. To identify subgrain boundaries, we consider a range of critical misorientation angles and conclude that a 1° threshold provides the optimal piezometric calibration. The mean line-intercept length, equivalent to the subgrain-size, is found to be inversely proportional to the von Mises equivalent stress for datasets both with and without the correction of Holyoke and Kronenberg (2010). These new piezometers provide stress estimates from EBSD analyses of polymineralic rocks without the need to discriminate between relict and recrystallised grains and therefore greatly increase the range of rocks that may be used to constrain geodynamic models

2.1 Introduction

Quantitative constraints on the stresses associated with past deformation events in the ductile portion of the lithosphere are key to developing and testing geodynamic models. One method of estimating past stress magnitudes is to measure microstructural elements that can be related to stress through experimental calibrations, a technique known as piezometry. Paleopiezometry has provided key estimates of the strength of continental (e.g., Kohlstedt & Weathers, 1980; Stipp, Stünitz, Heilbronner, & others, 2002; Weathers et al., 1979) and oceanic (e.g., Hansen et al., 2013; Jaroslow et al., 1996; Speckbacher et al., 2011; Warren & Hirth, 2006) fault zones, yielded insight into the mechanisms of localisation in outcrop-scale shear zones (e.g., Austin et al., 2008; Gueydan et al., 2005; Haertel & Herwegh, 2014; Linckens et al., 2011; Skemer et al., 2010, 2013), and enabled tests of the extrapolation of laboratory-derived rheological laws to geological conditions (e.g., Behr & Platt, 2011; Hansen & Warren, 2015; Hirth et al., 2001; Stipp, Stünitz, Heilbronner, & others, 2002; Wex et al.,

2019). Thus, paleopiezometry is an essential tool for field-based quantitative investigations of the mechanical behaviour of the lithosphere.

The most frequently used piezometers are based on the size of dynamically recrystallised grains, herein referred to as grain size (Karato et al., 1980; Rutter, 1995; Schmid et al., 1980; Stipp & Tullis, 2003; Twiss, 1986; Van der Wal et al., 1993). However, piezometers based on grain size are only applicable to monophase aggregates as secondary minerals may modify grain size by limiting grain-boundary mobility and thus inhibiting grain growth, an effect known as 'pinning' (Evans et al., 2001; Hiraga et al., 2010; Smith, 1948; Tasaka, Zimmerman, Kohlstedt, Stünitz, & Heilbronner, 2017).

Like grain size, subgrain size varies systematically with differential stress during steady-state deformation (Luton & Sellars, 1969; Twiss, 1986). Piezometers based on subgrain size are advantageous for two reasons: 1) subgrain sizes are not modified by grain-boundary pinning (Hansen & Warren, 2015; White, 1979), and 2) subgrains can form over relatively small strain intervals ($\leq 10\%$, Biberger & Blum, 1992; Ross et al., 1980) in both relict and recrystallised grains. Therefore, subgrain-size piezometry can be applied to samples subject to small strains and obviates the need to identify grains that formed by dynamic recrystallisation. Subgrain-size piezometry therefore provides a tool to evaluate past stress experienced by a broader range of rocks, including polymineralic rocks (e.g., Hansen & Warren, 2015).

Relationships between applied stress and subgrain size measured using optical microscopy or transmission electron microscopy (TEM) have been established for quartz (Mercier et al., 1977), olivine (Durham et al., 1977; Goetze, 1975; Karato et al., 1980; Toriumi, 1979), and calcite (Friedman & Higgs, 1981; Platt & De Bresser, 2017). In addition, subgrain-size piezometers applicable to multiple minerals have previously been proposed (Shimizu, 1998; Twiss, 1986). However, different methods for measuring microstructural features have different detection limits, which can lead to systematic offsets between piezometric relationships for the same mineral (Cross et al., 2017; Hansen et al., 2011). Currently, no subgrain-size piezometers have been calibrated for data collected by electron backscatter diffraction (EBSD), despite the relatively simple sample preparation, rapid data acquisition, and precision in misorientation angles of better than $\pm$ 0.3° (Figure 4 in Wallis, Hansen, et al., 2019) associated with this technique.

Here, we present EBSD measurements of subgrain size in experimentally deformed olivine and quartz samples and derive a single piezometric relationship for both minerals. We explore the sensitivity of the piezometric calibration to the lower cut-off of subgrain-boundary misorientation angles and provide tests for the number of intercept lines, the number of grains, and the step size required to accurately capture the subgrain size. The resulting piezometer greatly extends the range of rocks for which EBSD data can provide quantitative stress estimates.

2.2 Method

2.2.1 Sample Description

Samples from three sets of experiments conducted on quartz and olivine were analysed. The experimental conditions associated with each sample can be found in the supplementary material (Table A.1). Each stress reported in Table A.1 is the von Mises equivalent stress (hereafter referred to solely as the equivalent stress, σ) experienced by the sample, which is assumed to be associated with the microstructures observed at the end of the experiment. All samples were deformed in a regime in which deformation is rate-limited by the motion of dislocations.

Quartz Experiments

Quartz samples prepared from Black Hills Quartzite were deformed in two sets of experiments, denoted Qz-1 and Qz-2. Qz-1 samples were deformed in a Griggs apparatus at Brown University (Stipp & Tullis, 2003). Qz-2 consists of samples deformed in a Griggs apparatus either at Texas A&M University or at Brown University (Holyoke & Kronenberg, 2013; Holyoke & Tullis, 2006). Both sets of experiments were conducted at a confining pressure of 1.50–1.56 GPa and temperatures in the range 800°–1100°C. Samples included in the calibration lay within recrystallisation regimes 2 and 3 as defined by Hirth and Tullis (1992), as the relationship between subgrain size and stress appears to change in regime 1 (cf., Stipp & Tullis, 2003).

The Qz-1 samples consisted of cylinders deformed in axial compression at constant displacement rates of 1.8×10^{-6}–1.7×10^{-3} mm/s. Flow stress, taken as an average of the value between 10% strain and the value at the final strain (17–41%) in each experiment,

ranged between 34 ± 16 and 268 ± 40 MPa (Stipp & Tullis, 2003).

Qz-2 samples were subjected to either general shear or axial compression at constant equivalent strain rates of 1.6×10^{-6}–1.15×10^{-5} s^{-1}. Final shear strains ranged from 50% to 610%. The only experiment deformed in axial compression in Qz-2, TMQ-7, reached a final axial strain of 15.6%. All Qz-2 samples, excluding W-1105, were deformed to their yield point. The ability of subgrains to keep pace with the stress after very little strain means the lack of steady-state conditions should not influence the piezometric calibration. Therefore the final flow stress, converted into the equivalent stress, was taken as the stress associated with the final microstructures.

Correction of the mechanical data for the friction on the σ_1 piston was performed in Qz-1 according to the procedures of Gleason and Tullis (1995) and Stipp and Tullis (2003) and in Qz-2 according to the procedures of Holyoke and Tullis (2006). We then compare two sets of stresses to subgrain size, either with or without a second friction correction described by Holyoke and Kronenberg (2010, 2013) to account for increased friction due to a Poisson effect on the load column during loading of the sample.

Olivine Experiments

Data from olivine samples deformed in a number of different axial compression and torsion experiments were compiled to form the 'Ol' dataset (Hansen et al., 2011, 2012; Pommier et al., 2015; Tasaka et al., 2016; Tasaka, Zimmerman, Kohlstedt, Stünitz, & Heilbronner, 2017). Polycrystalline Fo_{90} and Fo_{50} samples were fabricated from San Carlos olivine (Hansen et al., 2011) or from a combination of oxide powers and San Carlos olivine (Tasaka, Zimmerman, & Kohlstedt, 2017), respectively. Experiments were conducted in a servo-controlled, internally heated, gas-medium apparatus (Paterson, 1990) at the University of Minnesota at a confining pressure of 300 MPa and temperatures of 1150°–1250°C. Equivalent strain rates were 9×10^{-6}–1.48×10^{-3} s^{-1}. Stress was measured with an internal load cell and controlled to ± 1 MPa for axial compression experiments (Hansen et al., 2011) and ± 2 MPa for torsion experiments (Tasaka et al., 2016). Stresses measured during torsion experiments were converted to equivalent stress following Paterson and Olgaard (2000). In axial compression experiments, maximum axial strains reached up to 20%. In torsion experiments, except PT-0966, strain was recorded as the shear strain at the outer radius and reached up to 880%. For sample PT-0966 the shear strain, recorded as 500%, was calculated

from an originally vertical crease in the jacket formed during the initial pressurisation of the sample.

2.2.2 Acquisition of Microstructural Data

For EBSD analyses, samples deformed in axial compression were cut parallel to the cylindrical axis (Hansen et al., 2011; Holyoke & Kronenberg, 2013; Stipp & Tullis, 2003). For samples deformed in torsion, tangential sections were chosen for analysis (Hansen et al., 2012; Tasaka et al., 2016; Tasaka, Zimmerman, Kohlstedt, Stünitz, & Heilbronner, 2017). In the direct shear geometry, sections parallel to the shear direction and perpendicular to the shear plane were chosen (Holyoke & Tullis, 2006). The sectioned surfaces were prepared by polishing with diamond lapping films or suspensions with decreasing grit sizes from 30 to 0.05 µm and most samples were finished by polishing with 0.03 or 0.04 µm colloidal silica.

EBSD data were collected with an FEI Quanta 650 FEG E-SEM in the Department of Earth Sciences, University of Oxford, equipped with Oxford Instruments AZtec (Version 3.3) acquisition software and a NordlysNano EBSD camera. Samples, were tilted at 70° and mapped in low vacuum (50–60 Pa, H_2O) at accelerating voltages of 20–30 kV with step sizes of 0.1–1.0 µm. Noise reduction was performed using Oxford Instruments Channel5 software. Non-indexed points with ≥ 6 indexed neighbours within the same grain were assigned the average orientation of their neighbours. In addition, pixels in images of quartz that were systematically misindexed due to pseudosymmetry were corrected by applying a rotation of 60° around [0001] (Trimby et al., 2002).

For our piezometer, subgrains were measured using the line-intercept method. This method, compares adjacent pixels on evenly spaced lines transecting the sample (Figure 2.1a). Along each line, misorientations greater than a specified angle, the critical misorientation angle, are detected and the intercept length between misorientations recorded. As such, both subgrain boundaries and grain boundaries are captured in this measurement. The number of intercept lines is increased until the measured mean line-intercept length stabilises ($\pm$ 2.5%), thus ensuring the number of intercepts is sufficient to accurately estimate the mean value.

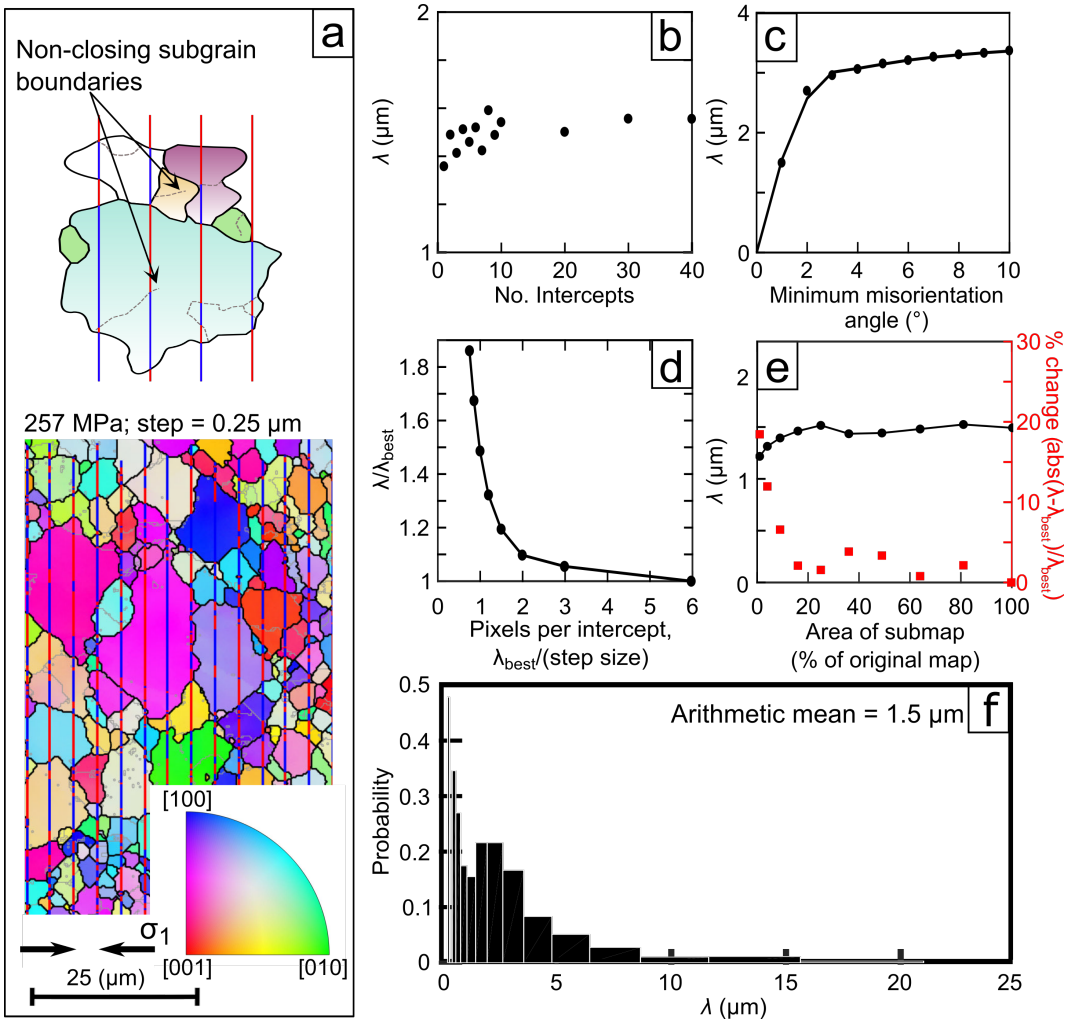

Figure 2.1: Full analysis of PI-1523 (olivine), where λ is the measured mean line-intercept length, and λ_{best} is the value of λ associated with the smallest step size and largest map area. (a) Schematic and example of the line-intercept method on a map of the sample coloured by normal to the section. (b) Mean line-intercept length versus the number of intercept lines taken in both the vertical and the horizontal direction. (c) Mean line-intercept length versus minimum misorientation angle used to define a subgrain boundary. (d) Analysis of the sensitivity to step size. See main text for description. (e) Analysis of the sensitivity to map area. See main text for description. (f) Histogram of line-intercept lengths with a logarithmic bin width.

The line-intercept method is preferred over other grain-size measurement techniques because it includes non-closing subgrain boundaries. When analysing subgrain boundaries with small misorientation angles, it is important to include such primitive structures because subgrain boundaries do not always fully enclose an isolated region (e.g., Figure 2.1a & Figure 2.2). Additional benefits compared to alternative area-based subgrain-size measurement include lower sensitivity to changes in step size (Mingard et al., 2007; Valcke et al., 2006), faster processing times (Humphreys, 2001), and lower sensitivity to anomalous clusters of data points missed during post-processing (Hansen et al., 2011).

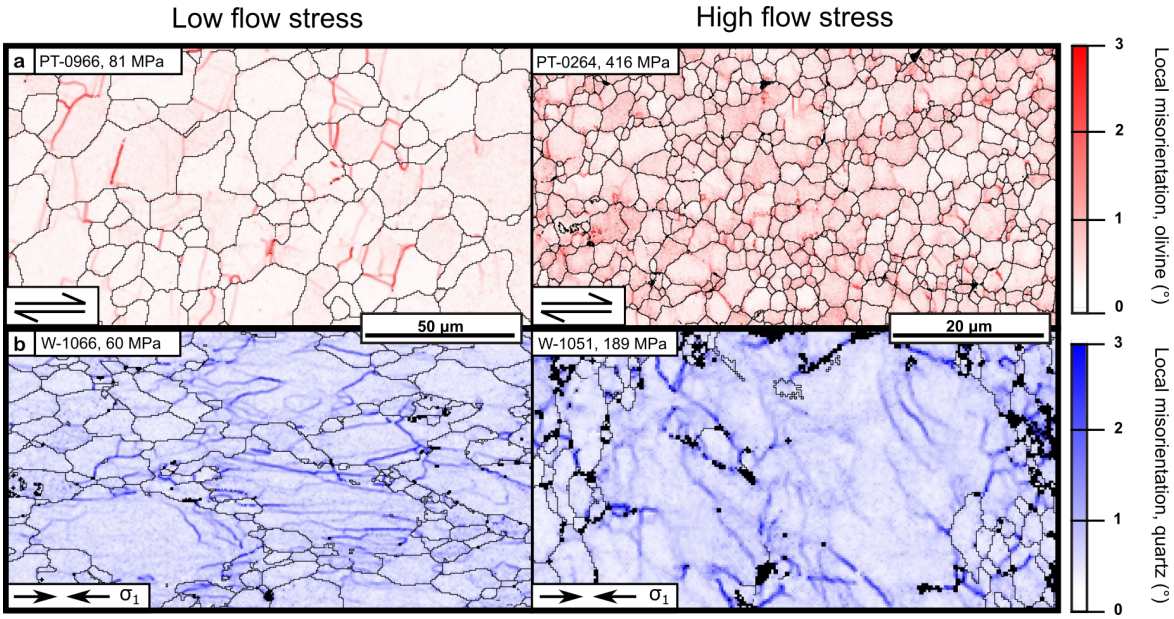

Figure 2.2: Maps of local misorientation for (a) olivine and (b) quartz samples deformed at low and high flow stresses. Black lines are grain boundaries (misorientation $\geq 10°$). Unindexed pixels are also plotted in black. Experiments conducted at high flow stresses have higher densities of subgrain boundaries.

To obtain sample averages, we use the arithmetic mean of the line-intercept lengths. This approach provides the mean spacing between all boundaries with misorientation angles above the chosen critical value. An alternative average, the geometric mean, is more sensitive to misindexed pixels and variations in step-size (Mingard et al., 2007). In previous studies, a stereological correction was commonly applied to convert the mean line-intercept length from a 2-D section to the mean grain diameter in 3-D (Hansen et al., 2011; Hansen and Warren, 2015; Underwood, 1970, pages 80–93; Valcke et al., 2006). As the choice of 3D correction adds an additional layer of uncertainty to the data processing, we avoid any correction and simply use the mean line-intercept length, λ, as the microstructural length scale in our piezometric calibration.

2.2.3 Sensitivity Tests

As EBSD maps only examine a portion of a deformed material, we devised two tests to assess whether a mapped area is representative of the bulk sample. These tests examine the effect of the size and spatial resolution of the map on the measured values of mean line-intercept length. MATLAB® scripts to perform these tests are presented in the Supplemental Material (A.1).

As increasing the step size of an EBSD map leads to overestimates of grain size (Cross et al., 2017; Humphreys, 2001), we tested the influence of step size on measured subgrain size. We evaluated the spatial resolution by implementing the same step-size analysis test as Cross et al.(2017). In this procedure, the resolution of the map is artificially reduced (i.e., the effective step size increased) by selecting subsets of points in the map on a regular grid. The mean line-intercept length is then measured and compared to the mean line-intercept length associated with the smallest step size, λ_{best}. We refer to the ratio of λ to λ_{best} as the intercept variation factor. The spatial resolution is deemed sufficient if the measured mean line-intercept length is not sensitive to the effective step size. For each sample in Figures 2.1d and A.2, decreasing the pixels per intercept length (defined as the λ_{best} divided by the effective step size) had an insignificant effect on the mean line-intercept length. The presence of an asymptote at an intercept variation factor of 1 is evidence that that step size is small enough to capture the mean line-intercept length.

In the second test, we evaluated the size of the map relative to the mean line-intercept length, that is, whether a sufficient number of intercepts were measured for their mean value to be representative of the sample mean. We propose that, rather than being fixed (Humphreys, 2001, 2004; Valcke et al., 2006), the number of required subgrains (or intercept lengths) is likely to depend on the variance of the true subgrain-size distribution. Therefore, for each map, we tested the effect of map area on the mean line-intercept length by measuring the mean line-intercept length from a centred sub-area of the original map. Initially, this sub-area was 1% of the size of the original map. We then measured the mean line-intercept length as the sub-area was progressively increased in size. As the size of the sub-area increases, the mean line-intercept length should asymptotically approach the mean for the entire map, indicating the full map area is sufficiently large. Examples of the area-analysis technique are presented in Figures 2.1e and A.3. Samples that demonstrated a strong dependence of mean line-intercept length on the size of the sub-area (e.g., Figure A.4) were mapped multiple times. The mean line-intercept length was then calculated as the average intercept length across all the maps to ensure representative measurement.

2.3 Results

To identify a general piezometric relationship applicable to both quartz and olivine, the equivalent stress and the mean line-intercept length were normalised by the shear modulus, μ, and the Burgers vector, b, respectively. We then explored the effect of the choice of critical misorientation angle on mean line-intercept length, testing angles ranging from 1° to 10° (e.g., Figure 2.1c). We did not evaluate critical misorientation angles below 1°, the minimum angle that has previously been used to define a subgrain boundary (e.g., Ambrose et al., 2018; Hansen & Warren, 2015). Reanalysis of a number of our maps (e.g., Figure A.6) with high-angular resolution EBSD (Wallis, Parsons, and Hansen, 2019; Appendix A.3) found the resolution adequate for subgrain-size piezometry. We did not evaluate critical misorientation angles above 10° as we consider this value to be the lower bound of the definition for a high-angle grain boundary (Karato, 2012, page 243; Trimby et al., 1998). For all values of the critical misorientation angle, in all three datasets, the mean line-intercept length exhibits a power-law relationship with the equivalent stress (Figure A.5). The three datasets coincide best at lower critical misorientation angles. The discrepancy between the quartz datasets and the olivine dataset increases as a function of increasing critical misorientation angle. Therefore, we used a critical misorientation angle of 1° in our calibrations.

We fit a power-law equation using least squares linear regression on the logarithmic transformation of mean line-intercept length against equivalent stress, yielding the following equations:

$$\frac{\lambda}{b} = 10^{0.6\pm0.7}\left(\frac{\sigma}{\mu}\right)^{-1.2\pm0.3} \tag{2.1}$$

and

$$\frac{\lambda}{b} = 10^{1.2\pm1.0}\left(\frac{\sigma}{\mu}\right)^{-1.0\pm0.4} \tag{2.2}$$

Equations 2.1 and 2.2 represent piezometers with and without the calibration of Holyoke and Kronenberg (2010) discussed above in Section 2.2.1, respectively. Uncertainties are reported as 95% confidence intervals. Here we use b = 0.51 nm, 0.48 nm, or 0.48 nm and μ = 42.0 GPa, 77.8 GPa, or 62.6 GPa for quartz Fo_{90}, and Fo_{50}, respectively (see supplementary Text A.2 for discussion).

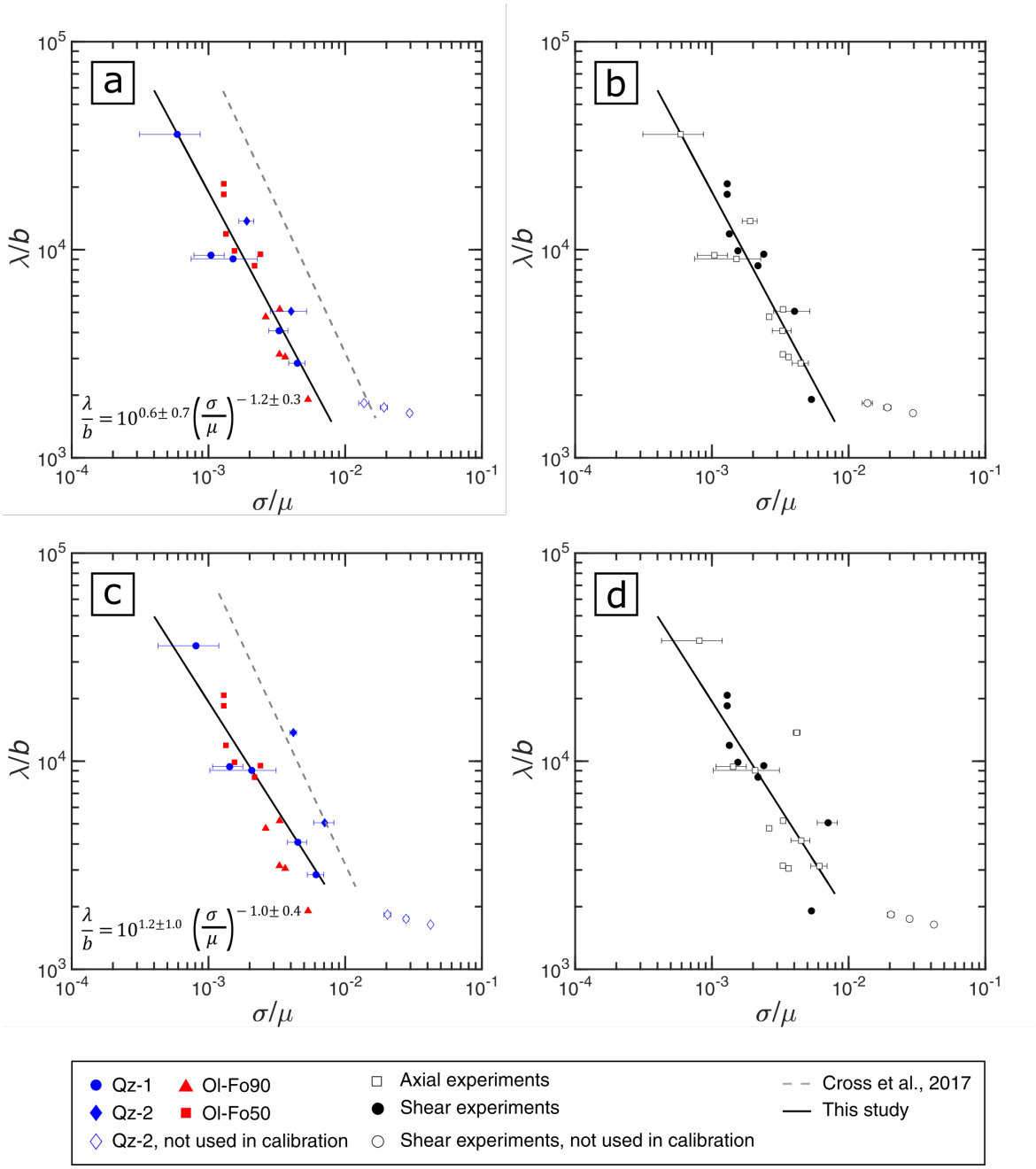

Figure 2.3: Mean line-intercept length, normalised by the Burgers vector as a function of the equivalent stress, normalised by the shear modulus. In (a) and (b) the correction from Holyoke and Kronenberg (2010) was applied to the quartz data, whereas in (c) and (d) the correction was not applied. (a) and (c) data are coloured by phase, with the recrystallised grain-size piezometer of Cross et al. (2017), also calibrated for EBSD, plotted for comparison. (b) and (d) plot the same data as in (a) and (c), respectively, coloured by deformation geometry. Axial experiments refer to those conducted in pure shear and shear experiments refer to those conducted in general shear or simple shear.

2.4 Discussion

The organisation of dislocations into subgrain boundaries is driven by the associated reduction in the strain energy of the system (e.g., Raj & Pharr, 1986; Read, 1953, page 226). During deformation, the mean subgrain size varies systematically with the applied stress. Normalising the stress by the shear modulus and the subgrain size by the Burgers vector collapses mineral-specific piezometers into a single relationship (e.g., Twiss, 1986). Our results thus define a subgrain-size piezometer that can be used on multiple minerals. As our piezometer is calibrated by EBSD, it differs from calibrations obtained by different measurement techniques (Durham et al., 1977; Goetze, 1975; Karato et al., 1980; Mercier et al., 1977; Toriumi, 1979). We also provide a set of tests that assess the suitability of a dataset for analysis by this method based on factors including the number of linear intercepts, the step size, and the map area. The ability to perform these tests routinely in an automated and objective manner provides clear benefits over existing quality control measures (e.g., Humphreys, 2001, 2004; Valcke et al., 2006).

Subgrain-size piezometry has several benefits compared to grain-size piezometry. First, subgrain-size piezometry is insensitive to the presence of secondary minerals and the pinning of grain boundaries (Hansen & Warren, 2015; White, 1979). As most rocks are polymineralic and the presence of secondary phases leads to smaller-than-expected recrystallised grains, the majority of existing stress estimates were derived from spatially restricted monomineralic rocks or domains. In contrast, in polymineralic rocks, subgrain-size piezometry should record the average stress supported by the analysed phase, regardless of the fraction of secondary phases. Thus, the subgrain-size piezometer can be used to analyse the stress supported by each phase deforming by dislocation creep in polymineralic rocks. Consequently, estimates of stresses supported by the lithosphere based on grain-size piezometery (e.g., Behr & Platt, 2014; Weathers et al., 1979; White, 1979) can be compared to new data acquired using subgrain-size piezometry on more representative rock types.

Grain-size piezometry also requires the user to distinguish between recrystallised and relict grains, the proportions of which depend on total strain. Previously, the bimodal grain-size distribution of partially recrystallised rocks allowed the characterization of recrystallised and relict grains on the basis of size (e.g., A. Post & Tullis, 1999; Stipp & Tullis, 2003). This method truncates the grain-size distribution, thereby modifying the mean grain

size and the resulting stress calculated from that grain size. More recent work used the degree of intracrystalline lattice distortion within each grain to identify recrystallised grains on the assumption that relict grains have a greater degree of internal distortion than recrystallised grains (Cross et al., 2017). Although this new method provides a working calibration, it adds additional steps and assumptions to the analysis. In deforming materials with active subgrain formation, both recrystallized and relict grains develop subgrain boundaries that fall on a single piezometric relationship (Ross et al., 1980). Because our calibration contains subgrains both from relict and recrystallised grains, as long as both sets of grains contain subgrains in the sample to be analysed, no distinction between them is necessary in measuring subgrain size. Instead, we only need to define a critical misorientation angle. A 1° critical misorientation angle is consistent with previous observations in NaCl that subgrain boundaries tend to have misorientation angles $< 2°$ at strains of 15% and $< 5°$ at strains of 50% (Pennock et al., 2005). In addition, Trimby et al. (1998), observed that subgrains in relict and recrystallized grains of quartz were the same size based on a 1° critical misorientation.

Finally, subgrain-size piezometry is independent of flow geometry. In contrast, samples deformed in general shear and axial compression may exhibit different grain sizes at the same equivalent stress. Experiments by Heilbronner and Kilian (2017) revealed that quartzites deformed in general shear developed a larger grain size at a given stress than would be expected from piezometers calibrated with experiments conducted in axial compression. In addition, the compilation of data for quartz presented by Tokle et al. (2019) demonstrates experiments conducted in general shear yield a different grain-size piezometer than experiments conducted in axial compression. To explore whether the flow geometry also affects subgrain sizes, we regrouped the data according to whether the samples were deformed in a pure shear (i.e., axial compression) or general or simple shear, geometry. In Figures 2.3b and 2.3d, there is no obvious dependence of the mean line-intercept length on the deformation geometry. Therefore, we suggest that our single subgrain-size piezometer can be applied to a wide range of rocks, regardless of flow geometry.

It is necessary to highlight two potential limitations of subgrain-size piezometry. First, it appears that the observed relationship between subgrain size and stress is not applicable to deformation at high stresses (Figure 2.3). The relationship between subgrain

size and stress may change at higher stresses as the recrystallisation mechanism changes, similar to the relationships observed for the size of recrystallised grains of quartz (Stipp & Tullis, 2003), which is why the three samples deformed in this high-stress regime were not included in our calibrations. Similarly, differences in the processes of subgrain formation or in the mechanisms of dynamic recrystallisation might require different calibrations at significantly lower stresses (e.g., Valcke et al., 2007, 2015; Stipp et al., 2010). Therefore, we recommend that our piezometer should be applied within the normalised subgrain size and stress range over which it was calibrated. This range corresponds to mean line-intercept lengths of 1–9 µm for olivine and 1–18 µm for quartz and a similar range for other silicate minerals. These limits on subgrain size correspond to stress ranges of 60–420 MPa and 20–240 MPa for olivine and quartz, respectively.

Second, the potential for modifying subgrain size through static annealing or stress relaxation after deformation remains poorly constrained. Ross et al. (1980) suggested that subgrains record the highest stress in rocks subjected to complex deformation histories. However, we demonstrate that a strong correlation between subgrain size and final stress is apparent, even in cases in which the larger stresses were experienced earlier in the deformation history (Hansen et al., 2012; Holyoke & Tullis, 2006). Furthermore, experiments on steel by Qin et al. (2003) revealed that subgrains were only able to coarsen with additional strain while under stress of a reduced magnitude, whereas they did not coarsen during static annealing. These observations suggest that subgrain sizes best reflect the last increments of deformation, although further work exploring the effect of stress changes is clearly required to fully investigate the mobility of subgrain boundaries in minerals. In comparison, the response of the grain size to non-steady-state creep in geological materials has been the focus of recent field studies (e.g., Campbell & Menegon, 2019) and experimental work (e.g., Kidder et al., 2016), and as such, is better constrained than that of the subgrain size. If the subsequent modification of subgrain size occurs on a different timescale than the modification of other microstructural features such as dislocation density or recrystallized grain size, then combined analysis using multiple piezometers may yield information about complex stress histories (Kohlstedt & Weathers, 1980; White, 1979).

2.5 Conclusions

1. We present a subgrain-size piezometer calibrated for EBSD with a 1° critical misorientation angle. This piezometer, which was derived from data for olivine and quartz, should be applicable to other phases.

2. The size of subgrains calculated based on a critical misorientation angle of 1° appears to be independent of the deformation geometry, that is, whether the specimen is deformed in simple/general shear or pure shear.

3. It is recommended that our piezometer should be applied over the normalised subgrain size and stress range with which it was calibrated. This corresponds to mean line-intercept lengths of 1–9 µm for olivine and 1–18 µm for quartz corresponding to stresses of 60–420 MPa and 20–240 MPa, respectively

4. MATLAB® scripts, provided in the Supplemental Material, can be used to test the suitability of input data for stress estimates specifically in terms of spatial resolution and size of the data set.

Acknowledgements

The authors thank Andrew Cross for useful discussions. Jon Wade and Phillip Gopon are gratefully acknowledged for technical support on the SEM. We thank Luca Menegon and Phil Skemer for insightful reviews and Steve Jacobsen for editorial handling. This research was supported by the NERC Environmental Research DTP grant NE/L002612/1, University of Oxford, RMG, and National Science Foundation (NSF) Awards EAR-1755805 to DLK, EAR-1806791 to KMK and EAR-1848380 to CWH. Qz-2 experiments were performed by CWH with support from NSF grants EAR-0208150 to Jan Tullis and EAR-1321882 to CWH and Andreas K. Kronenberg. In addition, DW acknowledges support from the Netherlands Organisation for Scientific Research, User Support Programme Space REsearch, grant ALWGO.2018.038. EBSD data sets are available from Oxford University Research Archive (DOI: https://doi.org/10.5287/bodleian:9R9GMgO25).

Statement of Authorship for joint/multi-authored papers for PGR thesis

To appear at the end of each thesis chapter submitted as an article/paper

The statement shall describe the candidate's and co-authors' independent research contributions in the thesis publications. For each publication there should exist a complete statement that is to be filled out and signed by the candidate and supervisor **(only required where there isn't already a statement of contribution within the paper itself).**

Title of Paper	A Subgrain-Size Piezometer Calibrated for EBSD
Publication Status	**X** Published □ Accepted for Publication □Submitted for Publication □Unpublished and unsubmitted work written in a manuscript style
Publication Details	Goddard, R.M., Hansen, L. N., Wallis, D., Stipp, M., Holyoke, C.W.III, Kumamoto, K, M., & Kohlstedt, D.L. (2020). A subgrain-size piezometer calibrated for EBSD. *Geophysical Research Letters, 47,* e2020GL090056. https://doi.org/10.1029/2020GL090056.

Student Confirmation

Student Name:	Catherine Goddard		
Contribution to the Paper	I collected EBSD data for all the quartz samples. Olivine EBSD maps were collected by either Lars Hansen or David Wallis. I wrote scripts: *No_intercepts_check.m, undersampling.fun.m, Undersampling_Step_Size.m, Area_Analysis_reduction.m, ProcessEBSD_LinearIntercepts.m,* Stress_Calulation_fun.m. I updated scripts *ProcessEBSD_fun.m, LinearIntercepts_fun.m,* which were originally written by Lars Hansen. I made all Figures expect Figure 1, which Kathryn Kumamoto made. I interpreted all the data and wrote the manuscript, which was edited and reviewed by all co-authors.		
Signature	Catherine Goddard	Date	19/06/2021

Supervisor Confirmation

By signing the Statement of Authorship, you are certifying that the candidate made a substantial contribution to the publication, and that the description described above is accurate.

Supervisor name and title: Professor Lars Hansen		
Supervisor comments		
Signature	Date	21/06/2021

3 Comparing *in-situ* and *ex-situ* stress measurements in polymineralic rocks

Abstract

In this study, we test the application of a subgrain-size piezometer, recently calibrated using electron backscatter diffraction (EBSD) measurements on monomineralic rocks, as a proxy for the local stress state in polymineralic rocks. We deformed synthetic mixtures of olivine and orthopyroxene in a Deformation-DIA apparatus. These experiments offer the unique possibility of simultaneously deforming the sample and measuring the average stresses within each phase using X-ray diffraction. Subgrain-size piezometry was then applied to each phase within the recovered samples.

Many of the samples contained grains smaller than the subgrain size predicted by the piezometer, indicating that grain size can limit the applicability of subgrain-size piezometry. In addition, subgrain boundaries in orthopyroxene were sparse due to low strains attained in the olivine-pyroxene mixtures, also limiting the applicability of subgrain-size piezometry. For the remaining samples, those deformed at stresses falling within the original calibration range of the subgrain-size piezometer displayed good agreement between *in-situ* and *ex-situ* stress measurements in olivine, both in monomineralic and polymineralic samples. In the one experiment that contained pervasive subgrain boundaries in orthopyroxene, the *ex-situ* stress measurements fell within the range of *in-situ* stress measurements calculated from three diffraction peaks.

The stresses measured from X-ray diffraction also offered insight into the uniformity of stress within mixtures. At the high pressure experimental conditions of this study, orthopyroxene supports higher stresses in the mixture than olivine. Therefore, within its calibration range, the subgrain-size piezometer offers an important tool for exploring how stress partitions in polymineralic rocks. However, using piezometric measurements to determine the macroscopic stress applied to a polymineralic rock is not straightforward and requires additional study.

3.1 Introduction

Estimates of the stresses supported by lithospheric rocks are critical to understanding the mechanical state of Earth's lithosphere (e.g., Kohlstedt & Weathers, 1980), strain localisation along plate boundaries (e.g., Boutonnet et al., 2013), and elastic loading of the mid-crust through the earthquake cycle (e.g., Trepmann & Seybold, 2018). The

most commonly applied method for measuring paleostresses ('paleopiezometry') from rocks deformed in the ductile lithosphere is to analyse microstructural features for which there are experimentally calibrated relationships with applied stress (e.g., Nicolas, 1978; J. Tullis, 1979). The most widely implemented piezometric measurement is the size of dynamically recrystallised grains which, in monomineralic rocks, is inversely proportional to the applied stress (e.g., Luton & Sellars, 1969; Karato et al., 1980; Twiss, 1986; Stipp & Tullis, 2003; Shimizu, 2008; Siemes et al., 2011; Post, 1973). However, grain growth in a polymineralic rock can be inhibited by the presence of secondary phases that pin grain boundaries, preventing their migration (Smith, 1948; Evans et al., 2001; Hiraga et al., 2010; Tasaka, Zimmerman, Kohlstedt, Stünitz, & Heilbronner, 2017). Consequently, grain-size piezometry potentially overestimates paleostresses when applied to well-mixed polymineralic rocks (e.g., Hansen & Warren, 2015).

An alternative proxy for paleostress in polymineralic rocks is the subgrain size (Twiss, 1986), which offers three potential advantages over grain size: 1) subgrains are resistant to static annealing (e.g. Goetze & Kohlstedt, 1973), 2) subgrains form due to, and their size exhibits a relationship with, the applied stress both in relict and recrystallised grains (Trimby et al., 1998), and 3) subgrain size appears to be unaffected by the presence of secondary minerals (White, 1979; Hansen & Warren, 2015).

Until recently, subgrain-size piezometers were calibrated only by visible-light microscopy or transmission electron microscopy (e.g., Goetze, 1975; Durham et al., 1977; Mercier et al., 1977; Toriumi, 1979; Karato et al., 1980; Friedman & Higgs, 1981; Platt & De Bresser, 2017). As estimates of the length scale of microstructural features can differ significantly depending on the measurement method used (e.g., Hansen et al., 2011; Mingard et al., 2009), these subgrain-size piezometers could not be accurately applied to electron backscatter diffraction (EBSD) measurements, a now common method of subgrain characterisation (e.g., Kilian et al., 2011; Rahl & Skemer, 2016; Ambrose et al., 2018). In addition, these piezometers are calibrated for only a small number of minerals (e.g., Siemes et al., 2011; Speciale & Behr, 2014; Van der Wal et al., 1993; Cross et al., 2017; A. Post & Tullis, 1999; Rutter, 1995), limiting their practical application.

Recently, Goddard et al. (2020) calibrated a subgrain-size piezometer based on EBSD measurements of quartz and olivine. They present a linear inverse relationship in log space between subgrain size, normalised by the Burgers vector, and the von Mises equivalent stress, normalised by the shear modulus, as suggested theoretically by Twiss et al. (1977). This new normalised calibration offers the possibility of applying a single piezometer to a polyphase system. However, if this subgrain-size piezometer is to be widely used on naturally deformed mylonites, two questions must first be addressed:

1. Are subgrains truly immune to the pinning effects of secondary phases?

2. How accurate are stress estimates from the subgrain-size piezometer when applied to minerals other than those for which it was calibrated?

To address these questions, experiments were conducted on synthetic polymineralic samples of olivine and orthopyroxene (harzburgite) using a Deformation-DIA (D-DIA) apparatus at the synchrotron X-ray beamline 6-BM-B at the Advanced Photon Source, Argonne National Laboratory, Illinois. X-ray diffraction enabled measurements of the average stresses within each phase in the sample whilst it underwent deformation. These *in-situ* stress measurements were subsequently compared to stresses measured *ex-situ* by subgrain-size piezometry. The use of olivine and orthopyroxene mixtures tests the subgrain-size piezometer using a combination of a phase for which it was originally calibrated (olivine) acting as a control and a new phase (orthopyroxene), thereby testing its applicability to other minerals. The results of this work support the application of the newly derived subgrain-size piezometer as well as offering insight into its potential applications to polymineralic rocks both in the field and in experiments.

3.2 Methods

3.2.1 Experimental procedure

Figure 3.1 illustrates a typical sample assembly. All experiments consisted of two stacked samples, one of which was commonly an olivine sample used as a load cell. Other samples consisted of orthopyroxenite or harzburgite. The harzburgite composition was $f_{\mathrm{opx}} = 0.3$, where f_{opx} is the volume fraction of orthopyroxene. A detailed explanation of the sample synthesis is in Appendix B.1. Concentric sleeves of MgO and graphite were used as an insulator and resistive furnace, respectively. Temperature was estimated from a calibrated

relationship with heater power as the inclusion of a thermocouple tends to degrade the mechanical stability of the sample assembly (Dixon & Durham, 2018). Discs of nickel foil 25 µm thick were placed between each component within the assembly, along with a nickel wrap encasing the samples, to act as strain markers in the X-ray radiographs and set the oxygen fugacity at the Ni-NiO buffer.

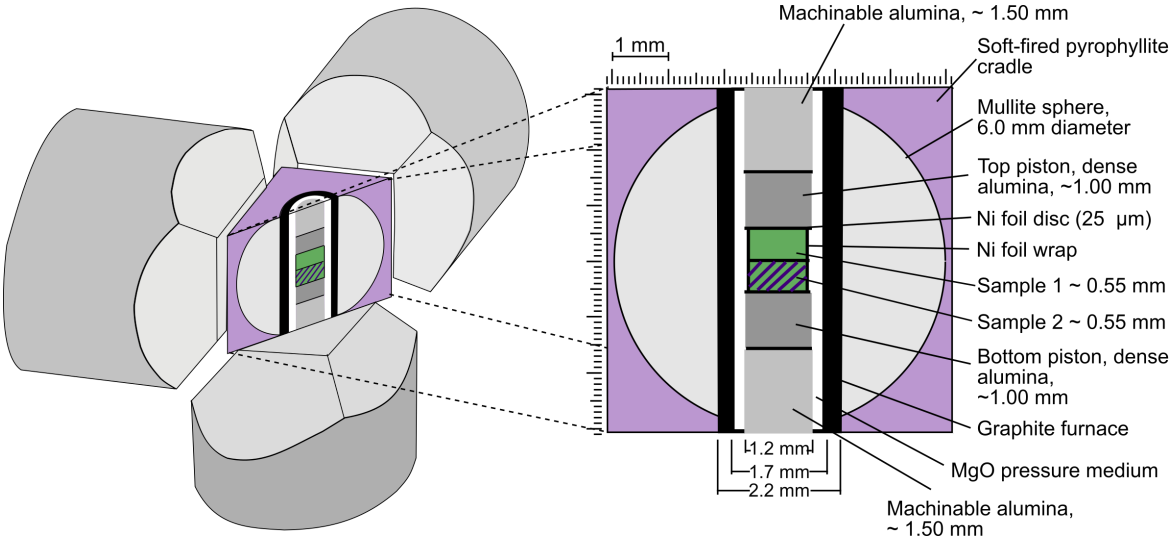

Figure 3.1: Schematic illustration of the D-DIA sample assembly used here, modified from Durham et al. (2002) and Hansen et al. (2019)

Pressure was applied to samples through a hydraulically-loaded anvil on each cube face (Mei et al., 2010). Pressurisation from the main loading ram applies a load to all the anvils simultaneously, generating a compressive mean stress, while the vertical anvils can be advanced or retracted independently of the main ram, producing a differential stress (Y. Wang et al., 2003; Durham et al., 2009; Mei et al., 2010; Weidner et al., 2010).

A high-energy, white X-ray source was used to make *in-situ* stress and strain measurements for each sample using energy-dispersive X-ray diffraction and X-ray radiography, respectively. Ten solid-state detectors were arranged downstream of the sample at a variety of fixed azimuths (Ψ) to the horizontal incident beam and at an angle of 6.5° to the beam direction (Figure 3.2). This Bragg angle (2θ) of 6.5° is fixed through conical slits and provides a collimated signal that ensures the diffracted X-rays arriving at the detectors were diffracted solely from the sample rather than the surrounding assembly components. The energy-to-d-spacing conversion as well as the Bragg angle were calibrated at least once every seven experiments using an alumina-powder standard.

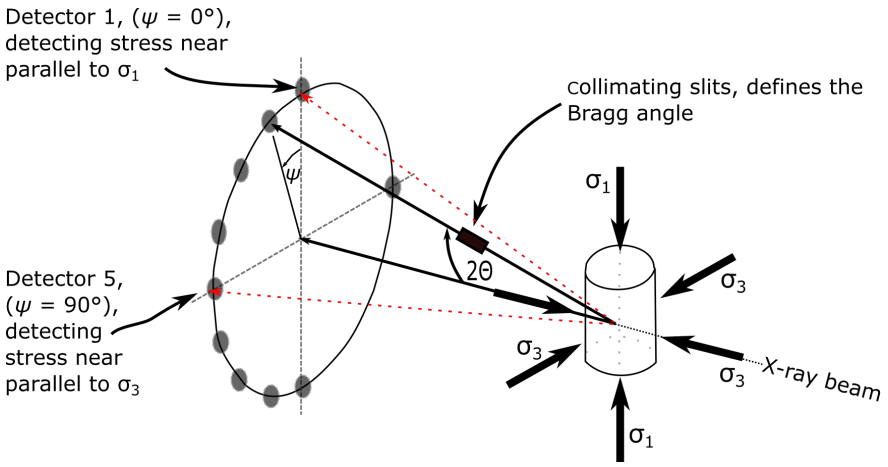

Figure 3.2: Schematic illustration of the detector-sample arrangement modified from Dixon and Durham (2018).

Energy-dispersive X-ray diffraction spectra were collected, alternating between the top and the bottom samples, for durations of 20 to 60 seconds, depending on the quality of the peaks. Different peaks in the diffraction pattern correspond to different $\{hkl\}$ planes in the diffracting medium. Peaks used in this analysis are highlighted in Figure 3.3 and correspond to the {130}, {131}, and {112} planes of olivine and the {421}, {610}, and {321} planes of orthopyroxene.

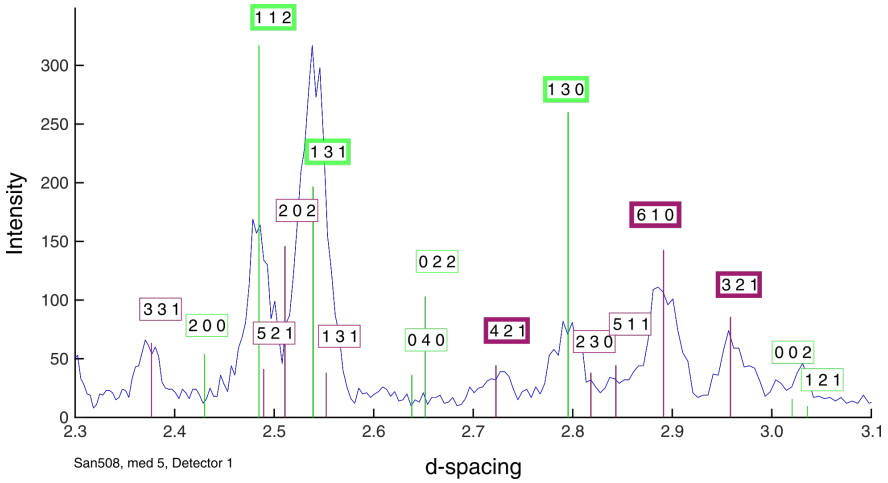

Figure 3.3: Example of diffraction spectrum in harzburgite sample. Green lines represent key diffracting planes in olivine and purple lines represent key diffraction planes in orthopyroxene. The measured data are plotted as a blue line. Peak labels outlined in bold are those used to measure stress in these experiments

Pressure and differential stress were calculated from the measured d-spacing of $\{hkl\}$ peaks following previous work (e.g., Hansen et al., 2019; Durham et al., 2009; Mei

et al., 2010; Y. Wang et al., 2013; Weidner et al., 2010). Pressure was measured from the {130} peak of olivine, calculated via the third-order Birch-Murnaghan equation of state for olivine,

$$P = \left(\frac{3\left(K_0 + K'_{\mathrm{T}}\Delta T\right)}{2}\right)\left[\left(\frac{V_{0,\mathrm{T}}}{V}\right)^{\frac{7}{3}} - \left(\frac{V_{0,\mathrm{T}}}{V}\right)^{\frac{5}{3}}\right]\left\{1 + \frac{3}{4}\left(K'_{\mathrm{P}} - 4\right)\left[\left(\frac{V_{0,\mathrm{T}}}{V}\right)^{\frac{2}{3}} - 1\right]\right\}, \quad (3.1)$$

where ΔT is the change in temperature relative to the temperature at which the thermal expansion measurements were made, K_0 is the bulk modulus and K'_{T} and K'_{P} are the temperature and pressure derivatives of K_0, respectively. Values of 129.4 GPa for K_0 and 4.29 for K'_{P} were taken from Abramson et al. (1997). For K'_{T}, a value of -0.0224 GPa·K^{-1} was taken from Kumazawa and Anderson (1969). The unit-cell volume, V, is calculated at any time during the experiment through

$$V = \left[d_{\mathrm{p}}\left(h^2 + k^2 + l^2\right)^{\frac{1}{2}}\right]^3, \quad (3.2)$$

where $d_{\mathrm{p}} = \frac{d_{\mathrm{v}} + 2d_{\mathrm{h}}}{3}$, d_{v} is the d-spacing measured from the detector at the vertical azimuth, and d_{h} is the d-spacing measured from the detector at the horizontal azimuth. To calculate d_{h} and d_{v}, a sine function was fit to d-spacing measurements as a function of Ψ. d_{h} and d_{v} were taken to be the maximum and minimum of the sine function. $V_{0,\mathrm{T}}$ is the unit cell volume at the test temperature and ambient pressure and is calculated as

$$V_{0,\mathrm{T}} = V_0 \exp\left(2.55E-5(T - T_0) + \frac{1}{2}1.15E-8\left(T^2 - T_0^2\right)\right), \quad (3.3)$$

where V_0 is the unit-cell volume at ambient temperature and pressure, T is the temperature, and T_0 is the temperature at which the thermal expansion measurements were made.

The differential stress, σ, was calculated using the difference in d-spacing in the horizontal and vertical directions ($d_{\mathrm{h}} - d_{\mathrm{v}}$),

$$\sigma = \left(\frac{1}{2G_{\mathrm{R}}}\right)^{-1}\frac{d_{\mathrm{h}} - d_{\mathrm{v}}}{d_{\mathrm{p}}}, \quad (3.4)$$

where G_{R} is the X-ray shear modulus calculated assuming the Reuss (isostress) condition (Singh et al., 1998) and using the elastic constants from Abramson et al. (1997) and Isaak (1992).

Prior to fitting peaks to the diffraction data, the intensity versus d-spacing data were smoothed by the MATLAB® $sgolayfit$ function, which applies a Savitzky-Golay filter. Data were subsequently subjected to the *spline* smoothing function. Due to the complicated diffraction patterns present in mixtures of olivine and orthopyroxene, peak locations were identified by fitting Gaussians to the highest intensity portions of each individual peak rather than fitting a mixing model of multiple Gaussians. When compared to the peak-fitting model (*peakfit.m*, O'Haver, 2018, page 340–358) utilised by Hansen et al. (2019) on a representative set of diffraction patterns for olivine, stress and pressure measurements were comparable.

Deformation experiments were conducted at temperatures and pressures of 800°–1250°C and 2.1–8.3 GPa, respectively. Prior to deformation, each sample was left to anneal at temperatures of 800–1100°C for between 5 and 20 minutes to relax any internal stress heterogeneity resulting from pressurisation (Wallis et al., 2020). Vertical rams were advanced at a rate controlled by hydraulic syringe pumps to produce a deviatoric stress on the sample assembly. For each stress measurement, an axial strain measurement was obtained through X-ray radiography, using image cross-correlation on the radiographs to precisely measure strain. A peak-interpolation algorithm allowed subpixel resolution, resulting in precisions in strain of 10^{-5} to 10^{-4} (Hansen et al., 2019). At the end of the experiments, samples were quenched, the vertical anvils were withdrawn, and the pressure from the main loading ram was decreased under approximately hydrostatic conditions.

3.2.2 Microstructural analysis

To prepare the samples for EBSD analysis, the deformed sample assembly, including sample pistons and graphite furnace, was extracted and mounted on a glass slide. Samples assemblies were then ground down to expose the centre of the sample. All surfaces were prepared by polishing with a Planocloth polishing cloth, 0.3 µm alumina, and water for between 2 to 4 hours. Samples were subsequently polished with colloidal silica for ∼20 minutes. To minimise charging during EBSD analysis, a 50 Å carbon coat was applied to samples mapped at the University of Minnesota. For a more detailed account of the sample preparation, see Appendix B.2.

EBSD data were collected on a FEG scanning electron microscope (SEM) either at the Department of Earth Sciences, University of Oxford, or the Characterisation Facility, University of Minnesota. At Oxford, the SEM was equipped with Oxford Instruments AZtec acquisition software and a NordlysNano EBSD camera. At Minnesota, EBSD data were collected using a JEOL 6500 FEG SEM using a CMOS-based Symmetry S2 EBSD detector and Oxford Instruments AZtec acquisition software. Samples were tilted at 70° and maps were collected at an accelerating voltage of 20–30 kV, at low vaccum (50–70 Pa, H_2O) at Oxford and high vacuum at Minnesota. The electron beam was rastered across the sample using steps sizes of 0.075 to 0.3 µm.

Data were cleaned using a combination of Oxford Instruments Channel5 software and the MTEX toolbox (Bachmann et al., 2010; Mainprice et al., 2011) for MATLAB®. First, in places where olivine was systematically misindexed due to pseudosymmetry, the orientations of these points were corrected by applying a rotation of 60° around [100] (Bystricky et al., 2006), using Oxford Instruments Channel5 software. EBSD data were then processed in MATLAB® using the MTEX toolbox. Isolated pixels and grains that were less than 3 pixels were removed. Pixels with mean angular deviation values of $> 1°$ were similarly removed. After this noise reduction procedure, non-indexed pixels, which made up 11–48% of each map, were removed, and all pixels no longer assigned a phase were filled by MTEX using the method of nearest neighbour, whereby pixels are assigned the average orientation of the surrounding points. Phase maps of the EBSD data prior to the infill of non-indexed regions are presented in Appendix B.3.

3.2.3 Subgrain-size piezometry

The noise levels in the EBSD maps in this study were higher than 1°. As such, any stresses calculated from these maps using the subgrain-size piezometer of Goddard et al. (2020), which analyses misorientations as small as 1°, would likely overestimate the differential stress. A modified subgrain-size piezometer using a critical misorientation of 2° (Figure 3.4) was recalibrated from the maps originally used by Goddard et al. (2020). Unlike the original calibration, maps used in this new calibration also include the additional cleaning step of removing pixels with mean angular deviation values of $> 1°$. As was the case for Eq. 1 in the Goddard et al. (2020), the stresses applied to quartz in Figure 3.4 have been corrected for friction in accordance with Holyoke and Kronenberg (2010).

In keeping with Goddard et al. (2020), subgrain size was measured via the line-intercept method. To ensure that we used the correct number of intercepts required to accurately measure the subgrain size, we ran the *No_intercepts_check.m* script from Goddard et al. (2020). The number of intercepts was considered sufficient when the line-intercept length became essentially invariant with further increases in the number of intercepts (varying $< 2.5\%$ from the previous measurement). The arithmetic mean intercept length was calculated from intercepts measured both parallel and perpendicular to σ_1. The mean grain size for each phase was also measured using the line-intercept method, with the minimum misorientation of a grain boundary defined as 10°. For grain size, line intercepts of the same length as the step sizes of the EBSD maps were removed on the assumption they were likely to result from noise in the orientation measurements.

We correct the shear moduli and Burgers vectors for the pressures of these experiments (2.1–8.3 GPa), which were considerably larger than pressures in the experiments used to calibrate the subgrain-size piezometer (Goddard et al., 2020). The implemented pressure derivatives are presented in Table 3.1. However, we note that this pressure correction is considerably smaller that the errors in estimated stress inherently associated with the piezometer.

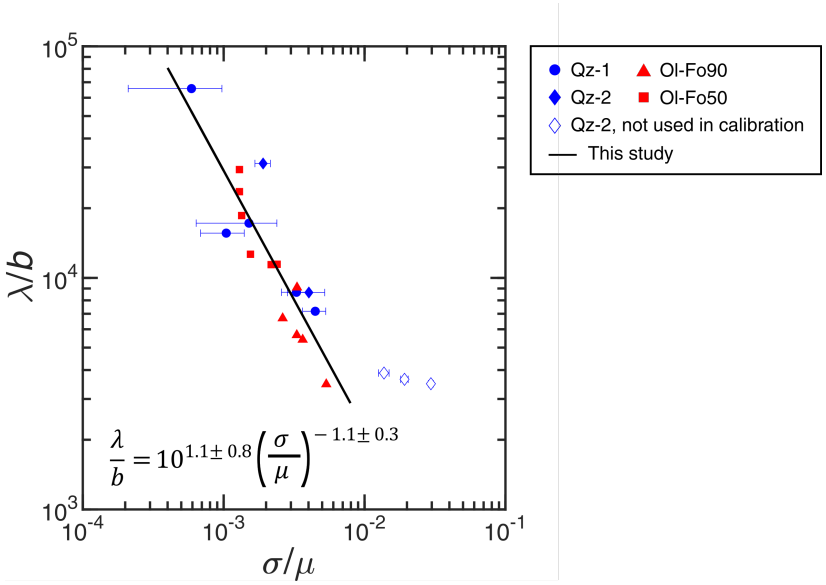

Figure 3.4: Mean line-intercept length, λ, normalised by the Burgers vector, b, as a function of the equivalent stress, σ, normalised by the shear modulus, μ. The minimum misorientation of a subgrain boundary has been set at 2°

Table 3.1: Pressure dependence of shear moduli and Burgers vectors for olivine and orthopyroxene

Mineral	μ (GPa)	$\partial\mu/\partial P$	$\partial^2\mu/\partial^2 P$ (GPa^{-1})	b (µm)		$\partial b/\partial P$ (µmGPa^{-1})	$\partial^2 b/\partial^2 P$ (µmGPa^{-2})
Olivine	77.8*	1.71◇	-0.054◇	a direction	4.75E-4°	-8.377E-3◇	2.088E-4◇
Orthopyroxene	78.1▷	1.45▷	0	c direction	5.2E-4⋆	-1.548E-6•	8.2180E-8•

μ = shear modulus used in the Goddard et al. (2020) piezometric calibration (at room temperature and pressure)
*Mao et al. (2015)
◇Abramson et al. (1997)
°Deer et al. (1992, page 4)
⋆Deer et al. (1992, page 158)
▷Chai et al. (1997)
•Angel and Hugh-Jones (1994)

3.3 Results

3.3.1 Mechanical data

We performed seven experiments: one with a dunite load cell against a sample of orthopyroxenite, five with a dunite load cell against a sample of harzburgite, and one with two samples of harzburgite. Key parameters for each experiment can be found in Table 3.2. The average and final stresses from each diffraction peak can be found in Appendix B.4.

Dunite versus orthopyroxenite

Mechanical data for San502, which consisted of an orthopyroxenite sample against a dunite load cell, are displayed in Figure 3.5. Initially, stress increased with strain. The apparent modulus from this segment is too low to represent purely elastic deformation (∼40 GPa compared to 200 GPa, for olivine) and therefore samples must have yielded nearly instantaneously and progressively hardened. Samples were deformed at a temperature of 800°C and at strain rates of 1.7×10^{-5} s^{-1} and 2.1×10^{-5} s^{-1}, for orthopyroxenite and dunite, respectively until 3% strain. At 3% strain, the temperature was increased to 900°C so that deformation could continue at a lower differential stress. After the change in temperature, the orthopyroxenite and the dunite load cell deformed at strain rates of 2.3×10^{-5} s^{-1} and 4.3×10^{-5} s^{-1}, respectively.

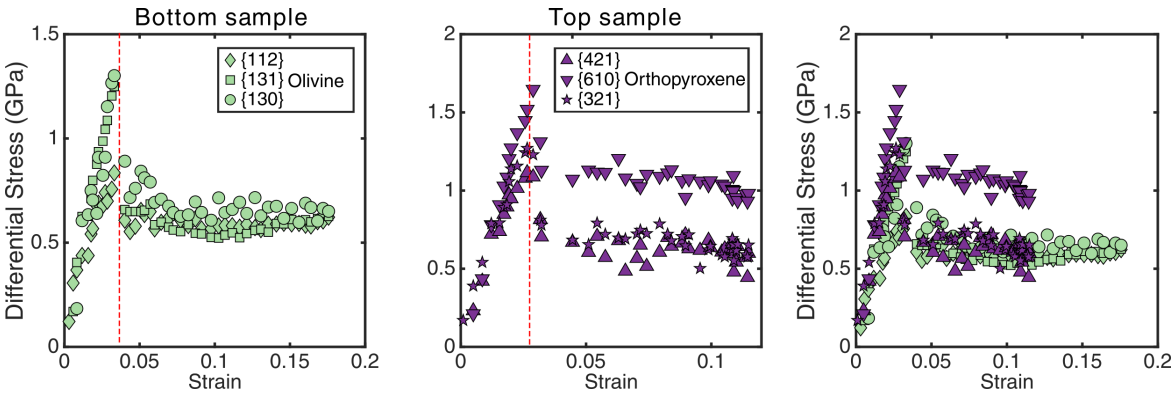

Figure 3.5: Stress versus strain graphs for experiment San502. The top sample is orthopyroxenite, and the bottom sample is San Carlos olivine. Red dotted lines indicate a change in temperature from 800˚ to 900˚C. The legends indicate the different diffraction peaks used to calculate stress in olivine and orthopyroxene

The constant flow stresses in the dunite load cell (570–650 MPa) were similar to those measured in the {421} and {321} peaks in orthopyroxene within the orthopyroxenite sample (610 MPa and 640 MPa, respectively). However, stress measured from the {610} peak in orthopyroxene was considerably higher, averaging 1030 MPa.

Dunite versus olivine-orthopyroxene mixtures

Mechanical data for experiments consisting of a harzburgite and a dunite load cell are presented as stress-strain curves in Figures 3.6 and 3.7. Four of these experiments were deformed at 1100˚–1250˚C and average pressures of 4.9–8.3 GPa, whereas experiment San508 was deformed at an average pressure of 2.1 GPa and temperature of 900˚C.

In all samples except the load cells in San391 and San404, stress initially increased with strain. Low apparent moduli from these portions of the stress-strain curves suggest that yielding was instantaneous. Steeper gradients at $< 1\%$ strain in the mixtures in San390 and San404 suggest deformation may have initially been elastic, but data in these portions of the graphs are sparse. Within the load cells in San391 and San404 initial loading of the sample was not captured in the collected data.

Table 3.2: Experimental conditions

Experiment	Top or bottom	Sample	Starting material name	Temp (°C)	Strain rate ($\times^{-5}s^{-1}$)$^{\triangleleft}$	Pressure (GPa)$^{\triangledown}$	End pressure (GPa)	Total Strain
San390	Top	Ol	33	1100	22.3	5.0 ± 0.5	4.1	0.41
San390	Bottom	Hz (Px30)	PT-1299 HiFe	1100	2.5	4.9 ± 0.5	4.1	0.06
San391	Bottom	Ol	33	1100/ 1150	1.8/2.6	5.2 ± 0.3	4.6	0.29
San391	Top	Hz (Px30)	PT-1299 HiFe	1100/ 1150	0.6/0.6	5.0 ± 0.3	4.5	0.08
San396	Bottom	Ol	1166	1100/ 1250	2.3/8.1 /22.0$^{\triangle}$	8.3 ± 1.3	5.6	0.32
San396	Top	Hz (Px30)	PT-1299 HiFe	1100/ 1250	1.2/2.2 /8.8	8.1 ± 1.1	5.5	0.13
San404	Top	Ol	LT-DrySC	1100	8.6/1.3	7.0 ± 0.1	6.9	0.22
San404	Bottom	Hz (Px30)	PT-1299 HiFe	1100	0.7/0.6	7.0 ± 0.0	6.9	0.07
San409$^{\oslash}$	Top	Hz (Px30)	PT-1299 HiFe	1100/ 1150/ 1250/ 1200	1.6/2.1/ 4.1/4.4	6.4 ± 1.2	5.0	0.28
San409$^{\oslash}$	Bottom	Hz (Px30)	PT-1299 HiFe	1100/ 1150/ 1250/ 1200	1.6/2.1/ 4.1/4.4	6.6 ± 1.1	5.4	0.28
San502	Top	Opx	PI-2056 -opx	800/ 900	1.7/2.3	n/a	n/a	0.11
San502	Bottom	Ol	PI-2056 -ol	800/ 900	2.1/4.3	2.5 ± 0.4	2.1	0.17
San508	Top	Hz (Px30)	PI-2056	900	3.3/5.5	2.1 ± 0.5	2.3	0.22
San508	Bottom	Ol	PI-2056 -Ol	900	1.4/4.9	2.1 ± 0.4	2.3	0.16

$^{\triangleleft}$Strain rate is taken as the gradient of the line-of-best fit between strain and time
$^{\triangledown}$Mean stress, calculated using the {130} peak in olivine
$^{\triangle}$First change in strain rate relates to a change in temperature. The second relates to a change in the displacement rate of the differential rams
$^{\oslash}$Due to imperfections in the middle foil, strains for individual samples were not measurable. Reported strains are those for the entire sample assembly.

At points throughout a number of experiments, the temperature and/or the displacement rate of the vertical rams was modified. During experiments San391 and San396, the temperature was raised to decrease the differential stress. In experiment San404, the displacement rate of the vertical rams, and as such the differential stress, was dropped. In contrast, in experiments San396 and San508, the displacement rate was increased. These changes in displacement rate and temperature are indicated in the stress-strain curves presented in Figures 3.6 and 3.7.

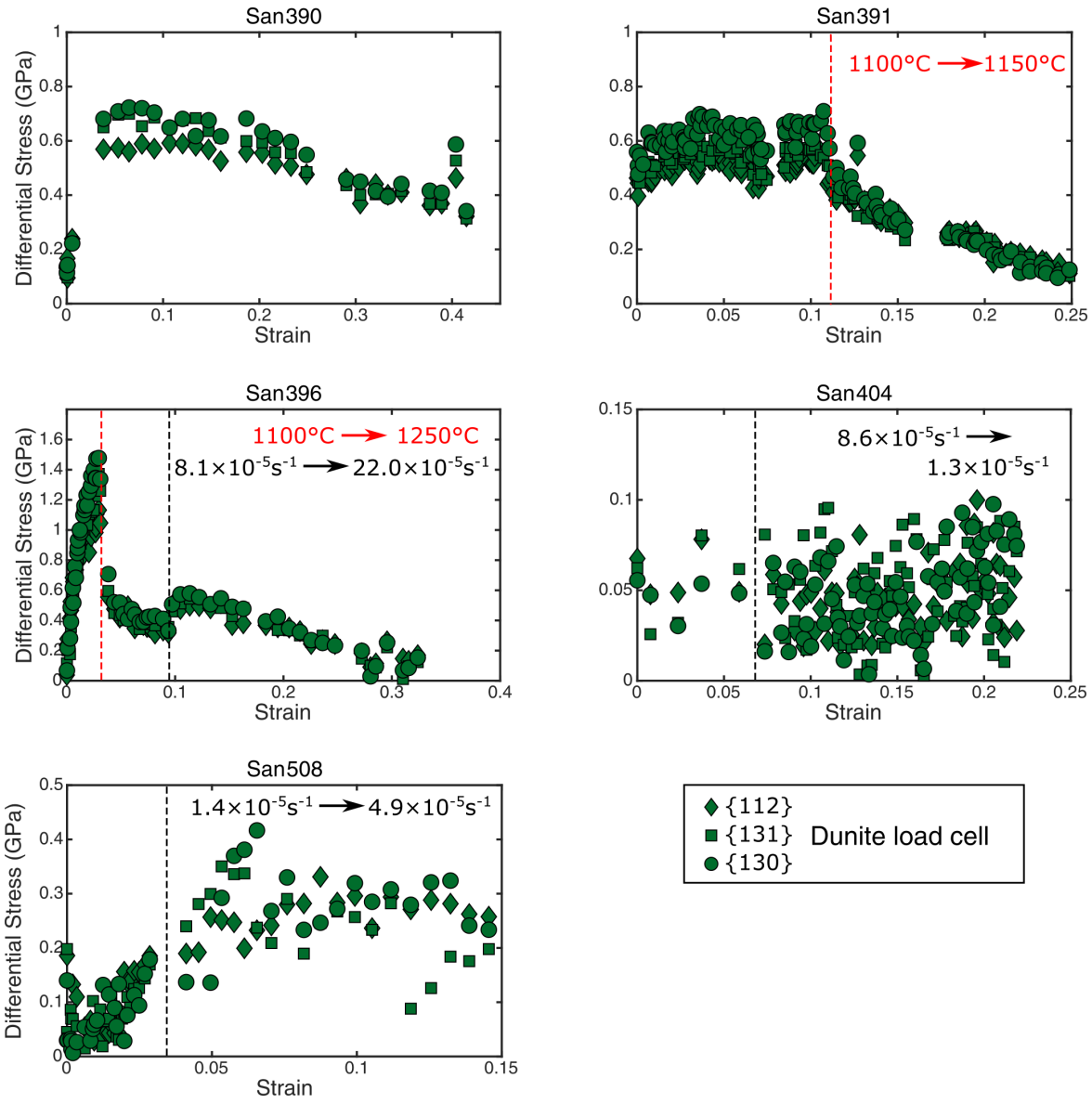

Figure 3.6: Stress versus strain for dunite load cells paired against olivine-orthopyroxene mixtures. The red and black vertical dotted lines represent changes in temperature and displacement rate, respectively

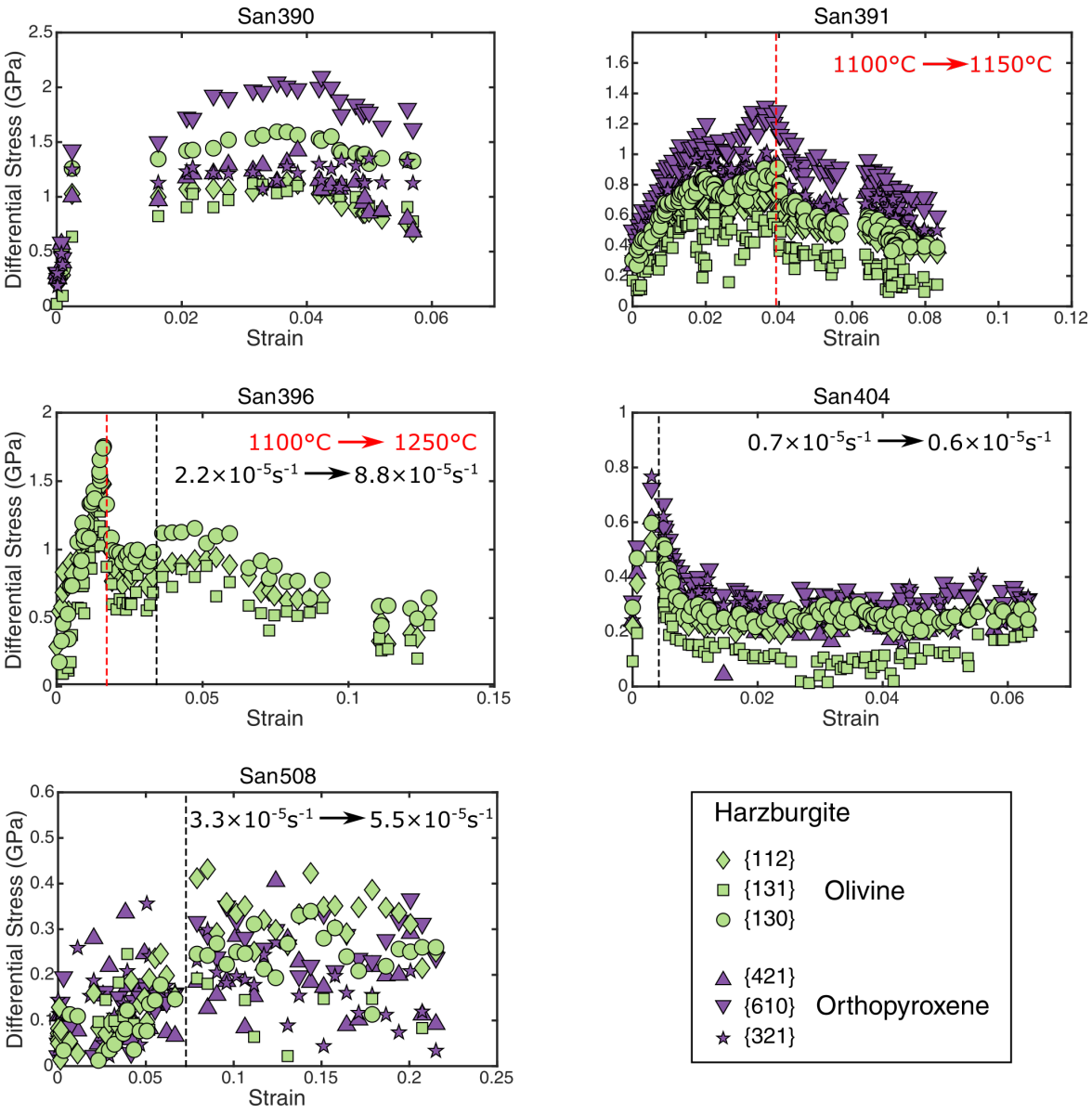

Figure 3.7: Stress versus strain for olivine-orthopyroxene mixtures. Stresses from olivine and orthopyroxene are in green and purple, respectively. The red and black vertical dotted lines represent changes in temperature and displacement rate, respectively

Samples San404 and San508 evolved to a constant flow stress, whereas stress in the other experiments dropped progressively over time. This reduction in stress may be due to an increase in temperature as a result of changes to the furnace during deformation. A matching apparent drop in the pressure curves (see Appendix B.5) supports the suggestion that the temperature increased, as inputting a lower temperature into Eq. 3.3 would thus underestimate the unit cell volume at the test temperature and ambient pressure and hence the pressure calculated in Eq. 3.1.

In the dunite load cells, stresses from the three measured peaks were typically consistent to within approximately ± 40 MPa (1 s.d.). For olivine within the mixtures, stresses from the three peaks varied by up to ± 250 MPa (1 s.d.) with the {130} peak typically giving the highest stress. For orthopyroxene, the standard deviation of stresses calculated from peaks {421} and {321} was within ± 80 MPa, whereas if stresses from the {610} peak were included, the range in stress increased to ± 370 MPa.

For experiments that included harzburgite, except San508, the strain in the dunite load cell (22–41%) was significantly higher than that in the mixture (6–13%), indicating the latter was stronger at the high pressures (4.9–8.3 GPa) of these experiments. Also within these experiments, stresses measured through X-ray diffraction were, in all cases, greater in the orthopyroxene than in the olivine in the mixture. It should be noted that in experiment San396, the diffraction patterns in orthopyroxene in the mixture were too noisy to measure stress, and as such it was not possible to compare how stress was distributed between olivine and orthopyroxene.

In experiment San508, which was conducted at a relatively low pressure of 2.1 GPa and a temperature of 900°C, strain was greater in the mixture (22%) than in the dunite load cell (16%). Within the mixture, the average stresses calculated from the peaks in orthopyroxene (170–280 MPa) lay within the range of absolute stresses calculated from the peaks in the olivine (70–330 MPa).

Harzburgite-only experiments

To increase the strain within the harzburgite mixtures, two like samples were stacked against each other and deformed together in a single experiment, reaching a total strain of 28% (Figure 3.8). The apparent initial moduli are much lower than the predicted elastic modulus of harzburgite, and thus both samples are considered to have yielded instantly and the apparent moduli represent progressive strain hardening. In an attempt to reach a steady-state differential stress, the temperature was modified at three points during the experiment. The temperature was first increased from 1100°C to 1150°C, then subsequently increased further to 1250°C. After ∼10% strain, the temperature was reduced to 1200°C to prevent the stress from relaxing below the noise level. These changes in temperature led to strain rates ranging from 1.6×10^{-5} s^{-1} to 4.4×10^{-5} s^{-1}.

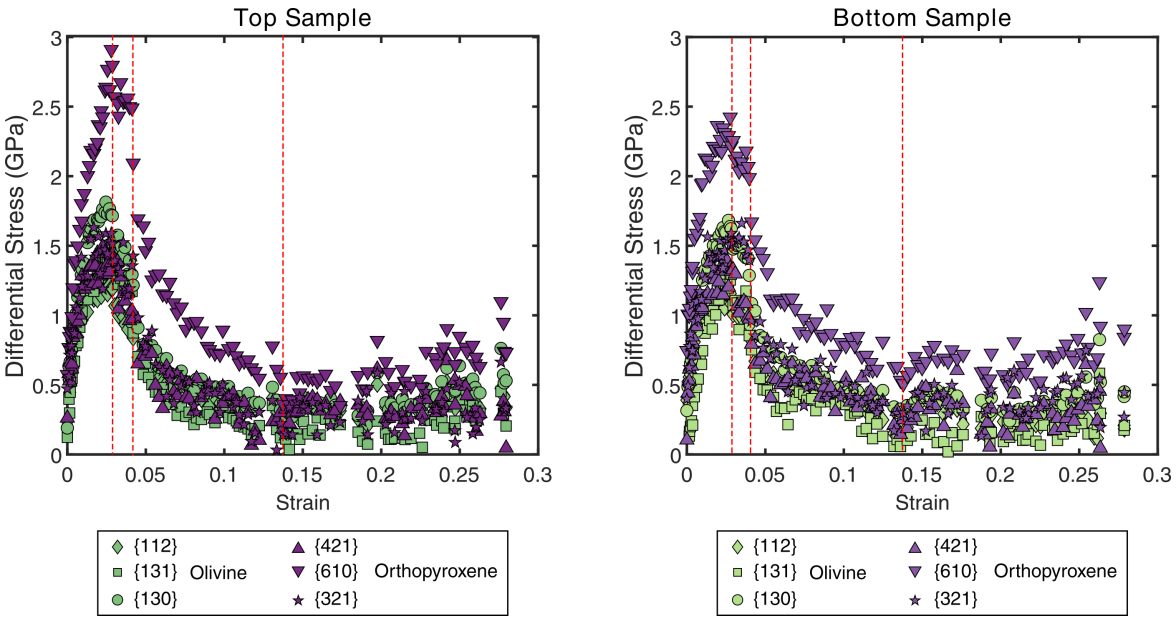

Figure 3.8: Stress versus strain curves for harzburgites in San409. The central Ni foil was not useable for strain measurements in this experiment, and therefore, stresses for each sample are plotted instead against the total strain of the combined sample stack. Red vertical lines indicate changes in temperature from 1100°C→1150°C→1250°C→1200°C

Average stresses—from 18% strain onwards—calculated from the {421} and {321} peaks in orthopyroxene (290–400 MPa) are consistent with the stresses from the olivine peaks (170–410 MPa), whereas stresses calculated from the {610} peaks were considerably higher (620 MPa and 700 MPa for the top and bottom samples, respectively).

Microstructural analysis

Local misorientation maps for each sample are presented in Figure 3.9. Within the mixtures, subgrain boundaries are present in olivine, particularly in samples deformed at high temperature ($\geq$ 1100°C). In orthopyroxene, subgrains are sparse, if present at all, except for in sample San409, which was deformed at high temperature (1100°–1250°C) and to a large strain (28%). Within the dunite load cells, subgrain boundaries are present but are typically not as prevalent as within olivine in the mixtures.

Average grain-size measurements are presented in Table 3.3. In the mixtures, average grain sizes range from 2.9–6.4 µm and 2.6–4.8 µm for olivine and orthopyroxene, respectively. Average grain sizes are larger in the dunite load cells, ranging from 4.6–11.5 µm.

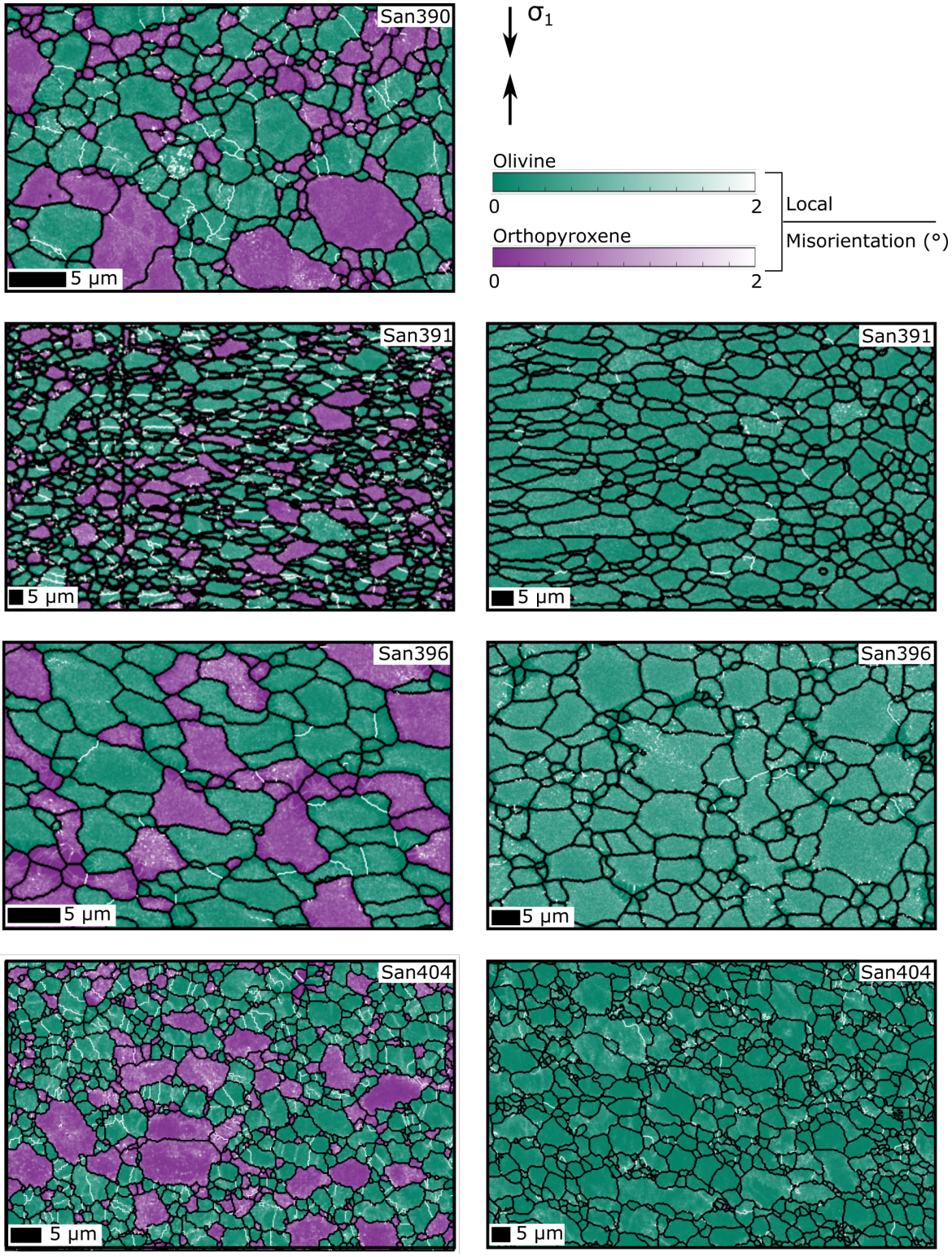

Figure caption on the next page

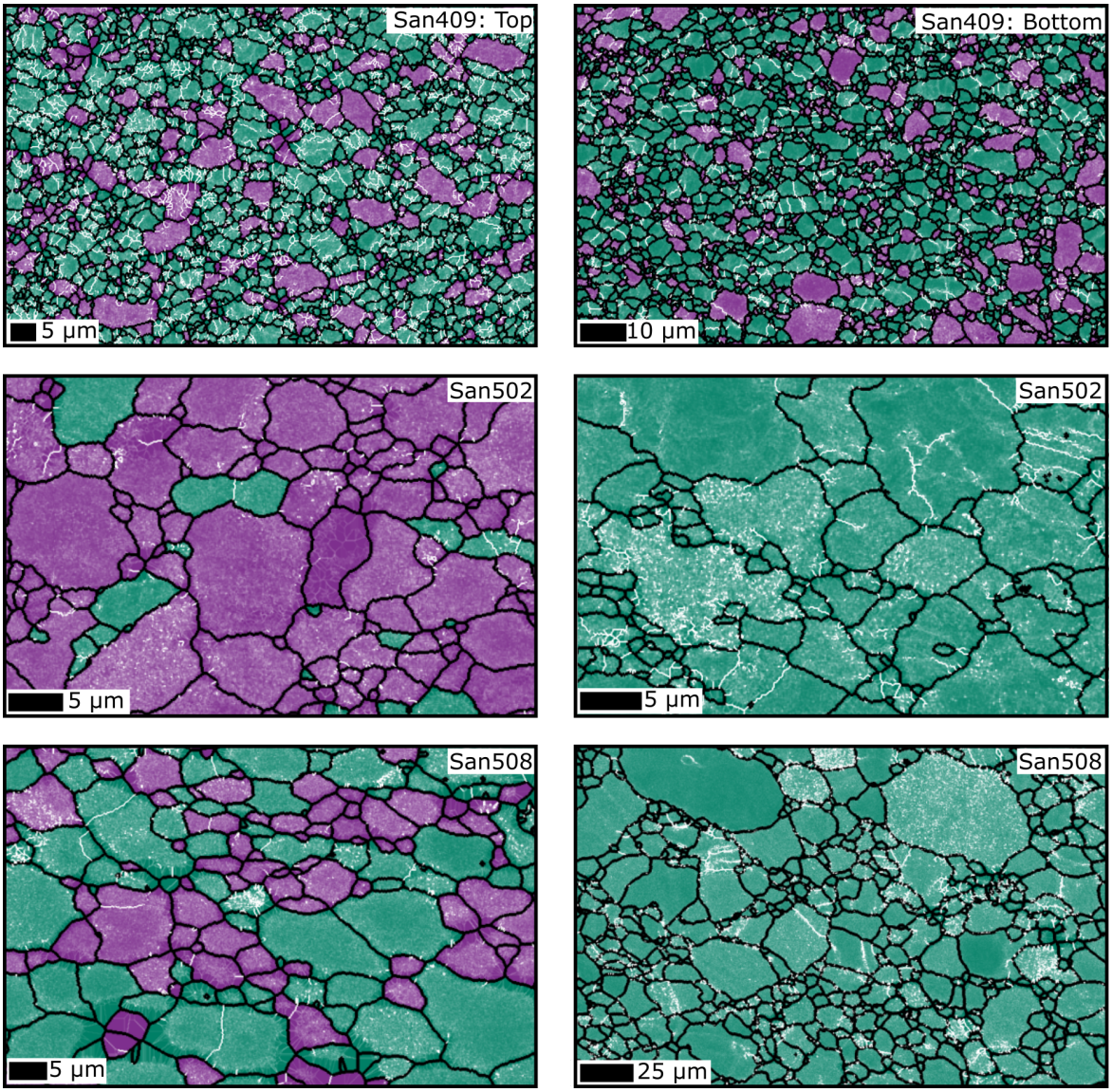

Figure 3.9: Subsets of local misorientation maps from EBSD data. Maps of the full datasets are located in Appendix B.3. Grain and subgrain boundaries are displayed in black and white, respectively and are defined as boundaries with misorientations of $\geq 10^{\circ}$ *and* $\geq 2^{\circ}$*, respectively*

3.3.2 Subgrain-size piezometry

Mean line-intercept lengths for each EBSD map can be found in Table 3.4. For the dunite load cells, mean line-intercept lengths are in the range of 1.9–5.2 µm, which correspond to stresses of 430–170 MPa predicted by the subgrain-size piezometer. In the mixtures, mean line-intercept lengths for olivine (1.2–3.1 µm) and orthopyroxene (1.5–2.9 µm) correspond to predicted stresses of 690–280 MPa and 600–330 MPa, respectively.

Table 3.3: Grain-size measurements

Experiment	Top sample				Bottom sample			
	Phase	No. Intercepts	λ_{gs} (µm)	d^* (µm)	Phase	No. Intercepts	λ_{gs} (µm)	d^* (µm)
San390					Ol	60	1.9	2.9
					Opx	50	1.7	2.6
San391	Ol	60	3.0	4.5	Ol	50	3.2	4.7
	Opx	40	3.2	4.8				
San396	Ol	40	2.4	3.6	Ol	70	3.7	5.5
	Opx	80	2.8	4.2				
San404	Ol	40	3.1	4.6	Ol	30	2.1	3.2
					Opx	70	2.1	3.2
San409	Ol	60	1.9	2.9	Ol	60	1.9	2.9
	Opx	80	2.4	3.6	Opx	60	1.9	2.8
San502	Ol	100	2.7	4.0	Ol	60	3.4	5.1
	Opx	60	3.2	4.8				
San508	Ol	70	4.1	6.4	Ol	30	7.7	11.5
	Opx	70	3.2	4.8				

*A stereological correction of 1.5 was applied to convert the mean line-intercept length (λ_{gs}) into the mean grain diameter in 3-D (d) (Underwood, 1970, page 80–93)

Table 3.4: Subgrain boundary spacing, that is, the mean-line intercept length (λ), and associated piezometric stresses

Experiment	Top sample				Bottom sample			
	Phase	No. Intercepts	λ (µm)	Stress (MPa)	Phase	No. Intercepts	λ (µm)	Stress (MPa)
San390					Ol	60	1.5	550
					Opx	60	1.5	600
San391	Ol	60	2.5	350	Ol	70	3.0	300
	Opx	60	2.9	330				
San396	Ol	70	2.2	400	Ol	70	3.2	280
	Opx	70	2.5	380				
San404	Ol	60	2.7	340	Ol	70	1.6	540
					Opx	70	1.8	530
San409	Ol	60	1.2	690	Ol	60	1.5	560
	Opx	80	1.5	600	Opx	80	1.6	570
San502	Ol	70	2.2	380	Ol	70	1.9	430
	Opx	70	2.7	340				
San508	Ol	70	3.1	280	Ol	60	5.2	170
	Opx	80	2.8	330				

3.4 Discussion

3.4.1 Subgrain-size piezometry in polymineralic rocks

To evaluate the application of the subgrain-size piezometer to polymineralic rocks, it is first necessary to consider which stresses measured from X-ray diffraction are most in agreement with stresses predicted by subgrain-size piezometry. Specifically, two situations require consideration: 1) when complex stress histories exist and 2) when stresses measured from X-ray diffraction are anisotropic.

For complicated stress histories, such as those in these experiments, it is unclear how much strain is required to set or reset the stress recorded by the subgrain boundary spacing. Previous work on olivine by Ross et al. (1980) compared constant strain-rate and constant stress experiments on olivine to experiments in which the stress, strain rate, or temperature was varied incrementally. In these experiments, the subgrain size decreased with increasing stress but did not coarsen with decreasing stress. Therefore, the subgrain size appeared to be set by the maximum stress applied to a sample. Experiments on steel by Qin et al. (2003) found that subgrains were resistant to coarsening during static annealing but did coarsen when continuously strained under stress of a reduced magnitude. The subgrain-size piezometer calibrated by Goddard et al. (2020) demonstrated a correlation between subgrain-boundary spacing and the final stress experienced by the sample, despite some samples having experienced higher stresses during their deformation history, and one example having not reached a constant flow stress. To remain consistent with Goddard et al. (2020), we compare stress measured through subgrain-size piezometry to the final stress measured by X-ray diffraction for each sample.

In plastically anisotropic, polycrystalline materials subjected to a non-hydrostatic stress field, grains of different orientations undergo different amounts of plastic strain. This heterogeneity in plastic strain is accompanied by heterogeneity in the elastic strain. As such, subpopulations of grain orientations, as manifested by different $\{hkl\}$ peaks diffracting to a given detector, experience different stresses (e.g., Y. Wang et al., 2003; Li et al., 2006; Weidner et al., 2010). Thus, the stresses measured from X-ray diffraction vary in both olivine and orthopyroxene depending on which diffraction peak is analysed. For olivine, the {130} peak resulted in stresses on average 1.5 times larger than the other peaks, consistent with

previous observations (e.g., Weidner et al., 2010). For orthopyroxene, the {610} peak gave the highest stress, on average 1.8 times larger than peaks {421} and {321}. Previous studies have taken the average of the stress measured from individual diffraction peaks to represent the differential stress experienced by the sample (e.g., Li et al., 2006), however it is unclear whether the stresses measured from different diffraction peaks should be evenly weighted. Therefore, in this study we compared the stresses measured from subgrain-size piezometry to the stresses measured from X-ray diffraction of individual peaks.

Before comparing the *in-situ* and *ex-situ* stress measurements, it is important to ensure that significant substructure exists for subgrain-size piezometry. The lack of clear subgrain structure within most orthopyroxene samples is likely due to their fine grain sizes, which are generally smaller than the predicted subgrain sizes. This effect was predicted by Twiss (1977), who suggested that subgrain-size and grain-size piezometers cross at a given stress, and as such recrystallized grains would be too small to develop subgrains at high stresses. To test whether the grain size was large enough for subgrains to form, we calculated the predicted λ using the final stress measured from each X-ray peak and the pressure corrected Burgers vectors and shear moduli. The predicted values of λ are presented

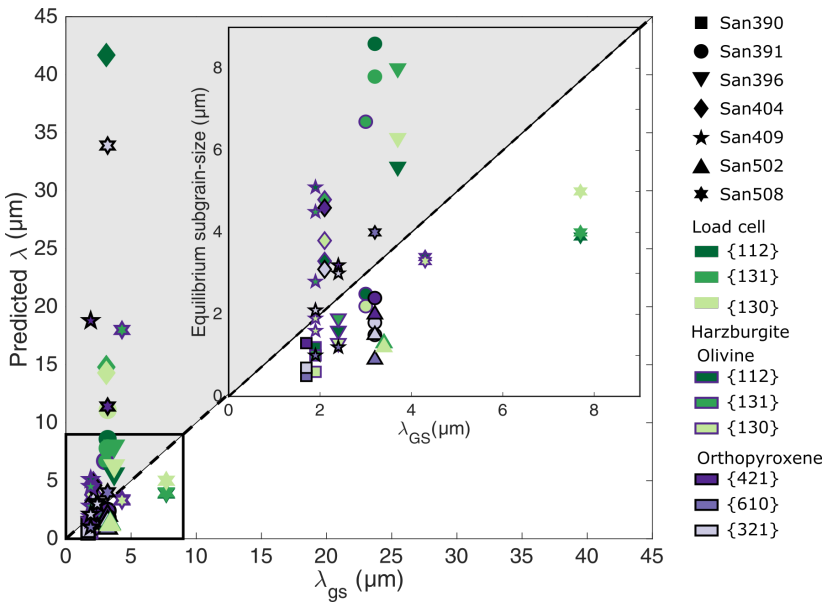

Figure 3.10: Mean-line intercept length, λ, predicted using the Goddard et al. (2020) subgrain-size piezometer and the absolute value of the stress from each peak measured by X-ray diffraction, as a function of the measured λ_{gs}, the unstereologically corrected grain size. Stresses measured from X-ray diffraction are those at the end of the experiment. The grey region indicates where the grain size is too small to accomodate subgrains of the size predicted based on the stress measured by X-ray diffraction. The insert is a magnification of the section of graph outlined in black at small grain sizes and subgrain sizes.

in Appendix B.6. This predicted λ is compared to the measured grain size in Figure 3.10. To better compare the grain size with λ, the former was not stereologically corrected.

For the dunite load cells in San391, San396, and San404, the predicted λ calculated based on the stresses measured from the three peaks all exceeded the measured λ_{gs}. Similarly, the predicted λ in both olivine and orthopyroxene in the harzburgite samples of San404 and San508 and the bottom sample of San409 exceeded the λ_{gs} of the rock. Thus, these samples have not been considered when comparing *in-situ* and *ex-situ* stresses.

The stresses from X-ray diffraction and subgrain-size piezometry in olivine for the remaining data are compared in Figure 3.11. Individual peaks within a sample that gave predicted λ larger than the λ_{gs} of the sample are plotted in grey. The dashed line indicates the maximum stress of 420 MPa applied to the olivine samples used in calibration of the piezometer. Below this upper limit, there is a correlation between *in-situ* and *ex-situ* stress measurements for olivine, in both monomineralic and polymineralic rocks.

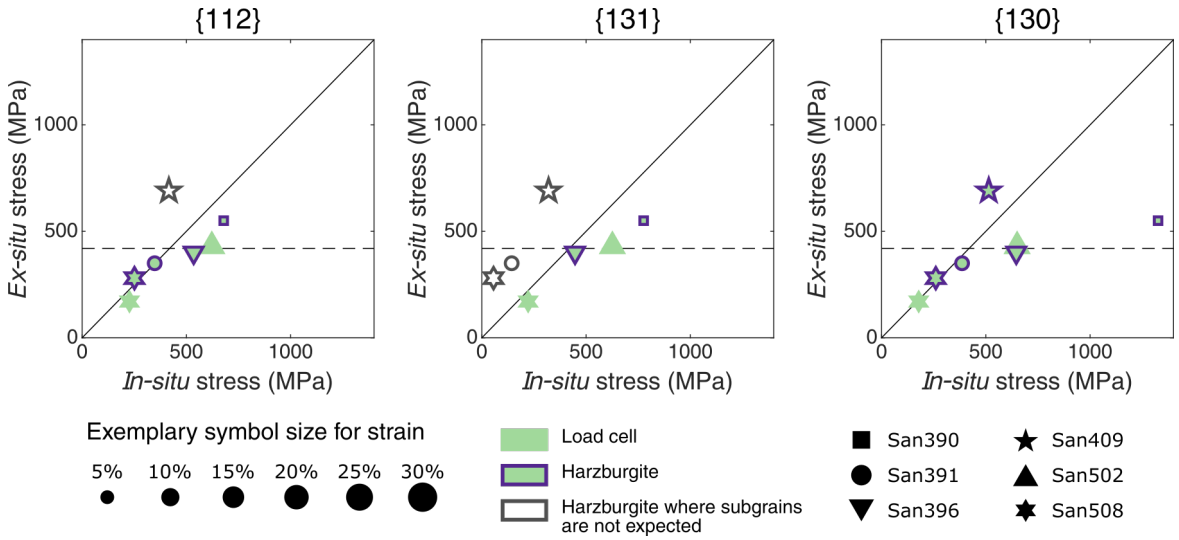

Figure 3.11: Comparison of ex-situ *stress, from subgrain-size piezometry, and* in-situ *stress, from X-ray diffraction for olivine in both monomineralic and polymineralic samples. The size of the data points is scaled by the amount of strain experienced by the sample. Individual peaks within a sample that gave predicted λ larger than the λ_{gs} of the sample are plotted in grey. The black solid line is 1:1. The dotted line represents the calibration limit for olivine in the subgrain-size piezometer (Goddard et al., 2020).*

At stresses at and above the 420 MPa limit of the calibration, the subgrain-size piezometer typically underestimates the stress relative to that measured by X-ray diffraction. A similar effect was observed in the quartz samples deformed at high stress (> 300 MPa)

in the original calibration (Goddard et al., 2020), for which a change in recrystallisation mechanism was proposed to be responsible (Stipp & Tullis, 2003; Goddard et al., 2020). It is possible that a similar process accounts for the deviation identified in olivine. The offset of the piezometric stresses from those measured by X-ray diffraction above 420 MPa does support the possibility of a different piezometric relationship at high stress.

Samples containing orthopyroxene that had λ_{gs} greater than the λ predicted by the piezometer, are plotted in Figure 3.12. The subgrain-size piezometer is only valid for values of $\sigma/\mu < 0.01$ (Goddard et al., 2020), which is comparable to a stress of 420 MPa in orthopyroxene. In samples San390, San391, and San502 stresses measured from subgrain-size piezometry, while in good agreement with stresses calculated from the {421} peak, appear to underestimate measurements from peaks {610} and {321}. However, these samples lacked clear subgrain boundaries in EBSD maps, which may have led to underestimation of the stresses measured by X-ray diffraction. In San409, where strains were high (28%) and subgrains visible, the stress from subgrain-size piezometry lies within the range calculated from the different diffraction peaks. Subgrain-size piezometry in San409 may therefore represent the average stress from the three diffraction peaks, even outside the calibration limits of the piezometer from Goddard et al. (2020).

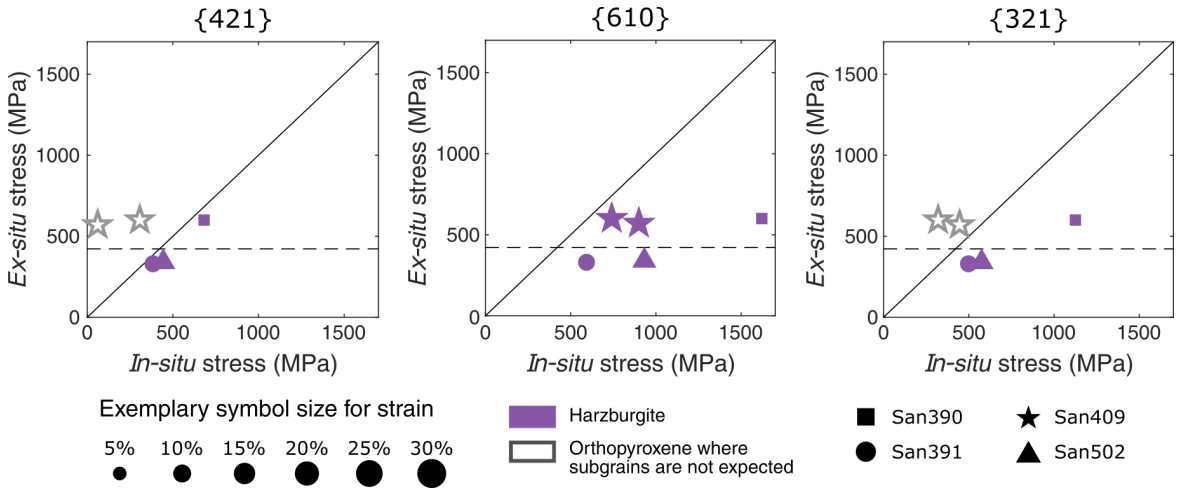

Figure 3.12: Comparison of ex-situ *stress, from subgrain-size piezometry, and* in-situ *stress, from X-ray diffraction for orthopyroxene in harzburgite. The size of the data points is scaled by the amount of strain experienced by the samples. Individual peaks within a sample that gave predicted λ larger than the λ_{gs} of the sample are plotted in grey. The black solid line is 1:1. The dotted line represents the expected calibration limit for orthopyroxene.*

It should be noted that the bottom sample in San409 and the harzburgite sample in San404 contain a significant amount of substructure within the olivine, despite their fine grain sizes. For San409, the stress recorded by the subgrain-size (560 MPa) matches neither the average stresses from the steady-state portion of the experiment (170–390 MPa) nor the peak stresses (1180–1680 MPa). However, in San404 the stress measured by the subgrains (540 MPa) matches the peak stresses measured from X-ray diffraction (470—600) MPa. Interestingly, the result from San404 is consistent with previous observations that suggest subgrains require relatively small strains to form (Biberger & Blum, 1992; Ross et al., 1980), and once formed are unable to grow (e.g., Ross et al., 1980). However, the correlation between subgrain-size and the peak stress experienced by the olivine in the mixture in San404 is in contradiction to the subgrain-size piezometry calibration and the relationship identified in Figure 3.11, which both use the final stress. It should also be noted that the peak stress in experiment San404 is outside the calibration range of the subgrain-size piezometer.

3.4.2 Stress partitioning from X-ray diffraction

The results of this study are, to the best of our knowledge, the first to provide direct evidence that subgrains at low stresses reflect the average stress within each phase deforming in an aggregate. A relevant question that still remains, however, is how these measured stresses relate to the macroscopic stress applied to a rock. In the work presented here, the lack of subgrains in orthopyroxene inhibits the use of subgrain-size piezometry as a tool for exploring stress partitioning. However, stress partitioning can still be explored via X-ray diffraction. Only a few studies have utilised X-ray diffraction in this manner (Li et al., 2007; Y. Wang et al., 2013), none of which were in olivine-orthopyroxene systems. We use the average stresses for each diffraction peak to compare the range in stresses measured in olivine and orthopyroxene within the harzburgite samples (Figure 3.13). In experiments performed at high pressure (> 5 GPa) and temperature (1100°–1250°C), orthopyroxene was supporting a greater stress than olivine. However, in experiments San390 and San508, which were deformed at lower pressures of ≤ 5.0 GPa, the stresses supported by olivine and orthopyroxene are more comparable.

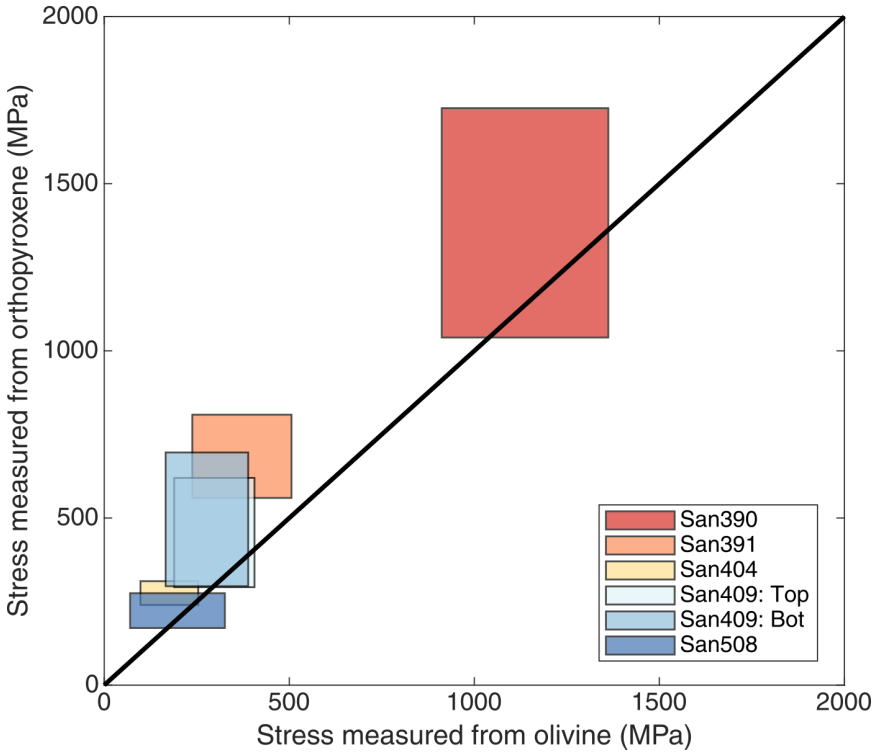

Figure 3.13: Comparison of the absolute value of the differential stresses measured in olivine and orthopyroxene from X-ray diffraction. Stresses from individual peaks are taken either over the final 10–20% strain or the full range of strains after temperature changes. The size of the box covers the full range of stresses from the different diffraction peaks measured in each phase.

It can be concluded from the results of this study that at mantle conditions, stress is not constant throughout polymineralic samples; therefore the stress measured in an individual phase cannot be inferred to be the macroscopic stress experienced by the rock. The higher stress supported by the orthopyroxene at high pressure also has interesting implications for current mixing models. As the harzburgites presented here consist mainly of olivine (∼70%), and orthopyroxene is expected to be stronger than olivine at our experimental conditions (e.g., Raterron et al., 2016), their microstructures can be categorised as interconnected weak layers (IWL, Handy, 1990). Stresses within the individual phases in an IWL are modelled to comply with the isostress condition (Handy, 1990) and have been observed to do so experimentally (e.g., Ji et al., 2001). However, the higher stress within the strong orthopyroxene phase in our experiments does not fit with the isostress condition. Similarly, work by Li et al. (2007) using X-ray diffraction to explore stresses within composites of varying proportions of MgO and spinel measured higher stresses within the strong phase when it comprised just 25% of the mixture. Clearly, further work is necessary to examine polymineralic mixing models using *in-situ* stress measurements, such as X-ray diffraction.

3.5 Conclusions

We deformed olivine, orthopyroxenite, and olivine-orthopyroxene mixtures in a D-DIA apparatus at temperatures and pressures analogous to mantle conditions. *In-situ* stress measurements from X-ray diffraction are compared to *ex-situ* measurements from subgrain-size piezometry. A good correlation between stresses from subgrain-size piezometry and X-ray diffraction in olivine in both monomineralic and polymineralic aggregates demonstrates that subgrain size is immune to the effects of grain-boundary pinning by secondary minerals. Subgrain size also displays a good correlation with the final stress experienced by the sample. However, this study identifies a number of important factors to consider when applying subgrain-size piezometry to natural rocks. First, the subgrain-size pieozometer from Goddard et al. (2020) should only be applied to stresses within its calibration range. The application of the subgrain-size piezometer to rocks deformed at stresses higher than those used in the piezometric calibration will potentially underestimate stress. Second, very fine-grained rocks may not have grain sizes sufficiently large to host subgrains that have formed under low stresses. Finally, for the compositional ratios and high pressure (5.0–8.3 GPa) conditions of this study, the stresses supported by orthopyroxene and olivine are not equal. As such, care must be taken when extrapolating the stress measured from an individual phase to the bulk stress experienced by the sample.

4 Insights into the deformation of olivine-orthopyroxene aggregates from subgrain-size piezometry

Abstract

To assess the mechanisms by which polymineralic rocks deform, we apply subgrain-size piezometry to experiments conducted on mixtures of olivine and orthopyroxene, with orthopyroxene fractions (f_{px}) of 0.20, 0.40, 0.70, and 0.93. Samples were synthesised from San Carlos olivine and Bamble orthopyroxene and were deformed to strains of 0.34–0.43 in a servo-controlled, internally heated gas-medium apparatus at a confining pressure of 300 MPa and a temperature of 1250°C. While the samples containing the highest and lowest fractions of orthopyroxene exhibited similar strengths, the intermediate sample (f_{px} = 0.40) exhibited anomalous weakening beyond that which can be accounted for through the grain-size sensitivity of common deformation mechanisms. Results from subgrain-size piezometry indicate that weakening occurred solely in orthopyroxene, which we propose deformed by interface-reaction-controlled diffusion creep. However, this effect is not observed in previous experiments on high-purity, synthetic harzburgites. We suggest therefore that impurities, such as Ca, segregate at phase boundaries in olivine-orthopyroxene mixtures, enhancing the reaction at and/or diffusivity along phase boundaries, which in turn appears to increase the deformation kinetics.

4.1 Introduction

Knowledge of the high-temperature flow of mantle rocks is important for our understanding of geological processes such as convection (e.g., van den Berg et al., 1993), the dip of downgoing slabs (e.g., Tovish et al., 1978), and slab penetration of the 670 km discontinuity (e.g., Goes et al., 2008). As the upper mantle is predominantly composed of olivine ($\geq$ 60%), flow laws for steady-state creep of olivine are often used to describe the bulk behaviour of the upper mantle and generally take the form of

$$\dot{\varepsilon} = A\sigma^n d^{-p} \exp\left(\frac{-Q}{RT}\right), \tag{4.1}$$

where $\dot{\varepsilon}$ is strain rate, A is a material-dependent constant, σ is differential stress, n is the stress exponent, d is grain size, p is the grain-size exponent, Q is the activation enthalpy, R is the gas constant, and T is temperature. However, the mantle is polymineralic and thus application of olivine flow laws assumes a negligible effect of other phases on macroscopic

behaviour.

To test this assumption, extensive experimental work has explored the strength of polyphase aggregates (e.g., Dimanov & Dresen, 2005; Bystricky et al., 2006; Marques et al., 2011; Dresen et al., 1998; Marques et al., 2010). Many of these past studies have compared the bulk strength of an aggregate to predictions from two composite models, in which either the strain rate or the stress is assumed to be spatially homogeneous. These two models provide theoretical upper and lower bounds to the strength of the aggregate. In the majority of experimental data, the bulk stress does lie between these bounds (e.g., Barnhoorn et al., 2005; Covey-Crump et al., 2013; Rybacki et al., 2003). Handy (1994) suggested that the applicability of either the iso-strain or the iso-stress model is dependent on the microstructural arrangement of the two phases in the aggregate. If the stronger phase is interconnected to form a load-bearing framework, the strains in both phases may be the same. However, if the weaker phase forms interconnected layers, it will localise strain (Bruhn et al., 1999; Ross et al., 1987) and control the strength of the aggregate (Bystricky et al., 2006; Handy, 1990).

In a minority of studies, the flow stress of an aggregate does not fall between these upper- and lower- strength bounds. For example, the addition to olivine of 30% ferropericlase, a mineral expected to be three to four times weaker than olivine at equivalent conditions, actually increased the strength of the sample (Wiesman et al., 2018). Alternatively, aggregates with approximately equal volume fractions of the constituent minerals have exhibited excessive weakening, deforming at stresses much lower than their end-members at the same conditions (e.g., Sundberg & Cooper, 2008; Bruhn et al., 1999; Zhao et al., 2019). One possible explanation for such behaviour is that diffusion creep in these mixtures is enhanced because of phase-boundary diffusion (e.g., Bruhn et al., 1999; Zhao et al., 2019).

The stress supported by individual phases during deformation provides key insight into the details of the operating deformation mechanisms. In the few experimental studies that attempt to quantify local stresses in polymineralic rocks, most rely on either examining pre- and post-deformation microstructures (e.g., Bloomfield & Covey-Crump, 1993) or using imprinted microgrids (e.g., Cho & Gurland, 1988) to infer strains, and thus strain rates, from which stress can be estimated through previously calibrated flow laws. However, these methods still assume that phases in polymineralic rocks behave the same as the end-member

monomineralic aggregates. Li et al. (2007) directly measured the stress within MgO and spinel in composites using synchrotron X-ray radiation and found a non-linear relationship between the flow stress and the volume fraction. Wang et al. (2013) similarly used X-ray diffraction to compare the bulk stress of $CaGeO_3$ perovskite to that of $CaGeO_3$ perovskite with the addition of 20% MgO. They found that the volumetrically averaged stresses of the composite were identical to those in the single phase deformed under similar conditions, consistent with the iso-strain model. However, no observations have yet been made of the stress partitioning in polymineralic aggregates that exhibit flow stresses outside of the iso-stress and iso-strain bounds.

Here we implement a new method to investigate the stresses supported by individual phases in polymineralic aggregates. Previous work in this thesis has linked subgrain-boundary spacing to the local stress (Chapter 3). This suggests that subgrain-size piezometry offers an alternative tool to explore the strength of polymineralic aggregates, which is more readily available than X-ray diffraction and applicable to a wide range of minerals. Here we apply the subgrain-size piezometer of Goddard et al. (2020) to olivine and orthopyroxene mixtures comparable to those previously documented to exhibit flow stresses outside of the iso-stress and iso-strain bounds. We then use these stresses measured within the constituent phases to better understand the mechanism by which analogous weakening of polymineralic rocks occurs.

4.2 Experimental Methods

4.2.1 Sample preparation

Polycrystalline samples were fabricated from powders of San Carlos olivine (Fo_{90}) and Bamble enstatite (En_{85}) with pyroxene volume fractions of $f_{px} = 0.93$, 0.70, 0.40, and 0.20. These samples are hereafter referred to as Px93, Px70, Px40, and Px20. Powders were combined and tumbled for ∼24 hours with large single crystals of olivine to prevent clumping of the powder. The powders were then dried for 12 hours in a gas-mixing furnace at 1000°C using a mixture of CO and CO_2 set to maintain the oxygen fugacity at the Ni:NiO buffer.

To synthesise samples, prepared powders were first uniaxially cold pressed (∼150 MPa, differential stress) into nickel cans and capped with a Ni disc. Encapsulated samples

were stacked between alumina and zirconia pistons and inserted into an iron jacket. Samples were hot pressed at temperatures of 1240°–1250°C and confining pressures of 150–300 MPa in a gas-medium apparatus (Paterson, 1990) in the Rock and Mineral Physics Lab at the University of Minnesota. A small end load corresponding to 2 MPa differential stress was maintained on the sample to help monitor densification. Hot pressing was stopped once the shortening rate decreased below a measurable level, which took between 30 and 100 mins.

4.2.2 Deformation Experiments

Samples were deformed in two servo-controlled, internally heated gas-medium apparatus (Paterson, 1990) at a confining pressure of 300 MPa and temperatures of 1240°–1250°C. Those experiments with prefix 'PI' were carried out using apparatus PI-3, and the experiment with prefix 'PT' was carried out on apparatus PI-10. Temperature was controlled to within ± 2°C of the target temperature (1250°C) except for PI-2072 (Px70), which is discussed below. After reaching pressure and temperature, samples were annealed for 40–60 minutes. After annealing, samples were deformed in axial compression.

For all samples except Px93, the deformation was imposed by maintaining a constant displacement rate with the axial actuator. In contrast, Px93 was initially deformed under load control at a differential stress of ∼260 MPa until a steady-state displacement rate was reached at a strain of 12%. At this point, the control was switched to a constant displacement rate to match the steady-state value, corresponding to a strain rate of 2.4×10^{-4} s^{-1}. At five points throughout the experiment, the actuator was frozen, and the stress was allowed to relax to conduct a load-relaxation test. Two of these tests were conducted early in the experiment, prior to switching to constant displacement rate, and three were conducted after switching to constant displacement rate. A similar load-relaxation test was conducted on Px20. The rate of elastic strain with time during the load-relaxation tests was calculated using the time derivative of stress, the stiffness of the rig and the Young's modulus of the sample (see Appendix C.1 for details). The stiffness of the rig was calculated from the machine's compliance and the length and area of the sample at the initiation of the load-relaxation test. All other samples were deformed solely at constant displacement rate, yielding strain rates between 2.3 and 3.6×10^{-4} s^{-1}. For a full list of experimental conditions, see Table 4.1.

For those experiments conducted using PI-3, displacements were measured external to the pressure vessel and corrected for the compliance of the apparatus and the compliance of the sample assembly. The compliance of the apparatus (0.0175 mm/kN) was measured with a an elastic standard at room temperature. The compliance of the sample assembly (0.0085 mm/kN) was measured on a standard assembly at 1200°C and 300 MPa with alumina in place of the sample.

For those experiments conducted using PI-10, displacements were not recorded. However, piston displacement rates were constant throughout the experiments, from which displacement could be calculated at any given time. These displacements were corrected for compliance of the sample assembly (0.0085 mm/kN, as above), but no correction was made for the compliance of the apparatus because displacements on PI-10 are measured internal to the pressure vessel.

All load data from both apparatus were subsequently corrected for the load supported by the Ni and Fe jackets using flow laws reported in Frost and Ashby (1982).

All the samples except Px93 experienced some canting during deformation. To account for this canting, the load-bearing area was taken to be just that between the two pistons and hence can be modelled on the area of overlap of two intersecting circles (Appendix C.1).

Fluctuations of the temperature controller during experiment PI-2072 on Px70 produced oscillating temperatures within the range 1230°–1245°C. Data from this experiment were used to calculate the activation energy of deformation, assuming the deformation mechanism remained constant throughout the experiment.

Table 4.1: Experimental conditions

Sample name	Experiment Name	Opx/Ol mixture	Temperature (°C)	Strain rate ($\times 10^{-4}$ s^{-1})$^{\triangle}$	Steady-state stress (MPa)	Total strain
Px93	PI-2067	93/7	1250	2.4	292	0.34
Px20	PI-2069	20/80	1250	2.3	282	0.37
Px70	PI-2072	70/30	1230–1245	3.6	448*	0.34
Px40	PT-1451	40/60	1250	3.3	187	0.43

$^{\triangle}$ Strain rates are the mean of the steady-state section of the experiment. For PI-2067 this refers to the steady-state portion after stress recovered from the final stress-relaxation test.
* The steady-state stress normalised to a temperature of 1250°C using the Arrhenius plot in Figure 4.3.

4.2.3 Microstructural analysis

To characterise the microstructures, we collected electron backscatter diffraction (EBSD) data with a JEOL 6500 field emission gun scanning electron microscope at the Department of Earth Science, University of Minnesota using a CMOS-based Symmetry S2 EBSD detector. To prepare for analysis, samples were cut parallel to the principal stress axis (σ_1) and polished using progressively finer-grained diamond lapping films or suspensions. Samples were finished with a colloidal-silica polish. To minimise potential charging of the sample during analysis, a 50 Å thick carbon coated was applied. During acquisition of EBSD data, samples were tilted at 70° and mapped in high vacuum at an accelerating voltage of 20 kV. The electron beam was rastered across the sample using step sizes of 0.1 to 0.5 µm.

EBSD data were processed and analysed using Oxford Instruments Channel5 software and the MTEX toolbox (Bachmann et al., 2010; Mainprice et al., 2011) in MATLAB®. Oxford Instruments Channel5 software was used to identify pixels with an apparent misorientation of 60° around [100] relative to their neighbours. This misorientation relationship is a common misindexing error due to the pseudosymmetry of olivine (Bystricky et al., 2006) and therefore these pixels were corrected by applying a rotation of 60° in Channel5. MTEX was then used to remove noise from, and subsequently analyse, the data. Grains that were made up of three pixels or fewer were removed on the assumption that they were likely to be noise. Pixels with a mean angular deviation (MAD) $> 1°$ between bands detected in the diffraction pattern and those in the indexed solution, and non-indexed regions, which make up 18 to 26% of the map, were also removed. All pixels that were no longer assigned a phase were filled by MTEX using the method of nearest neighbour interpolation whereby non-indexed pixels are assigned the average orientation of the surrounding points.

Both the grain and subgrain sizes were measured using the line-intercept method, using critical misorientation angles of 10° and 2°, respectively. When calculating the mean line-intercept length from boundaries with misorientation angles $\geq 10°$ (λ_{gs}), line intercepts that were the same length as the step size of the map were assumed to be noise and removed. In keeping with the method of Goddard et al. (2020), however, this process was not applied to line intercepts from boundaries with misorientation angles $\geq 2°$ (λ). The number of intercepts required to accurately measure grain and subgrain size (Tables 4.2 and 4.3) were determined using the *No_intercepts_check.m* script from Goddard et al. (2020).

To explore the existence and strength of crystal preferred orientations (CPO) and the presence of preferred crystallographic misorientation axes in our deformed samples, we plotted pole figures and misorientation inverse pole figures, respectively. For pole figures, EBSD data were plotted as one point per grain and contoured on multiples of uniform distribution (MUD). For misorientation inverse pole figures, misorientation axes were plotted for neighbouring pixels with misorientation angles between 2° and 10°. We assess the strength of CPOs using the M-index, which is defined as the difference between the observed distribution of uncorrelated misorientation angles, and the distribution of uncorrelated misorientation angles for a random fabric (Skemer et al., 2005). Here uncorrelated misorientation angles are those calculated from the complete set of possible grain pairs including those not in direct contact.

4.2.4 Subgrain-size piezometry

We estimated stresses in individual phases using subgrain sizes measured from EBSD data. The noise levels in the EBSD maps in this study were higher than 1°. As a result, we use the modified 2-degree subgrain-size piezometer calibrated in Chapter 3 (Section 3.2.3).

The experiments were conducted within the same temperature and pressure range as those used to calibrate the subgrain-size piezometer. Therefore, we use the same shear modulus and Burgers vector used for olivine, at room temperature and pressure, by Goddard et al., (2020): 77.8 GPa (J. Wang et al., 2015) and 4.8 Å (a unit cell dimension, Deer et al., 1992, page 4), respectively. The structure and properties of orthopyroxene, however, are potentially more complex at the experimental conditions of this study. At low confining pressures (< 1 GPa) and high temperatures (> 1000°C), orthopyroxene may be in the protoenstatite stability field (Gasparik, 1990). However, for Ca-bearing orthopyroxene, the conditions for our experiments fall on the proto-orthoenstatite boundary (Ohi et al., 2010). Bamble enstatite also contains iron, which is postulated to stabilise orthoenstatite at high temperature and low pressure (Zhang et al., 2020). Finally, the orthoenstatite-protoenstatite transition is expected to be slow at the conditions of our experiments (Smyth, 1974). Thus, we assume the orthopyroxene in our experiments deformed in the orthoenstatite stability field. We therefore use a shear modulus and Burgers vector of 78.1 GPa (Chai et al., 1997) and 5.2 Å (Deer et al., 1992, page 156), respectively. The Burgers vector corresponds to

the c unit cell dimension, consistent with dominance of the (100)[001] slip system at high temperatures in orthopyroxene (e.g., Bystricky et al., 2016).

4.3 Results

4.3.1 Mechanical results

Mechanical data are presented as stress-strain curves in Figure 4.1. All samples exhibited the same general mechanical behaviour. Samples yielded almost instantly (after strains of $< 0.1\%$) and then exhibited transient strain-hardening behaviour before approaching a steady-state stress. The deviation from steady-state stress in Px20 is the result of a small fluctuation in the temperature at the end of the experiment.

The steady-state portions of the graphs from Px20 and Px93 are comparable, with flow stresses and strain rates within error of each other. However, the intermediate composition, Px40, is substantially weaker than the other samples, with a flow stress that is approximately two-thirds of the stress of the others and a strain rate that is higher by a factor of $\sim$1.4.

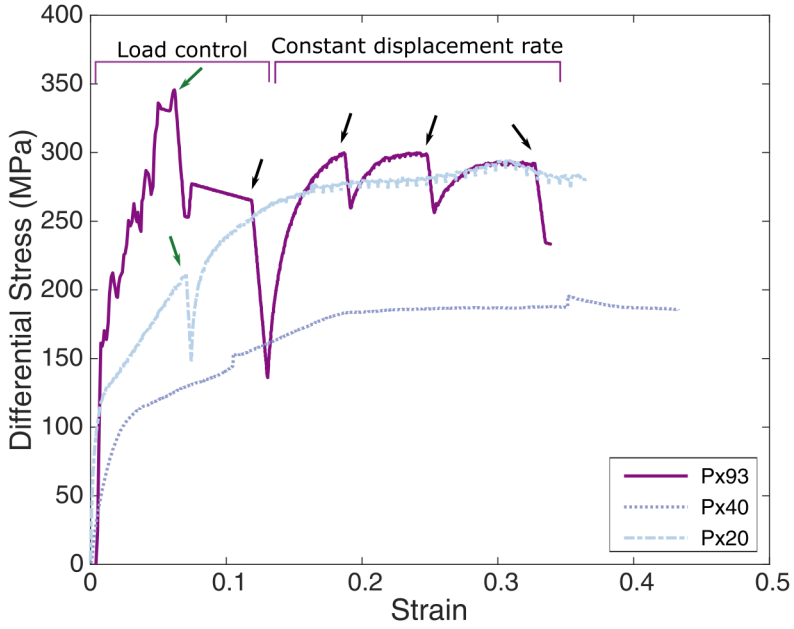

Figure 4.1: Differential stress versus logarithmic strain for experiments conducted at temperatures of 1250 ± 2°C. Black arrows indicate load-relaxation tests during steady-state deformation while green arrows indicate load-relaxation tests performed during transient periods. For Px93, the portions of the experiment that were load controlled and displacement-rate controlled are labelled. All other experiments were controlled at constant displacement rate throughout.

Results from load-relaxation tests are presented in Figure 4.2. The load relaxation in Px20 and Test 1 in Px93 occurred during the transient-creep portion of the experiment. At these points, the stress dependence of the strain rate is represented by power laws with stress exponents of 3.5 ± 0.5 and 4.0 ± 0.4, respectively. The remainder of the load-relaxation tests occurred during steady-state creep and yield power-law exponents in the range of 1.5–2.4. The agreement between the average steady-state stress and strain rate of experiment Px92 and load-relaxation Tests 3–5 suggest the latter are representative of steady-state conditions.

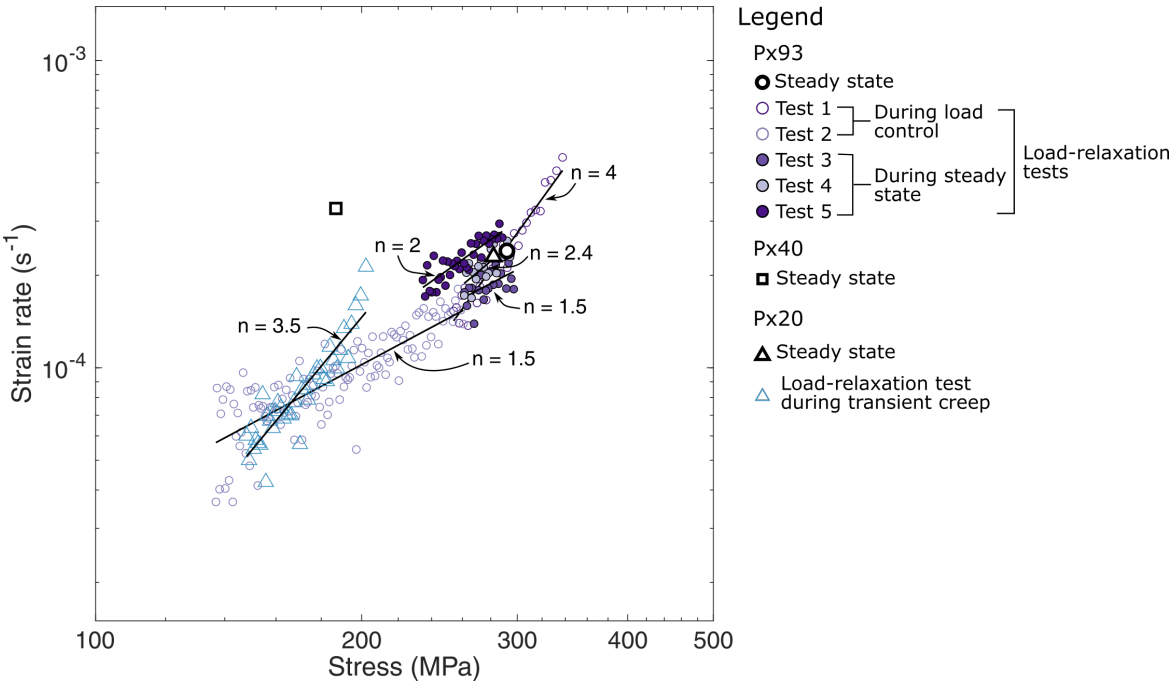

Figure 4.2: Logarithmic plot of differential stress against strain rate during load-relaxation tests. The steady-state strain rates and stresses are plotted in white for comparison.

The mechanical data and temperature profile for Px70 are presented in Figure 4.3. The natural logarithm of the stress was plotted against the oscillating temperature to produce an Arrhenius plot. The linear relationship between $\ln(\sigma)$ and T^{-1} seen in Figure 4.3 indicates that Px70 was deforming by steady-state creep. The gradient of the Arrhenius plot, Q/n, was calculated as 233 kJ·mol^{-1}.

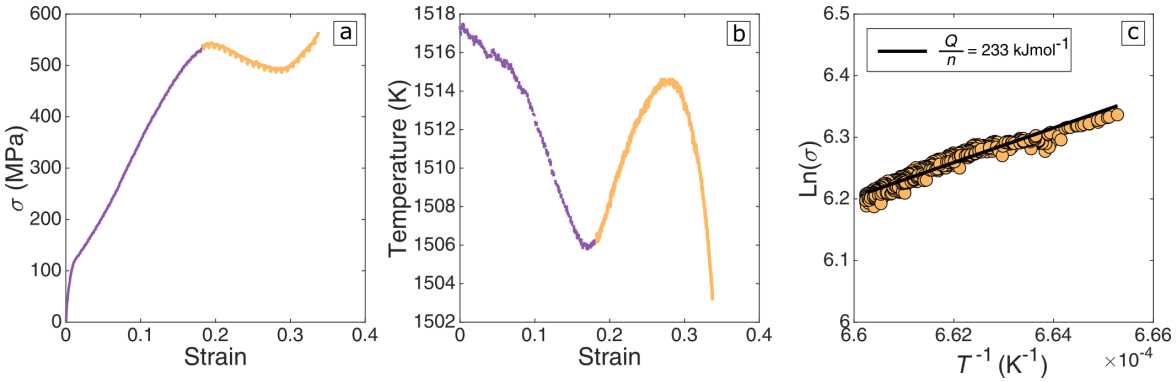

Figure 4.3: Mechanical data for experimental Px70: a) Differential stress plotted against strain, b) temperature profile against strain and c) an Arrhenius' plot for the portion of the experiment highlighted in yellow in b) and c).

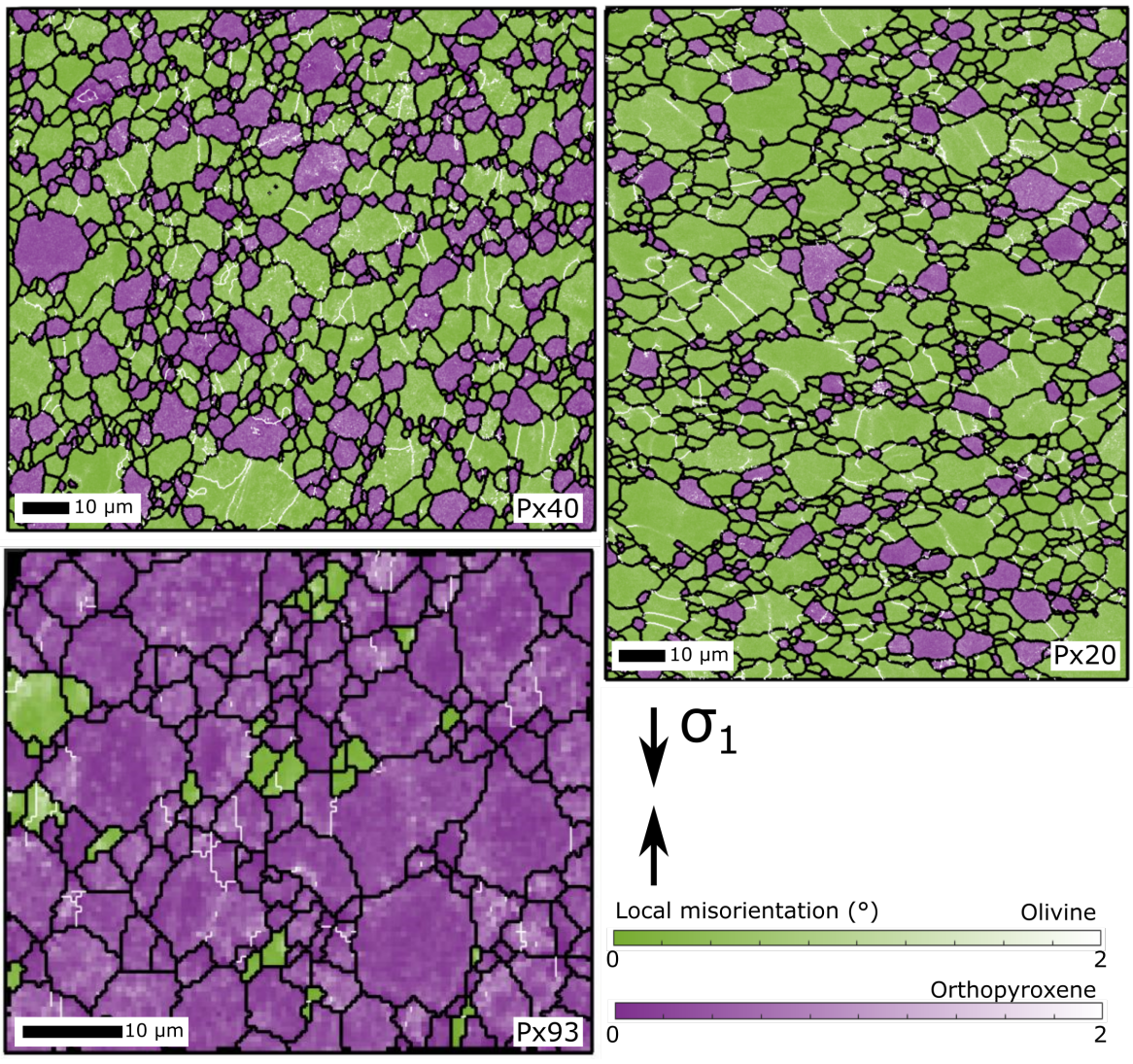

Figure 4.4: Local misorientation maps for each sample. Grain boundaries (misorientation angles of ≥ 10°) are in black and subgrain boundaries (misorientation angles of ≥ 2°) are in white. All non-index regions have been filled by MTEX using the method of nearest neighbour.

4.3.2 Microstructural results

EBSD maps of each sample are provided in Figure 4.4. Olivine and orthopyroxene grains are typically elongate with their long axes approximately perpendicular to the shortening direction. For both Px40 and Px20, orthopyroxene grains have negligible internal deformation. Subgrains are prevalent in larger grains of olivine in these two samples, though they are absent in smaller grains. In Px93, subgrains are present in both olivine and orthopyroxene.

Grain-size distributions are plotted in Figure 4.5. Distributions take a log-normal form with little variation in the mean grain size between samples, ranging from 3.4–5.6 µm and 3.8–6.3 µm for olivine and orthopyroxene, respectively. In Px20 and Px40, olivine has a grain size ∼1.3 times larger than orthopyroxene, whereas the orthopyroxene is ∼3 times larger than olivine in Px93.

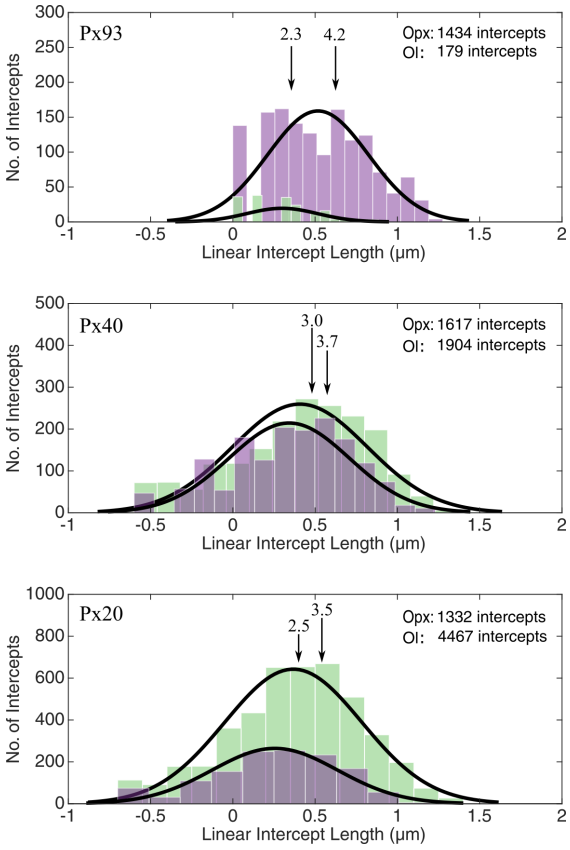

Figure 4.5: Line-intercept lengths between boundaries with misorientation angles ≥ 10° for olivine (green) and orthopyroxene (purple). Mean-line intercepts for each mineral are labelled.

Table 4.2: Grain-size measurements. Mean line-intercept lengths and grain sizes are reported to two significant figures

Sample	Olivine			Orthopyroxene		
	No. Intercepts	λ_{gs} (µm)	Grain size* (µm)	No. Intercepts	λ_{gs} (µm)	Grain size* (µm)
Px93	70	2.3	3.4	70	4.2	6.3
Px20	80	3.5	5.2	80	2.5	3.8
Px40	50	3.7	5.6	60	3.0	4.5

*A stereological correction of 1.5 (Underwood, 1970, page 80–93) is applied to convert mean line-intercept length to grain size.

Pole figures for olivine and orthopyroxene are plotted in Figure 4.6. In all instances, olivine and orthopyroxene present weak CPOs with no obvious link between CPO strength and orthopyroxene volume fraction. In the olivine fraction of Px20 and Px40, distributions of [100] and [001] axes form a girdle perpendicular to σ_1, and the distributions of [010] form a cluster parallel to σ_1, all of which are consistent with deformation on the (010)[100] slip system (e.g., Hansen et al., 2011; Michibayashi et al., 2016). In Px93, only 26 olivine grains are available for analysis. Even so the distributions of the [100] and [010] axes are similar to those observed in samples with lower pyroxene fractions. However no discernible pattern is present in the distribution of [001]. Therefore, it is difficult to confidently draw conclusions about the active slip system in olivine in Px93. For orthopyroxene in all samples, distributions of [001] form a girdle perpendicular to σ_1, and the distributions of [100] form a cluster parallel to σ_1. Both observations are consistent with deformation on the (100)[001] slip system (Jung et al., 2010).

Misorientation inverse pole figures for olivine and orthopyroxene are also plotted in Figure 4.6. In olivine, concentrations of misorientation axes parallel to [001] and [010] are characteristic of (100) and (001) tilt boundaries, as well as (010) twist boundaries formed of [100] and [001] dislocations. However, the alignment of [100] axes perpendicular to σ_1 implies that this is the dominant Burgers vector and therefore that (100) tilt boundaries are likely more common than (001) tilt boundaries. In orthopyroxene, concentrations of low-angle misorientation axes around [010], combined with the alignment of [001] perpendicular to the σ_1 indicated the presence of (001) tilt walls. The presence of concentrations of misorientation axes parallel to [001] in Px20 and Px40 are also consistent with the presence of (100) or (010) tilt walls or (001) twist boundaries

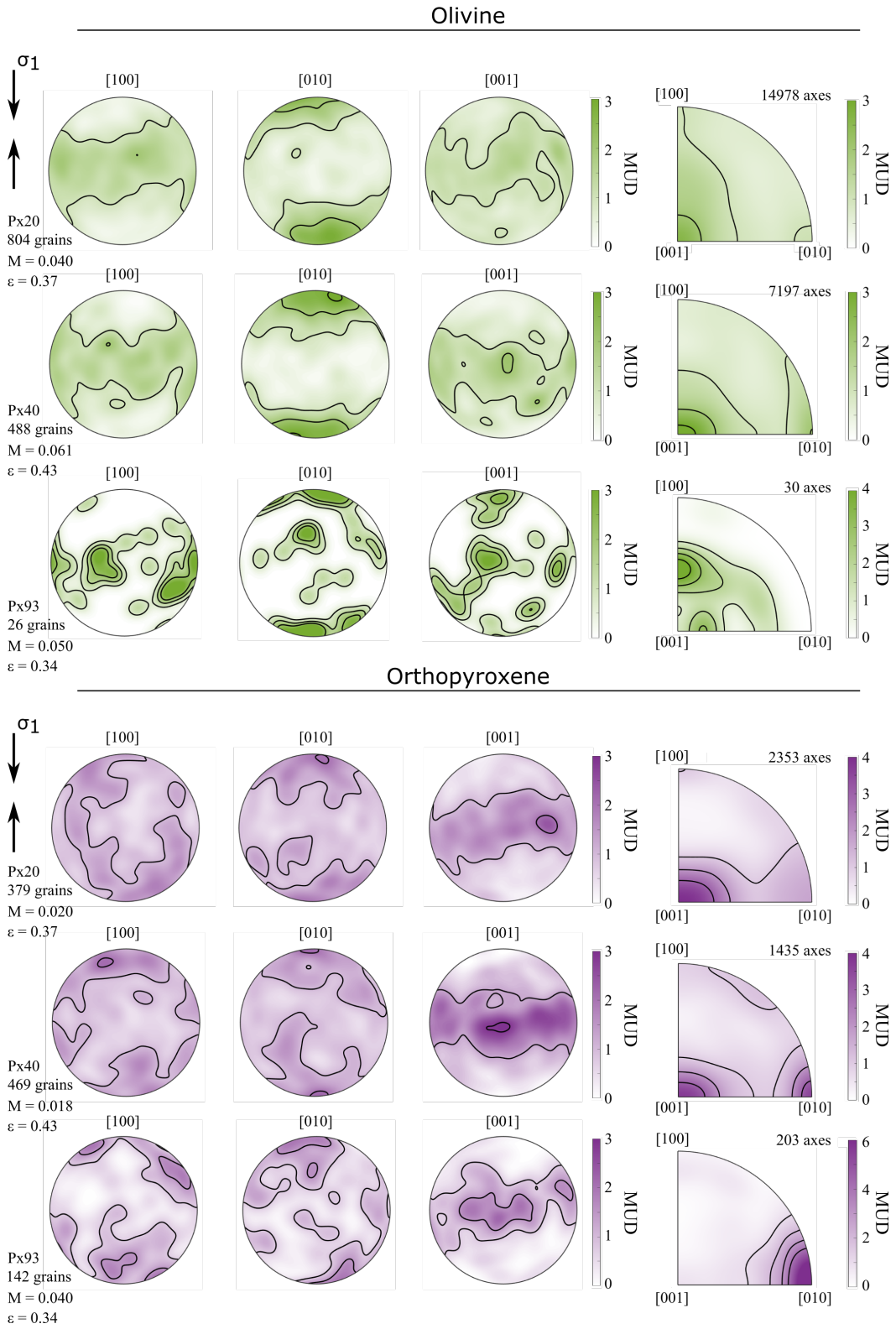

Figure 4.6: Pole figures and misorientation inverse pole figures for olivine (green) and orthopyroxene (purple) for all samples. Figures were constructed using a half-width of 10. The colour scales represent multiples of uniform distribution (MUD). Pole figures were constructed using one point per grain and with the compression axis vertical. For each sample, the composition, number of grains, M-index, and total strain are indicated. For misorientation inverse pole figures, misorientation axes were plotted for neighboring pixels with misorientation angles between 2° and 10°.

4.3.3 Subgrain-size piezometry

Mean line-intercept lengths for subgrain spacing are presented in Table 4.3 along with the associated piezometric stresses. In olivine and orthopyroxene, the mean line-intercept lengths are in the ranges 2.0–3.0 µm and 2.1–3.7 µm, which correspond to stresses of 400–280 MPa and 410–250 MPa, respectively.

Table 4.3: Subgrain-size piezometry results. Mean line-intercept lengths and differential stresses are reported to two significant figures

Sample	Olivine			Orthopyroxene		
	No. Intercepts	λ (µm)	Differential Stress (MPa)	No. Intercepts	λ (µm)	Differential Stress (MPa)
Px93	70	2.0	400	50	3.7	250
Px20	40	2.8	290	60	2.1	410
Px40	50	3.0	280	60	2.7	330

4.4 Discussion

We deformed, and analyzed the microstructures of, olivine and orthopyroxene aggregates with compositions of $f_{\mathrm{px}} = 0.93$, 0.40 and 0.20. While the samples with the highest (Px93) and lowest (Px20) pyroxene fractions exhibited similar strengths, the sample with intermediate composition, Px40, was significantly weaker. Here, we utilise subgrain-size piezometry in an attempt to provide a mechanistic explanation for the behaviour seen at intermediate composition.

4.4.1 Grain-size variation as a source of weakening in polymineralic rocks

Previous experimental work has explored the strength of olivine and orthopyroxene aggregates. These experiments were conducted on mixtures synthesised from high-purity oxides (Ji et al., 2001; McDonnell et al., 2000; Tasaka et al., 2013), natural rocks (e.g., Farla et al., 2013; Sundberg & Cooper, 2008; Hitchings et al., 1989), or a combination of the two (e.g., Tasaka, Zimmerman, & Kohlstedt, 2017; Tasaka et al., 2020). Reported deformation mechanisms have included dislocation creep (e.g., Hitchings et al., 1989), dislocation-accommodated grain boundary sliding (disGBS) (e.g., Tasaka, Zimmerman, & Kohlstedt, 2017; Tasaka et al., 2020), and diffusion creep (Sundberg & Cooper, 2008; McDonnell et al., 2000).

Other than studies by Tasaka et al. (2017; 2020), this previous work has generally found that the weakest samples were those with intermediate compositions. Most of these studies suggested that weakening was a result of finer grain sizes in the intermediate compositions in combination with grain-size sensitive deformation mechanisms (e.g., Ji et al., 2001; Farla et al., 2013; McDonnell et al., 2000; Tasaka et al., 2013). Those analyses indicate that the magnitude of weakening is completely explained by the differences in grain size. To look for a similar effect in our experiments, we examine the bulk stress of each sample normalised to a grain size of 5 µm and a strain rate of 2.2×10^{-4} s^{-1} in Figure 4.7. The iso-stress and iso-strain mixing models have been plotted for comparison. We explore normalising the data using a variety of stress and grain-size sensitivities (n and p, respectively), considering that the precise deformation mechanism operating in each phase in our samples is not well constrained. Regardless of the flow-law parameters used, the bulk stress observed in Px40 is well below the bounds of the end-member models. Thus, we conclude that differences in grain size are not fully responsible for the weakening observed for intermediate compositions in our samples.

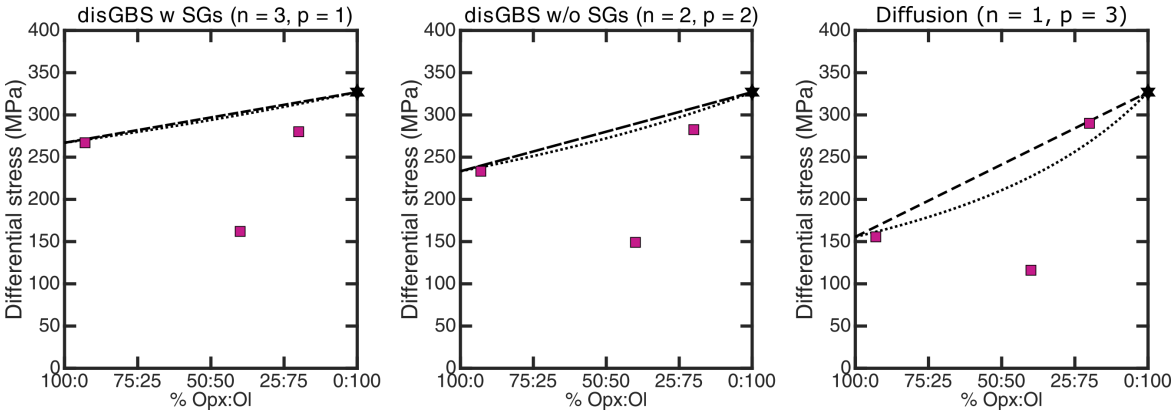

Figure 4.7: Bulk differential stresses, normalised to a grain size of 5 µm *and a strain rate of* $2.2 \times 10^{-4} s^{-1}$*, plotted against orthopyroxene fraction. The measured grain sizes used to normalise the stress were the averages calculated from all grains in the sample irrespective of phase. The dashed line represents the iso-strain condition (upper bound), while the dotted line represents the iso-stress condition (lower bound). The end-member strength for olivine (plotted as a black star) was calculated using the disGBS flow law from Hansen et al. (2011). The* $f_{px} = 0.93$ *is taken to be an approximation of the end-member strength of orthopyroxene.*

4.4.2 An alternative mechanism for weakening in polymineralic rocks

As the weakening in our samples cannot be accounted for by grain-size reduction, an alternative mechanism must be operative. As noted above, this observation is in conflict with many previous investigations of olivine-orthopyroxene aggregates. However, there are a few previous studies in which the observed weakening also cannot be explained by grain size (e.g., Sundberg & Cooper, 2008; Hitchings et al., 1989). A key difference between the anomalous weakening observed here and elsewhere as opposed to the weakening explained by grain size is that, in the former, samples were prepared from natural orthopyroxene. Sundberg and Cooper (2008) deformed composites of Bamble enstatite and Balsam Gap olivine ranging from $f_{\mathrm{px}} = 0.65$ to $f_{\mathrm{px}} = 0$ within the diffusion creep regime. They found that intermediate compositions deformed an order of magnitude faster than predicted for olivine alone. This weakening was attributed to interface-reaction-controlled diffusion creep, whereby ionic silicon—the slowest moving and therefore rate-controlling species—is available in both olivine and orthopyroxene via a reaction at the boundary (Chen, 1982; Wheeler, 1992). Similarly, experiments conducted at comparable conditions to our study by Hitchings et al. (1989) used olivine and orthopyroxene aggregates synthesised from a natural spinel lherzolite nodule. They also found that intermediate compositions were weaker than the end-member compositions in all cases. However, this study did not quantify grain size, so it is not possible to completely eliminate its contribution to the weakening.

Anomalous weakening has also been observed in geological composites of other phases. Bruhn et al. (1999) defomed calcite-anhydrite aggregates synthesised from natural rocks and found that a reduction in grain size could not solely account for the weakening that occurred at intermediate phase fractions. Zhao et al. (2019) deformed 50:50 mixtures of clinopyroxene and olivine and observed strain rates almost an order of magnitude faster than the end-member phases under the same conditions. In both of these studies, weakening was attributed to enhanced kinetic processes along phase boundaries, which allows for faster overall strain rates during diffusion-accommodated grain-boundary sliding.

A similar model to those described above for other systems can only apply to our samples if the dominant deformation mechanism is rate limited by grain-boundary diffusion. To better understand the deformation mechanism occurring in the experiments presented here, we conducted load-relaxation tests on Px93. During steady-state creep, we measured

stress exponent values of 1.5–2.4, which is consistent with diffusion creep rate limited by either grain-boundary diffusion or an interface reaction. There is also a possibility that these samples were deforming by disGBS. The subdivision of disGBS into mechanisms with and without subgrains was proposed by Langdon (1994, 2006) and discussed in the context of olivine and orthopyroxene by Tasaka, Zimmerman, and Kohlstedt (2017). DisGBS with subgrains has values of $n = 3$ and $p = 1$, whereas disGBS without subgrains has $n = 2$ and $p = 2$. DisGBS with subgrains could be the dominant deformation mechanism for olivine within Px20 and Px40, and for orthopyroxene within Px93, where the minerals exhibit clear subgrain structure. However, the lack of subgrain development in the orthopyroxene within Px20 and Px40 is consistent with either disGBS without subgrains or diffusion creep as the dominant mechanism. Notably, the microphysics of disGBS without subgrains discussed by Langdon (2006) is rate-limited by grain-boundary diffusivities.

The Arrhenius plot, yielding a value of Q/n for sample Px70 in Figure 4.3, offers further insight into the dominant deformation mechanism in orthopyroxene in the presence of phase boundaries. Assuming a value of $n = 1$, as would be the case for diffusion creep, results in a value of $Q = 233$ kJmol^{-1}. This is in good agreement with the published activation energy for wet orthopyroxene deforming in diffusion creep ($\sim$ 200 kJmol^{-1}, Zhang et al., 2017). A diffusion creep mechanism is therefore consistent with the available data.

The difference in the deformation behavior of the two phases in Px40 is also illustrated by the stress heterogeneity measured through subgrain-size piezometry. Olivine appears to support a much higher stress than the bulk stress. Therefore, the orthopyroxene must support a considerably lower stress such that the average stress is equal to the bulk stress. To estimate the stress supported by orthopyroxene, we use the stresses measured in olivine through subgrain-size piezometry and the bulk stress experienced by the sample to calculate the stress supported by orthopyroxene using the iso-strain condition,

$$\sigma_{\mathrm{agg}} = \sigma_{\mathrm{w}}\phi_{\mathrm{w}} + \sigma_{\mathrm{s}}\phi_{\mathrm{s}}, \tag{4.2}$$

where σ_{agg} is the bulk stress experienced by the sample, ϕ refers to volume fraction of a given phase, σ is the stress supported by that phase, and the subscripts w and s represent the weak and strong phase, respectively (Voigt, 1928; T. E. Tullis et al., 1991). The results of this calculation are presented in Figure 4.8 and suggest that orthopyroxene in Px40 is

only supporting a stress of about 50 MPa. In addition, the comparative stresses measured in olivine in Px20 and Px40 confirm that all the weakening in the former is accommodated by orthopyroxene. Furthermore, based on the apparent stress supported by olivine in Px40, the strain rate predicted by the disGBS flow law for olivine ($1.3 \times 10^{-4}\mathrm{s}^{-1}$) is the same order of magnitude as the macroscopic strain rate of the bulk sample, ($3.3 \times 10^{-4}\mathrm{s}^{-1}$). Therefore, the orthopyroxene is deforming at a similar rate even though it supports much lower stresses.

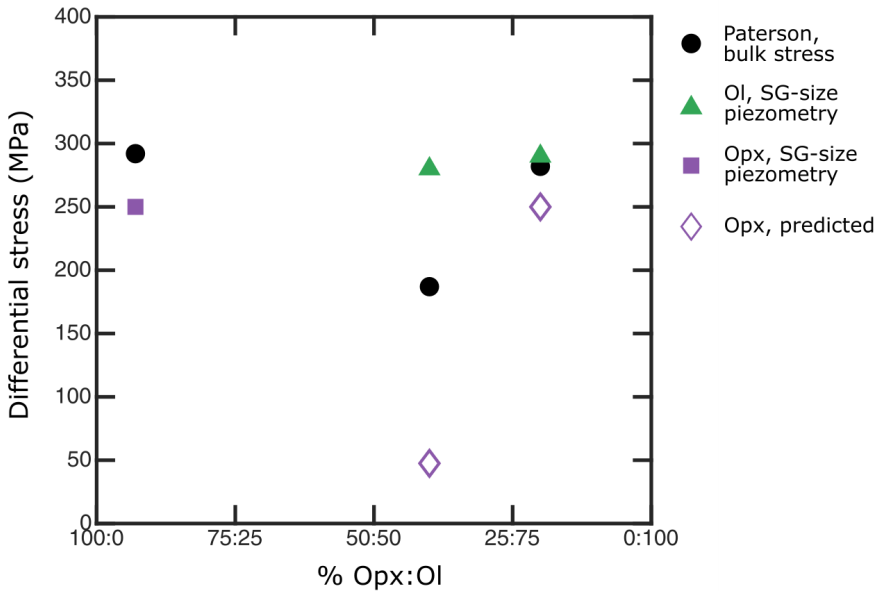

Figure 4.8: Stress partitioning within olivine-orthopyroxene aggregates plotted as a function of percentage orthopyroxene. Bulk stresses measured from the Paterson experiments are plotted as black circles. Variations in the grain size between samples have not been accounted for in this figure. Stresses measured using the 2° subgrain-size piezometer are plotted as green triangles and purple squares for olivine and orthopyroxene, respectively. Where no subgrain boundaries are present, the stresses predicted for orthopyroxene through the rule of mixtures (Eq. 4.2) are used instead and plotted as open diamond

The microstructures, apparent stress exponent, activation energy, and low stress in orthopyroxene all suggest that deformation rates are linked to fast phase-boundary diffusion. In this case, we expect that the macroscopic stresses would fall as the volume fraction of phase boundaries increases. Indeed, this trend was observed for a small proportion of the experiments reported by Bruhn et al. (1999). Of those displaying this trend, most were 50:50 composites. We plot the strength of our sample against the phase boundary proportion in Figure 4.9. This analysis shows significant weakening occurs when $\geq 40\%$ of the boundaries are between phases, consistent with the observation of Bruhn et al. (1999).

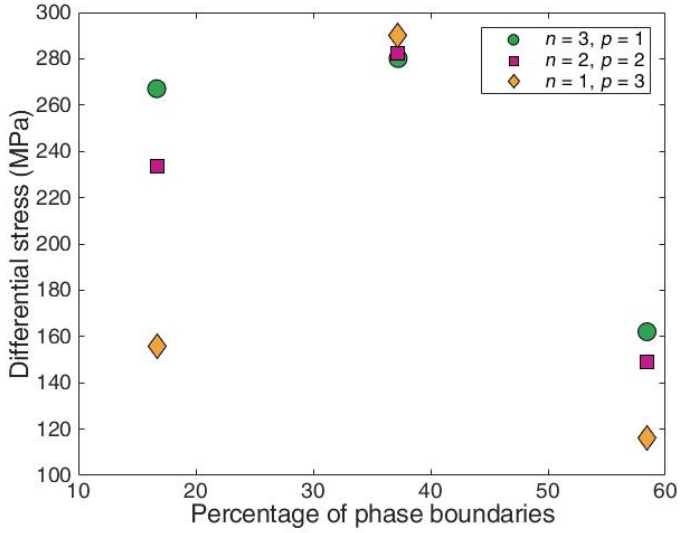

Figure 4.9: Percentage of phase boundaries out of the total boundaries (phase and grain) plotted against the differential stress, normalised to a grain size of 5 µm *and a strain rate of* $2.2 \times 10^{-4} s^{-1}$. *The measured grain sizes used to normalise the stress were the averages for the line-intercept lengths of both phases. Differential stresses are shown normalised using a variety of stress exponents (n) and grain-size exponents (p).*

As noted above, previous experiments that do not contain natural orthopyroxene do not reveal anomalous weakening (Ji et al., 2001; Farla et al., 2013; McDonnell et al., 2000; Tasaka et al., 2013; Tasaka, Zimmerman, & Kohlstedt, 2017; Tasaka et al., 2020). By definition, this means that they also do not exhibit a correlation between phase-boundary percentage and strength (Tasaka et al., 2020), even for samples deforming definitively in the diffusion-creep field (McDonnell et al., 2000). The most obvious impurity ubiquitously present in natural orthopyroxene and not present in synthetic orthopyroxene is Ca. Calcium is a major impurity in the Bamble enstatite (Bowey et al., 2001) used in this study. Calcium also occurs in San Carlos olivine (Abramson et al., 1997) and has been shown to strongly segregate at grain-boundaries (Hiraga et al., 2004). Yabe et al. (2020) recently demonstrated that Ca segregated at olivine grain boundaries greatly enhances both reaction and mass transport and thus creep rates. We hypothesize that Ca similarly segregates to phase boundaries in our olivine-orthopyroxene mixtures, offering a likely mechanism for enhanced phase-boundary diffusivities and the associated weakness of samples with high proportions of phase boundaries.

4.4.3 Implications for deformation in the upper mantle

When combined with previous experiments, the results here suggest that harzburgite synthesised from natural samples may exhibit anomalous weakening beyond that which can be accounted for through the grain-size sensitivity of classic deformation mechanisms.

This weakening seems particularly prevalent when at least one phase is deforming by diffusion creep, for which the reaction at and diffusivity of the phase boundaries appears to enhance the deformation kinetics. Earth's upper mantle consists of 30–40% orthopyroxene, which, assuming that phases are randomly distributed and of similar grain size, suggests approximately half of the boundaries present in the upper mantle would be interphase boundaries (Zhao et al., 2019). Therefore, interface-reaction-controlled diffusion offers an additional critical mechanism for weakening in well-mixed regions and the associated formation of mantle shear zones.

Further work is required to quantitatively extrapolate the implications of this mechanism to geological conditions. The standard iso-strain and iso-stress models for polymineralic rocks work for the end-member compositions and for high-purity composites. However, in samples where impurities are present, work is required to derive a flow law for diffusion creep in the presence of phase boundaries for incorporation into traditional mixing models.

4.5 Conclusions

1. Subgrain-size piezometry offers a useful tool for investigating the weakening of polymineralic aggregates during high-temperature creep.

2. Individual phases in polyphase materials do not necessarily deform by the same mechanism as in monophase materials.

3. Interface-reaction controlled diffusion creep is dominant, and may only be active, in the presence of impurities such as Ca and when a critical percentage of the boundaries are between phases ($> 40\%$).

4. Polymineralic flow laws and mixing models that make the assumption that phases are deforming by the same mechanisms available in monomineralic rocks should be extrapolated to natural rocks with caution.

5 The stress-depth profile of a major continental strike-slip shear zone

Abstract

Knowledge of the strength of the ductile mid-crust is critical to understanding the seismic cycle. Stresses supported by frictional fault surfaces prior to failure are applied, in part, by relaxation of these mid-crustal stresses. Although the strength-profiles of fault zones with dip-slip movement are well characterised, detailed studies of how the strength varies with depth for strike-slip boundaries are limited.

We measure stress in quartz using subgrain-size piezometry, newly calibrated for electron backscatter diffraction, across a transect of the Early Proterozoic Great Slave Lake shear zone (GSLsz). Exhumation of the GSLsz through shallower crustal levels occurred contemporaneously with dextral strike-slip shearing. The combination of deformation and uplift resulted in exposure at the surface of a progressively narrow, down-temperature sequence of fault rocks. The GSLsz therefore presents an ideal opportunity to explore the different structural levels of a strike-slip fault zone.

To calculate a depth for each stress measurement, we measured the temperature using amphibole-plagioclase, Ti-in-amphibole, Ti-in-biotite, and Ti-in-quartz thermometry. To ascertain which method best records the temperature of deformation, we compared thermometry results to the temperature range inferred from the quartz microstructures. Amphibole-plagioclase and Ti-in-amphibole thermometry are found to measure the peak temperature associated with the mineral assemblage, while Ti-in-quartz best represents the temperature of deformation.

The strength profile of the GSLsz is compared to those previously reported for other fault zones on the basis of grain-size piezometry. The lower-crustal rocks of the GSLsz are found to be stronger than other shear zones that operated under similar conditions. A number of possible explanations for this disparity exists. First, the subgrain-size piezometer may be correctly measuring the bulk stress, and the GSLsz represents an anomalously hot, high-stress shear zone. Second, the subgrain size and grain size may evolve at different rates, and thus represent different portions of the deformation history. Finally, the stress measured in quartz in polymineralic regions may not equal the bulk stress experienced by the sample, and thus subgrain-size piezometry on multiple minerals is required to enable accurate comparisons of this study to those with stress estimates from grain-size piezometry.

5.1 Introduction

The tectonic strain accommodated by the continental crust is localised in shallow, brittle faults, which extend to form ductile shear zones at depth (Kirby, 1985). This two layer rheological model was first conceptualised by Sibson (1977) based on fieldwork on the Outer Hebrides thrust, Scotland, and was supported theoretically by Scholz (1988) to form the commonly referred to 'Sibson-Scholz fault-zone model'. Subsequent work to test and validate the crustal strength profile assumed in this model has been motivated by the need to understand the distribution of earthquakes (e.g., Liu & Zoback, 1997; Behr & Platt, 2014) and continental-scale patterns of deformation (e.g., England et al., 1985). The strength of seismogenic faults in the upper crust is relatively well constrained (e.g., McKenzie & Brune, 1972; Byerlee, 1978; Marone, 1998; Holdsworth et al., 2011; Wallis et al., 2015; Copley, 2018). As the stress supported by the mid- to lower crust influences the distribution and magnitude of stresses and styles of deformation in the overlying crust (e.g., Kirby & Kronenberg, 1987; Roy & Royden, 2000; Ellis et al., 2006; Lapusta & Rice, 2003; Barbot et al., 2012), understanding the stress supported by the lower portion of the Sibson-Scholz fault profile remains an important source of uncertainty in modelling fault-zone processes (e.g., Bürgmann & Dresen, 2008; Menegon et al., 2011; Behr & Platt, 2014).

The magnitudes of differential stress supported by the ductile lower crust can be estimated by the examination of exhumed rocks with microstructural elements that have a known relationship with stress—a process known as paleopiezometry (e.g., Kohlstedt & Weathers, 1980). By far the most common microstructure used in piezometry is the size of dynamically recrystallised grains, for which the grain size in monophase regions is inversely proportional to the differential stress at the time of deformation (e.g., Karato et al., 1980; Schmid et al., 1980; A. Post & Tullis, 1999; Stipp & Tullis, 2003; Cross et al., 2017).

Stress estimates based on grain-size piezometry have characterised the strength profile of numerous shear zones (e.g., Behr & Platt, 2014). However, the full strength envelopes of shear zones have mostly been obtained from those that experienced a significant component of dip-slip movement that facilitates exhumation of rocks from the middle and lower crust (e.g., Behr & Platt, 2014; Kidder et al., 2012). In contrast, detailed knowledge of how the strength of strike-slip shear zones varies with depth is limited as the exhumation of lower-crustal rocks in such contexts requires significant erosion without the aid of uplift

driven by motion on the fault. As such, the range of depths recorded in exposures of strike-slip shear zones are typically more limited than in those from shear zones with a significant dip-slip component. Most studies on strike-slip shear zones have instead focused on exploring how stress varies in one crustal slice (e.g., Türkoğlu et al., 2016; Czertowicz et al., 2019), with particular emphasis on the brittle-plastic transition, in which pseudotachylytes and ductile rocks appear to have occurred contemporaneously (e.g., Orlandini & Mahan, 2020; Melosh et al., 2018).

Depth profiles of stress measurements for strike-slip shear zones have, however, been constructed in some instances. Van der Werf et al. (2017) inferred the strength of the Baja California strike-slip shear zone at depth using deformed xenoliths from a nearby (< 20 km) volcanic field. However, xenoliths lack information on the relative horizontal placement of different samples and on their orientation relative to the external stress field. Stipp et al. (2002) measured a variety of stresses in the Tonale strike-slip fault zone, which exhibits a temperature gradient from $\sim$250°C to $\sim$700°C. However, this temperature gradient existed as a result of emplacement of the adjacent Adamello pluton, which occurred contemporaneously with dextral shearing and as such, gives little information of how the strength of the Tonale strike-slip fault zone varied with depth.

The Great Slave Lake shear zone (GSLsz), Northwest Territories, Canada offers the perfect field site to explore the strength profile of a strike-slip shear zone. This early Proterozoic continental-scale strike-slip structure underwent deformation and exhumation contemporaneously, such that the rocks now exposed at the surface were affected by progressively narrower zones of deformation with decreasing depth that result in partial overprinting of the broader zones of rocks deformed at greater depths (Hanmer & Lucas, 1985; Hanmer, 1988). Near-continuous exposure of the GSLsz also allows the relationship between different units to be easily established. Large portions of the structure run through homogenous felsic intrusive lithologies, thus allowing the structural deformation in the shear zone to be examined largely independently of potential protolith effects. Recent phase-equilibria modelling and thermobarometry indicate the final conditions recorded by each metamorphic unit fall on a single metamorphic field gradient, implying that they record deformation during a single orogenic cycle (Dyck et al., 2020).

We apply the subgrain-size piezometer recently calibrated by Goddard et al. (2020) for electron backscatter diffraction (EBSD) to a transect through the different metamorphic units of the GSLsz to construct a stress profile for a continental-scale strike-slip fault. Subgrain size, which is also inversely proportional to the differential stress experienced by a rock during deformation (e.g., Luton & Sellars, 1969; Twiss, 1986; Mercier et al., 1977; Goetze, 1975; Friedman & Higgs, 1981), can be used to measure the stress in polymineralic rocks (Hansen & Warren, 2015; White, 1979) and thus greatly expands the samples available for analysis. To the best of our knowledge, this dataset is the first study that spans the full lower crust and measures stress using a single consistent protocol, which eliminates the systematic biases among different studies. We constrain the temperatures at which samples were deformed using Ti-in-biotite, Ti-in-quartz, Ti-in-amphibole, and amphibole-plagioclase geothermometry. As the aforementioned geothermal gradient is well established (Dyck et al., 2020), the temperatures constrain the depth of deformation and allow construction of a crustal strength profile of the GSLsz. This lower-crustal strength profile can be used as an analogue for the buried portions of plate-boundary scale strike-slip faults that are active today, such as the San Andreas Fault.

5.2 Geological context

5.2.1 Regional setting

The GSLsz lies between the Archean Slave and Rae cratons (Figure 5.1a; Hoffman, 1987; Hanmer et al., 1992). The Slave micro-continent underwent oblique east-dipping subduction beneath the Rae province (Hoffman, 1987) that initiated at 1.97 Ga (Hanmer et al., 1992). The tectonic boundary between the Slave and the Rae cratons consists of, from north to south, the Thelon Tectonic Zone (TTZ), the GSLsz, and the Taltson Magmatic Zone (TMZ). The TTZ is a deformed continental arc, related to the collision of the Slave craton and the northwest part of the Rae craton during the Thelon orogeny at ca. 1.97 Ga (Hanmer et al., 1992). The TMZ (2.0–1.9 Ga.) is made up of granitoids, metasedimentary gneisses, granitic basement gneisses, and amphibolites (Chacko et al., 2000) but lacks the high-grade mylonites that are seen in the GSLsz and TTZ.

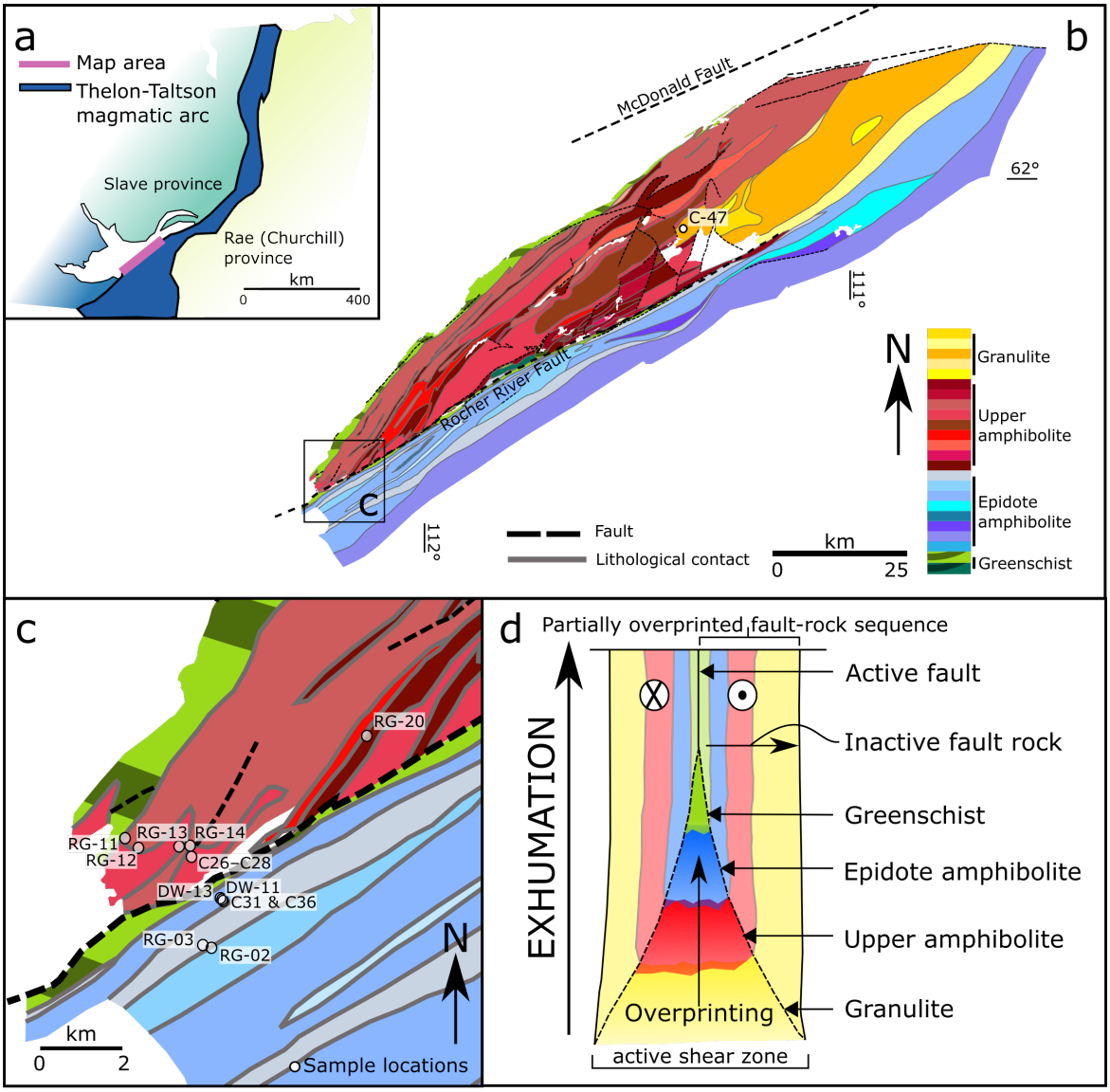

Figure 5.1: (a) Regional geological context of the GSLsz. (b) Geological map of the GSLsz, modified from Figure 3 in Hanmer (1988). Different shades of colour within each metamorphic unit represent different lithologies as defined by Hanmer (1988). For descriptions of these lithospheric units see the Figure D.1. (c) Locations of samples used in this study. The location of (c) in the shear zone is identified by the black box in (b). (d) Schematic sketch showing the progressive uplift, cooling, and narrowing of a strike-slip shear zone resulting in a partially overprinting down-temperature sequence of fault rocks exposed at the surface.

5.2.2 Great Slave Lake shear zone

The GSLsz is a vertical shear zone (Hanmer, 1988) that was once a continental transform fault accommodating indentation of the Slave craton into the margin of the Churchill province (Rae craton) (Figure 5.1a; Hoffman, 1987; Hanmer, 1988). The shear zone is up to ∼25 km wide (Hanmer, 1988) and likely extends to the base of the crust, maintaining a steep dip down to the Moho (Eaton & Hope, 2003). Using aeromagnetic data, the GSLsz can be delineated for over 1300 km, stretching from the foothills of the Rocky Mountains in the west to the Thelon Basin in the east (Eaton & Hope, 2003). Deflections of magnetic anomalies suggest that the GSLsz accommodated up to 700 km of dextral displacement (Hoffman, 1987; Eaton & Hope, 2003). Recent geothermobarometric data indicate that the presently exposed rocks within the shear zone underwent syntectonic exhumation from pressures of > 1 GPa to < 0.4 GPa and concomitant cooling from ∼800°C to < 450°C (Dyck et al., 2020).

The GSLsz consists of rocks metamorphosed and deformed across four metamorphic grades: granulite, upper amphibolite, epidote amphibolite, and greenschist (Hanmer, 1988). Figure 5.1b presents the distributions of rocks of each metamorphic grade along the SE shore of the Great Slave Lake. The majority of these rocks are derived from the megacrystic Laloche batholith, which ranges from leucocratic biotite-hornblende granite to tonalite in composition and intrudes the sillimanite-cordierite-garnet metagranites and migmatitic paragneiss of the Churchill province to the southeast (Hanmer, 1988). Muscovite-sillimanite bearing Archean granites of the Slave craton are present to the northwest of the GSLsz. The fairly homogenous granitoid composition of the GSLsz mylonites allows the microstructural effects of the deformation conditions to be isolated by limiting the effects of variation in protolith composition.

The exhumation of rocks through progressively shallower crustal levels resulted in overprinting of a progressively narrower, down-temperature sequence of fault rocks (Figure 5.1d; Hanmer, 1988). This combination of localisation and exhumation allows different structural levels of the fault zone to be investigated with a lateral transect across the structure. Hence, the GSLsz represents an ideal location to probe the strength of the lower crust over depths of approximately 15–40 km.

In addition to gradients resulting from progressive localisation and exhumation, several units of different metamorphic grade are juxtaposed by late brittle faulting. Two major brittle faults, the McDonald fault and the Rocher River fault, run parallel to the strike of the mylonitic foliation of the GSLsz (Figure 5.1b). The McDonald fault is situated to the north of the GSLsz and juxtaposes greenschist-grade ultramylonites against foliated plutonic rocks of the Slave craton. The Rocher River fault cuts along the centre of the GSLsz, separating amphibolite-grade mylonites from greenschist-grade mylonite. The offset accommodated by these faults is unknown.

The mylonitic foliation dips steeply, commonly near vertical, and strikes NE-SW (Hanmer, 1988; Hanmer et al., 1992). The lineation is typically subhorizontal (Hanmer, 1988; Hanmer et al., 1992) or shallowly plunging (Hanmer & Connelly, 1986) and is observable in the alignment of individual mineral grains (e.g., sillimanite, biotite, and hornblende), quartzo-feldspathic aggregates, and boudins (Hanmer, 1988). Throughout the history of ductile shear in the GSLsz, the shear direction was parallel to the lineation, as evidenced by shear sense indicators including but not limited to rotated porphyroclasts, C' and S' planes, asymmetrical pressure shadows, and shear-band foliation (Hanmer, 1988). The GSLsz deformed through a combination of simple shear and pure shear with oblate deformation sub-fabrics (e.g., transposed banding and chocolate-tablet boudinage), asymmetrical extensional shear-band fabrics, and in-plane wings on rotated mylonitic porphyroclasts indicating a component of shortening across the shear plane (Hanmer et al., 1992). The timing of the mylonitisation is not clear for any of the metamorphic belts. U-Pb dating of zircons in syntectonic granites defines a minimum duration for ductile shear of 2.03 to 1.95 Ga (Hoffman, 1987), while displacement along transverse faults indicate the brittle structures both predate and postdate the greenschist mylonites (Hanmer et al., 1992).

Mafic and pelitic enclaves within the GSLsz enable geothermobarometric constraints for the different metamorphic units (Hanmer, 1988; Hanmer et al., 1992; Dyck et al., 2020). Recent work by Dyck et al. (2020) used phase-equilibria modelling and thermobarometry to constrain pressure–temperature paths for all metamorphic units of the GSLsz. The final equilibrium conditions for all units lie on a single metamorphic field gradient (Figure 5.2), consistent with the units having formed in a single structure during a single orogenic cycle. This analysis of the metamorphic history suggests that the GSLsz is consistent with

the model shear zone presented by Sibson (1977) and Scholz (1988), where deeper metamorphic units experienced progressive overprinting during exhumation. Dyck et al. (2020) also demonstrated that the northern Rae margin underwent crustal thickening, with an initial crustal thermal gradient of $\sim$600°C·GPa^{-1}, increasing to $\sim$1000°C·GPa^{-1}. This elevation in metamorphic field gradient, in addition to the superposition of GSLsz fabrics on peak metamorphic assemblages, suggests that ductile deformation was active while the thickened Rae margin was still relatively hot.

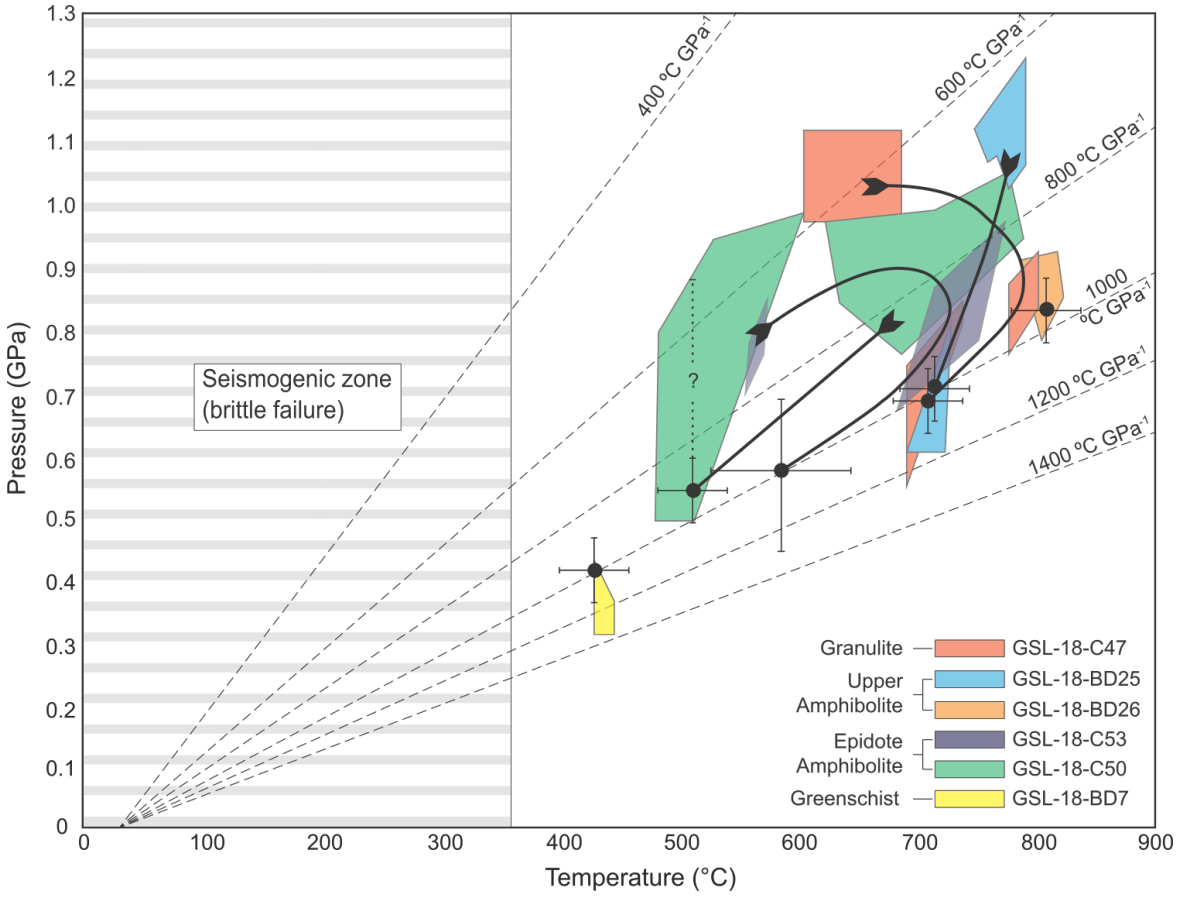

Figure 5.2: Pressure–temperature paths for all the metamorphic units of the GSLsz. Metamorphic conditions are from phase equilibria modelling and thermobarometry on pelitic, mafic, and felsic GSLsz mylonites. Black circles represent the best estimates of the last recorded equilibrium conditions. Error bars are 1 s.d.. Reproduced from Figure 11 in Dyck et al. (2020).

5.3 Methods

5.3.1 Sample selection

In total, nine hand specimens and five cores were selected from a profile transecting the southwestern exposure of the GSLsz for paleopiezometry, nine of which were then selected for geothermometry. Paleopiezometry was conducted on one additional core, GSL-18-C-47, collected along strike (∼90 km to the northeast) in an area mapped as granulite facies. All sample locations are marked in Figure 5.1.

5.3.2 Sample preparation

Hand samples were cut perpendicular to their foliation and parallel to their lineation. When a mineral lineation was not present, the sample was sectioned perpendicular to foliation and parallel to the lineation present in nearby samples. Core samples were cut perpendicular to their long axes, which have variable orientations relative to the foliation and lineation. Thin sections were lapped down to 30 µm thickness using first 14 µm and then 0.3 µm aluminium oxide powder. Samples used for paleopiezometry were given a final polish with colloidal silica. All thin sections were coated with ∼15 nm of carbon to reduce charging.

5.3.3 Analytical methods

Mineral compositions were acquired at Utrecht University on a JEOL JXA-8530F field-emission gun electron microprobe equipped with five tunable wavelength dispersive spectrometers and Probe for EPMA software version 12.5.8. Data were collected with a beam energy of 15 keV, a beam current of 10 nA, and a beam diameter of 10 µm. For the high-precision Ti-in-quartz measurements, the beam current was increased to 100 nA. To analyse biotite crystals < 10 µm across, the spot size was reduced to 5 µm.

For Ti-in-quartz analysis, we employed a total on-peak count time of 600 seconds for all spectrometers, alternating between peak and background in 30 blocks of 20 seconds each. An exponential fit to long counting-time wavescans was used as the background-correction calculation model. Count rates from two spectrometers were combined following the process of Donovan et al. (2011) to improve the efficiency of the EPMA. Calibration standards of Al_2O_3 and TiO were used. In addition, an in-house quartz standard was used as

a quantitative blank (see Donovan et al., 2011) and measured regularly, yielding an average Ti concentration of 1.5 ± 4.9 ppm (n = 14).

Figure 5.3 presents example spot locations for Ti-in-quartz measurements. To reduce errors introduced by secondary fluorescence from phases with high Ti concentrations, the data used for temperature estimates were collected from locations ≥ 100 µm away from visible rutile, ilmenite, or titanite. To explore the magnitude of any secondary fluorescence, a number of points were also collected in close proximity to phases with high concentrations of Ti (Figure 5.3).

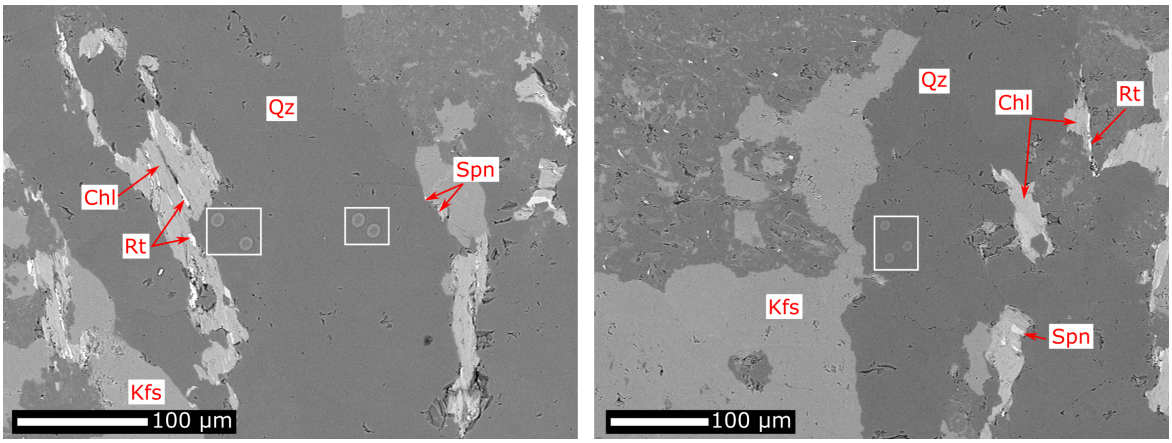

Figure 5.3: Backscattered electron images of GSL-18-RG-14 indicating the spot locations used for Ti-in-quartz analysis (white boxes), where Chl is chlorite, Kfs is potassium feldspar, Rt is rutile, Spn is sphere (titanite), and Qz is quartz.

For analysis of amphibole, plagioclase, and biotite, peak count times of 20 seconds and background count times of 10 seconds on each side of the peak were used for a linear background calculation method. Measurements were made from adjacent amphibole and plagioclase crystals. In-house natural and endmember synthetic standards, and the elements for which they were used as a calibration, were: diopside (Si, Ca), forsterite (Mg), corundum (Al), hematite (Fe), jadeite (Na), $KTiPO_5$ (K), chromium metal (Cr), tephroite (Mn), and TiO (Ti).

To measure the subgrain size for paleopiezometry, EBSD maps were collected at the Department of Earth Sciences, University of Oxford and at Utrecht University. At the University of Oxford, data were collected on a FEI Quanta 650 FEG E-SEM equipped with Oxford Instruments AZtec acquisition software and a NordlysNano EBSD camera. Samples, tilted at 70° were mapped in high vacuum with an accelerating voltage of 30 kV. The electron

beam was rastered across the sample using step sizes of 1.0–2.0 µm. At Utrecht University EBSD maps were collected on a Zeiss GeminiSEM 450 with Gemini 2 column and FEG equipped with Oxford Instruments AZtec acquisition software and a Symmetry S2 EBSD camera. Samples were tilted at 70° and mapped either in high or low vacuum (using N_2), with an accelerating voltage of either 20 kV or 30 kV. The electron beam was rastered across the sample using step sizes of 1.0–4.2 µm.

EBSD data were processed and analysed using a combination of Oxford Instruments Channel5 software and the MTEX toolbox (Bachmann et al., 2010; Mainprice et al., 2011) in MATLAB®. At some locations, quartz was systematically misindexed due to pseudosymmetry. The orientations at these points were corrected by applying a rotation of 60° around [0001] (Trimby et al., 2002) using Oxford Instruments Channel5 software. Also in Channel5, non-indexed points with ≥ 6 indexed neighbours within the same grain were assigned the average orientation of their neighbours. Further noise reduction was performed using the MTEX toolbox. The nature of the noise reduction was unique to each map due to variations in step size, indexing rate, phases present, and noise threshold. Descriptions of the full cleaning process for each map can be found in Appendix D.1.

Sample	**Thermometer**	**No. of analyses**
GSL-18-RG-02	Ti-in-quartz Amphibole-plagioclase Ti-in-biotite	11 points 13 pairs 29 points
GSL-18-RG-11	Ti-in-quartz Amphibole-plagioclase Ti-in-biotite	10 points 67 pairs 22 points
GSL-18-RG-12	Ti-in-quartz	9 points
GSL-18-RG-14	Ti-in-quartz	9 points
GSL-18-RG-20	Ti-in-biotite	95 points
GSL-18-C-27	Amphibole-plagioclase	44 pairs
GSL-18-C-28	Amphibole-plagioclase Ti-in-biotite	38 pairs 7 pairs
GSL-18-C-31	Ti-in-quartz	9 points
GSL-18-C-36	Ti-in-quartz Amphibole-plagioclase Ti-in-biotite	7 points 28 pairs 41 points

Table 5.1: Geothermometers used to calculate temperature in each sample. 'Points' refer to the number of spot analyses in each thin section, while 'pairs' refer to the number of amphibole spot analysis and plagioclase spot analysis pairs. Spots in the amphibole-plagioclase pairs did not have to be unique.

5.3.4 Geothermometry

We applied a range of geothermometers to the samples depending on the mineralogy. A summary of the different chemistry-based geothermometers applied to each sample is presented in Table 5.1. On three samples, all the thermometers were applied. The use of multiple thermometers enables a comparison of their relative accuracy at recording the temperatures associated with deformation. For five samples EPMA analyses were not available. Temperatures were instead inferred from the quartz microstructures.

Amphibole-plagioclase thermobarometry

Amphibole-plagioclase thermobarometry was applied to samples that contained unaltered plagioclase grains in close proximity to amphibole grains. Pressure was estimated using the barometers of Anderson and Smith (1995) and Bhadra and Bhattacharya (2007). The Anderson and Smith (1995) calibration is based on the increase in total Al in hornblende with pressure and temperature. It can be applied in the ranges 100–1000 MPa and 675°–760°C for samples containing plagioclase with compositions of $X_{\mathrm{An}} = 0.25$–0.35, where $X_{\mathrm{An}} = \mathrm{Ca}/(\mathrm{Ca}+\mathrm{Na})$ and Ca and Na are in atoms per formula unit (a.p.f.u.). This barometer was calibrated using two experimental datasets (Schmidt, 1992; Johnson & Rutherford, 1989) from melt-bearing assemblages and as such is only appropriate for the melt-bearing upper amphibolites of the GSLsz. The barometer of Bhadra and Bhattacharya (2007) is based on the reaction of tremolite ($Ca_2Mg_5Si_8O_{22}(OH)_2$) + tschermakite ($Ca_2Mg_3Al_4Si_6O_{22}(OH)_2$) + 2 albite ($NaAlSi_3O_8$) = 2 pargasite ($NaCa_2Mg_4Al_3Si_6O_{22}(OH)_2$) + 8 quartz ($SiO_2$) and can be applied to the melt-free epidote-amphibolite samples. For these calculations, the volume change of the reaction, ΔV, was taken to be -1.72433 kJ/Kbar, which represents ΔV at 8 kbar and 800°C, which lies in the middle of the pressure-temperature range of the calibration. The Bhadra and Bhattacharya (2007) barometer is applicable to amphiboles in the compositional ranges of 6.09–7.23 Si, $\leq$ 0.29 Ti, 0.76–2.63 Fe, 1.38–1.88 Ca, $\leq$0.27 K, 0.9–2.65 Al, 1.79–4.32 Mg, $\leq$ 0.09 Mn, 0.23–0.77 Na, and 1.73–2.67 (Ca+Na+K) a.p.f.u. based on 23 oxygens.

Temperature was estimated using Otten's (1984) Ti-in-amphibole thermometer and Holland and Bundy's (1994) amphibole-plagioclase thermometer. Thermometer B of Holland and Bundy (1994) is based on the exchange of NaSi and CaAl in the reaction of

edenite ($NaCa_2Mg_5Si_4(AlSi_3)O_{22}(OH)_2$) + albite ($NaAlSi_3O_8$) = richterite ($Na(CaNa)Mg_5Si_8O_{22}(OH)_2$ + anorthite ($CaAl_2Si_2O_8$). This thermometer is calibrated for temperatures in the range 500°–900°C, for plagioclase in the compositional range of X_{An} = 0.1–0.9 and amphiboles with $X_{Na}^{M4} > 0.03$, $Al^{vi} < 1.8$ a.p.f.u, and Si of 6.0–7.7 a.p.f.u., based on 23 oxygens. The Otten (1984) thermometer is an empirical calibration based on natural ilmenite-bearing samples. Samples lacking ilmenite may be undersaturated in Ti and, in such conditions, the thermometer will give a minimum temperature.

Pressures using the Anderson and Smith (1995) barometer and temperatures using the Otten (1984) and Holland and Bundy (1994) thermometers were calculated using a modified version of the "Plagioclase-Hornblende Thermobarometry" spreadsheet, which is available from the Mineralogical Society of America at:

http://www.minsocam.org/msa/rim/ rim69.html.

Pressures from the barometer of Bhadra and Bhattacharya (2007) were calculated using Supplement 2 from Wallis et al. (2014) and were used to calculate temperatures with the Holland and Bundy (1994) thermometer for the epidote-amphibolite samples. The method described in Holland and Blundy (1994) was used to recalculate the ferric iron content of the amphiboles based on stoichiometric constraints.

Ti-in-Biotite geothermometry

For samples that contained abundant biotite grains large enough for EPMA analysis ($\geq$ 5 µm across), the Ti-in-biotite geothermometer was applied. Ti-in-biotite temperatures were calculated using the Henry et al. (2005) calibration, which is based on the relationship between temperature, Ti (a.p.f.u) in biotite, and X_{Mg} in biotite, where X_{Mg} = $Mg/(Mg+Fe^{2+})$ assuming a base of 22 oxygens. The calibration is applicable to biotite with compositions in the ranges of X_{Mg} = 0.275–1.000, Ti = 0.04–0.6 and metamorphosed at temperatures and pressures in the ranges 480–800°C and 3–6 kbar, respectively. Further information on Ti-in-biotite thermometry can be found in Appendix D.2.

The data from the original calibration are from graphitic, peraluminous rocks that contain either ilmenite or rutile, indicating saturation of Ti, Si, and Al in biotite. None of our samples contain graphite. However, work by Erić et al. (2009) successfully applied the Ti-in-biotite geothermometer to non-graphitic peraluminous metapelites with a positive

relationship between X_{Mg} and Ti (a.p.f.u.), a condition met by our data.

In keeping with Henry et al. (2005), all Fe is assumed to be ferrous and a.p.f.u. are calculated based on 22 oxygens. In three of our samples, titanite was the only Ti-rich phase. For these samples we cannot be confident that Ti is at its maximum levels, and therefore, their estimated temperatures may represent lower bounds.

Ti-in-quartz geothermometry

For samples containing Ti-rich phases, we calculated temperatures using the Ti-in-quartz geothermometer (Wark & Watson, 2006; Thomas et al., 2010). This geothermometer is based on the exchange of Si^{4+} for Ti^{4+} on tetrahedral sites in quartz, with more titanium substitution at higher temperatures (Thomas et al., 2010). The initial calibration was based on static experiments at temperatures from 600°C to 1000°C, at a pressure of 1.0 GPa, in which quartz was in equilibrium with rutile in the presence of either an aqueous fluid or a silicate melt (Wark & Watson, 2006). Comparisons of this calibration to natural, lower pressure samples, for which the temperature had been measured via Zr-in-sphene thermometry, found no apparent pressure dependence (Wark & Watson, 2006). However, further piston-cylinder experiments by Thomas et al. (2010), conducted at temperatures from 700°C to 940°C and pressures between 0.5 GPa and 2 GPa, demonstrated a systematic decrease in solubility of Ti with increased pressure.

We calculated temperatures using both the pressure-dependent and the pressure-independent Ti-in-quartz geothermometers (Wark & Watson, 2006; Thomas et al., 2010). Details of these calculations can be found in Appendices D.3 and D.4. The Ti activities ($a_{\mathrm{TiO_2}}$) of samples containing rutile, ilmenite, and titanite were set to 1, 0.85, and 0.5, respectively (Ashley et al., 2014). These activities represent the lower bound for rocks containing ilmenite or titanite and as such can result in a maximum error in the temperature of < 1.5 % and < 7 %, respectively.

5.3.5 Microstructural analysis

The mechanism by which recrystallisation occurs in quartz has previously been associated with the deformation temperature (e.g., Hirth & Tullis, 1992; Stipp, Stünitz, Heilbronner, & Schmid, 2002; Passchier & Trouw, 2005, pages 40–41). Stipp, Sünitz, Heil-

bronner, Schmid (2002) compared temperatures calculated from syn-kinematic mineral assemblages with microstructures found in adjacent quartz veins in the Tonale fault zone, in the Italian Alps. Three recrystallisation mechanisms were inferred: bulging (BLG) recrystallisation, subgrain-rotation (SGR) recrystallisation, and grain-boundary migration (GBM) recrystallisation. Microstructures with small bulges at grain boundaries, of similar size to adjacent recrystallised grains, are indicative of BLG (Urai et al., 1986; Passchier & Trouw, 2005, page 40) and were found to occur within the temperature range 280°–390°C. Microstructures with elongate recrystallised grains of similar size and orientation to subgrains in porphyroclasts are indicative of SGR (Hobbs, 1968; Passchier & Trouw, 2005, page 41) and were associated with temperatures in the range of 420°–490°C. Between 390°–420°C, both recrystallisation by BLG and SGR were active. Where quartz grains presented cuspate and lobate grain boundaries, recrystallisation was predominately by GBM (Guillope & Poirier, 1979; Passchier & Trouw, 2005, page 41), which dominated at temperatures of 530°–650 °C. From 490°C–530°C microstructures indicated recrystallisation by both SGR and GBM. These temperature ranges can be used as a geothermometer for GSLsz mylonites, assuming conditions similar to those present at the Tonale fault zone, including differential stresses $<$ 200 MPa, strain rates in the range 10^{-12}–10^{-14} s^{-1}, and water-saturated conditions (Stipp, Stünitz, Heilbronner, & Schmid, 2002). These assumptions are broadly consistent with the microstructures and mineralogies described below. For those samples for which EPMA data were not available, the principal means of estimating temperature is the microstructural observations as described above.

The temperatures estimated from the recrystallisation mechanisms of quartz can be supported by observing the relative activity of different slip systems. As demonstrated schematically in Figure 5.4, with increasing temperature, the active slip system changes from a combination of basal-<a>, rhomb-<a>, and prism-<a> to dominantly prism-[c] slip (Law et al., 2013). Therefore, for samples cut in the correct reference frame, that is parallel to the lineation and perpendicular to the foliation, quartz CPOs can be linked to deformation within an approximate temperature range (e.g., J. Tullis, 1972; J. Tullis et al., 1973; Kruhl, 1998; Morgan & Law, 2004) and therefore often show systematic correlations with recrystallisation regimes (e.g., Stipp, Stünitz, Heilbronner, & Schmid, 2002; Stipp, Stünitz, Heilbronner, & others, 2002; Langille et al., 2010). However, it is important to note that in addition to temperature, quartz CPOs are also sensitive to the strain rate, the degree of hydrolytic

weakening, and the strain geometry (Law et al., 2013; Lister & Hobbs, 1980) and therefore provide only an approximate guide to deformation temperatures. More precise temperature estimates can be obtained from c-axis thermometry, whereby the angle between two c-axis girdles increases with temperature (J. Tullis et al., 1973; Kruhl, 1998; Morgan & Law, 2004). However, c-axis opening angles were not present in our dataset.

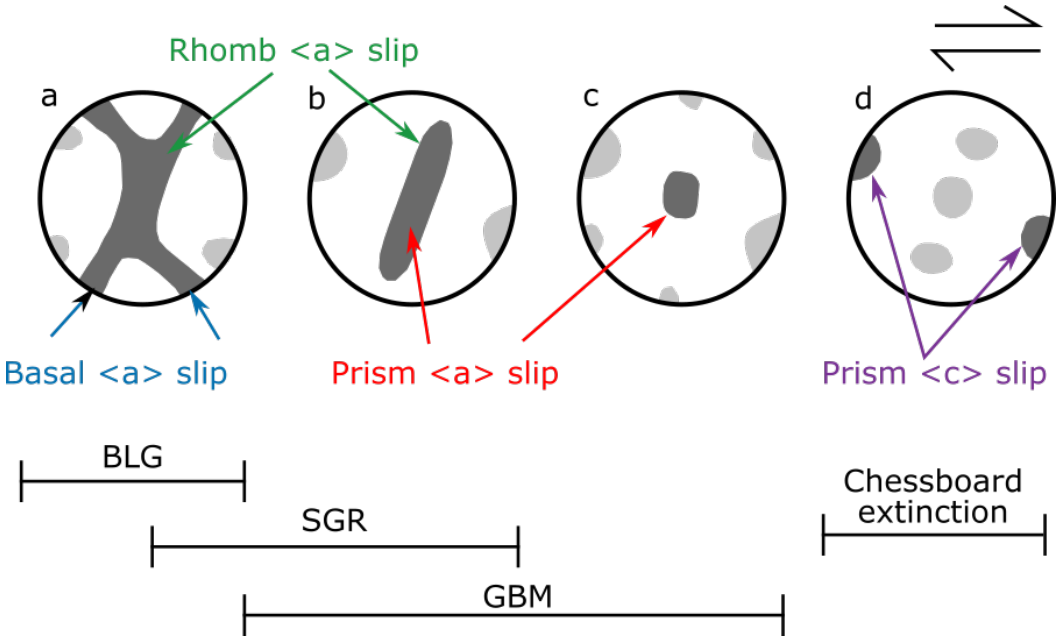

Figure 5.4: Schematic [c] (dark grey) and <a> (light grey) pole figures for quartz modified from Figure 5a in Langille et al. (2010). Deformation mechanisms consistent with the available slip systems indicated below.

Of the five samples where EPMA data were not available, it was possible to cut four in the correct reference frame. For these four samples, GSL-18-RG-03, GSL-18-RG-13, GSL-18-DW-11, and GSL-18-DW-13, we plot pole figures for [c] and <a> axes from the EBSD data to explore the activity of different slip systems. For the [c] and <a> pole figures, data are plotted as one point per grain and contoured by multiples of uniform distributions (MUD). In addition, to confirm the samples were cut in the correct reference frame, we also plot misorientation pole figures. We assume that, for kinematics dominated by simple shear, the misorientation axes of subgrain boundaries will be approximately parallel to the macroscopic vorticity axis (Michels et al., 2015) and therefore will be normal to a correctly cut thin section. For the misorientation pole figures, we plot misorientation axes for subgrain boundaries defined as neighbouring pixels with misorientation angles between 2° and 10°.

5.3.6 Subgrain-size piezometry

We estimated the average differential stress within quartz in each sample using subgrain-size piezometry (Goddard et al., 2020). To avoid erroneously large stress measurements, which can result from noisy EBSD data, we use the 2° calibration presented earlier in this thesis (Section 3.2.3). Consistent with Goddard et al. (2020), we use the mean line-intercept length (λ) between subgrain boundaries as an approximation for subgrain-size. The arithmetic mean-intercept length was calculated from intercepts measured in two perpendicular directions. To ensure the number of intercepts was sufficient to capture a mean-line intercept representative of the sample, we ran *No_intercepts_check.m* script from Goddard et al. (2020), whereby the number of intercepts is increased, and the mean-line intercept subsequently measured. The number of intercepts was deemed adequate when the mean-line intercept length stabilised to ± 2.5%.

In the Goddard et al. (2020) piezometer, the differential stress is normalised by the shear modulus and the mean line-intercept length is normalised by the Burgers vector. For quartz analyzed in this study, we use the same shear modulus (42 GPa, Birch, Table 7–16 in Clark, 1966) and Burgers vector (5.1 Å, average of the a and c unit cell dimensions, Deer et al., 1992, page 458) for normalisation as Goddard et al. (2020).

5.4 Results

5.4.1 Mineralogical descriptions

Greenschist facies

Two greenschist samples were selected for analysis: GSL-18-DW-11, and GSL-18-DW-13. Samples exhibited evidence of deformation during greenschist-facies metamorphism despite being located in a region designated as epidote-amphibolite in Hanmer's (1988) lithological map. These samples are protomylonitic to mylonitic, metamorphosed granodiorites, consisting mostly of quartz, plagioclase, k-feldspar, and chlorite. Porphyroclasts are predominantly plagioclase, most of which have broken down to sericite.

Epidote-amphibolite facies

Four epidote-amphibolite samples were selected for analysis: GSL-18-RG-02, GSL-

18-RG-03, GSL-18-C-31, and GSL-18-C-36. All samples are granodiorite protomylonites and mylonites. They contain plagioclase, quartz, k-feldspar, and biotite with three of the four samples also including amphibole. Titanite, epidote, and chlorite are present in small amounts (1–3%) in some samples. Accessory minerals across the facies include: allanite, (fluor-)apatite, ilmenite, pyrite, zircon, and zoisite.

A moderate to strong foliation defined by flattened and aligned quartz, K-feldspar, and biotite is present in all samples. Amphibole and plagioclase are only present as porphyroclasts. Plagioclase in all places has locally broken down to sericite. A late-stage localised epidote-rich shear zone is also present in GSL-18-C-31.

Upper-amphibolite facies

Eight upper-amphibolite samples were selected for analysis: GSL-18-RG-11, GSL-18-RG-12, GSL-18-RG-13, GSL-18-RG-14, GSL-18-RG-20, GSL-18-C-26, GSL-18-C-27, and GSL-18-C-28. Samples GSL-18-C-26, -27, and -28 were collected from a locality that presented evidence for *in-situ* melting of biotite in the form of restite feldspar and garnet 'pools' in the strain shadows of amphibolites. We therefore have assumed that all the upper amphibolites were deformed in the present of melt (Dyck et al., 2020).

Samples are granodiorite protomylonites and mylonites, which all contain plagioclase, k-feldspar, and quartz in varying proportions. Other prominent minerals are amphibole, garnet, biotite, and chlorite, but these phases are not present in all samples. Accessory minerals vary between samples but include: allanite, apatite, epidote, graphite, hematite, ilmenite, monazite, pyrite, rutile, titanite, and zircon.

Plagioclase is present as large, heavily-sericitized porphyroclasts. Garnet and amphibole, when present, are also porphyroclasts. In orientated samples, asymmetric and winged clasts indicate a right-lateral sense of shear. A strong foliation is defined by elongate grains and compositional banding of phases within the matrix which include quartz, K-feldspar, biotite, and chlorite. Interfingering biotite and chlorite in some samples suggests the latter is the result of a retrograde breakdown of the former. In GSL-18-RG-C-28, chlorite has also filled fractures in the sample. Epidote, where present, has overgrown the foliation and hence is retrograde, postdating the deformation. In GSL-18-RG-14, epidote veins also crosscut the foliation.

Granulite facies

One granulite sample, GSL-18-C-47, was selected for analysis. This sample, described in detail in Dyck et al. (2020), was collected from a metre-scale pelitic paragneiss raft within a larger body of garnet-monzogranite. The sample comprises garnet, plagioclase, quartz, sillimanite, biotite, and k-feldspar with accessory titanite and ilmenite (Dyck et al., 2020). Minor muscovite is intergrown within the fine-grained biotite, quartz, and sillimanite, and is likely to be associated with retrograde deformation. No clear foliation or lineation can be found in the sample, but chessboard subgrains are present in quartz.

5.4.2 Quartz deformation microstructures

Figure 5.5 presents examples of quartz microstructures from each metamorphic grade. The quartz microstructures present in the greenschist facies sample GSL-18-DW-13 (Figure 5.5) as well as the epidote-amphibolite sample GSL-18-C-31 have grains and subgrains of equal size and similar orientations when viewed through a gypsum plate, consistent with dynamic recrystallisation dominated by SGR. Microstructures from the greenschist sample GSL-18-DW-11, epidote-amphibolite sample GSL-18-C-36 (Figure 5.5), and upper-amphibolite sample GSL-18-C-27 also indicate that recrystallisation by SGR was dominant. However, in places within these latter samples, quartz grains have cuspate and lobate boundaries indicating that GBM was also significant. Epidote-amphibolite sample GSL-18-RG-02 and upper-amphibolite sample GSL-18-C-28 are dominated by microstructures indicative of GBM but contain microstructures indicative of SGR in places. For the remaining upper-amphibolite samples as well as epidote-amphibolite sample GSL-18-RG-03, the microstructures indicate recrystallisation primarily by GBM (e.g., sample GSL-18-RG-20, Figure 5.5). In sample GSL-18-C-47, the sole granulite sample within this study, quartz contains chessboard subgrains, which have been associated with temperatures of > 700°C (Faleiros et al., 2016; Kruhl, 1998; Wallis, Parsons, & Hansen, 2019).

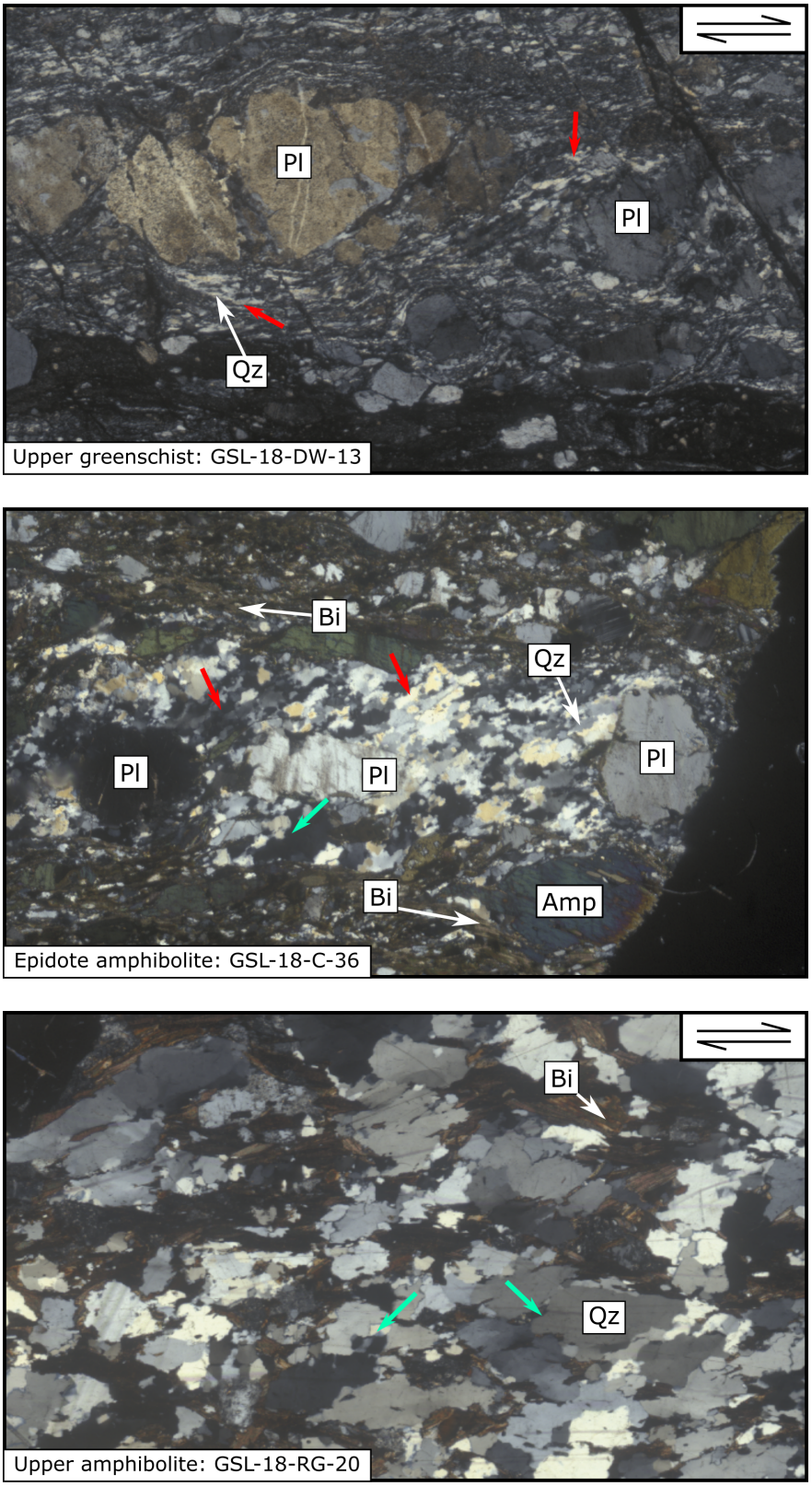

Figure 5.5: Thin section slide scans from samples representing SGR, GBM, and a combination of the two microstructures. Images are in cross-polarised light. The shear sense, where known, is indicated in the top right-hand corner. Red and green arrows indicate microstructures indicative of SGR and GBM, respectively.

Pole figures and misorientation pole figures are plotted in Figure 5.6 for samples where quartz microstructures were the only thermometry method available. Samples GSL-18-RG-13 and GSL-18-DW-13 have maxima of misorientation axes aligned approximately with the Y-axes of the strain ellipsoid (Figure 5.6) and therefore are consistent with the sample having been cut in the correct reference frame. For samples GSL-18-RG-03 and GSL-18-DW-11 the maxima are slightly offset from the centre indicating the samples may be cut slightly out of the optimum reference frame. For upper-greenschist sample GSL-DW-11 the girdle of <a> axes parallel to the foliation and the high density of [c] axes perpendicular to the foliation indicate dominance of the basal-<a> slip system, whilst the partial girdle of [c] axes indicates a subordinate contribution of the rhomb-<a> slip system (e.g., Figure 5.4b; Schmid & Casey, 1986). For upper-greenschist sample GSL-18-DW-13 an asymmetrical partial girdle of [c] axes centred on Y and extending towards Z is present, indicating activity of the rhomb-<a> and prism-<a> slip systems (Schmid & Casey, 1986). For epidote-amphibolite sample GSL-18-RG-03 and upper-amphibolite sample GSL-18-RG-13, [c]-axis maxima parallel to the Y-direction are indicative of deformation by prism-<a> slip (Schmid & Casey, 1986).

5.4.3 Pressure estimates for geothermometry

To conduct Ti-in-quartz thermometry it is first necessary to establish the pressure at which the Ti equilibrated. For three of the six samples from which Ti-in-quartz data were collected, the amphibole-plagioclase thermobarometer was also applied. However, the pressures calculated from the amphibole-plagioclase barometer were inconsistent with those of Dyck et al. (2020), with higher-than-expected pressures for epidote-amphibolite samples and lower-than-expected pressures for upper-amphibolite samples (Appendix D.5). It is therefore unclear whether the amphibole-plagioclase compositions equilibrated on the timescale of the Ti-in-quartz and, as such, whether it is appropriate to use these pressures for Ti-in-quartz analysis.

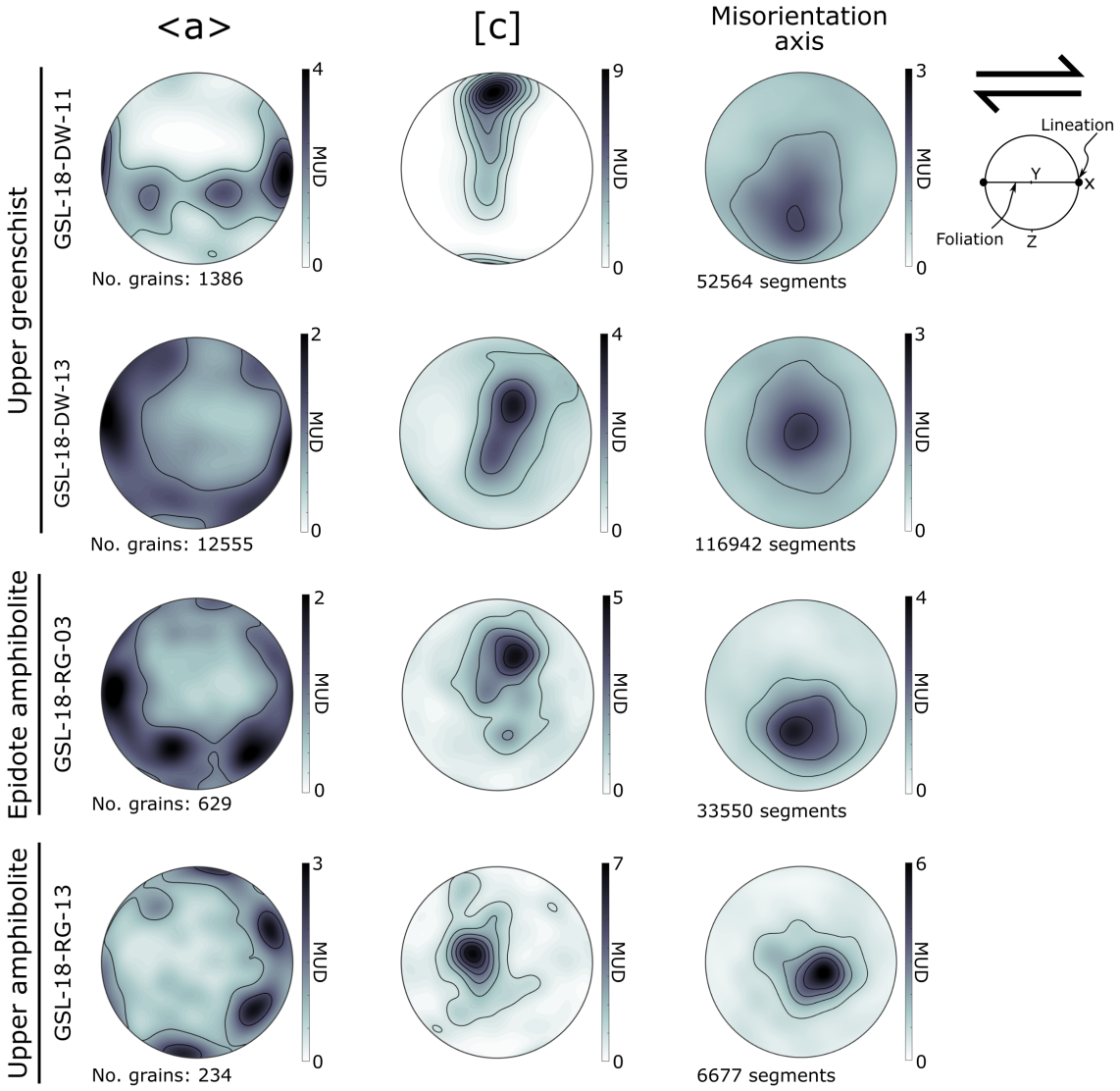

Figure 5.6: Pole figures for <a> and [c] axis, and misorientation pole figures, with misorientation axes plotted for neighbouring pixels with misorientation angles between 2°and 10°. Figures were constructed with a halfwidth of 10 and one point per grain. The colour scales represent multiples of uniform distribution (MUD).

To calculate the pressure to be used in the thermometer of Thomas et al. (2010), samples were instead grouped into metamorphic facies based on their location within the metamorphic units mapped by Hanmer (1988). Each sample was then assigned the final pressure of that metamorphic facies as determined by Dyck et al. (2020). Samples that were within the epidote-amphibolite facies and had microstructures indicative of dynamic recrystallisation dominantly by SGR (Section 5.4.2) were given a final pressure of 550 MPa, the last predicted pressure associated with the cooler of the epidote-amphibolite samples (GSL-18-C-50) analysed by Dyck et al. (2020). Sample GSL-18-RG-02, though located

close to other epidote-amphibolite samples, presented microstructural evidence for dynamic recrystallisation by GBM (Section 5.4.2), indicating hotter temperatures during deformation. As such, sample GSL-18-RG-02 was assigned a final pressure of 575 MPa, which is that associated with the final pressure of GSL-18-C-53, the hottest epidote-amphibolite sample from Dyck et al. (2020). Samples located within the upper-amphibolite facies were assigned a pressure of 700 MPa based on sample GSL-18-BD-25 (Dyck et al., 2020). The temperature calculation is not particularly pressure sensitive. For example, an error of $\pm$ 150 MPa, which is the pressure range from greenschist to granulite facies in these rocks, would result in a change in temperature of $< 4\%$.

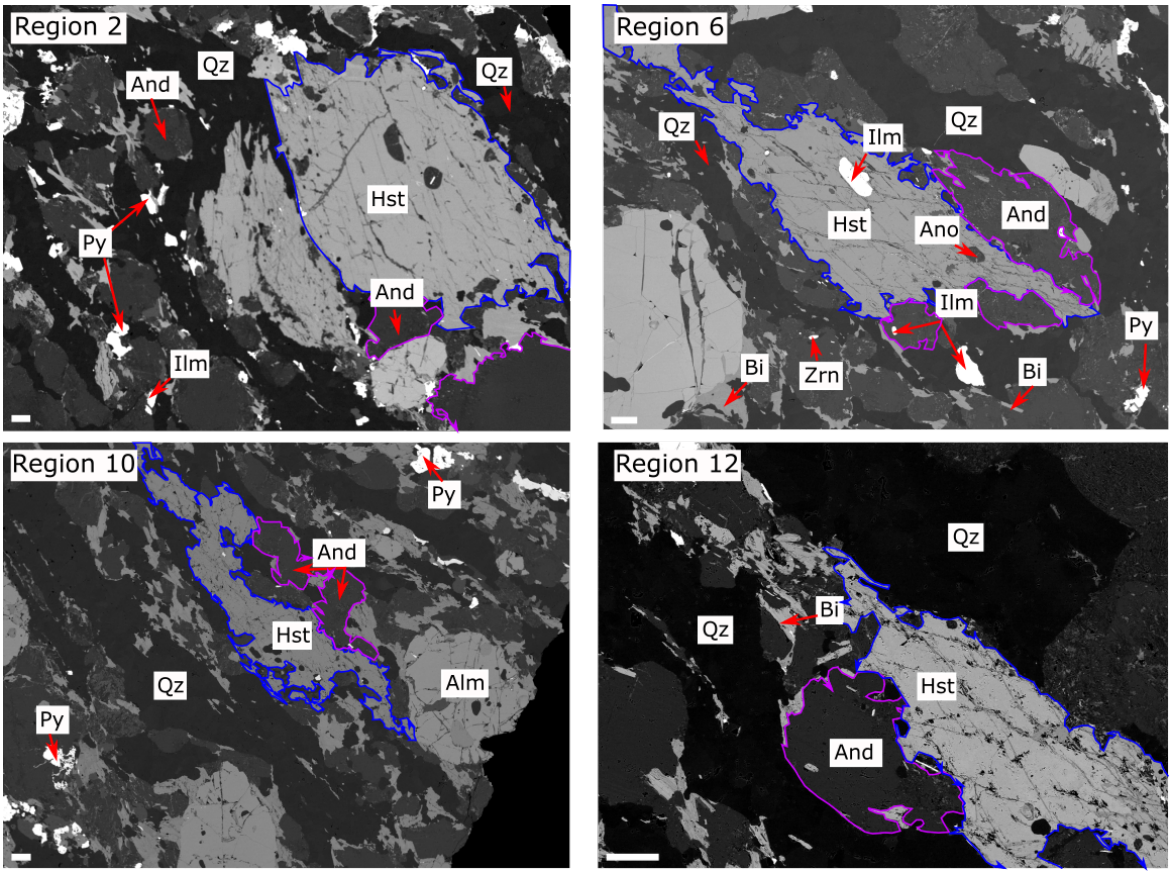

Figure 5.7: Backscatter electron images of GSL-18-C-28 regions analysed using the electron probe micro-analyzer. Labelled minerals were identified using energy dispersive X-ray spectroscopy. Abbreviations: And is andesine, Ano is anorthoclase, Bi is biotite, Hst is hastingite, Ilm is ilmenite, Py is pyrite, Qz is quartz, and Zrn is zircon. Amphiboles and plagioclases used in geothermometry are outlined in blue and purple, respectively. Scale bars are 100 µm.

5.4.4 Geothermobarometry

Amphibole-plagioclase

Exemplary amphibole-plagioclase pairs are presented in Figure 5.7, while compositional data are presented in Table 5.2 and represented graphically in Figures 5.8 and 5.9, respectively. Only analyses with EPMA totals between 99 and 101% were used. Compositions are based on 23 oxygens for amphibole and 8 oxygens for plagioclase. Results from thermometry can be found in Table 5.3.

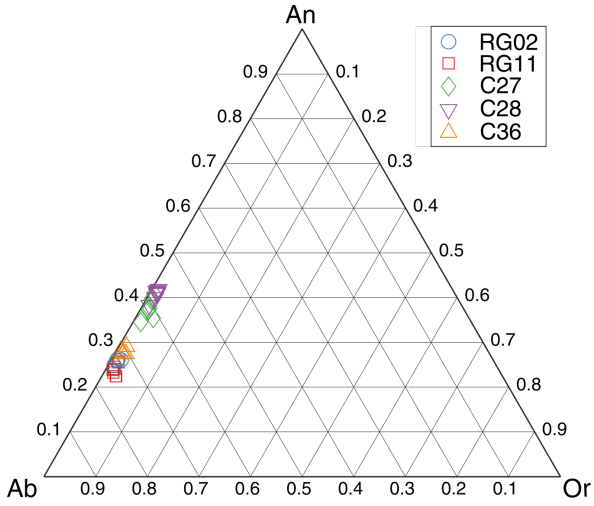

Figure 5.8: A ternary diagram with the GSLz feldspar compositions plotted with respect to the three end members: anorthite (An), albite (Ab), and orthoclase (Or). Each point represents the average composition of a region within the thin section.

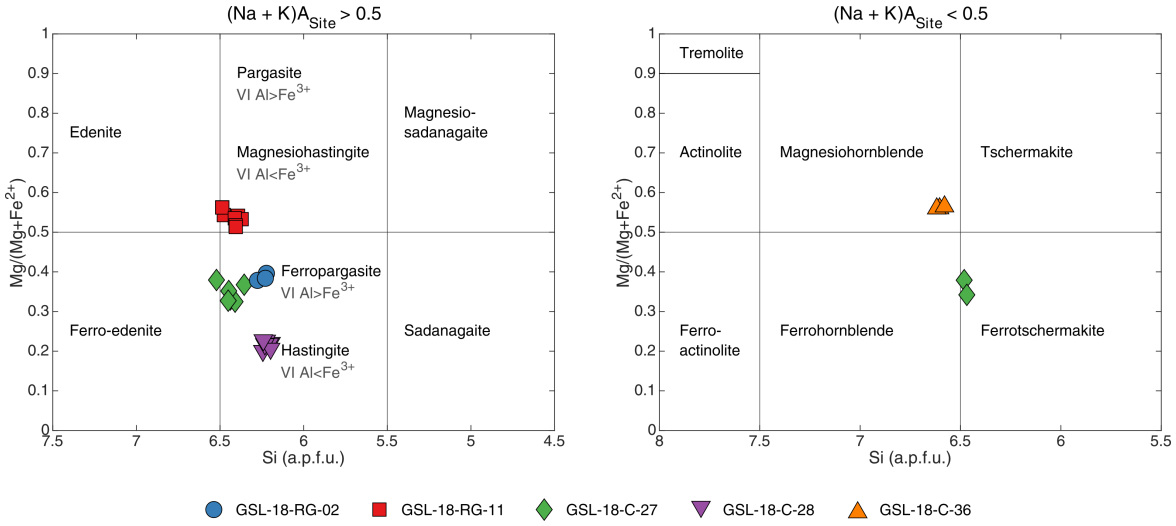

Figure 5.9: Amphibole classification (based on Leake et al., 1997, 2004) using Si (a.p.f.u.) and Mg/(Mg+Fe^{2+}). The method described in Holland and Blundy (1994) was used to recalculate the ferric iron content of the amphiboles based on stoichiometric constraints.

Table 5.2: Representative oxide concentrations and atomic concentrations of minerals used for geothermobarometry. $X_{Mg} = Mg/(Mg + Fe^{2+})$. For biotite all the Fe is assumed to be ferrous. $X_{An} = Ca/(Ca + Na)$. H_2O was calculated based on stoichiometric constraints.

Sample	RG-02			RG-11			RG-20	C-27		C-28			C-36		
Lat.	61°37'08.9"N			61°38'33.0"N			61°39' 53.7"N	61°38'19.7"N		61°38'19.7"N			61°37'45.3"N		
Long.	112°10'18.8"W			112°12'41.5"W			112°06' 11.2"W	112°10'54.5"W		112°10'54.5"W			112°10'02.1"W		
Mineral	Bi	Amp	Plag	Bi	Amp	Plag	Bi	Amp	Plag	Bi	Amp	Plag	Bi	Amp	Plag
No. analysis	29	12	13	22	67	67	95	44	44	7	38	35	41	21	28
SiO_2	36.03	40.23	61.43	37.05	42.46	62.49	34.47	42.06	58.65	34.20	39.69	57.79	36.95	43.85	61.00
Al_2O_3	14.44	10.68	23.71	13.44	9.57	23.05	17.52	10.27	25.68	14.11	11.60	26.17	14.78	9.22	24.06
MgO	8.39	6.44	0.00	11.38	9.45	0.00	7.00	6.26	0.00	4.73	3.56	0.00	11.91	9.94	0.03
CaO	0.06	11.41	5.76	0.07	11.60	4.89	0.02	11.37	7.98	0.34	11.24	8.78	0.06	11.79	6.05
FeO	23.90	18.12	0.14	20.40	15.00	0.15	23.35	19.81	0.10	30.11	22.88	0.15	19.83	13.84	0.13
Fe_2O_3	0.00	6.26	0.00	0.00	5.02	0.00	0.00	3.70	0.00	0.00	4.47	0.00	0.00	5.44	0.00
Na_2O	0.07	1.45	8.53	0.10	1.53	8.78	0.19	1.28	7.18	0.11	1.30	6.78	0.07	1.24	8.29
K_2O	9.69	1.67	0.23	9.71	1.38	0.38	9.47	1.26	0.26	7.87	1.54	0.23	9.80	1.18	0.29
MnO	0.40	0.62	0.01	0.32	0.51	0.01	0.27	0.50	0.01	0.31	0.53	0.01	0.38	0.59	0.01
TiO_2	2.82	1.17	0.01	3.98	1.67	0.01	3.40	1.63	0.02	4.15	1.77	0.01	1.75	0.90	0.01

Continued on next page

Continuation of Table 5.2															
Cr_2O_3	0.02	0.01	0.01	0.02	0.03	0.01	0.08	0.03	0.01	0.01	0.00	0.01	0.08	0.08	0.00
H_2O	3.86	1.90	0.00	3.93	1.96	0.00	3.88	1.93	0.00	3.77	1.89	0.00	3.95	1.97	0.00
Total	99.68	99.97	99.84	100.41	100.16	99.77	99.65	100.9	99.87	99.72	100.48	99.93	99.56	100.03	99.87
Oxygen	22	23	8	22	23	8	22	23	8	22	23	8	22	23	8
Si	5.62	6.25	2.74	5.64	6.43	2.78	5.36	6.47	2.63	5.47	6.22	2.60	5.65	6.59	2.72
Al	2.66	1.95	1.25	2.41	1.71	1.21	3.21	1.87	1.36	2.66	2.14	1.39	2.66	1.63	1.26
Mg	1.95	1.49	0.00	2.58	2.13	0.00	1.62	1.44	0.00	1.13	0.83	0.00	2.72	2.23	0.00
Ca	0.01	1.90	0.28	0.01	1.88	0.23	0.00	1.87	0.38	0.06	1.89	0.42	0.01	1.90	0.29
Fe^{2+}	3.12	2.35	0.01	2.60	1.90	0.01	3.03	2.55	0.00	4.03	3.00	0.01	2.54	1.74	0.00
Fe^{3+}	0.00	0.73	0.00	0.00	0.57	0.00	0.00	0.43	0.00	0.00	0.52	0.00	0.00	0.62	0.00
Na	0.02	0.44	0.74	0.03	0.45	0.76	0.06	0.38	0.62	0.03	0.39	0.59	0.02	0.36	0.72
K	1.93	0.33	0.01	1.89	0.27	0.02	1.88	0.25	0.01	1.61	0.31	0.01	1.91	0.23	0.02
Mn	0.05	0.08	0.00	0.04	0.07	0.00	0.04	0.06	0.00	0.04	0.07	0.00	0.05	0.07	0.00
Ti	0.33	0.14	0.00	0.46	0.19	0.00	0.40	0.19	0.00	0.50	0.21	0.00	0.20	0.10	0.00
Cr	0.00	0.00	0.00	0.00	0.00	0.00	0.01	0.00	0.00	0.00	0.00	0.00	0.01	0.01	0.00
Sum	15.69	15.66	5.02	15.66	15.60	5.01	15.60	15.51	5.01	15.52	15.59	5.01	15.78	15.48	5.01
X_{An}			0.27			0.24			0.38			0.42			0.29
X_{Mg}	0.38	0.39		0.50	0.53		0.35	0.36		0.22	0.22		0.52	0.56	

Sample	Temperature (°C)	Measurement error (2 s.d.) (±°C)	Calibration error (±°C)	Combined error (±°C)
GSL-18-RG-02	**H05:** 660	43	24	50
	HB^{BB}94: 750	18	50	50
	HB^{AS}94: 750	16	50	50
	O84: 710	17	25	30
GSL-18-RG-11	**H05: 730**	36	24	40
	HB^{BB}94: 730	28	50	60
	HB^{AS}94: 740	29	50	60
	O84: 770	86	25	90
GSL-18-RG-20	**H05:** 690	31	24	40
GSL-18-C-27	HB^{BB}94: 750	26	50	60
	HB^{AS}94: 740	32	50	60
	O84: 770	94	25	100
GSL-18-C-28	**H05:** 710	46	24	50
	HB^{BB}94: 780	24	50	60
	HB^{AS}94: 770	27	50	60
	O84: 800	67	25	70
GSL-18-C-36	**H05:** 590	67	24	70
	HB^{BB}94: 720	17	50	50
	HB^{AS}94: 710	18	50	60
	O84: 670	12	25	30

Table 5.3: Results from Ti-in-biotite, Ti-in-amphibole, and amphibole-plagioclase thermometry. H05 refers to Henry et al. (2005), O84 refers to Otten (1984), HB^{BB}94 and HB^{AS}94 refer to temperatures from the Holland and Blundy (1994) geothermometer using pressures from Bhadra and Bhattacharya (2007) and Anderson and Smith (1995), respectively. Temperatures and combined errors have been rounded to the nearest 10°C. Samples in bold are plotted in Figure 5.11.

Amphiboles in upper-amphibolite sample GSL-18-C-27 have the greatest spread in composition with the majority being ferropargasite, but some regions averaging to ferrotschermakite or ferro-edenite. Al_{Tot} range 1.65–2.02 (average 1.86) a.p.f.u.. Average values for Ca and Na are 1.87 and 0.38 a.p.f.u., respectively. X_{An} values for plagioclases are fairly uniform ranging from 0.34 to 0.42, with an average of 0.38, catogrising them as andesine. These amphibole and plagioclase compositions give pressure and temperature estimates of 490 ± 90 MPa, and 740 ± 60°C, respectively. The Ti contents of the amphiboles range 0.09–0.24 (average 0.19) a.p.f.u., which gives a temperature of 770 ± 100°C, within error of those from amphibole-plagioclase compositions.

Amphiboles in upper-amphibolite sample GSL-18-C-28 were hastingite in composition. Al_{Tot} ranges 0.30–0.49 (average 0.36) a.p.f.u. Average values for Ca and Na are 1.89 and 0.39 a.p.f.u., respectively. X_{An} values in plagioclase range from 0.39 to 0.44 with an average composition of 0.42 categorising it as andesine. These amphibole and plagioclase

compositions give pressure and temperature estimates of 770 ± 60°C and 540 ± 100 MPa, respectively. The Ti content in amphiboles range from 0.11–0.25 (average 0.21) resulting in a temperature of 800 ± 70°C.

Amphiboles in upper amphibolite sample GSL-18-RG-11 are magnesiohastingsite in composition but verging towards edenite. Al_{Tot} range 1.41–1.86 (average 1.71) a.p.f.u.. Average values for Ca and Na are 1.88 and 0.45 a.p.f.u., respectfully. X_{An} values range from 0.21 to 0.26 with an average of 0.24 making the plagioclase oligoclase in composition. These amphiboles and plagioclase compositions give pressure and temperature estimates of 740 ± 60°C and 420 ± 90 MPa, respectively. The Ti content of amphibole is 0.10–0.23 (0.19) a.p.f.u, resulting in an average temperature of 770 ± 90°C.

Epidote-amphibolite sample GSL-18-C-36 contains amphiboles with a composition of magnesiohornblende. Al_{Tot} range 0.18–0.32 (average 0.23) a.p.f.u., with mean Ca and Na components of 1.90 and 0.36 a.p.f.u., respectively. X_{An} values range from 0.27 to 0.32 averaging at 0.29, making the plagioclase mostly oligoclase with some andesine. These amphibole and plagioclase compositions give pressure and temperature estimates of 720 ± 50°C and 640 ± 220 MPa, respectively. The Ti content of amphibole is 0.09–0.11 (average 0.10) a.p.f.u., resulting in an average temperature of 670 ± 30°C.

Epidote-amphiboltie sample GSL-18-RG-02 contains amphibole with a composition of ferropargasite. AlTot values are in the range of 1.90–2.00 (average 1.95) a.p.f.u.. Mean Ca and Na components are 1.90 and 0.44 a.p.f.u., respectively. Plagioclase has X_{An} values of between 0.26 and 0.29 with an average of 0.27, making them oligoclase in composition. These amphibole and plagioclase compositions give pressure and temperature estimates of 750 ± 50°C and 600 ± 210 MPa, respectively. The Ti content of amphibole is 0.12–0.14 (average 0.14) a.p.f.u. resulting in an average temperature of 710 ± 30°C.

Ti-in-biotite

Table 5.2 presents compositional data for biotite as oxide concentrations and atomic concentrations based on 22 a.p.f.u. of oxygen. For the Ti-in-biotite geothermometer, EPMA totals in the range of 98 to 101% were accepted. The slightly larger extent of this range, as compared to amphibole analyses, is due to the likely presence of F, which is difficult to detect with EPMA. Results from thermometry can be found in Table 5.3.

The compositions of biotite in all samples except GSL-18-C-28 were within the calibration range of the Ti-in-Biotite thermometer. Sample GSL-18-C-28 has a Ti content of 0.50 ± 0.07 a.p.f.u. and X_{Mg} value of 0.22 ± 0.02 and as such is outside the range of X_{Mg} used to calibrate the thermometer. Thus, the Ti-in-biotite temperature for this sample (710 ± 50°C) should be considered with caution.

Biotite compositions in upper-amphibolite samples GSL-18-RG-11 and GSL-18-RG-20 have Ti contents of 0.46 ± 0.07 a.p.f.u. and 0.40 ± 0.04 a.p.f.u and X_{Mg} values of 0.50 ± 0.01 and 0.35 ± 0.01, respectively. These measurements correspond to temperatures of 730 ± 40°C and 690 ± 40°C for GSL-18-RG-11 and GSL-18-RG-20, respectively.

Epidote-amphibolite samples GSL-18-RG-02 and GSL-18-C-36 contain biotite with average Ti values of 0.33 ± 0.05 a.p.f.u. and 0.20 ± 0.04 a.p.f.u. and X_{Mg} values of 0.38 ± 0.02 and 0.52 ± 0.01, respectively. These measurements correspond to temperatures of 590 ± 50°C and 600 ± 70°C for GSL-18-RG-02 and GSL-18-C-36, respectively.

Sample GSL-18-RG-20 is the only sample to have equilibrated in the presence of rutile and as such has the lowest internal spread in temperature from the Ti-in-biotite thermometer. The larger spread in temperature measurements within the other samples may be associated with local areas being undersaturated in Ti with titanite and, in the case of GSL-18-C-28, ilmenite being the only Ti-rich mineral(s).

Ti-in-quartz

Ti concentrations in quartz and the associated temperatures are recorded Table 5.4. For the Ti-in-quartz geothermometer, only analyses with EPMA totals between 99 and 101% were used. A few points that were deliberately measured close to Ti-rich phases had erroneously high temperatures (1.2–1.5 times the average) due to secondary fluorescence and were not included in the temperature estimates. In all instances, temperatures from the Thomas et al. (2010) geothermometer were lower than those from the Wark and Watson (2006) calibration. This systematic offset is expected as pressure has an inverse relationship with Ti concentration, and our samples equilibrated at pressures lower than those of Wark and Watson (0.55–0.7 GPa, as compared to 1 GPa).

Ti-in-quartz thermometry was performed on samples GSL-18-RG-02, GSL-18-C-31, and GSL-18-C-36 in the epidote-amphibolite suite. Ti concentrations of 0.6–18.37 ppm

(average 6.97) were measured in quartz in GSL-18-RG-02, resulting in average temperatures of 530 ± 160°C and 470 ± 140°C for the Wark and Watson (2006) and Thomas et al. (2010) thermometers, respectively. In sample GSL-18-RG-31, Ti concentrations of 1.69–21.31 (average 10.65) ppm give temperatures of 530 ± 110°C and 470 ± 100°C for the same thermometers. Lastly, Ti concentrations in GSL-18-RG-36 range from 0.27–18.68 (average 10.07) resulting in average temperatures of 560 ± 190°C and 490 ± 160°C.

Three upper amphibolite facies samples were also analysed: GSL-18-RG-11, GSL-18-RG-12, and GSL-18-RG-14. In GSL-18-RG-11, Ti concentrations range from 8.1–44.3 (average 26.01) giving average temperatures of 660 ± 120°C and 610 ± 110°C, for the Wark and Watson (2006) and Thomas et al. (2010) thermometers, respectively. For sample GSL-18-RG-12, Ti-concentrations ranged from 7.21–36.49 (average 16.6), resulting in temperatures of 560 ± 90°C and 520 ± 80°C for the Wark and Watson (2006) and Thomas et al. (2010) thermometers, respectively. Lastly, sample GSL-18-RG-14 has Ti concentrations of 10.79–48.68 (average 20.45) resulting in temperatures of 580 ± 70°C and 540 ± 70°C for the Wark and Watson (2006) and Thomas et al. (2010) thermometers, respectively.

Table 5.4: Ti concentration (ppm) in quartz and equivalent temperatures (°C). WW06 refers to Wark and Watson (2006) and T10 refers to Thomas et al. (2010). See text for explanation over the allocation of Ti activity and pressure. Average temperatures and combined errors are rounded to the nearest 10°C

Sample	Ti phase	Ti activity	Allocated pressure (GPa)	Ti (ppm)	Temperature (°C)	
					WW06	T10
GSL-18-RG-02	Titanite	0.5	0.575	8.5	571	507
				10.9	592	525
				6.7	552	491
				6.0	543	483
				1.3	442	394
				0.6	398	355
				9.7	583	517
				18.4	640	567
				3.2	497	443
				10.8	591	525
				0.7	408	364
				Average	**530**	**470**
				2 s.d.	**160**	**140**
GSL-18-RG-11	Titanite	0.5	0.7	14.8	619	574
				13.7	613	568
				8.1	567	528
				17.6	636	589
				16.8	631	585
				19.6	646	598
				42.8	729	671
				44.3	733	674
				38.8	718	661
				43.5	731	672
				Average	**660**	**610**
				2 s.d.	**120**	**110**

Continued on next page

Continuation of Table 5.4						
GSL-18-RG-12	Rutile and Titanite	1.0	0.7	19.5	583	541
				14.7	560	521
				12.7	548	510
				36.5	639	592
				22.0	593	551
				19.8	584	543
				7.4	508	474
				9.6	527	491
				7.2	506	473
				Average	**560**	**520**
				2 s.d.	**90**	**80**
GSL-18-RG-14	Rutile and Titanite	1.0	0.7	23.3	598	555
				17.8	575	535
				48.7	668	617
				19.6	583	542
				16.6	569	529
				10.8	535	499
				13.0	550	512
				14.8	560	521
				24.0	600	557
				16.0	566	527
				Average	**580**	**540**
				2 s.d.	**80**	**70**

Continued on next page

Continuation of Table 5.4						
GSL-18-C-31	Titanite and Ilmenite	0.85	0.55	6.3	508	448
				7.3	519	457
				5.3	496	438
				1.7	425	375
				14.8	573	504
				6.9	514	453
				12.9	562	495
				21.3	604	531
				19.3	596	524
				Average	**530**	**470**
				2 s.d.	**110**	**100**
GSL-18-C-36	Titanite	0.5	0.55	10.3	587	516
				12.6	605	531
				5.6	538	474
				9.5	580	510
				0.3	359	317
				18.7	641	563
				13.7	612	538
				Average	**560**	**490**
				2 s.d.	**190**	**160**

5.4.5 Subgrain-size piezometry

Local misorientation maps of quartz in samples representative of each metamorphic facies are presented in Figure 5.10, while maps for all other samples are presented in Appendix D.6. Overall indexing rates ranged from 53% to 97%, averaging at 78%. In all maps, the indexing rate of quartz was high, with poor indexing rates of other phases (e.g., plagioclase and amphibole) accounting for the low percentages in some maps. Within quartz, noise levels are relatively low, and subgrain boundaries with misorientation angles in the range 2°–10° are pervasive in all samples. Mean line-intercept lengths for quartz and associated differential stresses are recorded in Table 5.5. Mean line-intercept lengths are in the range 6.4–86.0 µm, which corresponds to differential stresses of 79–7 MPa.

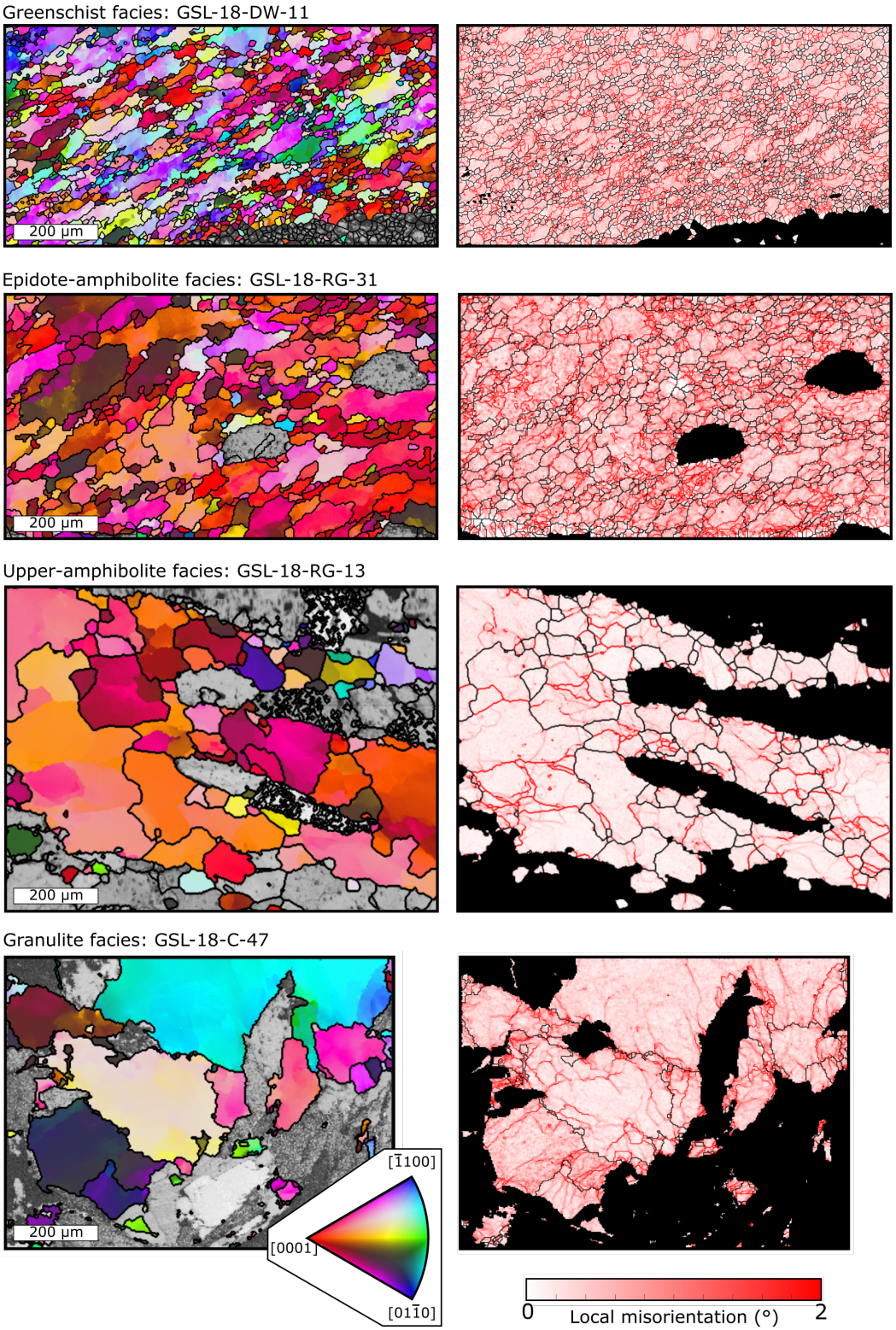

Figure 5.10: EBSD data for quartz in samples representative of each metamorphic facies. (left) Crystal orientations coloured by the crystal direction aligned normal to the map as indicated by the inverse pole figure. (right) local misorientation within kernels of 3 × 3 pixels. Black lines indicate grain boundaries, defined as having misorientation angles ≥ 10° are in black.

Sample	No. Intercepts	λ (µm)	σ (MPa)
Greenschist facies			
GSL-18-DW-11	50	9.2	57
GSL-18-DW-13	60	6.4	79
Epidote-amphibolite facies			
GSL-18-RG-02	70	21.7	26
GSL-18-RG-03	50	17.4	32
GSL-18-C-31	60	16.5	33
GSL-18-C-36	60	23.3	24
Upper amphibolite facies			
GSL-18-RG-11	60	27.1	21
GSL-18-RG-12	50	44.0	14
GSL-18-RG-13	80	50.4	12
GSL-18-RG-14	80	28.1	21
GSL-18-RG-20	60	86	7
GSL-18-C-26	70	51.3	12
GSL-18-C-27	60	14.1	38
GSL-18-C-28	50	27.6	21
Granulite facies			
GSL-18-C-47	70	32.6	18

Table 5.5: Results of subgrain-size piezometry. Mean-line intercept length (λ) is reported to one decimal place, while the equivalent stress is reported to two significant figures.

5.5 Discussion

5.5.1 Comparison of geothermometry results

Figure 5.11 compares the temperature estimates from the different geothermometers. Error bars represent the combined error of the thermometer and the standard deviation of multiple measurements by taking the square root of the sum of the two squared errors (Powell, 1978, page 284). The comparison of temperatures measured from different thermometers enables an evaluation of the method that best represents the final temperature of deformation. Here, the temperature range indicated by the recrystallisation mechanisms of quartz is assumed to be broadly indicative of the last deformation event experienced by the rock. Whilst temperatures estimated from the recrystallisation mechanisms provide only loose constraints and are subject to the caveats of potential differences in deformation conditions relative to the benchmark of the Tonale Fault Zone (Stipp, Stünitz, Heilbronner, & Schmid, 2002; Law et al., 2013), they have the advantage that the recrystallisation is intimately linked to any modification of subgrain size. In contrast, the geothermometers based on mineral chemistry provide more precise temperature estimates in some instances, but the

potential for slow diffusion on the retrograde metamorphic path leads to the possibility that temperatures may record chemical equilibration prior to the final deformation experienced by each rock.

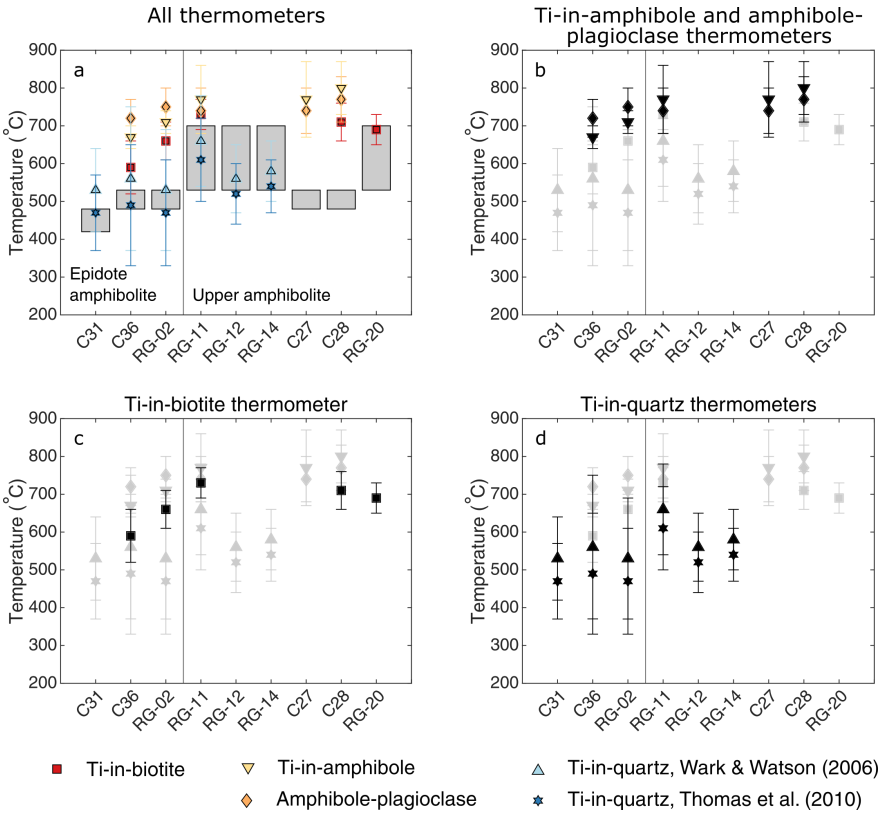

Figure 5.11: a) All geothermometry results from this study. The vertical line divides samples of different metamorphic facies. Grey bars represent temperatures estimated from the quartz microstructures by comparison to the samples of Stipp, Sünitz, Heilbronner, Schmid (2002). Bars represent the combined uncertainty of the thermometer and the standard deviation of measurement from each sample by taking the square root of the sum of the two squared uncertainties (Powell, 1978, page 284). b–d) Geothermometry data from a) replotted to highlight the results from individual thermometers. Points in black correspond to the labelled geothermometer while all other points are plotted in grey.

Temperatures from amphibole-plagioclase thermometry and Ti-in-amphibole thermometry are constant within error across the shear zone, broadly matching the final temperatures associated with upper amphibolite- and granulite-facies metamorphism (700°–800°C). The slow intracrystalline diffusion of Na and Si coupled with Ca and Al (the exchange occurring during the Holland and Blundy (1994) thermometer) in plagioclase suggest that temperatures measured by amphibole-plagioclase thermometry represent those at the time of crystallisation (Spear & Florence, 1992). For example, Spear and Florence (1992) calculated characteristic diffusion length scales, in the temperature range of 500°–900°C, of 2×10^{-6} to 2

μm per 10 Ma, far smaller than the plagioclase grains used in this analysis. It is possible that recrystallisation offers faster diffusion pathways, with mobile shortcuts in the form of subgrain and grain boundaries sweeping through the material (e.g., Chakraborty, 2008; Grujic et al., 2011). However, recrystallisation is not pervasive throughout the plagioclase porphyroclasts in the GSLsz, and the uniform compositional profiles across the plagioclase grains exhibit little evidence of compositional changes between the rims and the cores. Therefore, we can be confident that the plagioclase-amphibole temperatures do not match those under which the final deformation occurred and are more likely to instead record the crystallisation temperatures.

Temperatures from Ti-in-biotite are systematically lower than those from amphibole-plagioclase, except for GSL-18-RG-11, for which the temperatures from these two thermometers are similar. However, the consistency of temperatures in GSL-18-RG-11 from Ti-in-biotite and amphibole-plagioclase thermometry suggests that the biotite grains may also represent a temperature associated with the amphibolite-facies metamorphism. Similarly, for sample GSL-18-RG-20, the Ti-in-biotite temperature is at the upper limit of the broad range of temperatures inferred from the quartz microstructures, suggesting that it too may not necessarily record the temperature of final deformation. The offset of the Ti-in-biotite temperatures from the amphibole-plagioclase temperatures in GSL-18-RG-02 and GSL-18-RG-36 could be explained by the absence of rutile and associated understaturation in Ti (Henry et al., 2005). However, GSL-18-RG-11 is also undersaturated in Ti but has Ti-in-biotite temperatures consistent with those from amphibole-plagioclase thermometry. Alternatively, the minor degrees of chloritisation of biotite could leave it depleted in Ti (Henry et al., 2005). However, this explanation requires the additional precipitation of oriented sagenitic rutile (Henry et al., 2005), which has not been observed in these samples. Though it is unclear exactly what portion of the tectonometamorphic history the temperatures from Ti-in-biotite thermometry represent, it is evident that they are generally hotter than those associated with the final deformation structures.

In deforming quartz-rich rocks, the Ti-in-quartz thermometers are potentially affected by the dynamic recrystallisation mechanisms in quartz (Grujic et al., 2011) and the total amount of strain (Bestmann & Pennacchioni, 2015). Grujic et al. (2011) applied the Ti-in-quartz geothermometer to the Tonale Fault Zone in the Alps and found that, while Ti

concentrations in quartz with evidence for GBM provided a good record of the deformation temperatures, Ti concentrations remained at the regional background level in quartz in which recrystallisation was dominated by SGR. Grujic et al. (2011) suggested that microstructural evolution in the GBM regime enhances apparent diffusivities of Ti in quartz. In addition, Bestmann and Pennacchioni (2015) applied the Ti-in-quartz geothermometer to shear zones in the Lake Edison pluton in California and found no evidence for enhanced diffusivity in samples deformed to low strains, regardless of the recrystallization mechanism. However, in samples deformed to higher strains, the authors did observe some re-equilibration, indicating that the magnitude of strain is as/or more important than the recrystallisation mechanism. The temperatures estimated using the Thomas et al. (2010) calibration of the Ti-in-quartz thermometer match those inferred from quartz microstructures. Pervasive recrystallisation of quartz within the GSLsz samples indicates large strains, which give additional confidence in the temperatures from Ti-in-quartz thermometry. These considerations suggest that Ti-in-quartz thermometry provides the most accurate estimate of the temperature associated with the deformation microstructures.

5.5.2 The lower-crustal strength of the GSLsz

To construct a strength-depth profile, it is necessary to determine the depths at which the stresses measured by subgrain-size piezometry were set. This is possible by estimating the depth associated with the temperature at which the subgrain-size was established. Where available, we use the Ti-in-quartz temperatures. For samples that lacked Ti-in-quartz temperatures, we use the middle of the temperature range indicated by the microstructures. The characteristic pairings of CPO type and recrystallisation mechanism often observed within particular temperature ranges were present, where available, within our samples giving additional confidence in these temperature ranges. We first calculated a pressure from the temperatures using the geothermal gradient present during the final period of shear-zone activity (1000°C·GPa^{-1}, Dyck et al., 2020). We then calculated depths from these pressures using an average overburden density of 2,750 kg·m^{-3}, which is consistent with the value used by Dyck et al. (2020). Table 5.6 summaries the preferred temperature and depth estimates for each sample.

Sample	Temperature estimate	Temperature (°C)	Depth (km)
Greenschist facies			
GSL-18-DW-11	Quartz microstructures	510 ± 20	18.9 ± 0.7
GSL-18-DW-13	Quartz microstructures	455 ± 35	16.9 ± 1.3
Epidote-amphibolite facies			
GSL-18-RG-02	Ti-in-quartz	470 ± 140	17.5 ± 5.2
GSL-18-RG-03	Quartz microstructures	590 ± 60	21.9 ± 2.2
GSL-18-C-31	Ti-in-quartz	470 ± 100	17.4 ± 3.7
GSL-18-C-36	Ti-in-quartz	490 ± 170	18.2 ± 6.3
Upper-amphibolite facies			
GSL-18-RG-11	Ti-in-quartz	610 ± 110	22.6 ± 4.1
GSL-18-RG-12	Ti-in-quartz	520 ± 80	19.3 ± 3.0
GSL-18-RG-13	Quartz microstructures	590 ± 60	21.9 ± 2.2
GSL-18-RG-14	Ti-in-quartz	540 ± 70	20.0 ± 2.6
GSL-18-RG-20	Quartz microstructures	590 ± 60	21.9 ± 2.2
GSL-18-C-26	Quartz microstructures	590 ± 60	21.9 ± 2.2
GSL-18-C-27	Quartz microstructures	510 ± 20	18.9 ± 0.7
GSL-18-C-28	Quartz microstructures	510 ± 20	18.9 ± 0.7
Granulite facies			
GSL-18-C-47	Calculated equilibria and Ti-in-biotite (Dyck et al., 2020)	710 ± 25	26.3 ± 0.9

Table 5.6: Temperatures and calculated depths associated with the piezometric measurements in quartz. Depth was calculated using an average overburden density of 2,750 kg·m^{-3} and a geothermal gradient of 1000°C·GPa^{-1} (Dyck et al., 2020)

We compare the stress-depth relationship measured by subgrain-size piezometry in the GSLsz to Behr and Platt's (2014) compilation of stress-depth profiles calculated from grain-size piezometry in Figure 5.12. In their original plot, Behr and Platt (2014) calculated a shear stress from the piezometric values of equivalent stress by dividing by $\sqrt{3}$. However, this factor actually relates to the conversion from torsional deformation to the equivalent stress (Paterson & Olgaard, 2000), with the conversion between shear stress (τ) and equivalent stress (σ) for general shear actually following the relationship of

$$\sigma = 2\tau. \tag{5.1}$$

We therefore recalculate the shear stresses in Behr and Platt (2014) using Eq. 5.1.

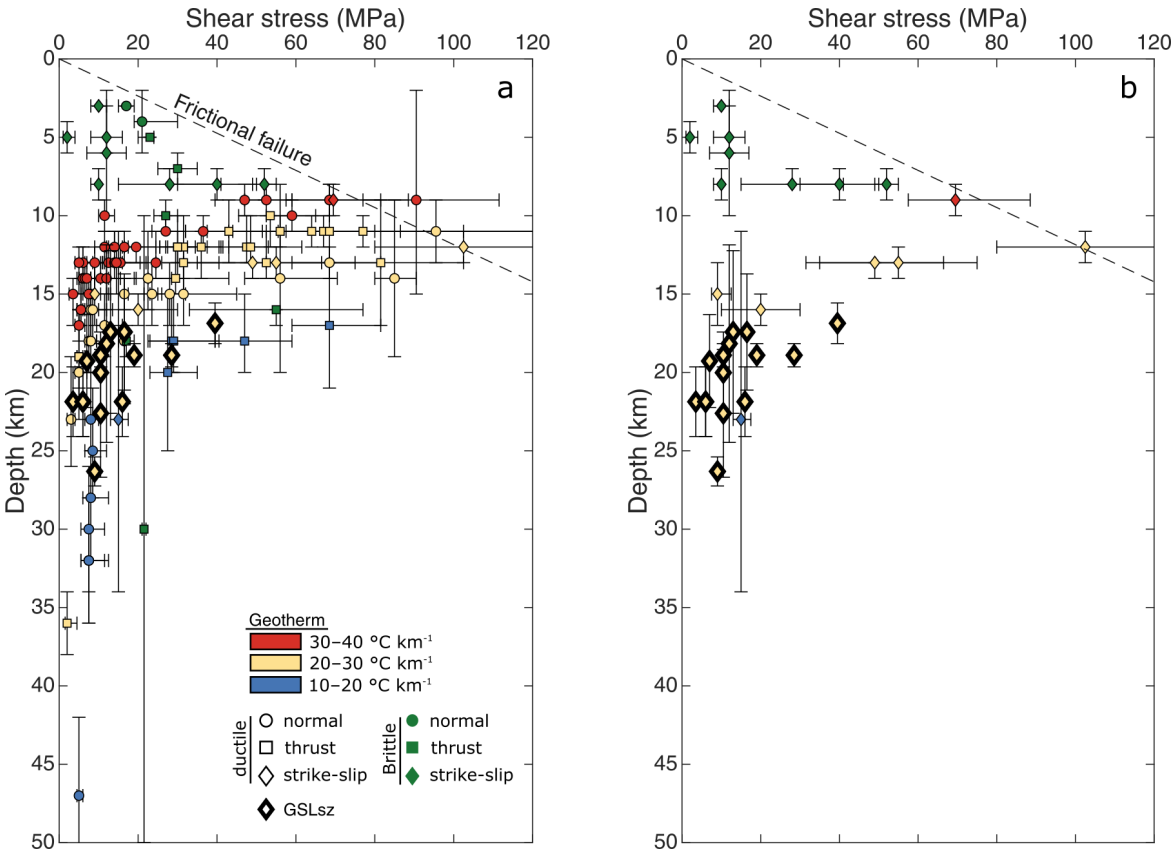

Figure 5.12: Stress-depth data from subgrain-size piezometry on the GSLsz overlain on (a) stress-depth data from grain-size piezometry compiled by Behr and Platt (2014) and (b) those data obtained from other strike-slip shear zones. Error bars on grain-size piezometry represent a combined error of pressure, temperature, and grain size. For subgrain-size piezometry error bars only represent the error on temperature, converted to depth. The frictional shear stress as a function of depth, assuming a crustal density of 2750 kg·m^{-3}, is plotted based on the Mohr-Coulomb failure criteria.

The general shape of the crustal strength profile of the GSLsz matches those seen elsewhere (Figure 5.12). However, the stresses supported by the lower crust in the GSLsz appear higher than those measured in other shear zones that deformed under similar conditions and thermal regimes. The geothermal gradient of 1000°C·GPa^{-1} during activity of the GSLsz (Dyck et al. 2020) is equivalent to 27°C·km^{-1}. Therefore, the stresses estimated from the GSLsz might be expected to fall near the low-stress end of the data from geothermal gradients of 20–30°C·km^{-1} in the compilation of Behr and Platt (2014) (yellow points in Figure 5.12). Instead, the stress estimates from the GSLsz plot near the high-stress end of that subset of data from Behr and Platt (2014) and partially overlap with data from even lower geothermal gradients of 10–20°C·km^{-1} (blue points in Figure 5.12).

To better compare shear zones with different geothermal gradients, stress measurements are plotted against temperature in Figure 5.13. The flow law of Hirth et al. (2001) for dislocation creep of quartz is plotted for comparison (see Table 5.7 for parameters). The

data from the GSLsz are consistent with strain rates on the order of 10^{-11} s^{-1} to 10^{-12} s^{-1}. The strain rates on the order of 10^{-11} s^{-1} are higher than previous estimates associated with temperatures of approximately 450°–700°C. The GSLsz therefore could represent a particularly high-stress, high-strain rate shear zone.

Table 5.7: Hirth et al. (2001) flow law parameters

Flow law	**log(A) (MPa^{-n}/s)**	**m**	**n**	**Q (kJ/mol)**
$\dot{\varepsilon} = A f_{H_2O}^m \sigma^n \exp\left(\frac{-Q}{RT}\right)$*	-11.2 ± 0.6	1	4	135 ± 15

*Where $f_{H_2O}^m$ is the water fugacity calculated using the temperature and pressure at any one point and the Aaron Springstroh online water fugacity calculated, found at https://aaron-sp.github.io/fugacity/index.html.

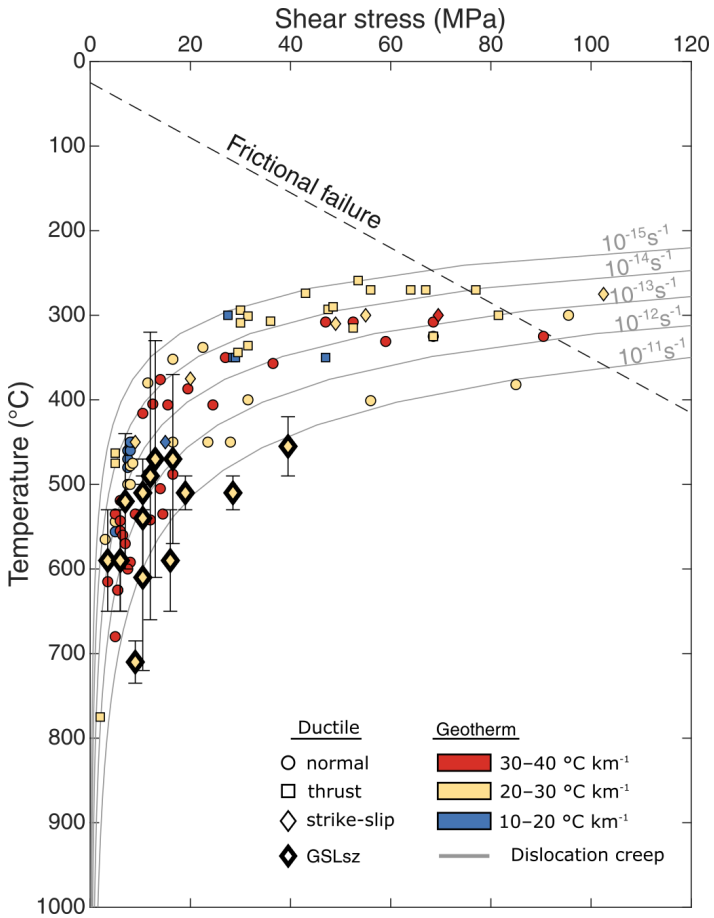

Figure 5.13: Data from Figure 5.12 re-plotted against temperature. The dislocation-creep flow law from Hirth et al. (2001) is plotted for comparison. Frictional shear stress is plotted as a function of temperature, calculated from depth assuming a geothermal gradient of 1000°C·GPa^{-1}.

Another hypothesis to explain the high stresses recorded by subgrain sizes in the GSLsz is that the sizes of grains and subgrains evolve at different rates under changing stress conditions during exhumation. Grain size has previously been found to record the last increments of stress experienced by a sample subjected to rapid increases and decreases in stress (e.g., Kidder et al., 2016; Ross et al., 1980). However, more analogous to the GSLsz, Soleymani et al. (2020) conducted deformation experiments on quartz, during which stress was increasing gradually as a result of cooling from 900°C to 800°C. Under these conditions the grain size was unable to maintain the evolving piezometric value as stress increased, with final grain sizes being nearly twice as large as predicted by grain-size piezometry. As natural shear zones commonly undergo synkinematic cooling at rates of temperature change with strain similar to those employed by Soleymani et al. (2020), it is possible that stresses estimated by grain-size piezometry, such as those presented in Behr and Platt (2014), may often provide only lower bounds on the stress during the final increments of ductile deformation during exhumation.

Previous work on the effect of transient stress on subgrain size is inconclusive, with subgrains postulated to both be able to (Qin et al., 2003) and be unable to (Ross et al., 1980) grow when subjected to a stress of a reduced magnitude. The subgrain-size piezometer of Goddard et al. (2020) was calibrated using the final stress. A strong agreement was also found between stresses measured using subgrain-size piezometry and the final stress experienced by the sample measured from X-ray diffraction in Chapter 3. This experimental work supports the general principle that stresses estimated by subgrain-size piezometry represent the final stress rather than the peak stress experienced by a rock. Even if subgrains did record the peak stresses, given that stress increased monotonically as the GSLsz exhumed, the most recent stress was likely also the peak stress imposed on each sample. However, this supposition would not necessarily hold if the rocks were subjected to significant transient high stresses due to earthquakes on the overlying frictional faults.

An alternative explanation for the elevated stresses in the GSLsz is that they are measured in polymineralic rocks. We collected maps from polymineralic regions where quartz is prevalent and in nearly all instances interconnected. Theoretical (e.g., Handy, 1990) and experimental (e.g., Ji et al., 2001) studies have suggested that rocks in which a weak phase is interconnected should deform under isostress conditions. The pervasive recrystallisation

of quartz compared to the large relict plagioclase porphyroclasts, imply that the former is the weaker of the two main rock-forming minerals. Therefore, the stresses measured through subgrain-size piezometry should represent the bulk (iso-)stress. However, these theoretical assumptions have been shown not to apply to olivine and orthopyroxene mixtures (Chapter 3). It is possible therefore that the stress supported by quartz within the GSLsz likewise did not equate to the bulk stress and that other minerals within the rocks, such as weak phyllosilicates, experienced erroneously low stresses.

Although the results of this study indicate that the GSLsz is an anomalously high stress shear zone, further work is clearly required to constrain how stresses recorded within subgrains in a phase relate to the macroscopic stress. In addition, the application of grain-size piezometry to the GSLsz is a clear first step for future work.

5.6 Conclusion

We present a stress-depth profile for the GSLsz, an early Proterozic strike-slip transform fault. Amphibole-plagioclase, Ti-in-amphibole, Ti-in-biotite, and Ti-in-quartz thermometers constrain the thermal history of the rocks. Ti-in-quartz thermometry gave temperatures consistent with those inferred from the quartz microstructures, whereas Ti-in-biotite, Ti-amphibole, and amphibole-plagioclase temperatures matched those of peak metamorphic conditions. The Ti-in-quartz temperatures were used to calculate a corresponding depth, using the geothermal gradient established by Dyck et al. (2020).

Stresses measured by subgrain-size piezometry in the polymineralic rocks of the GSLsz were higher than those measured from other shear zones via grain-size piezometry. Three potential possibilities are put forward to explain this discrepancy. First, the stresses from subgrain-size piezometry are representative of the bulk stress experienced by the shear zone and the GSLsz simply deformed under particularly high stresses. Second, grain-size piezometry potentially underestimates the stresses during synkinematic cooling. Finally, stresses within the quartz are not representative of the bulk stress experienced by the rock. To distinguish between these three possibilities further work, such as the application of grain-size piezometry, is required.

6 Conclusion

6.0.1 Summary of results

The aim of this research was to develop and test a tool for measuring the average stress within each phase in a polymineralic rock and to use this tool to explore assumptions and models for their strength. Here I summarise the main points from each chapter.

Chapter 2

We used electron backscatter diffraction data to calibrate a new subgrain-size piezometer for olivine and quartz. We explored a range of different boundary misorientations and concluded that low critical misorientation angles (e.g., 1° or 2°) provide the best piezometric calibrations. Unlike grain-size piezometry, these calibrations obviate the need to discriminate between relict and recrystallised grains.

Chapter 3

Triaxial compression experiments were conducted on olivine and orthopyroxene mixtures, and end-members, using a Deformation-DIA at the Advanced Photon Source, Argonne National Laboratory. We compared stresses in individual phases measured *in-situ* through X-ray diffraction to those measured *ex-situ* through subgrain-size piezometry. Subgrain sizes successfully record the stress in olivine in polymineralic rocks subject to two conditions. First, the piezometer should not be applied at stresses higher than those under which it was calibrated. Second, the subgrain-size piezometer should not be applied to samples with very fine grain sizes in which subgrain development is limited. Evaluation of the subgrain-size piezometer in orthopyroxene was limited in scope due to the sparsity of subgrain boundaries within this phase. However, preliminary results suggest that the stresses measured through subgrain-size piezometry are within the range of stresses measured from X-ray diffraction.

Chapter 4

The subgrain-size piezometer was also applied to mixtures of olivine and orthopyroxene, deformed in triaxial compression experiments in a gas-medium apparatus to explore the deformation mechanisms of polymineralic rocks. Intermediate samples exhibited

anomalous weakening, which could not be explained by the grain-size sensitivity of traditional deformation mechanisms. The stress measured in olivine by subgrain-size piezometry suggests that weakening occurred solely in the orthopyroxene, thought to have deformed predominantly by diffusion creep. This anomalous weakening at intermediate phases is not observed in high-purity aggregates. Therefore, it is proposed that impurities segregate at phase boundaries and enhance the deformation kinetics.

Chapter 5

The subgrain-size piezometer was applied to polymineralic rocks of the Great Slave Lake shear zone (GSLsz). The contemporaneous exhumation and localisation of the GSLsz allows for different structural levels of the fault zone to be investigated with a single lateral transect of the surface exposure. The estimates of stress presented here for the lower crust in the GSLsz and measured by subgrain-size piezometry are higher than estimates of stress presented by other studies of shear zones that deformed under similar conditions and thermal regimes and measured by grain-size piezometry. This discrepancy may arise from subgrain sizes and grain sizes recording different portions of the deformation history, with grain sizes representing the average stresses and subgrain sizes the final stresses experienced by a sample.

6.0.2 Future directions

A number of potential research avenues offer opportunities to broaden the application of subgrain-size piezometry. First, it has always been the intent for the subgrain-size piezometer to be applied to minerals for which it was not calibrated. Testing the subgrain-size piezometer against experiments or well-characterised natural samples of common rock-forming minerals is the obvious next step in expanding its application. Initial results from this project indicate that the piezometer may be applicable to orthopyroxene. However, due to the limited availability of subgrain boundaries within the orthopyroxene in our D-DIA experiments, it was not possible to demonstrate definitively that the subgrain-grain size piezometer applies. Analysis of additional orthopyroxene samples is therefore an intuitive next step. The high-stress measurements for the GSLsz obtained through the analysis of quartz also identify the need to also test the piezometric calibration against other silicates. The layered gabbro mylonites collected from the Southwest Indian Ridge, Ocean Drilling

Program Hole (735B), offer ideal natural samples to test the use of subgrain-size piezometers on plagioclase. Here, monomineralic layers exist and their strength has already been well characterised through grain-size piezometry (Mehl & Hirth, 2008).

Second, a detailed study of the stress recorded by subgrain sizes in samples that have been subject to complex deformation is required. Initial results from Chapters 2 and 3 imply that subgrains record the final stress experienced by a rock. However, the experiments in these chapters were not designed specifically with this purpose in mind. For grain-size piezometry, previous experiments have been designed specifically to address the evolution of microstructures in 'two-stage' stress experiments (Kidder et al., 2016) as well as experiments in which the stress increased gradually as a result of cooling (Soleymani et al., 2020). In Chapter 5 of this thesis, we hypothesise that, unlike grains, subgrains are able to record the stress in a sample that has undergone cooling. Therefore, testing this hypothesis against experiments similar to those of Soleymani et al. (2020) is another clear avenue for future work.

Appendices

Appendix A Chapter 2

Supplementary material provides descriptions of how to execute the MATLAB® scripts (A.1); discussion of the choice of shear moduli and Burgers vectors (A.2); a methodology for high-angular resolution EBSD (HR-EBSD) used to test the angular resolution of the data (A.3, Figure A.6); mechanical data for the experiment in Qz-2, which is published for the first time in this study (Figure A.1); analysis on the effect of EBSD step-size on measurements of subgrain size (Figure A.2); analysis on the effect of map area on the measurements of subgrain size (Figure A.3); examples of samples re-mapped as the area-analysis suggest the maps were too small to capture a representative subgrain-size (Figure A.4); analysis on the size of the critical misorientation angle used to define a subgrain boundary (Figure A.5); and information on the Experimental conditions (Table A.1) .

A.1 Instructions for using MATLAB® scripts

Codes are assessable on GitHub, following the link:

https://github.com/RellieGoddard/SGPiezometry.git

The MATLAB® scripts codes provided can be used on polymineralic samples. However, large poorly indexed areas will affect the mean line-intercept length. We recommend that you update and run the scripts in the following order:

1. Ensure MTEX (Version 5.1.1) is running and the following scripts are within the folder: *ProcessEBSD_fun.m, LinearIntercepts_fun.m, No_intercepts_check.m, undersampling.fun.m, Undersampling_Step_Size.m, Area_Analysis_reduction.m, ProcessEBSD_LinearIntercepts.m, Stress_Calulation_fun.m.*

2. The *ProcessEBSD_fun.m* script imports the EBSD data. It cleans the data by removing single pixels known as 'wildspikes' as well as grains that are less than three pixels in size described as 'shards'. No modifications are required for this script, if desired, there is the ability to expand into non-indexed regions by modifying the 'threshold' variable. The higher the threshold value the more of the non-index areas are infilled. A successful run should generate the following outputs: structures containing information

on EBSD, grains, and subgrains, a phase map if input **Phase_map** = 1, and a band contrast map if input **Band_contrast** = 1.

3. Run *No_intercepts_check.m*. This function checks the number of intercepts required to accurately capture the subgrain size. Required user inputs: **nx_max, gb_min, sg_min, cutoff, phase, crystal, test, include_low, CS, pname, fname**.

   (a) **nx_max:** The maximum number of intercepts that you want to test (recommended to start at either 30 or 40)

   (b) **gb_min:** Minimum misorientation angle to define a grain boundary in degrees (used for constructing maps).

   (c) **sg_min:** Minimum misorientation angle to define a subgrain boundary in degrees (only used for constructing maps).

   (d) **cutoff:** minimum misorientation angle to define a subgrain boundary in degrees. Used for piezometer calculations, recommended value is 1.

   (e) **phase:** name of phase of interest.

   (f) **crystal:** crystal system of the phase of interest.

   (g) **test:** when set to 1, reduces the size of the input EBSD map by taking every tenth pixel in both the horizontal and vertical direction. This function can be utilised to ensure the script runs correctly with a new sample file or for troubleshooting. During full analysis, test should be set to 0.

   (h) **include_low:** option to include low numbers of intercepts (1–9). To include, set to 1. Otherwise, set to 0.

   (i) **CS:** crystal symmetry class for all indexed phases in EBSD amps.

   (j) **pname:** path to data.

   (k) **fname:** file name combined with path.

   Expected results: figures presenting the line intercepts on top of EBSD data for each iteration, a figure plotting the mean line-intercept length against the number of intercepts, and a figure showing the change in mean line-intercept length relative to last. The test is successful if the measured mean line-intercept length stabilises (± 2.5 rela-

tive to previous value). If the mean line-intercept does not stabilise, increase **nx_max** and run again

4. Run *Undersampling_Step_Size.m*. This script tests that the step-size is small enough, that is, that the spatial resolution is sufficient to capture the subgrains. Required user inputs: **nx, Int_max, Image_title, Header_size, gb_min, sg_min, cutoff, phase, crystal, test, Phase_map, Band_contrast, CS, pname, fname**.

   (a) **nx:** The number of intercept lines, chosen based on analysis from *No_intercepts_check.m*.

   (b) **Int_max:** the number of times you want to reduce the step-size. The step-size at an iteration will be **Int_max** multiplied by the original step-size.

   (c) **Image_title:** Title for figure

   (d) **Header_size:** Number of lines, up to and including the line starting with *'phase'* in the *.ctf* file (open in Notepad)

   Expected results: a figure plotting the intercept variation factor against the number of pixels per intercept. If **Phase_map** = 1 and **Band_contrast** = 1 these maps will be additional outputs.The test is successful if the measured mean line-intercept length is not sensitive to the effective step size, which is represented by the presence of an asymptote at an intercept variation factor of 1. If such an asymptote doesn't exist, then either re-map the sample using a smaller step size, or use the subgrain-size stress measurement as a lower bound.

5. Run *Area_Analysis_reduction.m*. This script tests whether the map is large enough to capture the true subgrain size. Required user inputs: **nx, gb_min, sg_min, cutoff, phase, crystal, test, Phase_map, Band_contrast, CS, pname, fname**.
   Expected results: an EBSD map for each analysis is outputted with a red box outlining the analysed subarea and a figure showing the intercept analysis of the final subarea. A figure showing the mean line-intercept length plotted against the area as a percentage of the original map. On the right axis of the same figure the % change of the mean line-intercepts length relative to the full map is plotted against map area.
   The test is successful if, as the size of the sub-area increases, the mean line-intercept length asymptotically approaches the mean for the entire map. For all the samples

included in the subgrain-size piezometer, the % change in mean line-intercept length relative to the full map was $\leq$ 5% for a 20% reduction in map area. If the mean line-intercept length changes significantly as the map size is reduced then more maps or larger maps are required to accurately capture the subgrain size.

6. Run *ProcessEBSD_LinearIntercepts.m*. This script measures the mean line-intercept length between different boundaries. Required user inputs: **nx, gb_min, sg_min, cutoff, phase, crystal,test, Phase_map, Band_contrast, Check_different_misorientation, SG_piezometer, Piezometer_choice**

   (a) **Check_different_misorientation:** To measure the mean line-intercept length for minimum misorientation angles between 1°and 10°, set to 1. Otherwise, set to 0.

   (b) **SG_piezometer:** To calculate equivalent stress directly from measured subgrain size, set to 1. Otherwise, set to 0.

   (c) **Peizometer_choice:** If SG_piezometer = 1, **Piezometer_choice** sets which piezometer to use when calculating stress. If using Equation 2.1, which includes the Holyoke and Kronenberg (2010) friction correction, then **Piezometer_choice** = 1. If using Equation 2.2, which doesn't have the Holyoke and Kronenberg (2010) friction correction, then **Piezometer_choice** = 2.

   (d) **Burgers:** Burgers vector of phase of interest

   (e) **Shear_M:** shear modulus of the phase of interest

   Expected results: First, if input **Check_different_misorientation** = 1, a plot of mean line intercept length (vertical axis) plotted against the defined critical misorientation angle (horizontal axis). A sample containing subgrains will exhibit smaller mean line-intercept lengths for critical misorientation angles of $< 5°$ than at 10°. Second, a figure of the intercept analysis and a histogram of the line intercept lengths including the calculated arithmetic mean. Finally, optional outputs include a band contrast map and a phase map if inputs **Band_contrast** and **Phase_map** both = 1. If **SG_piezometer** = 1, a stress calculated from one of the Goddard et al., (2020) subgrain-size piezometers will also be printed in the command line.

A.2 Shear moduli and Burger's vector values

The Burger vector used for quartz was 5.10×10^{-4} µm (Deer et al., 1992, pp 458), which is an average of the a (4.9×10^{-4} µm) and c (5.4×10^{-4} µm) unit cell dimensions. For olivine, a Burgers vector of 4.8×10^{-4} µm (Deer et al., 1992, pp 447) was used, which corresponds to the a unit cell dimension. These Burgers vectors were chosen as they represent the dominant dislocations active within the conditions of the subgrain-size piezometer. The shear modulus for quartz, 4.2×10^4 MPa, was calculated from wave velocities at a confining pressure of 400 MPa (Birch, Table 7–16 in Clark, 1966). For olivine, shear moduli of 7.78×10^4 and 6.26×10^4 MPa were taken for Fo_{90} and the Fo_{50}, respectively (Mao et al., 2015), corresponding to room temperature and pressure. Although the shear modulus for olivine does have a pressure dependence the change within our pressure range (at room temperature) is $< 4\%$ (Abramson et al., 1997); therefore, the shear moduli for olivine remain those at room pressure.

To test the effect of temperature on the subgrain-size piezometric equation, we calculated the shear moduli for Fo_{90} and Fo_{50} at 1250°C as 6.53×10^4 and 5.01×10^4 MPa, respectively (Mao et al., 2015). The shear modulus of quartz remains that at room temperature as it is almost temperature-independent (Peng & Redfern, 2013). The temperature-modified subgrain-size piezometers are $\frac{\lambda}{b} = 10^{0.8\pm0.8}\left(\frac{\sigma}{\mu}\right)^{-1.2\pm0.3}$ when using Holyoke and Kronenberg (2010) correction and $\frac{\lambda}{b} = 10^{1.1\pm0.9}\left(\frac{\sigma}{\mu}\right)^{-1.1\pm0.4}$ without this correction. These new equations are within error of the room temperature subgrain-size piezometer. Hence, the shear moduli used in our work remain those of a mineral at room temperature.

A.3 Method, High-angular resolution EBSD

We reanalysed a number of samples with high-angular resolution EBSD (HR-EBSD) to assess the impact of orientation noise on the measured subgrain sizes. Recently, HR-EBSD based on the approach of Wilkinson et al. (2006) and Britton and Wilkinson (2011, 2012) has been adapted for geological materials including olivine (Wallis et al., 2016) and quartz (Wallis, Parsons, & Hansen, 2019). The high angular precision is beneficial for subgrain-size analysis because it removes noise that otherwise may have been wrongly identified as subgrain boundaries in traditional EBSD. HR-EBSD uses cross correlation between similar features in adjacent electron backscatter diffraction patterns to improve the angular resolution of standard EBSD (Britton & Wilkinson, 2012; Wallis et al., 2016; Wilkinson, 1996; Wilkinson & Randman, 2010). During conventional Hough-based EBSD, measurements of the misorientation angle between two pixels is limited to a precision of 0.2°–0.5° by the process of determining the band positions in Hough-space (Humphreys, 2004; Wilkinson & Randman, 2010). In HR-EBSD, the Hough transform is only used to determine the orientation of a single reference point within each grain (Britton & Wilkinson, 2011; Wilkinson et al., 2006). The orientations of all other pixels in the grain are then found by cross-correlating regions of interest (ROIs) within each EBSP with the same regions in the reference EBSP. A displacement gradient tensor is fitted to the shifts in the positions of the ROIs in each pattern, from which the lattice rotations relative to the reference point can be calculated (Britton & Wilkinson, 2011, 2012; Wilkinson et al., 2006). While this method improves the precision of misorientation angles to the order of 0.01° (Britton & Wilkinson, 2012; Wallis et al., 2016; Wilkinson, 1996; Wilkinson & Randman, 2010), it significantly increases the processing time.

We re-processed the data from two samples, TMQ-7 and W-1126, using HR-EBSD to test whether conventional EBSD measurements are sufficient for subgrain analysis. Figure A.6 presents a comparison of subgrain sizes measured by EBSD and HR-EBSD in sample TMQ-7. Subgrain sizes measured by HR-EBSD and standard EBSD differ slightly, with a greater divergence as the critical misorientation angle is reduced. For samples TMQ-7 and W-1126 there is a 27% change and a 11% change, respectively, between the subgrain sizes measured by HR-EBSD and standard EBSD when using a critical misorientation angle of 1°. Therefore, the orientation noise in standard EBSD data (which can vary among datasets

depending on pattern quality and other acquisition parameters) introduces uncertainty of about 19% in the stress. We conclude that, while HR-EBSD is preferable, conventional EBSD has sufficient angular resolution for our subgrain-size piezometer.

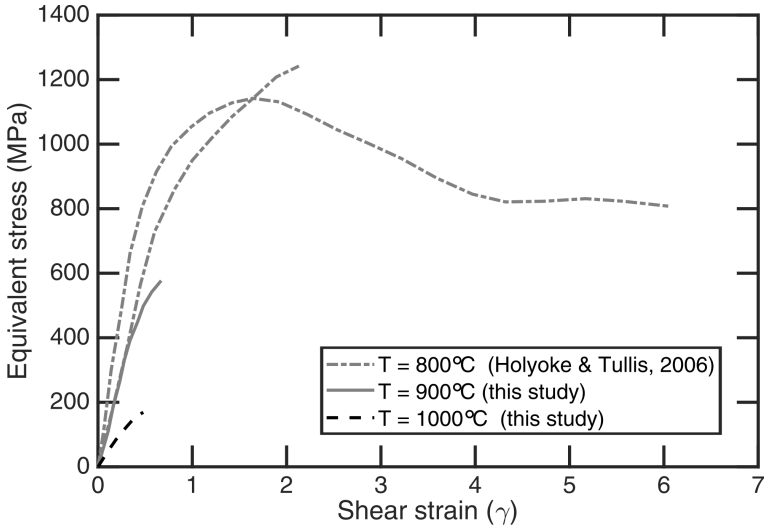

Figure A.1: Mechanical data for general shear experiments in Qz-2 some of which are published for the first time in this study. Peak equivalent stress of Black Hills Quartzite sample deformed at a confining pressure of 1500 MPa and an equivalent strain rate of $\sim 1.15 \times 10^{-5} s^{-1}$ *and temperatures of between* $800°C$ *and* $1000°C$*. The sample in black (W-1134) was included in the calibration of the subgrain-size piezometer. Mechanical data are corrected according to the methods in Holyoke and Kronenberg (2010). Equivalent stress and strain were calculated using the programs RigC and RigS2 by Renee Heilbronner (2002, 2006).*

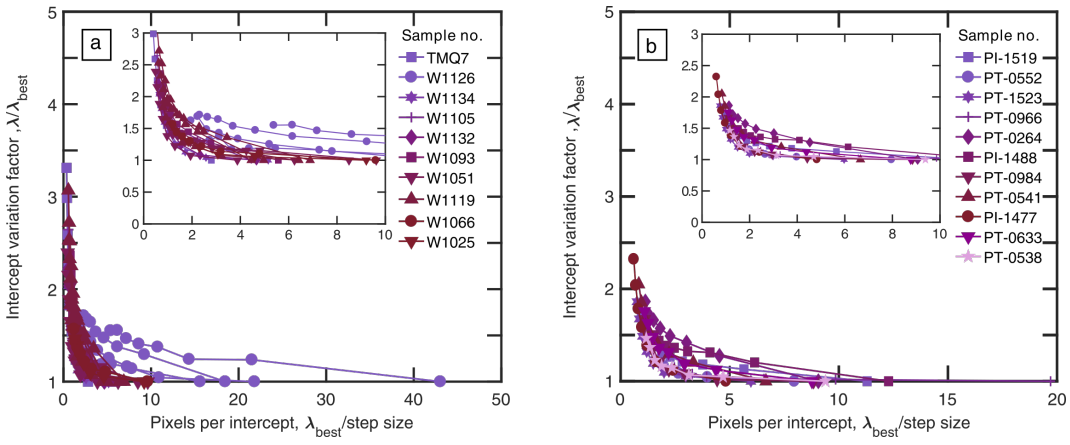

Figure A.2: Step-size analysis for (a) quartz samples and (b) olivine samples. The intercept variation factor (λ/λ_{best}), plotted on the vertical axis, represents the degree of change in the mean line-intercept length with change in step size. On the horizontal axis, the pixels per intercept (λ_{best}/(step size)) is based on the best estimate of mean line-intercept length, that is, the mean line-intercept length for the smallest step size. Maps originating from the same sample are plotted with the same symbol. For a map with high spatial resolution, the intercept variation factor will stabilise as the pixels per intercept increase.

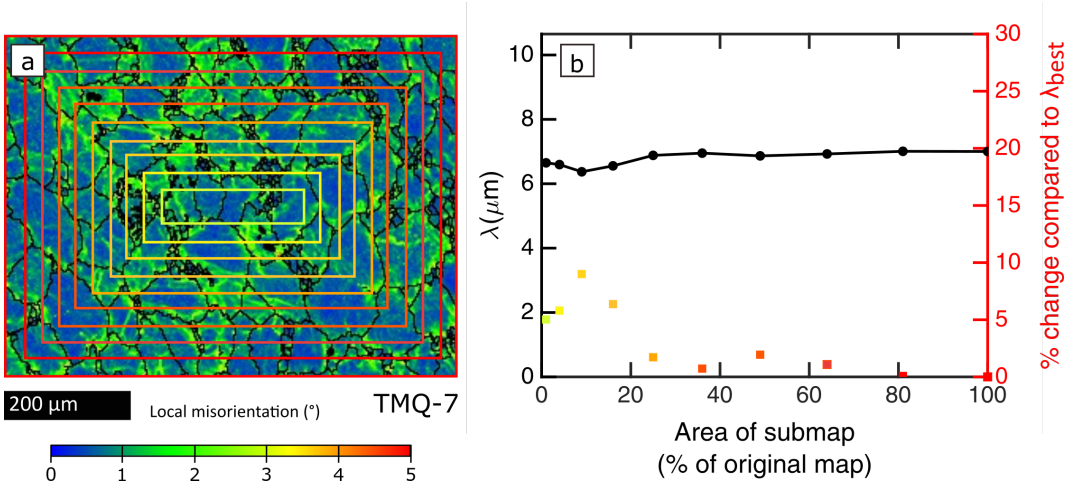

Figure A.3: Area analysis of quartz sample TMQ-7 using a critical misorientation angle of 1°. In this analysis, the size of the map is systematically reduced and the mean line-intercept length re-measured. (a) Local misorientation map for TMQ-7. Coloured boxes match the points in Figure A.3b and represent the areas mapped at each step. (b) The mean line-intercept length is plotted as black solid circles against the size of the map as a fraction of the size of the original map. The percentage change with respect to the best estimate for subgrain-size (mean line-intercept length of the full map) is plotted against the size of the submap, as solid square points coloured to match the submap areas shown in (a).

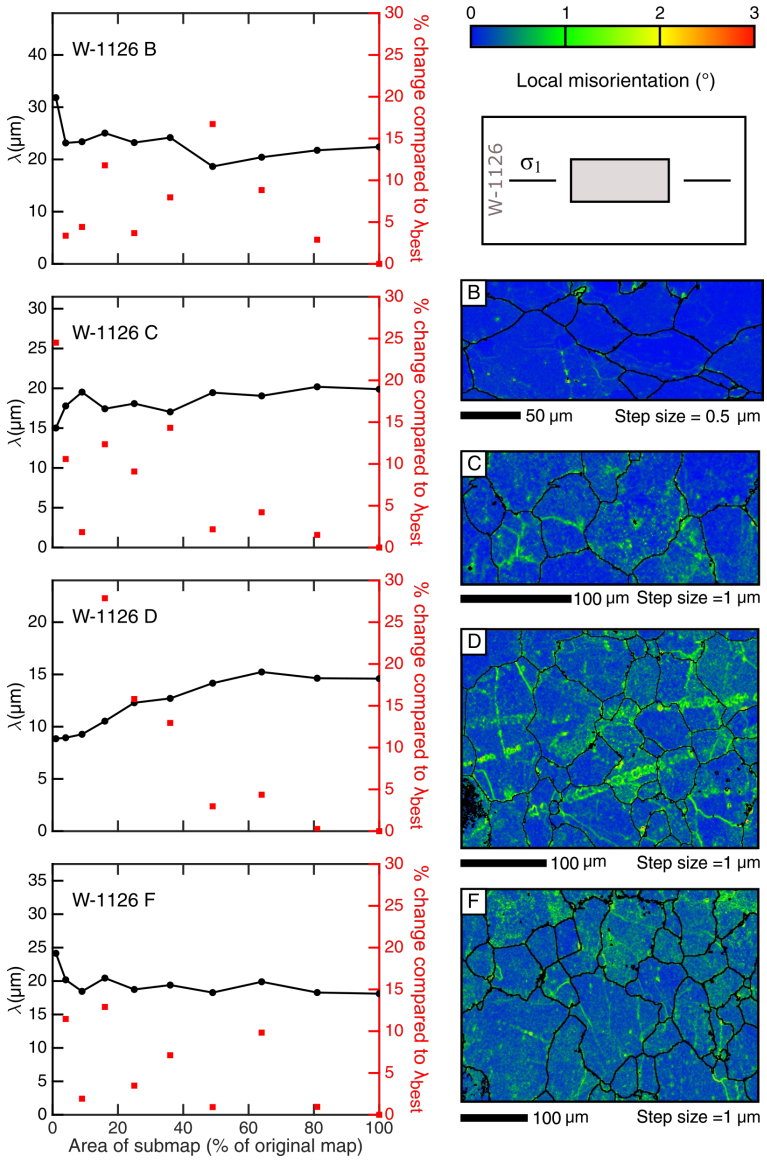

Figure A.4: Area analysis of quartz for multiple maps from sample W-1126 (mechanical data W1116) using a critical misorientation angle of 1°. This analysis is carried out with the same method described in Figure A.3. On the right, mean line-intercept length is plotted as black solid circles against the size of the map as a fraction of the size of the original map. The percentage change with respect to the best estimate for subgrain-size (mean line-intercept length of the full map) is plotted along the left-hand axis. Once the percentage change exceeds 30%, it is no longer plotted. Local misorientation maps for each area are shown to the right.

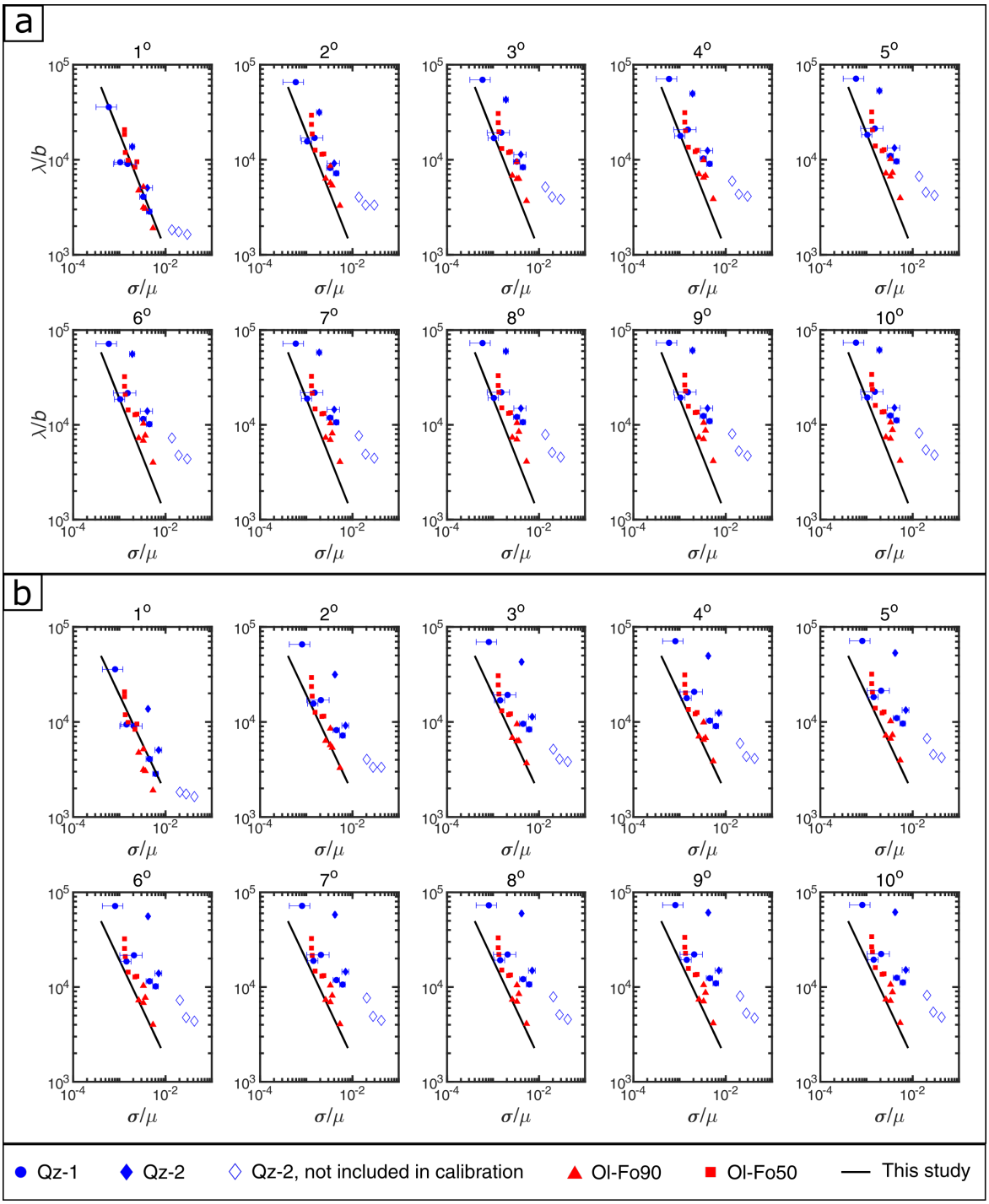

Figure A.5: Relationship between mean line-intercept length and stress for subgrains with critical misorientations of 1°–10°for (a) with the Holyoke and Kronenberg (2010) correction applied to the quartz data and (b) without the correction. Axes are the same as in Figure 2.3, as are the Burgers vector and the shear moduli used for each phase. For each map, the critical misorientation angle used to define a subgrain is labelled above the graph. The 1°-subgrain-size piezometer is plotted on each graph for comparison.

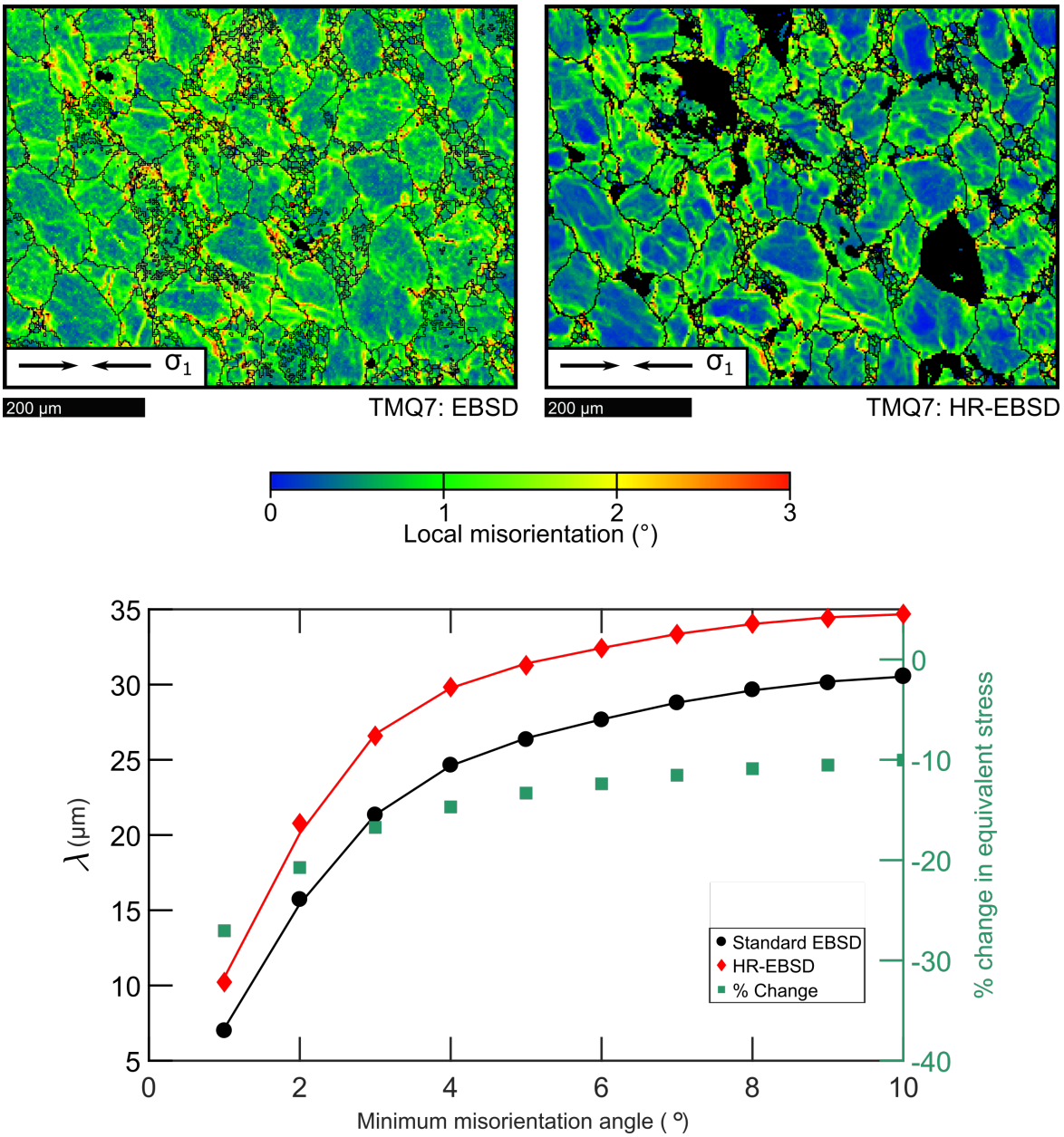

Figure A.6: HR-EBSD comparison for quartz sample TMQ-7. Top, the local misorientation maps are presented for standard EBSD (left) and HR-EBSD (right). Below, the mean line-intercept lengths are compared for a range of minimum misorientation angles for both EBSD and HR-EBSD. The right vertical axis and the green squares track the percent change in equivalent stress as a result of HR-EBSD compared to standard EBSD. It is important to highlight that the mean line-intercept method will extrapolate into the middle of non-indexed regions. As the HR-EBSD analysis was unsuccessful on a number of grains, this extrapolation accounts for a portion of the difference in equivalent stress between the two maps, particularly the difference at large critical angles.

Table A.1: Experimental conditions

Sample	Mineral	Experiment	Type: Molten Salt Assembly (MSA) or Solid Salt Assembly (SSA)	Temperature (°C)	Confining pressure (MPa)	Equivalent strain rate (10^{-5} s^{-1})	Total shear strain[1]	Total axial strain (%)	Equivalent flow stress not corrected as per Holyoke and Kronenberg (2010) (MPa)	Equivalent flow stress corrected as per Holyoke and Kronenberg (2010) (MPa)	1° mean line-intercept length (λ, µm)	Reference
Dataset 1 (Qz-1)												
W-1116 (W-1126)[2]	Qz	Axial compression	Griggs, MSA	1100	1500	0.021–0.023	-	21 (17)	34 ± 16[3]	25 ± 12	18.28[4]	Stipp & Tullis (2003)
W-1096 (W-1066)[2]	Qz	Axial compression	Griggs, MSA	1100	1500	0.20–0.25	-	32 (31)	60 ± 15[3]	44 ± 11	4.8	Stipp & Tullis (2003)
W-1025	Qz	Axial compression	Griggs, MSA	1050	1500	0.18–0.24	-	32	87 ± 17	64 ± 12	4.61	Stipp & Tullis (2003)
W-1051	Qz	Axial compression	Griggs, MSA	1000	1500	1.9–2.9	-	41	189 ± 30[3]	138 ± 22	2.08[4]	Stipp & Tullis (2003)
W-1119	Qz	Axial compression	Griggs, MSA	1100	1500	18–25	-	36	257 ± 35[3]	188 ± 26	1.45[4]	Stipp & Tullis (2003)
Dataset 2 (Qz-2)												
TMQ-7	Qz	Axial compression	Griggs, SSA	800	1560	0.16	-	15.6	175	80 ± 30	7	Holyoke & Kronenberg (2013)

Continued on next page

Continuation of Table A.1

W-1134	Qz	General, shear	Griggs, SSA	1000	1500	0.16	0.5	-	297	169	2.58	This study, Figure A.1
W-1132	Qz	General, shear	Griggs, SSA	900	1500	1.15	0.7	-	856	577	0.93	This study, Figure A.1
W-1105	Qz	General, shear	Griggs, SSA	800	1500	1.15	6.1	-	1171	807	0.89	Holyoke & Tullis (2006)
W-1093	Qz	General, shear	Griggs, SSA	800	1500	1.15	2.1	-	1767	1242	0.84	Holyoke & Tullis (2006)

Dataset 3 (Ol)

Sample	Mineral	Experiment	Type: Molten Salt Assembly (MSA) or Solid Salt Assembly (SSA)	Temperature (°C)	Confining pressure (MPa)	Equivalent strain rate (10^{-5} s^{-1})	Total shear strain[1]	Total axial strain (%)	Equivalent flow stress (MPa)	1° mean line-intercept length (λ, µm)	Reference
PI-1519	Fo_{90}	Axial, compression	Paterson	1250 ± 2	300 ± 1	9.719	-	< 20	204[5] ± 1	2.26	Hansen et al. (2011)
PI-1523	Fo_{90}	Axial, compression	Paterson	1250 ± 2	300 ± 1	8.912	-	< 20	257[5] ± 1	1.49	Hansen et al. (2011)
PI-1488	Fo_{90}	Axial, compression	Paterson	1150 ± 2	300 ± 1	0.905	-	5	258[5] ± 1	2.46	Hansen et al. (2011)
PI-1477	Fo_{90}	Axial, compression	Paterson	1250 ± 2	300 ± 1	14.40	-	< 20	283[5] ± 1	1.45	Hansen et al. (2011)
PT-0966	Fo_{50}	Torsion	Paterson	1200 ± 2	300	147.8	5.0[6]	-	81	9.85	Tasaka et al. (2016)

Continued on next page

Continuation of Table A.1											
PT-0633	Fo_{50}	Torsion	Paterson	1200 ± 2	250–300	3.6	8.7[8]	-	81[7]	8.77	Hansen et al. (2012)
PT-0541	Fo_{50}	Torsion	Paterson	1200 ± 2	250–300	4.5	7.6[8]	-	84[7]	5.66	Hansen et al. (2012)
PT-0538	Fo_{50}	Torsion	Paterson	1200 ± 2	250–300	11.9	6.8[8]	-	97[7]	4.69	Hansen et al. (2012)
PT-0552	Fo_{50}	Torsion	Paterson	1200 ± 2	250–300	51.1	8.8[8]	-	136[7]	3.98	Hansen et al. (2012)
PT-984	Fo_{50}	Torsion	Paterson	1200	300	47.7	4.2[8]	-	150	4.52	Tasaka et al. (2017)
PT-0264	Fo_{50}	Torsion	Paterson	1200	300	20.2	3.5[8]	-	416	0.91	Pommier et al. (2015)

[1]Rounded to 1 d.p.
[2]For Qz-1, the method of correcting for friction alters the microstructures. Therefore, a pair of experiments were conducted at each set of conditions, with one experiment providing the friction correction and the other providing the sample for microstructural analysis (Stipp & Tullis, 2003). The first sample name is the sample associated with the mechanical data. The second sample name, in brackets, refers to the sample from which the microstructural analysis has come.
[3]Flow stresses were taken as the average over the interval between 10% and the final strain. The error estimates are based on the maximum stress variations in the study range and on the different frictional correction methods used (see Stipp & Tullis, 2003, for a description of the friction correction methods).
[4]Mean of the sum of all line intercepts from four different maps.
[5]Stress is determined from load measurements using the instantaneous cross-sectional area of the sample. The cross-sectional area is calculated on the assumption of constant volume deformation. Corrections were also made to the measured load for the load supported by the iron jacket and nickel capsules. The stress presented is the last stress felt by the sample.
[6]Shear strain from the crease of the jacket of the sample.
[7]Steady state stress, mean of the values measured at the controlling strain rate, see Hansen et al.(2012)
[8]Outer radius shear strain

Appendix B Chapter 3

B.1 Sample preparation

LT-DrySC, a dry olivine sample, was synthesised at Brown University. San Carlos olivine (SC) was ground with an agate pestle and mortar and sieved to 10–32 µm. This dry olivine was made from a 'wet olivine' sample, which had ∼0.5–0.7 wt% deionised water added to the SC powder prior to hot pressing. Powders were sealed in a nickel jacket and then hot pressed for 24–26 hours in a Griggs 'all-salt' apparatus (Griggs et al., 1960) at a confining pressure of 1.3 GPa and temperature of 900°C. To dehydrate the sample, a section was placed in a 1 atm CO/CO_2 furnace at 1000°C at a PO_2 of $\sim 10^{-10}$ atm for 10 hours.

At the University of Minnesota, powders of Bamble enstatite (BE) and SC, with particle sizes $< 10\,\mu m$, were used to form 33, PT-1166, PT-1299 HiFe, and PI-2056. For 33 and PT-1166 powders of SC were combined with 1% orthopyroxene to buffer silica activity. For PT-1299 HiFe, BE was mixed in ethanol with SC powder in a 50:50 ratio. For PI-2056 powders of BE and pure SC were similarly prepared, as well as 70:30 ratios of BE to SC. Powders were tumbled for at least 12 hours in a plastic bottle with plastic-coated iron balls and subsequently dried on a hot plate at 60°C until all the ethanol had evaporated. Powders were placed in a gas-mixing furnace with CO/CO_2 buffering the oxygen fugacity to be at the Ni/NiO buffer, in which temperature ramped up to 1000°C over 10 hours and then kept at temperature for 12 hours before cooling. The powders were cold pressed at ∼100 MPa into a Ni can on top of a layer of NiO present to buffer oxygen fugacity. For sample PI-2056, the cold press consisted of roughly equal layers of the aforementioned different compositional ratios. Samples were vacuum hot-pressed in a gas-medium apparatus at a pressure on the interior of the jacket of $\sim$ 0.1 mbar and at a confining pressure of 300 MPa. Hot presses were carried out under a small load and at a temperature of 1250°C. For PT-1299 HiFe and PI-2056, the hot press was continued until no further compaction could be observed, which took between 0.5 and 1.3 hours. Samples 33 and PT-1166 were part of a series that were hot-pressed for between 3 and 60 hours to get variable starting grain sizes.

B.2 Thin-section preparation

To prepare the samples for EBSD analysis, the deformed experimental column, out to and including the graphite sleeve, was extracted and mounted on a thin section slide using Logitech Epothin resin, with care being taken to impregnate the sample at this stage to stop plucking during subsequent preparation stages. Thick sections were formed by grinding the experimental column down on a Buehler Petrothin, at the University of Oxford, until it was a thickness of 1200–1800 µm with a flat surface. The samples were subsequently remounted on fresh glass slides, rotated 180° around the long axis, and blobs of UV resin were placed around the edges of the slides to help stabilise the samples during final polishing. Samples were then reground on the Petrothin until an exposed flat central section remained, ranging in thickness 200–600 µm, ready for polishing. All surfaces were prepared by polishing with a Planocloth polishing cloth and 0.3 µm alumina and water for between 2 to 4 hours. Samples were subsequently colloidal silica polished for ∼20 minutes using a Struers' Tegramin preparation system at Utrecht University, the Netherlands.

B.3 Phase Maps

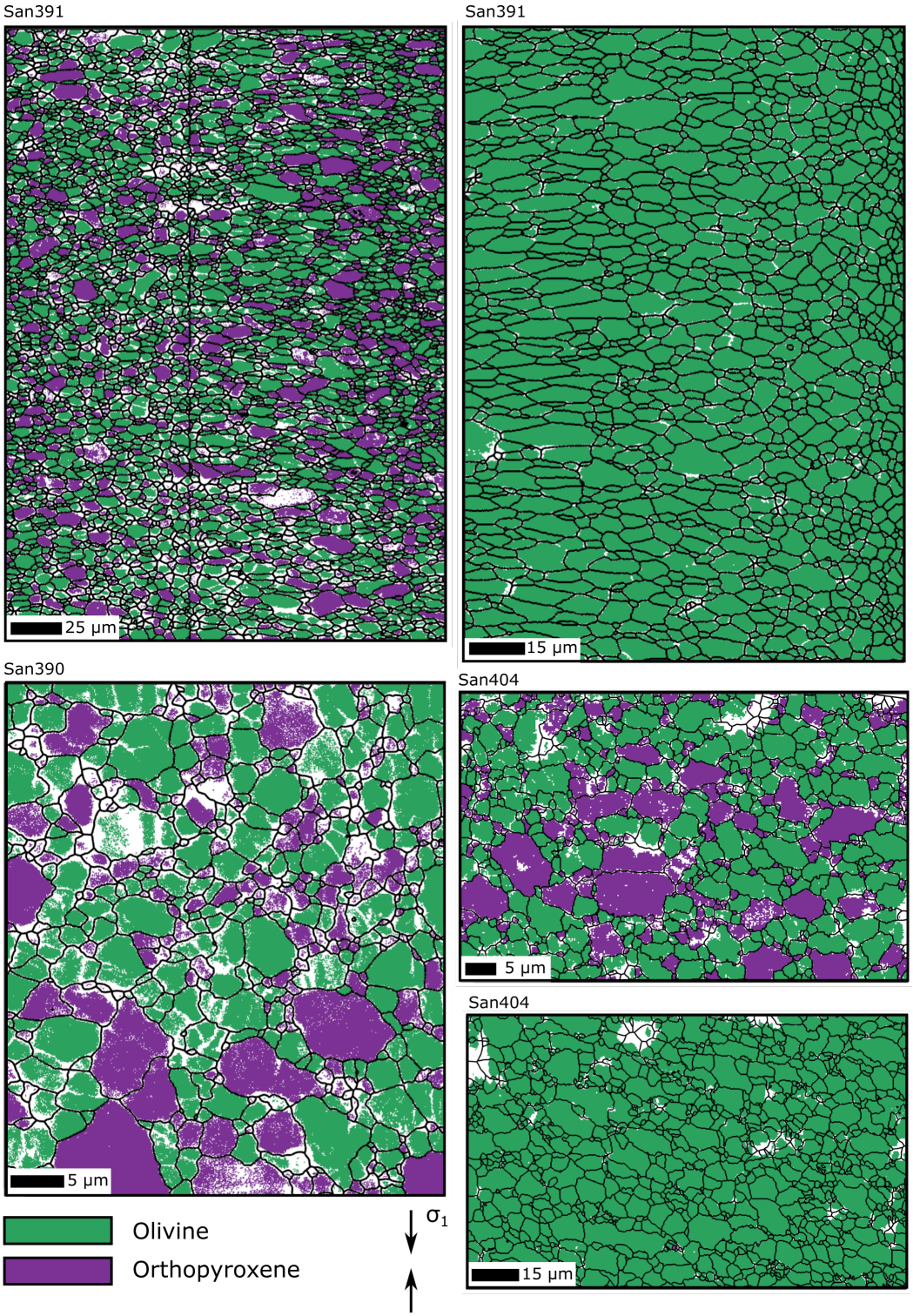

Figure caption on the next page

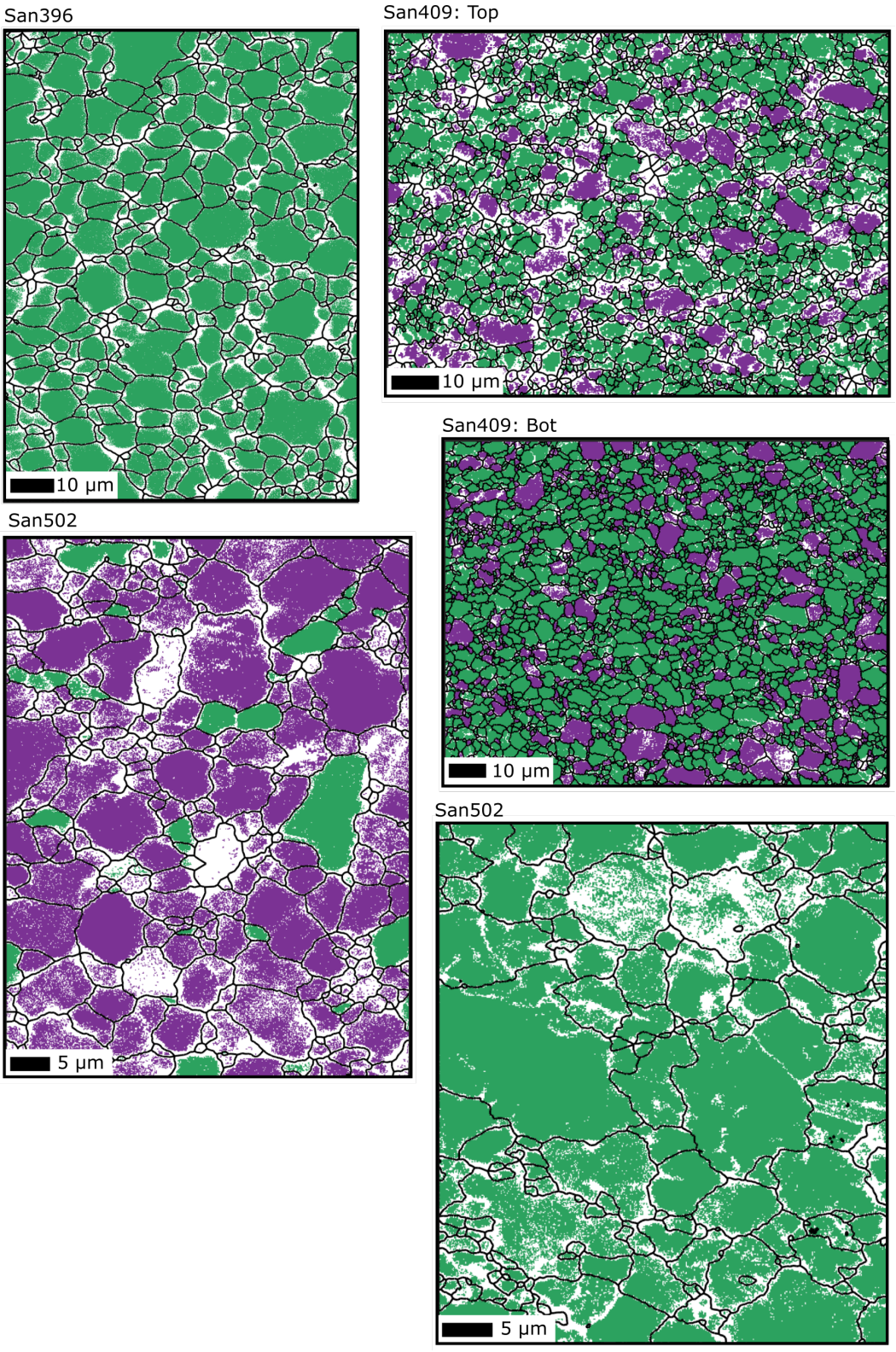

Figure caption on the next page

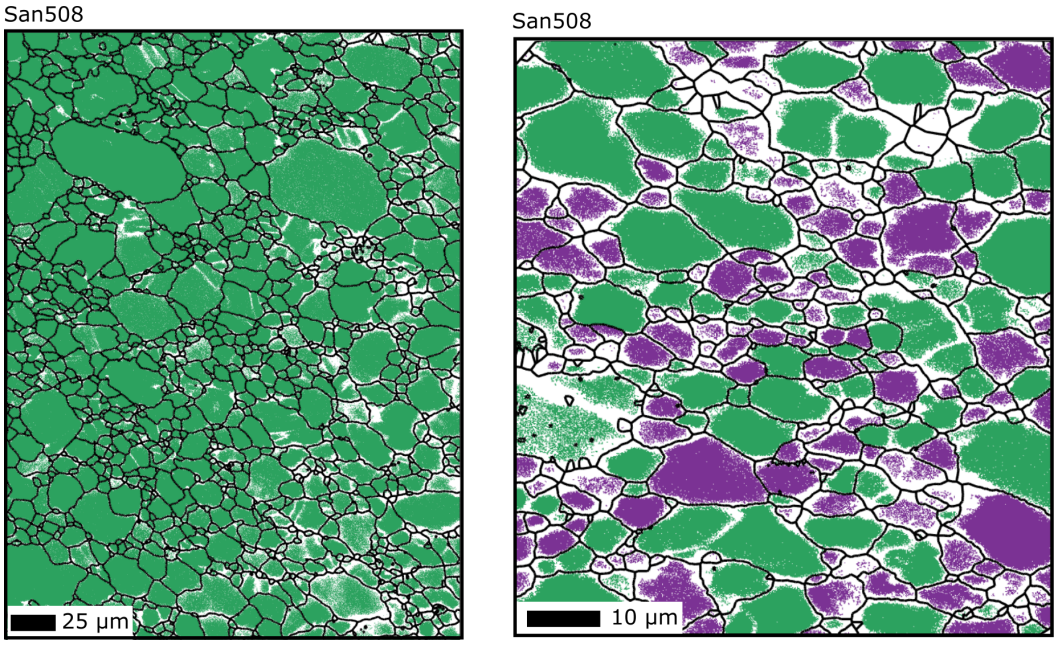

Figure B.1: Full EBSD phase maps. Grain boundaries, defined as having a misorientation angle of ≥ 10°, are drawn in black. EBSD data in the maps have been cleaned as described in Section 3.2.2, non-index regions, seen in white, have been left unfilled.

B.4 Stresses from X-ray diffraction

Table B.1: Final absolute stresses measured from X-ray diffraction

Experiment	Sample	Final stress: X-ray diffraction (MPa)					
		Olivine			Orthopyroxene		
		{112}	{131}	{130}	{421}	{610}	{321}
San390	LC	322	314	341	–	–	–
	HZ	679	776	1326	682	1621	1125
San391	LC	114	124	90	–	–	–
	HZ	348	143	386	384	593	498
San396	LC	170	124	153	–	–	–
	HZ	535	447	646	–	–	–
San404	LC	28	72	74	–	–	–
	HZ	283	200	245	223	320	326
San409	HZ: Top	416	320	514	307	741	320
	HZ: Bot	184	208	450	61	900	446
San502	LC	622	626	650	–	–	–
	Opx	–	–	–	444	932	575
San508	LC	227	222	178	–	–	–
	HZ	251	56	260	92	238	34

Table B.2: Average absolute stress measured from X-ray diffraction. Averages were taken for either the last 10–20% of strain in the sample or after a temperature change.

Experiment	Sample	Average stress: X-ray diffraction (MPa)					
		Olivine			Orthopyroxene		
		{112}	{131}	{130}	{421}	{610}	{321}
San390	LC	400	404	435	–	–	–
	HZ	934	912	1362	1040	1726	1149
San391	LC	236	223	237	–	–	–
	HZ	459	238	506	560	809	600
San396	LC	350	352	380	–	–	–
	HZ	731	585	886	–	–	–
San404	LC	35	44	42	–	–	–
	HZ	243	98	254	240	311	264
San409	HZ: Top	344	189	406	324	620	293
	HZ: Bot	277	166	389	296	696	397
San502	LC	590	571	654	–	–	–
	Opx	–	–	–	613	1027	646
San508	LC	259	236	277	–	–	–
	HZ	326	70	251	194	275	171

B.5 Pressure curves

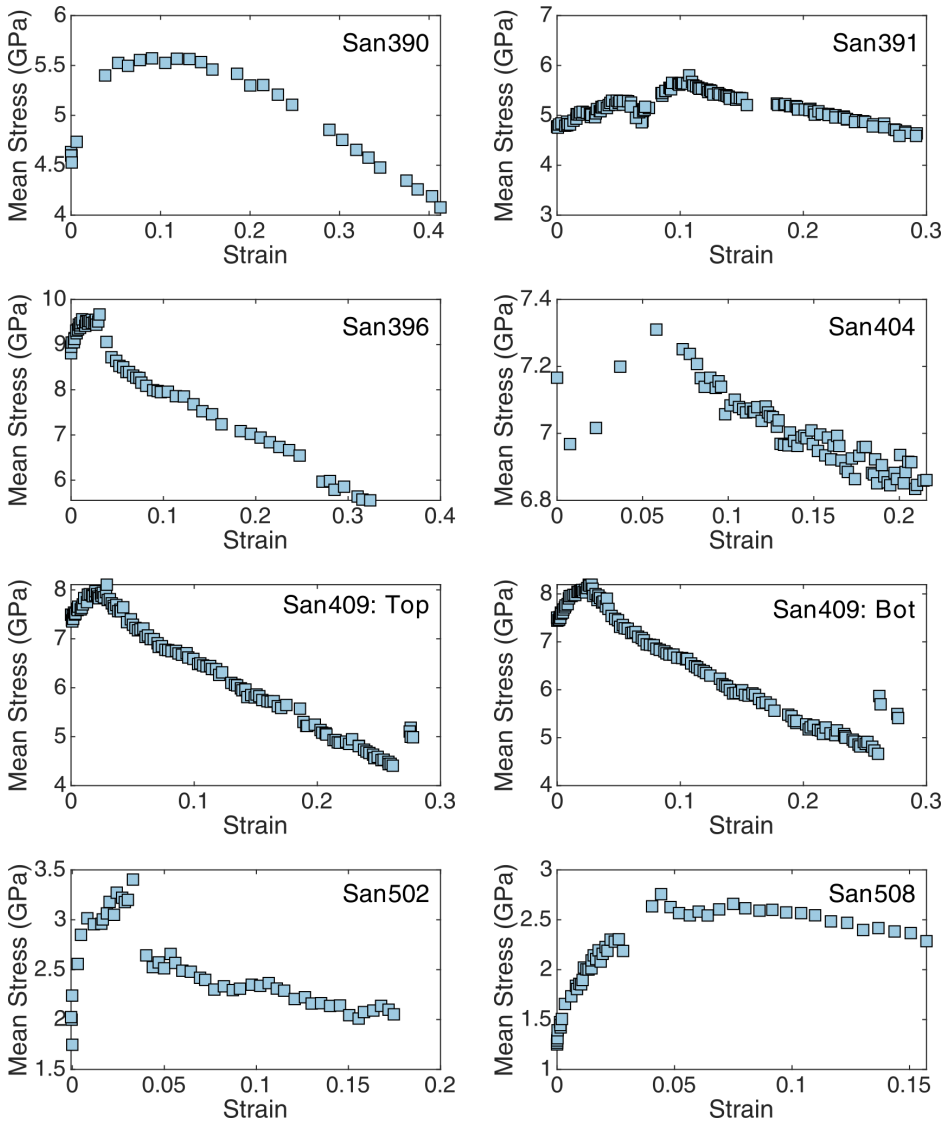

Figure B.2: Mean stress, that is pressure, measured from X-ray diffraction on the {130} peak within the dunite load cell except for experiment San409, where pressure is calculated from the {130} peak in the olivine in both the top and bottom mixtures.

B.6 Predicted subgrain-boundary spacing

Table B.3: Mean line-intercept length predicted using the 2°-subgrain-size piezometer, final stress measured from X-ray diffraction, and final pressure measured through X-ray diffraction on {130} *in olivine. A cross in the 'SGs' column indicates that the grain-size was large enough for subgrains to form.*

Experiment	Sample	Phase	Peak	End stress (MPa)	Pressure (GPa)	Predicted λ (µm)	λ_{gs} (µm)	SGs
San390	HZ	Ol	{112}	679	4.1	1.2	1.9	×
			{131}	776		1.0		×
			{130}	1326		0.6		×
		Opx	{421}	682	4.1	1.3	1.7	×
			{610}	1621		0.5		×
			{321}	1125		0.7		×
San391	LC	Ol	{112}	114	4.6	8.6	3.2	
			{131}	124		7.8		
			{130}	90		11.1		
	HZ	Ol	{112}	348	4.5	2.5	3.0	×
			{131}	143		6.7		
			{130}	386		2.2		×
		Opx	{421}	384	4.5	2.4	3.2	×
			{610}	593		1.5		×
			{321}	498		1.8		×
San396	LC	Ol	{112}	170	5.6	5.6	3.7	
			{131}	124		8.0		
			{130}	153		6.3		
	HZ	Ol	{112}	535	5.5	1.6	2.4	×
			{131}	447		1.9		×
			{130}	646		1.3		×

Continued on next page

Continuation of Table B.3

San404	LC	Ol	{112}	28	6.9	41.7	3.1	
			{131}	72		14.8		
			{130}	74		14.3		
	HZ	Ol	{112}	283	6.9	3.3	2.1	
			{131}	200		4.8		
			{130}	245		3.8		
		Opx	{421}	223	6.9	4.6	2.1	
			{610}	320		3.1		
			{321}	326		3.1		
San409	HZ: Top	Ol	{112}	416	5.0	2.1	1.9	
			{131}	320		2.8		
			{130}	514		1.6		×
		Opx	{421}	307	5.0	3.2	2.4	
			{610}	741		1.2		×
			{321}	320		3.0		
	HZ: Bot	Ol	{112}	184	5.4	5.1	1.9	
			{131}	208		4.5		
			{130}	450		1.9		
		Opx	{421}	61	5.4	18.8	1.9	
			{610}	900		1.0		×
			{321}	446		2.1		

Continued on next page

Continuation of Table B.3								
San502	LC	Ol	{112}	622	2.1	1.3	3.4	×
			{131}	626		1.3		×
			{130}	650		1.2		×
	HZ	Opx	{421}	444	2.1	2.0	3.2	×
			{610}	932		0.9		×
			{321}	575		1.5		×
San508	LC	Ol	{112}	227	2.3	3.9	7.7	×
			{131}	222		4.0		×
			{130}	178		5.0		×
	HZ	Ol	{112}	251	2.3	3.4	4.1	×
			{131}	56		18		
			{130}	260		3.3		×
		Opx	{421}	92	2.3	11.4	3.2	
			{610}	238		4.0		
			{321}	34		33.9		

Appendix C Chapter 4

C.1 Load-relaxation tests

When the length of a specimen is held constant during a load-relaxation test, the stored elastic strain energy in the specimen is dissipated through plastic deformation of the specimen, and as such, the stress supported by the specimen decays with time. In actuality, it is difficult to keep the sample length constant as holding the actuator actually holds the combination of the machine and sample length constant, and elastic strain in the machine must be dissipated as additional permanent deformation in the sample (Rutter et al., 1978). Therefore, the total strain of a sample is the sum of the elastic strain of the machine (ε_{M}) and the elastic (ε_{E}) and plastic strain (ε_{P}) of the sample. By plotting $\log(\varepsilon_{\mathrm{P}})$ against $\log(\sigma)$ it is possible to get an idea of the mechanical behaviour of the sample—specifically the stress exponent (n). Taking the differential of the total strain with time and the principle that the total strain remains constant, the resulting equation is:

$$\frac{\varepsilon_p}{dt} = -\left(\frac{1}{k} + \frac{1}{M}\right)\frac{d\sigma}{dt} \tag{C.1}$$

where k is the Young's modulus of the machine and M is the Young's modulus of the sample (Karato, 2012, page 111). For Px93, the Young's modulus for the sample was calculated as 191 GPa using the shear and bulk moduli of orthopyroxene (Chai et al., 1997). For Px20, the Young's modulus of olivine was used, similarly calculated from the shear and bulk moduli to be 195 GPa (Abramson et al., 1997). The stiffness of the machine was calculated by $l_{t0}/\left(a_{t0} \times S\right)$ where l_{t0} is the length of the sample at the initiation of the load drop, a_{t0} is the area of the sample at the initiation of the load drop and S is the compliance of the apparatus. The more compliant the machine, the greater the amount of permanent strain that is required for the specimen to produce a given amount of stress relaxation (Rutter et al., 1978). As such it has been suggested that $k >> M$ when conducting stress-relaxation experiments (Karato, 2012, page 111). This condition does not hold for our sample set, with our experiments giving k values of 7–12 GPa. However, the fact that we get clear linear relationships between ε_{P} and σ in log space indicates that the signal of the load-relaxation tests is not masked by the compliance of the apparatus.

C.2 Schematic illustration of sample canting

As can be seen in Figure C.1, all samples except PI-2067 (Px93) experienced a degree of canting during the experiment. Such off-axis shearing likely results in the axially applied force not being evenly distributed across the surface area of the sample. In the context of this study we make the simplifying assumption that the total force is borne by the volume of the material within the areal overlap of the offset upper and lower pistons (Figure C.1). Assuming constant volume of a sample throughout an experiment, and that the sample is a perfect cylinder, the areal overlap of the pistons during canting can be calculated as

$$A = 2r^2 \cos^{-1}\left(\frac{di}{2r}\right) - di\sqrt{r^2 - \frac{di^2}{4}}, \tag{C.2}$$

where di is the distance between the centre of the top and bottom circles, r is the radius, and the cosine is in radians (Assencio, 2021). It is further assumed that di starts at zero and increases linearly with time throughout the experiment.

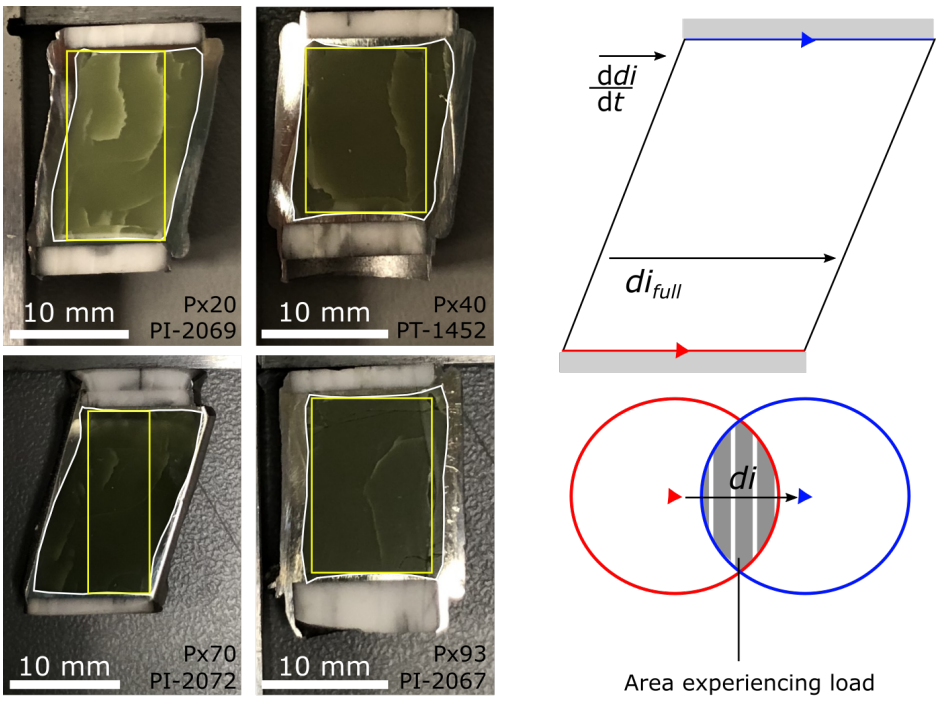

Figure C.1: Cross-sections of the samples after deformation cut parallel to the loading direction. The samples are outlined in white while the area between the overlapping regions of the pistons is outlined in yellow. (right) Schematic illustration of the area of the overlapping pistons as calculated in Eq. C.2.

Appendix D Chapter 5

Figure D.1: Full key for Figure 5.1

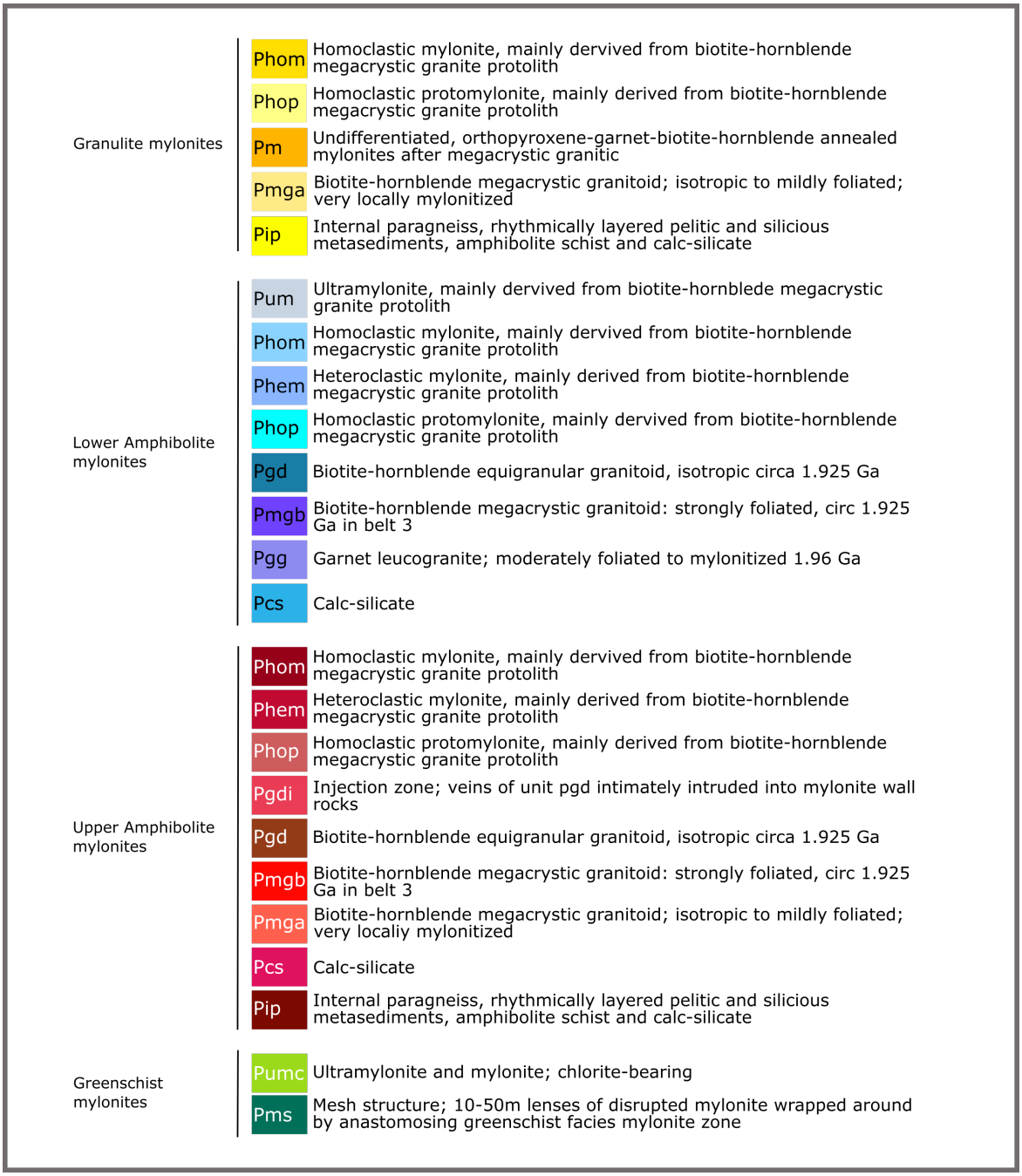

D.1 Individual EBSD-cleaning procedures

Noise reduction was performed on EBSD data in MATLAB® using the MTEX toolbox. The nature of the noise reduction was tailored to each map due to variations in step size, indexing rate, phases present, and noise threshold.

The noise-reduction procedure used in this thesis included the removal of grains (or 'shards') that were made up of fewer than four pixels on the assumption they were likely to be noise. For all EBSD data, bar those used in the original calibration of the 1°-subgrain-size piezometer, pixels with mean angular deviation values of $> 1°$ were also removed.

To ensure we accurately captured the subgrain size for piezometry, EBSD data for the GSLsz were collected using very fine step sizes (1.0–4.2 µm). Using such small steps compared to the grain-size of the rocks led to some erroneous shards that were greater than three pixels in size. These shards were therefore not removed in MTEX by the traditional cleaning technique. We therefore modified the limiting size of 'shards' as appropriate for each sample, as listed in Table D.1.

The current method for measuring the mean line-intercept length of each sample, the *ProcessEBSD_LinearIntercepts.m* script from Goddard et al. (2020), is sensitive to maps containing large non-indexed regions. The script extrapolates the intercept lengths into such regions, thereby overestimating the subgrain-size. To correct for this, after the above-mentioned noise reduction procedure, all non-indexed grains were removed and all pixels no longer assigned a phase were filled using the nearest neighbour method in MTEX.

In maps where the indexing rate was low, EBSD data on only the phase of interest, quartz, were collected, thereby leaving large areas of the map non-indexed. As these regions are likely to represent other minerals, extrapolation through the nearest-neighbour method would not be appropriate. To ensure that only the subgrain size of the phase of interest was captured, non-indexed phases were assigned an arbitrary mineral phase prior to execution of the *ProcessEBSD_LinearIntercepts.m* script, thereby automatically excluding them from the analysis. This process was applied to GSL-18-RG-20 and GSL-18-C-47, where only quartz data were collected, and in GSL-18-RG-02 and GSL-18-RG-11, where indexing of other phases was low.

The replacement of all non-indexed phases within a map with an arbitrary mineral also applies to areas within grains that would have been more appropriately infilled through the nearest neighbour method. Therefore, prior to the replacement of non-indexed phases with an arbitrary new mineral, non-indexed areas, defined by a 'threshold' number of pixels, were removed and filled through the MTEX nearest-neighbour method. The sample specific noise-reduction procedures are listed in Table D.1.

Table D.1: Noise-reduction procedures

Sample	Indexing rate (%)	Step size (µm)	'Shard' size (pixels)	Replacement of non-indexed phases with an arbitrary mineral	If yes, threshold value (pixels)
Greenschist facies					
GSL-18-DW-11	68	1	15	No	na
GSL-18-DW-13	84	1	3	No	na
Epidote-amphibolite facies					
GSL-18-RG-02	66	1	8	Yes	20
GSL-18-RG-03	81	1	20	No	na
GSL-18-C-31	95.3	3	15	No	na
GSL-18-C-36	97	3	3	Yes	na
Upper-amphibolite facies					
GSL-18-RG-11	75	2	3	No	15
GSL-18-RG-12	78	1.1	5	No	na
GSL-18-RG-13	91.2	2.0	5	No	na
GSL-18-RG-14	90	4.19	15	No	na
GSL-18-RG-20	82	3.0	3	Yes	50
GSL-18-C-26	76	1.5	10	No	Na
GSL-18-C-27	80	3.04	10	No	na
GSL-18-C-28	83	2.97	10	No	na
Granulite facies					
GSL-18-C-47	56	3.0	3	Yes	100

D.2 Ti-in-Biotite thermometry

With increasing metamorphic grade Ti substitutes for octahedrally coordinated divalent or trivalent cations in biotite (e.g., Kwak, 1968; Guidotti et al., 1977). The degree to which Ti substitutes in biotite involves relatively complex interactions between temperature, pressure, biotite crystal chemistry, and the coexisting mineral assemblage (Guidotti et al., 1977). Henry and Guidotti (2002) established that

$$\mathrm{Ln}(Ti) = -2.3353 + 4.343 \times 10^{-9}[T(^{\circ}C)]^3 - 1.6718(X_{\mathrm{Mg}})^3, \tag{D.1}$$

where Ti is in a.p.f.u. and X_{Mg} = (Mg/(Mg+Fe^{2+})) content. This calibration is based on $>$ 450 natural samples from the Acadian Orogeny of Western Maine, a well characterised metamorphic terrane. These samples were deformed at a constant pressure of 0.33 GPa and all contained graphite which, in metapelitic samples, limits them to low and fairly constant oxygen fugacities in addition to low amounts of Fe^{3+} ($\sim$ 12% of the Fe_{total}). The biotites used to calibrate the thermometer also have a wide range of Mg/(Mg+Fe^{2+}). For simplicity, and because of the low amount of Fe^{3+}, biotite was normalised on the base of 22 oxygen atoms.

Henry et al. (2005) further extended the Henry and Guidotti (2002) study with samples from Maine and South-Central Massachusetts, which were Silurian and Devonian metasedimentary rocks, intensely deformed and metamorphosed during the Acaidan orogeny. In total 529 samples were examined and the relationship between temperature and Ti content of biotite constrained to

$$\mathrm{Ln}(Ti) = -2.3594 + 4.6482 \times 10^{-9}[T(^{\circ}C)]^3 - 1.7283(X_{\mathrm{Mg}})^3. \tag{D.2}$$

Again these data come from graphitic, peraluminous, and Ti-saturated metapelitic rocks. This data from Massachusetts extends the temperature range of the geothermometer to 680–800°C as well as extending it to higher X_{Mg}, and to pressures up to 0.6 GPa. Errors on the geothermometer are temperature dependent: ± 24°C for 480–600°C, ±23°C for 600–700 °C and ± 12°C for 700–800°C .

D.3 Ti-in-quartz thermometry: Wark and Watson (2006)

Wark and Watson (2006), fit a linear regression to a T^{-1} against $\log(X_{\mathrm{Ti}})$ plot of experimental data where X_{Ti} is the concentration of Ti (ppm by weight). From this regression temperature (in °C) can be expressed as:

$$T(^{\circ}C) = \frac{-3765}{\log\left(X_{\mathrm{Ti}}^{\mathrm{Qz}} - 5.69\right)} - 273, \tag{D.3}$$

where $X_{\mathrm{Ti}}^{\mathrm{Qz}}$ is the concentration of Ti (ppm by weight) in quartz. Based purely on calculated uncertainties on the slope and intercept the thermometer has an error (2σ) of 5°C. Including the uncertainties for EMPA analysis (2σ) of quartz, using conditions similar to those within this analysis (100 nA, 120s counts on peaks and backgrounds), leads to ± 12°C and ± 40°C errors for T > 750°C and 600°C, respectively.

D.4 Ti-in-quartz thermometry: Thomas et al. (2010)

In the Thomas et al. (2010) calibration, the mole fraction of TiO_2 in quartz ($X_{\mathrm{TiO_2}}^{Qz}$) is used, which is calculated as:

$$X_{\mathrm{TiO_2}}^{Qz} = \frac{\frac{Ti(ppm)}{1E4\times 0.599\times 79.87}}{\frac{Ti(ppm)}{1E4\times 0.599\times 79.87} + \left[\left(100 - \frac{Ti(ppm)}{1E4\times 0.599\times 79.87}\right)\times \frac{1}{60.09}\right]}. \tag{D.4}$$

With $X_{\mathrm{TiO_2}}^{Qz}$ and the pressure (P, kilobars),temperature (T, K) can be calculated by:

$$T(K) = \frac{-60952 - 1741\cdot P}{R\left(\ln\left(X_{\mathrm{TiO_2}}^{Qz}\right) - \ln\left(a_{TiO_2}\right)\right) - 1.520}. \tag{D.5}$$

D.5 Pressure estimates from plagioclase-amphibole thermobarometry

Sample	Pressure (Kbar)	Error (Kbar)
Epidote-amphibolite facies		
GSL-18-C-36	AS: 4.3	0.8
	BB: 6.4	**2.2**
GSL-18-RG-02	AS: 5.0	0.8
	BB: 6.0	**2.1**
Upper-amphibolite facies		
GSL-18-RG-11	**AS: 4.2**	**0.9**
	BB: 2.6	3.0
GSL-18-RG-27	**AS: 4.9**	**1.1**
	BB: 8.1	3.0
GSL-18-C-28	**AS: 5.4**	**1.0**
	BB: 7.9	2.4

Table D.2: AS and BB stand for pressures measured using the Anderson and Smith (1995) and Bhadra and Bhattacharya (2007) barometers, respectively. For each sample, the pressures used in the Holland and Bundy's (1994) thermometer are in bold, depending on the presence or absence of melt (see Section 5.3.4 for explanation). Errors are calculated using the combined error of the thermometer and the standard deviation of multiple measurements by taking the square root of the sum of the two squared errors (Powell, 1978, page 284)

D.6 Local misorientation maps

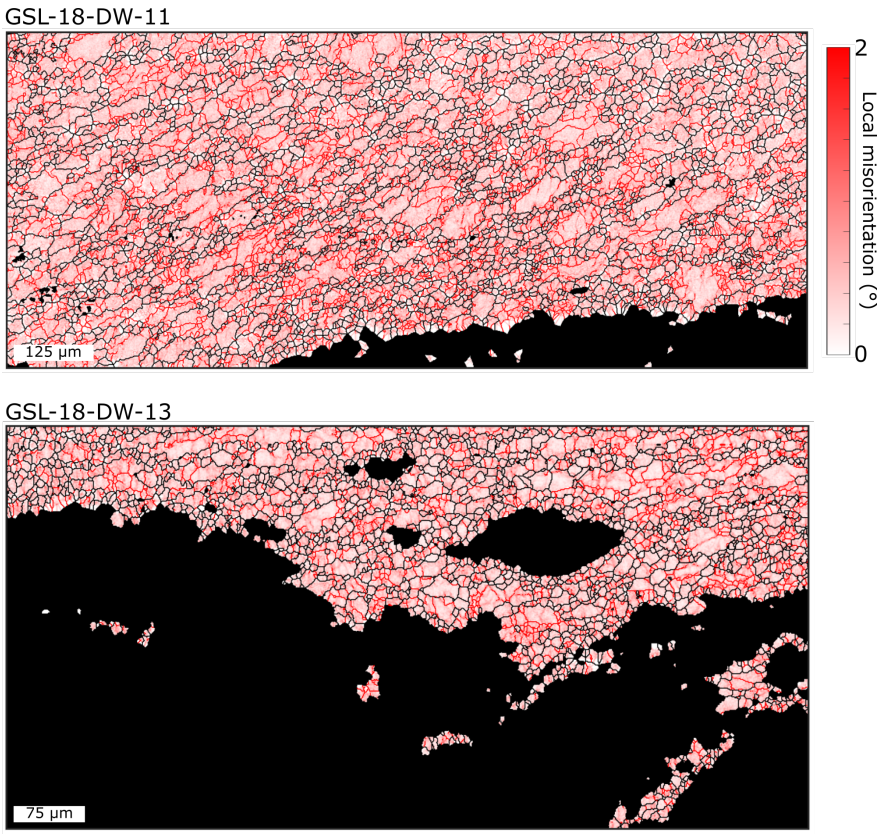

Figure D.2: Local misorientation maps of quartz derived from EBSD data on samples from the upper-greenschist facies. Grain boundaries, defined as having misorientation angles $\geq 10^{\circ}$are in black.

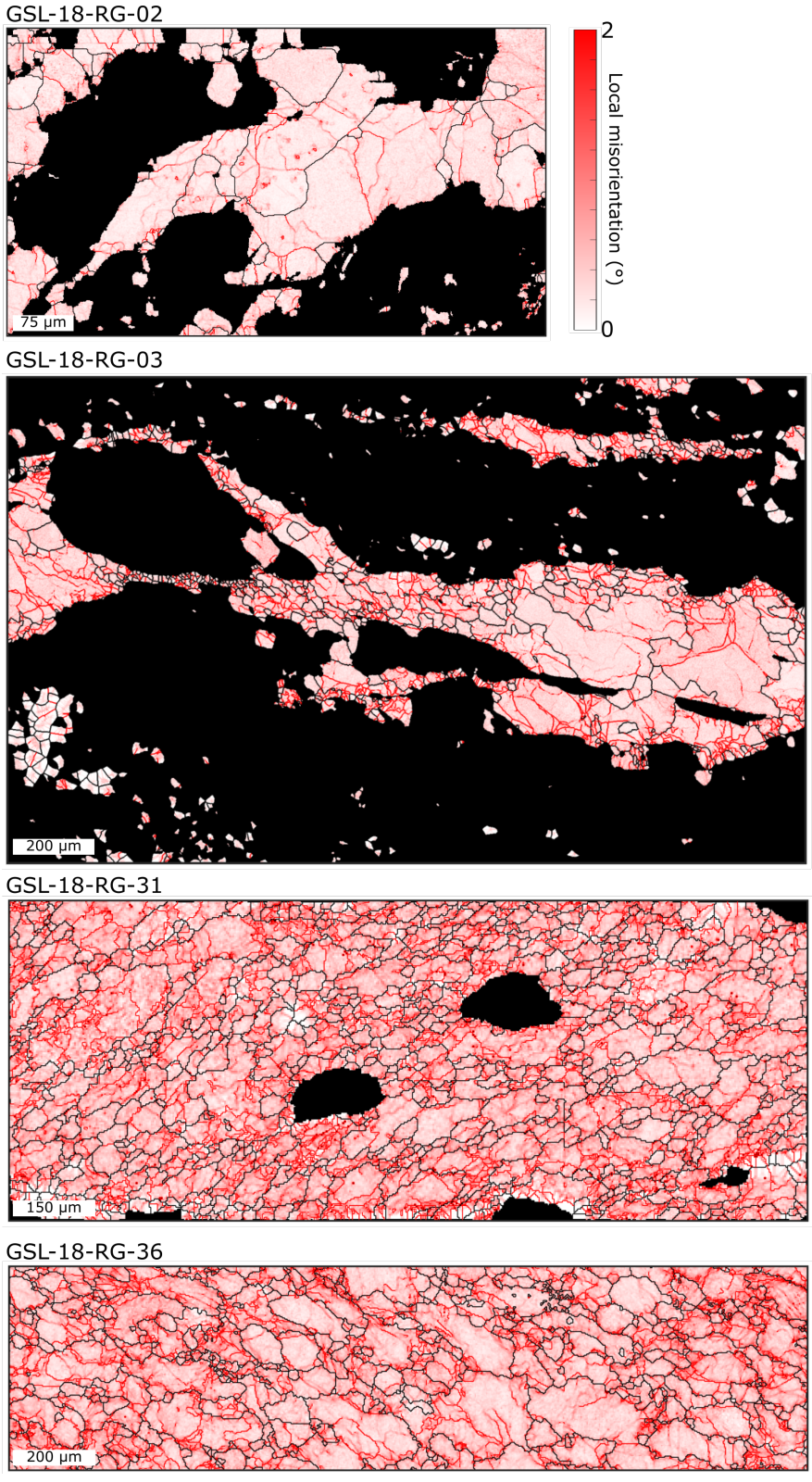

Figure D.3: Local misorientation maps of quartz derived from EBSD data on samples from the epidote-amphibolite facies. Grain boundaries, defined as having misorientation angles ≥ 10°are in black.

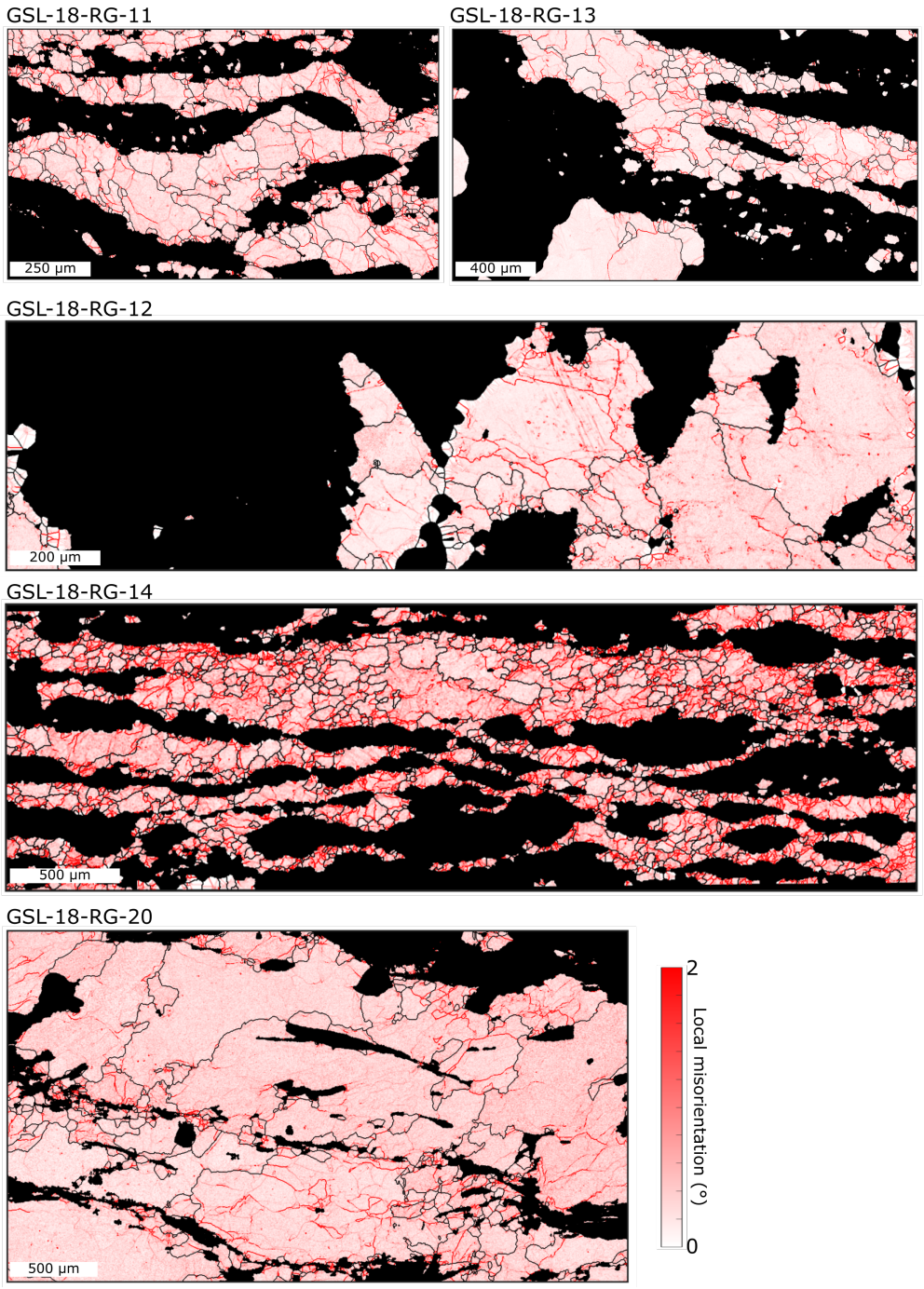

Figure caption on the next page

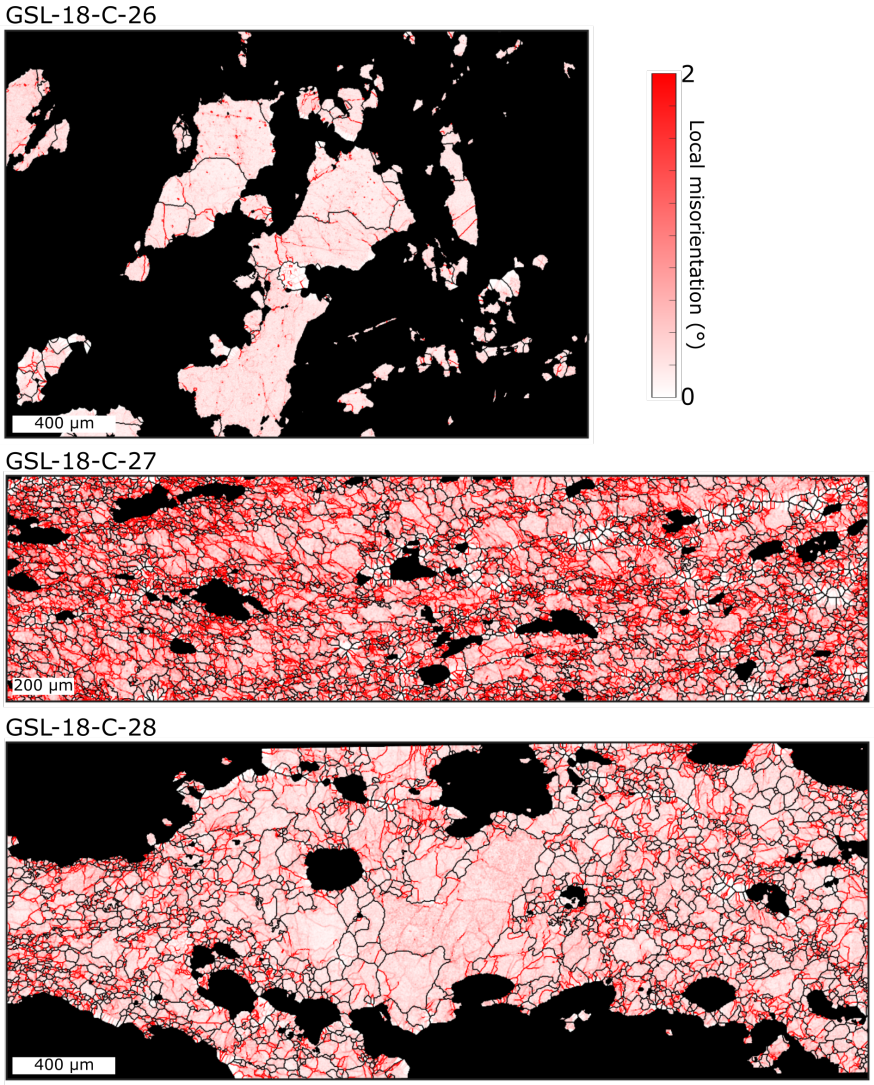

Figure D.4: Local misorientation maps of quartz derived from EBSD data on samples from the upper-amphibolite facies. Grain boundaries, defined as having misorientation angles $\geq 10^{\circ}$ are in black.

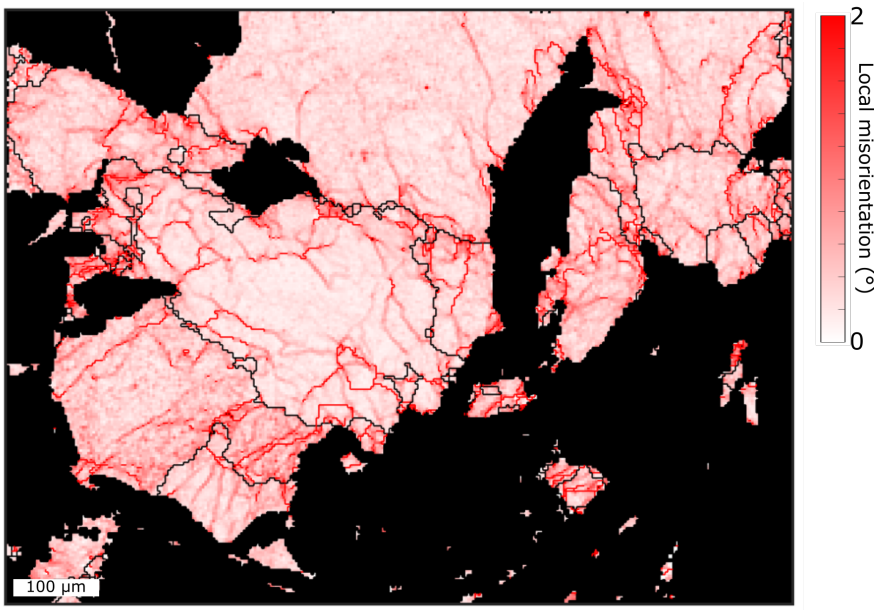

Figure D.5: Local misorientation maps of quartz derived from EBSD data on samples from the granulite facies. Grain boundaries, defined as having misorientation angles $\geq 10°$are in black.

References

Abramson, E. H., Brown, J. M., Slutsky, L. J., & Zaug, J. (1997, June). The elastic constants of san carlos olivine to 17 GPa. *J. Geophys. Res.*, *102*(B6), 12253–12263.

Ambrose, T. K., Wallis, D., Hansen, L. N., Waters, D. J., & Searle, M. P. (2018, June). Controls on the rheological properties of peridotite at a palaeosubduction interface: A transect across the base of the Oman–UAE ophiolite. *Earth Planet. Sci. Lett.*, *491*, 193–206.

Anderson, J. L., & Smith, D. R. (1995). The effects of temperature and fo on the al-in-hornblende barometer. *Am. Mineral.*, *80*(5-6), 549–559.

Angel, R. J., & Hugh-Jones, D. A. (1994, October). Equations of state and thermodynamic properties of enstatite pyroxenes. *J. Geophys. Res.*, *99*(B10), 19777–19783.

Ashley, K. T., Carlson, W. D., Law, R. D., & Tracy, R. J. (2014, October). Ti resetting in quartz during dynamic recrystallization: Mechanisms and significance. *Am. Mineral.*, *99*(10), 2025–2030.

Assencio, D. (2021). *The intersection area of two circles - diego assencio.* `https://diego.assencio.com/?index=8d6ca3d82151bad815f78addf9b5c1c6`.

Austin, N., & Evans, B. (2007, April). Paleowattmeters: A scaling relation for dynamically recrystallized grain size. *Geology*, *35*(4), 343–346.

Austin, N., Evans, B., Herwegh, M., & Ebert, A. (2008, September). Strain localization in the morcles nappe (helvetic alps, switzerland). *Swiss J. Geosci.*, *101*(2), 341–360.

Bachmann, F., Hielscher, R., & Schaeben, H. (2010). Texture analysis with MTEX- free and open source software toolbox. In *Solid state phenomena* (Vol. 160, pp. 63–68). Trans Tech Publ.

Bai, Q., & Kohlstedt, D. L. (1992, May). High-temperature creep of olivine single crystals, 2. dislocation structures. *Tectonophysics*, *206*(1), 1–29.

Barbot, S., Lapusta, N., & Avouac, J.-P. (2012, May). Under the hood of the earthquake machine: toward predictive modeling of the seismic cycle. *Science*, *336*(6082), 707–710.

Barnhoorn, A., Bystricky, M., Kunze, K., Burlini, L., & Burg, J.-P. (2005, December). Strain localisation in bimineralic rocks: Experimental deformation of synthetic calcite–anhydrite aggregates. *Earth Planet. Sci. Lett.*, *240*(3), 748–763.

Behr, W. M., & Platt, J. P. (2011, March). A naturally constrained stress profile through the middle crust in an extensional terrane. *Earth Planet. Sci. Lett.*, *303*(3), 181–192.

Behr, W. M., & Platt, J. P. (2014, November). Brittle faults are weak, yet the ductile middle crust is strong: Implications for lithospheric mechanics. *Geophys. Res. Lett.*, *41*(22), 2014GL061349.

Bestmann, M., & Pennacchioni, G. (2015, June). Ti distribution in quartz across a heterogeneous shear zone within a granodiorite: The effect of deformation mechanism and strain on ti resetting. *Lithos*, *227*, 37–56.

Bhadra, S., & Bhattacharya, A. (2007). The barometer tremolite+ tschermakite+ 2 albite= 2 pargasite+ 8 quartz: Constraints from experimental data at unit silica activity, with application to garnet-free natural .... *Am. Mineral.*.

Biberger, M., & Blum, W. (1992, March). Subgrain boundary migration during creep of lif: I. recombination of subgrain boundaries. *Philos. Mag. A*, *65*(3), 757–770.

Bloomfield, J. P., & Covey-Crump, S. J. (1993, August). Correlating mechanical data with microstructural observations in deformation experiments on synthetic two-phase aggregates. *J. Struct. Geol.*, *15*(8), 1007–1019.

Boese, C. M., Townend, J., Smith, E., & Stern, T. (2012, February). Microseismicity and stress in the vicinity of the alpine fault, central southern alps, new zealand: SEISMICITY IN THE CENTRAL SOUTHERN ALPS. *J. Geophys. Res.*, *117*(B2).

Boutonnet, E., Leloup, P. H., Sassier, C., Gardien, V., & Ricard, Y. (2013, August). Ductile strain rate measurements document long-term strain localization in the continental crust. *Geology*, *41*(8), 819–822.

Bowey, J. E., Lee, C., Tucker, C., Hofmeister, A. M., Ade, P. A. R., & Barlow, M. J. (2001, August). Temperature effects on the 15–85 μm spectra of olivines and pyroxenes. *Mon. Not. R. Astron. Soc.*, *325*(2), 886–896.

Britton, T. B., & Wilkinson, A. J. (2011, July). Measurement of residual elastic strain and lattice rotations with high resolution electron backscatter diffraction. *Ultramicroscopy*, *111*(8), 1395–1404.

Britton, T. B., & Wilkinson, A. J. (2012, September). Stress fields and geometrically necessary dislocation density distributions near the head of a blocked slip band. *Acta Mater.*, *60*(16), 5773–5782.

Bruhn, D. F., Olgaard, D. L., & Dell'Angelo, L. N. (1999). Evidence for enhanced deforma-

tion in two-phase rocks: Experiments on the rheology of calcite-anhydrite aggregates. *J. Geophys. Res. [Solid Earth]*, *104*(B1), 707–724.

Bürgmann, R., & Dresen, G. (2008, April). Rheology of the lower crust and upper mantle: Evidence from rock mechanics, geodesy, and field observations. *Annual Review of Earth and Planetary*.

Byerlee, J. (1978). Friction of rocks. In J. D. Byerlee & M. Wyss (Eds.), *Rock friction and earthquake prediction* (pp. 615–626). Basel: Birkhäuser Basel.

Bystricky, M., Heidelbach, F., & Mackwell, S. (2006, December). Large-strain deformation and strain partitioning in polyphase rocks: Dislocation creep of olivine–magnesiowüstite aggregates. *Tectonophysics*, *427*(1), 115–132.

Bystricky, M., Lawlis, J., Mackwell, S., Heidelbach, F., & Raterron, P. (2016). *High-temperature deformation of enstatite aggregates* (Vol. 121) (No. 9).

Campbell, L. R., & Menegon, L. (2019, October). Transient high strain rate during localized viscous creep in the dry lower continental crust (lofoten, norway). *J. Geophys. Res. [Solid Earth]*, *124*(10), 10240–10260.

Carter, N. L., Hansen, F. D., & Senseny, P. E. (1982, November). Stress magnitudes in natural rock salt. *J. Geophys. Res. [Solid Earth]*, *87*(B11), 9289–9300.

Chacko, T., De, S. K., Creaser, R. A., & Muehlenbachs, K. (2000). Tectonic setting of the taltson magmatic zone at 1.9 2.0 ga: a granitoid-based perspective. *Can. J. Earth Sci.*, *37*(11), 1597–1609.

Chai, M., Brown, J. M., & Slutsky, L. J. (1997). The elastic constants of an aluminous orthopyroxene to 12.5 GPa. *J. Geophys. Res. [Solid Earth]*, *102*(B7), 14779–14785.

Chakraborty, S. (2008, April). Diffusion in solid silicates: A tool to track timescales of processes comes of age.

Chapman, D. S. (1986, January). Thermal gradients in the continental crust. *Geological Society, London, Special Publications*, *24*(1), 63–70.

Chen, I.-W. (1982, August). Diffusional creep of two-phase materials. *Acta Metall.*, *30*(8), 1655–1664.

Cho, K., & Gurland, J. (1988, August). The law of mixtures applied to the plastic deformation of two- phase alloys of coarse microstructures. *Metall. Trans. A*, *19*(8), 2027–2040.

Chopra, P. N., & Paterson, M. S. (1984). The role of water in the deformation of dunite. *J.*

Geophys. Res. [Solid Earth], *89*(B9), 7861–7876.

Clark, S. P. (1966). *Handbook of physical constants*. Geological Society of America.

Copley, A. (2018, January). The strength of earthquake-generating faults. *J. Geol. Soc. London*, *175*(1), 1–12.

Covey-Crump, S. J., Schofield, P. F., Stretton, I. C., Daymond, M. R., Knight, K. S., & Tant, J. (2013, February). Monitoring in situ stress/strain behaviour during plastic yielding in polymineralic rocks using neutron diffraction. *J. Struct. Geol.*, *47*, 36–51.

Cross, A. J., Prior, D. J., Stipp, M., & Kidder, S. (2017, July). The recrystallized grain size piezometer for quartz: An EBSD-based calibration. *Geophys. Res. Lett.*, *44*(13), 6667–6674.

Czertowicz, T. A., Takeshita, T., Arai, S., Yamamoto, T., Ando, J.-I., Shigematsu, N., & Fujimoto, K.-I. (2019, March). The architecture of long-lived fault zones: insights from microstructure and quartz lattice-preferred orientations in mylonites of the median tectonic line, SW japan. *Progress in Earth and Planetary Science*, *6*(1), 25.

De Bresser J.H.P, Peach C. J, Reijs J.P.J, Spiers C.J. (1998). On dynamic recrystallization during solid state flow: Effects of stress and temperature. *Geophysical Research Letters*, *25*(18), 3457–3460.

De Bresser, J. H. P. (1996, October). Steady state dislocation densities in experimentally deformed calcite materials: Single crystals versus polycrystals. *J. Geophys. Res.*, *101*(B10), 22189–22201.

De Bresser, J. H. P., Evans, B., & others. (2002). On estimating the strength of calcite rocks under natural conditions. *Society, London, Special ...*.

Deer, W., Howie, R. A., & Zussman, J. (1992). *An introduction to the rock-forming minerals*. Longman.

Derby, B., & Ashby, M. F. (1987, June). On dynamic recrystallisation. *Scr. Metall.*, *21*(6), 879–884.

Dimanov, A., & Dresen, G. (2005). Rheology of synthetic anorthite-diopside aggregates: Implications for ductile shear zones. *J. Geophys. Res. [Solid Earth]*, *110*(B7).

Dixon, N. A., & Durham, W. B. (2018). Measurement of activation volume for creep of dry olivine at upper-mantle conditions. *J. Geophys. Res. [Solid Earth]*, *123*(10), 8459–8473.

Donovan, J. J., Lowers, H. A., & Rusk, B. G. (2011, February). Improved electron probe

microanalysis of trace elements in quartz. *Am. Mineral.*, *96*(2-3), 274–282.

Dresen, G., Evans, B., & Olgaard, D. L. (1998, April). Effect of quartz inclusions on plastic flow in marble. *Geophys. Res. Lett.*, *25*(8), 1245–1248.

Durham, W. B., Goetze, C., & Blake, B. (1977, December). Plastic flow of oriented single crystals of olivine: 2. observations and interpretations of the dislocation structures. *J. Geophys. Res.*, *82*(36), 5755–5770.

Durham, W. B., Mei, S., Kohlstedt, D. L., Wang, L., & Dixon, N. A. (2009, January). New measurements of activation volume in olivine under anhydrous conditions. *Phys. Earth Planet. Inter.*, *172*(1), 67–73.

Durham, W. B., Weidner, D. J., Karato, S.-I., & Wang, Y. (2002, January). New developments in deformation experiments at high pressure. *Rev. Mineral. Geochem.*, *51*(1), 21–49.

Dyck, B., Goddard, R. M., Wallis, D., Hansen, L. N., & Martel, E. (2020). Metamorphic evolution of the great slave lake shear zone. *J. Metamorph. Geol.*.

Eaton, D. W., & Hope, J. (2003, September). Structure of the crust and upper mantle of the great slave lake shear zone, northwestern canada, from teleseismic analysis and gravity modelling. *Can. J. Earth Sci.*, *40*(9), 1203–1218.

Ellis, S., Beavan, J., Eberhart-Phillips, D., & Stockhert, B. (2006). Simplified models of the alpine fault seismic cycle: stress transfer in the mid-crust. *Geophys. J. Int.*, *166*, 386–402.

England, P., Houseman, G., & Sonder, L. (1985). Length scales for continental deformation in convergent, divergent, and strike-slip environments: Analytical and approximate solutions for a thin viscous sheet model. *J. Geophys. Res.*, *90*(B5), 3551.

Erić, S., Logar, M., Milovanović, D., Babič, D., & Adnaević, B. (2009). Ti-in-biotite geothermometry in non-graphitic, peraluminous metapelites from crni vrh and resavski humovi (central serbia). *Geologica Carpathica*, *60*(1), 3–14.

Evans, B., Renner, J., & Hirth, G. (2001, May). A few remarks on the kinetics of static grain growth in rocks. *Int. J. Earth Sci.*, *90*(1), 88–103.

Faleiros, F. M., Moraes, R., Pavan, M., & Campanha, G. A. C. (2016, March). A new empirical calibration of the quartz c-axis fabric opening-angle deformation thermometer. *Tectonophysics*, *671*, 173–182.

Farla, R. J. M., Karato, S.-I., & Cai, Z. (2013, October). Role of orthopyroxene in rheological

weakening of the lithosphere via dynamic recrystallization. *Proc. Natl. Acad. Sci. U. S. A.*, *110*(41), 16355–16360.

Friedman, M., & Higgs, N. G. (1981). Calcite fabrics in experimental shear zones. In *Mechanical behavior of crustal rocks: The handin volume* (pp. 11–27). American Geophysical Union.

Frost, H. J., & Ashby, M. F. (1982, October). Deformation mechanism maps: the plasticity and creep of metals and ceramics.

Gasparik, T. (1990, October). A thermodynamic model for the enstatite-diopside join. *Am. Mineral.*, *75*(9-10), 1080–1091.

Gerald, J. D. F., Mancktelow, N. S., Pennacchioni, G., & others. (2006). Ultrafine-grained quartz mylonites from high-grade shear zones: Evidence for strong dry middle to lower crust.

Gleason, G. C., & Tullis, J. (1995, July). A flow law for dislocation creep of quartz aggregates determined with the molten salt cell. *Tectonophysics*, *247*(1), 1–23.

Goddard, R. M., Hansen, L. N., Wallis, D., Stipp, M., Holyoke, C. W., III, Kumamoto, K. M., & Kohlstedt, D. L. (2020). A subgrain-size piezometer calibrated for EBSD. *Geophys. Res. Lett.*, e2020GL090056.

Goes, S., Capitanio, F. A., & Morra, G. (2008, February). Evidence of lower-mantle slab penetration phases in plate motions. *Nature*, *451*(7181), 981–984.

Goetze, C. (1975, April). Sheared iherzolites: From the point of view of rock mechanics. *Geology*, *3*(4), 172–173.

Goetze, C., & Kohlstedt, D. L. (1973, October). Laboratory study of dislocation climb and diffusion in olivine. *J. Geophys. Res.*, *78*(26), 5961–5971.

Griggs, D. T., Turner, F. J., & Heard, H. C. (1960). Deformation of rocks at 500°C to 800°C. *Geol. Soc. America. Mem.*, *79*, 39–104.

Grujic, D., Stipp, M., & Wooden, J. L. (2011). *Thermometry of quartz mylonites: Importance of dynamic recrystallization on ti-in-quartz reequilibration* (Vol. 12) (No. 6).

Gueydan, F., Mehl, C., & Parra, T. (2005). Stress-strain rate history of a midcrustal shear zone and the onset of brittle deformation inferred from quartz recrystallized grain size. *Geological Society, London*, *243*, 127–142.

Guidotti, C. V., Cheney, J. T., & Guggenheim, S. (1977, June). Distribution of titanium between coexisting muscovite and biotite in pelitic schists from northwestern maine.

Am. Mineral., *62*(5-6), 438–448.

Guillope, M., & Poirier, J. P. (1979). *Dynamic recrystallization during creep of single-crystalline halite: An experimental study* (Vol. 84) (No. B10).

Haertel, M., & Herwegh, M. (2014, November). Microfabric memory of vein quartz for strain localization in detachment faults: A case study on the simplon fault zone. *J. Struct. Geol.*, *68*, 16–32.

Handy, M. R. (1990). The solid-state flow of polymineralic rocks. *J. Geophys. Res. [Solid Earth]*, *95*(B6), 8647–8661.

Handy, M. R. (1994, March). Flow laws for rocks containing two non-linear viscous phases: A phenomenological approach. *J. Struct. Geol.*, *16*(3), 287–301.

Hanmer, S. (1988, June). Great slave lake shear zone, canadian shield: reconstructed vertical profile of a crustal-scale fault zone. *Tectonophysics*, *149*(3), 245–264.

Hanmer, S., Bowring, S., van Breemen, O., & Parrish, R. (1992, July). Great slave lake shear zone, NW canada : mylonitic record of early proterozoic continental convergence, collision and indentation. *J. Struct. Geol.*, *14*(7), 757–773.

Hanmer, S., & Connelly, J. N. (1986). Mechanical role of the syntectonic laloche batholith in the great slave lake shear zone, district of mackenzie, NWT. *Bull. Geol. Surv. Can.*, 811–826.

Hanmer, S., & Lucas, S. B. (1985). Anatomy of a ductile transcurrent shear: the great slave lake shear zone, district of mackenzie, NWT (preliminary report). *Geol. Surv. Pap. Can. 85-1B*, 7–22.

Hansen, L. N., Cheadle, M. J., John, B. E., Swapp, S. M., Dick, H. J. B., Tucholke, B. E., & Tivey, M. A. (2013). Mylonitic deformation at the kane oceanic core complex: Implications for the rheological behavior of oceanic detachment faults. *Geochem. Geophys. Geosyst.*, *14*(8), 3085–3108.

Hansen, L. N., Kumamoto, K. M., Thom, C. A., Wallis, D., Durham, W. B., Goldsby, D. L., ... Kohlstedt, D. L. (2019). *Low-temperature plasticity in olivine: Grain size, strain hardening, and the strength of the lithosphere.*

Hansen, L. N., & Warren, J. M. (2015). Quantifying the effect of pyroxene on deformation of peridotite in a natural shear zone. *J. Geophys. Res. [Solid Earth]*, *120*(4), 2717–2738.

Hansen, L. N., Zimmerman, M. E., & Kohlstedt, D. L. (2011, August). Grain boundary sliding in san carlos olivine: Flow law parameters and crystallographic-preferred

orientation. *J. Geophys. Res.*, *116*(B8), B08201.

Hansen, L. N., Zimmerman, M. E., & Kohlstedt, D. L. (2012). The influence of microstructure on deformation of olivine in the grain-boundary sliding regime. *J. Geophys. Res. [Solid Earth]*, *117*(B9).

Heilbronner, R., & Kilian, R. (2017, October). The grain size(s) of black hills quartzite deformed in the dislocation creep regime. *Solid Earth*, *8*(5), 1071–1093.

Heilbronner, R., & Tullis, J. (2002, January). The effect of static annealing on microstructures and crystallographic preferred orientations of quartzites experimentally deformed in axial compression and shear. *Geological Society, London, Special Publications*, *200*(1), 191–218.

Heilbronner, R., & Tullis, J. (2006, October). Evolution of c axis pole figures and grain size during dynamic recrystallization: Results from experimentally sheared quartzite. *J. Geophys. Res.*, *111*(B10), B10202.

Heinemann, S., Wirth, R., Gottschalk, M., & Dresen, G. (2005, July). Synthetic [100] tilt grain boundaries in forsterite: 9.9 to 21.5°. *Phys. Chem. Miner.*, *32*(4), 229–240.

Henry, D. J., & Guidotti, C. V. (2002, April). Titanium in biotite from metapelitic rocks: Temperature effects, crystal-chemical controls, and petrologic applications. *Am. Mineral.*, *87*(4), 375–382.

Henry, D. J., Guidotti, C. V., & Thomson, J. A. (2005, February). The ti-saturation surface for low-to-medium pressure metapelitic biotites: Implications for geothermometry and ti-substitution mechanisms. *Am. Mineral.*, *90*(2-3), 316–328.

Hiraga, T., Anderson, I. M., & Kohlstedt, D. L. (2004, February). Grain boundaries as reservoirs of incompatible elements in the earth's mantle. *Nature*, *427*(6976), 699–703.

Hiraga, T., Tachibana, C., Ohashi, N., & Sano, S. (2010, March). Grain growth systematics for forsterite ± enstatite aggregates: Effect of lithology on grain size in the upper mantle. *Earth Planet. Sci. Lett.*, *291*(1-4), 10–20.

Hirth, G., Teyssier, C., & Dunlap, J. W. (2001). *An evaluation of quartzite flow laws based on comparisons between experimentally and naturally deformed rocks* (Vol. 90) (No. 1).

Hirth, G., & Tullis, J. (1992, February). Dislocation creep regimes in quartz aggregates. *J. Struct. Geol.*, *14*(2), 145–159.

Hitchings, R. S., Paterson, M. S., & Bitmead, J. (1989, June). Effects of iron and magnetite

additions in olivine-pyroxene rheology. *Phys. Earth Planet. Inter.*, *55*(3), 277–291.

Hobbs, B. E. (1968, November). Recrystallization of single crystals of quartz. *Tectonophysics*, *6*(5), 353–401.

Hoffman, P. F. (1987). *Continental transform tectonics: Great slave lake shear zone (ca. 1.9 ga), northwest canada* (Vol. 15). Journal.

Holdsworth, R. E., van Diggelen, E. W. E., Spiers, C. J., de Bresser, J. H. P., Walker, R. J., & Bowen, L. (2011, February). Fault rocks from the SAFOD core samples: Implications for weakening at shallow depths along the san andreas fault, california. *J. Struct. Geol.*, *33*(2), 132–144.

Holland, T., & Blundy, J. (1994, May). Non-ideal interactions in calcic amphiboles and their bearing on amphibole-plagioclase thermometry. *Contrib. Mineral. Petrol.*, *116*(4), 433–447.

Holyoke, C. W., III, & Kronenberg, A. K. (2010, October). Accurate differential stress measurement using the molten salt cell and solid salt assemblies in the griggs apparatus with applications to strength, piezometers and rheology. *Tectonophysics*, *494*(1-2), 17–31.

Holyoke, C. W., III, & Kronenberg, A. K. (2013, July). Reversible water weakening of quartz. *Earth Planet. Sci. Lett.*, *374*, 185–190.

Holyoke, C. W., III, & Tullis, J. (2006, April). Mechanisms of weak phase interconnection and the effects of phase strength contrast on fabric development. *J. Struct. Geol.*, *28*(4), 621–640.

Hull, D., & Bacon, D. J. (2001). *Introduction to dislocations*. Butterworth-Heinemann.

Humphreys, F. J. (2001). Grain and subgrain characterisation by electron backscatter diffraction. *J. Mater. Sci.*, *36*(16), 3833–3854.

Humphreys, F. J. (2004, October). Characterisation of fine-scale microstructures by electron backscatter diffraction (EBSD). *Scr. Mater.*, *51*(8), 771–776.

Isaak, D. G. (1992, February). High-temperature elasticity of iron-bearing olivines. *J. Geophys. Res.*, *97*(B2), 1871–1885.

Jaroslow, G. E., Hirth, G., & Dick, H. J. B. (1996, May). Abyssal peridotite mylonites: implications for grain-size sensitive flow and strain localization in the oceanic lithosphere. *Tectonophysics*, *256*(1), 17–37.

Ji, S., Wang, Z., & Wirth, R. (2001, November). Bulk flow strength of forsterite–enstatite

composites as a function of forsterite content. *Tectonophysics*, *341*(1), 69–93.

Johnson, M. C., & Rutherford, M. J. (1989, September). Experimental calibration of the aluminum-in-hornblende geobarometer with application to long valley caldera (california) volcanic rocks. *Geology*, *17*(9), 837–841.

Jung, H., Park, M., Jung, S., & Lee, J. (2010, October). Lattice preferred orientation, water content, and seismic anisotropy of orthopyroxene. *J. Earth Sci.*, *21*(5), 555–568.

Karato, S.-I. (2012). *Deformation of earth materials: An introduction to the rheology of solid earth*. Cambridge University Press.

Karato, S.-I., Toriumi, M., & Fujii, T. (1980). Dynamic recrystallization of olivine single crystals during high temperature creep. *Geophysical Research Letters*, *7*(9), 649–652.

Kassner, M. E. (2015). Fundamentals of creep in metals and alloys.

Kenkmann, T., & Dresen, G. (2002). *Dislocation microstructure and phase distribution in a lower crustal shear zone – an example from the Ivrea-Zone, italy* (Vol. 91) (No. 3).

Kidder, S., Avouac, J.-P., & Chan, Y.-C. (2012). Constraints from rocks in the taiwan orogen on crustal stress levels and rheology. *J. Geophys. Res. [Solid Earth]*, *117*(B9).

Kidder, S., Hirth, G., Avouac, J.-P., & Behr, W. (2016, February). The influence of stress history on the grain size and microstructure of experimentally deformed quartzite. *J. Struct. Geol.*, *83*, 194–206.

Kilian, R., Heilbronner, R., & Stünitz, H. (2011, August). Quartz grain size reduction in a granitoid rock and the transition from dislocation to diffusion creep. *J. Struct. Geol.*, *33*(8), 1265–1284.

Kirby, S. H. (1983). Rheology of the lithosphere. *Rev. Geophys.*, *21*(6), 1458.

Kirby, S. H. (1985, October). Rock mechanics observations pertinent to the rheology of the continental lithosphere and the localization of strain along shear zones. *Tectonophysics*, *119*(1), 1–27.

Kirby, S. H., & Kronenberg, A. K. (1987). Rheology of the lithosphere: Selected topics. *Rev. Geophys.*, *25*(6), 1219.

Kohlstedt, D. L., Evans, B., & Mackwell, S. J. (1995, September). Strength of the lithosphere: Constraints imposed by laboratory experiments. *J. Geophys. Res.*, *100*(B9), 17587–17602.

Kohlstedt, D. L., Goetze, C., Durham, W. B., & Sande, J. V. (1976, March). New technique for decorating dislocations in olivine. *Science*, *191*(4231), 1045–1046.

Kohlstedt, D. L., & Weathers, M. S. (1980, November). Deformation-Induced microstructures, paleopiezometers, and differential stresses in deeply eroded fault zones. *J. Geophys. Res.*, *85*(B11), 6269–6285.

Kronenberg, A. K., & Tullis, J. (1984). *Flow strengths of quartz aggregates: Grain size and pressure effects due to hydrolytic weakening* (Vol. 89) (No. B6).

Kruhl, J. H. (1998). *Prism-and basal-plane parallel subgrain boundaries in quartz: a microstructural geothermobarometer-reply.* BLACKWELL SCIENCE INC 350 MAIN ST, MALDEN, MA 02148.

Kumazawa, M., & Anderson, O. L. (1969). Elastic moduli, pressure derivatives, and temperature derivatives of single-crystal olivine and single-crystal forsterite. *J. Geophys. Res.*, *74*(25), 5961–5972.

Küster, M., & Stöckhert, B. (1999). High differential stress and sublithostatic pore fluid pressure in the ductile regime—microstructural evidence for short-term post-seismic creep in the sesia zone, western alps. *Tectonophysics*, *303*(1-4), 263–277.

Kwak, T. A. P. (1968, November). Ti in biotite and muscovite as an indication of metamorphic grade in almandine amphibolite facies rocks from sudbury, ontario. *Geochim. Cosmochim. Acta*, *32*(11), 1222–1229.

Langdon, T. G. (1994, July). A unified approach to grain boundary sliding in creep and superplasticity. *Acta Metall. Mater.*, *42*(7), 2437–2443.

Langdon, T. G. (2006, February). Grain boundary sliding revisited: Developments in sliding over four decades. *J. Mater. Sci.*, *41*(3), 597–609.

Langille, J. M., Jessup, M. J., Cottle, J. M., Newell, D., & Seward, G. (2010, July). Kinematic evolution of the ama drime detachment: Insights into orogen-parallel extension and exhumation of the ama drime massif, Tibet–Nepal. *J. Struct. Geol.*, *32*(7), 900–919.

Lapusta, N., & Rice, J. R. (2003, April). Nucleation and early seismic propagation of small and large events in a crustal earthquake model. *J. Geophys. Res.*, *108*(B4).

Law, R., Waters, D., Morgan, S., Stahr, D., Francsis, M., Ashley, K., ... Heaverlo, N. (2013, April). Quartz fabric-based deformation thermometry: examples of its application, relationships to petrology-based PT paths, and potential problems. In (pp. EGU2013–1789).

Leake, B. E., Woolley, A. R., Arps, C. E. S., Birch, W. D., Gilbert, M. C., Grice, J. D., ... Youzhi, G. (1997). *Nomenclature of amphiboles report of the subcommittee on*

amphiboles of the international mineralogical association commission on new minerals and mineral names (Vol. 9) (No. 3).

Leake, B. E., Woolley, A. R., Birch, W. D., Burke, E. A. J., Ferraris, G., Grice, J. D., ... Others (2004). Nomenclature of amphiboles: additions and revisions to the international mineralogical associations amphibole nomenclature. *Am. Mineral.*, *89*, 883–887.

Li, Li, L., Weidner, D., Raterron, P., Chen, J., Vaughan, M., ... Durham, B. (2006). *Deformation of olivine at mantle pressure using the D-DIA* (Vol. 18) (No. 1).

Li, L., Addad, A., Weidner, D., Long, H., & Chen, J. (2007, July). High pressure deformation in two-phase aggregates. *Tectonophysics*, *439*(1), 107–117.

Linckens, J., Herwegh, M., Müntener, O., & Mercolli, I. (2011, June). Evolution of a polymineralic mantle shear zone and the role of second phases in the localization of deformation. *J. Geophys. Res.*, *116*(B6), B06210.

Lister, G. S., & Hobbs, B. E. (1980, January). The simulation of fabric development during plastic deformation and its application to quartzite: the influence of deformation history. *J. Struct. Geol.*, *2*(3), 355–370.

Liu, L., & Zoback, M. D. (1997, August). Lithospheric strength and intraplate seismicity in the new madrid seismic zone. *Tectonics*, *16*(4), 585–595.

Luan, F. C., & Paterson, M. S. (1992). Preparation and deformation of synthetic aggregates of quartz. *J. Geophys. Res.*, *97*(B1), 301.

Lusk, A. D. J., Platt, J. P., & Roeske, S. M. (2020). The deep structure and rheology of a plate Boundary-Scale shear zone: Constraints from an exhumed caledonian shear zone, NW scotland. *Lithosphere*.

Luton, M. J., & Sellars, C. M. (1969, August). Dynamic recrystallization in nickel and nickel-iron alloys during high temperature deformation. *Acta Metall.*, *17*(8), 1033–1043.

Mainprice, D., Hielscher, R., & Schaeben, H. (2011). *Calculating anisotropic physical properties from texture data using the MTEX open-source package* (Vol. 360) (No. 1).

Mao, Z., Fan, D., Lin, J.-F., Yang, J., Tkachev, S. N., Zhuravlev, K., & Prakapenka, V. B. (2015, September). Elasticity of single-crystal olivine at high pressures and temperatures. *Earth Planet. Sci. Lett.*, *426*, 204–215.

Marone, C. (1998, May). LABORATORY-DERIVED FRICTION LAWS AND THEIR APPLICATION TO SEISMIC FAULTING. *Annu. Rev. Earth Planet. Sci.*, *26*(1), 643–696.

Marques, F. O., Burlini, L., & Burg, J.-P. (2010, March). Rheology and microstructure of synthetic halite/calcite porphyritic aggregates in torsion. *J. Struct. Geol.*, *32*(3), 342–349.

Marques, F. O., Burlini, L., & Burg, J.-P. (2011). Microstructural and mechanical effects of strong fine-grained muscovite in soft halite matrix: Shear strain localization in torsion. *J. Geophys. Res. [Solid Earth]*, *116*(B8).

McCormick, J. W. (1977). *Transmission electron microscopy study of experimentally deformed synthetic quartz* (Unpublished doctoral dissertation). Ph D Thesis. University of California, Los Angeles, p 171.

McDonnell, R. D., Peach, C. J., van Roermund, H. L. M., & Spiers, C. J. (2000). *Effect of varying enstatite content on the deformation behavior of fine-grained synthetic peridotite under wet conditions* (Vol. 105) (No. B6).

McKenzie, D., & Brune, J. N. (1972, August). Melting on fault planes during large earthquakes. *Geophys. J. Int.*, *29*(1), 65–78.

Mehl, L., & Hirth, G. (2008, May). Plagioclase preferred orientation in layered mylonites: Evaluation of flow laws for the lower crust. *J. Geophys. Res.*, *113*(B5).

Mei, S., Suzuki, A. M., Kohlstedt, D. L., Dixon, N. A., & Durham, W. B. (2010, August). Experimental constraints on the strength of the lithospheric mantle. *J. Geophys. Res.*, *115*(B8), Q08012.

Melosh, B. L., Rowe, C. D., Gerbi, C., Smit, L., & Macey, P. (2018, July). Seismic cycle feedbacks in a mid-crustal shear zone. *J. Struct. Geol.*, *112*, 95–111.

Menegon, L., Nasipuri, P., Stünitz, H., Behrens, H., & Ravna, E. (2011, October). Dry and strong quartz during deformation of the lower crust in the presence of melt. *J. Geophys. Res.*, *116*(B10), B10410.

Mercier, J.-C. C., Anderson, D. A., & Carter, N. L. (1977). Stress in the lithosphere: Inferences from steady state flow of rocks. In *Stress in the earth* (pp. 199–226). Birkhäuser, Basel.

Michels, Z. D., Kruckenberg, S. C., Davis, J. R., & Tikoff, B. (2015, September). Determining vorticity axes from grain-scale dispersion of crystallographic orientations. *Geology*, *43*(9), 803–806.

Michibayashi, K., Mainprice, D., Fujii, A., Uehara, S., Shinkai, Y., Kondo, Y., ... Ji, S. (2016, June). Natural olivine crystal-fabrics in the western pacific convergence region:

A new method to identify fabric type. *Earth Planet. Sci. Lett.*, *443*, 70–80.

Mingard, K. P., Roebuck, B., Bennett, E. G., Gee, M. G., Nordenstrom, H., Sweetman, G., & Chan, P. (2009, March). Comparison of EBSD and conventional methods of grain size measurement of hardmetals. *International Journal of Refractory Metals and Hard Materials*, *27*(2), 213–223.

Mingard, K. P., Roebuck, B., Bennett, E. G., Thomas, M., Wynne, B. P., & Palmiere, E. J. (2007, September). Grain size measurement by EBSD in complex hot deformed metal alloy microstructures. *J. Microsc.*, *227*(Pt 3), 298–308.

Morgan, S. S., & Law, R. D. (2004). *Unusual transition in quartzite dislocation creep regimes and crystal slip systems in the aureole of the eureka Valley–Joshua Flat–Beer creek pluton, california: a case for anhydrous conditions created by decarbonation reactions* (Vol. 384) (No. 1-4).

Muluneh, A. A., Kidane, T., Corti, G., & Keir, D. (2018, April). Constraints on fault and crustal strength of the main ethiopian rift from formal inversion of earthquake focal mechanism data. *Tectonophysics*, *731-732*, 172–180.

Nicolas, A. (1978). Stress estimates from structural studies in some mantle peridotites. *Philos. Trans. R. Soc. Lond. A*, *288*, 49–57.

O'Haver, T. (2018). *Pragmatic introduction to signal processing 2019: Applications in scientific measurement.* Independently Published.

Ohi, S., Miyake, A., & Yashima, M. (2010). Stability field of the high-temperature orthorhombic phase in the enstatite-diopside system. *Am. Mineral.*.

Ord, A., & Christie, J. M. (1984). Flow stresses from microstructures in mylonitic quartzites of the moine thrust zone, assynt area, scotland. *J. Struct. Geol.*.

Orlandini, O. F., & Mahan, K. H. (2020, December). Rheological evolution of a pseudotachylyte-bearing deep crustal shear zone in the western canadian shield. *J. Struct. Geol.*, *141*, 104188.

Otten, M. T. (1984, May). The origin of brown hornblende in the artfjället gabbro and dolerites. *Contrib. Mineral. Petrol.*, *86*(2), 189–199.

Passchier, C. W., & Trouw, R. A. J. (2005). *Microtectonics.* Springer Science & Business Media.

Paterson, M. S. (1990). Rock deformation experimentation. *The Brittle-Ductile Transition in Rocks, Geophys. Monogr. Ser*, *56*, 187–194.

Paterson, M. S., & Olgaard, D. L. (2000, September). Rock deformation tests to large shear strains in torsion. *J. Struct. Geol.*, *22*(9), 1341–1358.

Paterson, M. S., & Wong, T.-F. (2005). *Experimental rock deformation - the brittle field.* Springer Science & Business Media.

Peng, Z., & Redfern, S. A. T. (2013). Mechanical properties of quartz at the α-β phase transition: Implications for tectonic and seismic anomalies. *Geochem. Geophys. Geosyst.*, *14*(1), 18–28.

Pennock, G. M., Drury, M. R., & Spiers, C. J. (2005, January). The development of subgrain misorientations with strain in dry synthetic NaCl measured using EBSD. *J. Struct. Geol.*, *27*(12), 2159–2170.

Platt, J. P., & De Bresser, J. H. P. (2017, December). Stress dependence of microstructures in experimentally deformed calcite. *J. Struct. Geol.*, *105*, 80–87.

Poirier, J. P., & Guillopé, M. (1979). Deformation induced recrystallization of minerals. *Bulletin de Mineralogie*.

Pommier, A., Leinenweber, K., Kohlstedt, D. L., Qi, C., Garnero, E. J., Mackwell, S. J., & Tyburczy, J. A. (2015, June). Experimental constraints on the electrical anisotropy of the lithosphere–asthenosphere system. *Nature*, *522*, 202.

Post. (1973). *The flow laws of mt. burnett dunite* (Unpublished doctoral dissertation). University of California, Los Angeles.

Post, A., & Tullis, J. (1999, March). A recrystallized grain size piezometer for experimentally deformed feldspar aggregates. *Tectonophysics*, *303*(1), 159–173.

Powell, R. (1978). *Equilibrium thermodynamics in petrology: an introduction.* Harper & Row.

Qin, Y., Götz, G., & Blum, W. (2003, January). Subgrain structure during annealing and creep of the cast martensitic cr-steel G-X12CrMoWVNbN 10-1-1. *Materials Science and Engineering: A*, *341*(1), 211–215.

Rahl, J. M., & Skemer, P. (2016, June). Microstructural evolution and rheology of quartz in a mid-crustal shear zone. *Tectonophysics*, *680*, 129–139.

Raj, S. V., & Pharr, G. M. (1986, August). A compilation and analysis of data for the stress dependence of the subgrain size. *Int. J. Green Nanotech. Materials Sci. Eng.*, *81*, 217–237.

Raleigh, C. B., & Kirby, S. H. (1970). Creep in the upper mantle. *Mineral. Soc. Am. Spec.*

Pap., *3*, 113–121.

Ranalli, G. (1997). Rheology of the lithosphere in space and time. *Geological Society, London, Special Publications*.

Raterron, P., Fraysse, G., Girard, J., & Holyoke, C. W. (2016, September). Strength of orthoenstatite single crystals at mantle pressure and temperature and comparison with olivine. *Earth Planet. Sci. Lett.*, *450*, 326–336.

Read, W. T. (1953). *Dislocations in crystals*. McGraw-Hill.

Read, W. T., & Shockley, W. (1950, May). Dislocation models of crystal grain boundaries. *Phys. Rev.*, *78*(3), 275–289.

Rodriguez, P. (1996, December). Sixty years of dislocations. *Bull. Mater. Sci.*, *19*(6), 857–872.

Ross, J. V., Ave Lallemant, H. G., & Carter, N. L. (1980, December). Stress dependence of recrystallized-grain and subgrain size in olivine. *Tectonophysics*, *70*(1-2), 39–61.

Ross, J. V., Bauer, S. J., & Hansen, F. D. (1987, September). Textural evolution of synthetic anhydrite-halite mylonites. *Tectonophysics*, *140*(2), 307–326.

Roy, M., & Royden, L. H. (2000). Crustal rheology and faulting at strike-slip plate boundaries: 2. effects of lower crustal flow. *J. Geophys. Res. [Solid Earth]*, *105*(B3), 5599–5613.

Rutter, E. H. (1995, December). Experimental study of the influence of stress, temperature, and strain on the dynamic recrystallization of carrara marble. *J. Geophys. Res.*, *100*(B12), 24651–24663.

Rutter, E. H., Atkinson, B. K., & others. (1978). On the use of the stress relaxation testing method in studies of the mechanical behaviour of geological materials. *Geophys. J.*

Rybacki, E., Paterson, M. S., Wirth, R., & Dresen, G. (2003). Rheology of calcite–quartz aggregates deformed to large strain in torsion. *J. Geophys. Res. [Solid Earth]*, *108*(B2).

Schmid, S. M., & Casey, M. (1986). Complete fabric analysis of some commonly observed quartz c-axis patterns. *Geophysical Monograph*, *36*(6), 263–286.

Schmid, S. M., Paterson, M. S., & Boland, J. N. (1980, June). High temperature flow and dynamic recrystallization in carrara marble. *Tectonophysics*, *65*(3), 245–280.

Schmidt, M. W. (1992, April). Amphibole composition in tonalite as a function of pressure: an experimental calibration of the al-in-hornblende barometer. *Contrib. Mineral. Petrol.*, *110*(2), 304–310.

Scholz, C. H. (1988). The brittle-plastic transition and the depth of seismic faulting. *Geol. Rundsch.*, *77*(1), 319–328.

Scholz, C. H. (2000, February). Evidence for a strong san andreas fault. *Geology*, *28*(2), 163–166.

Servi, I. S., Norton, J. T., & Grant, N. J. (1952). Some observations of subgrain formation during creep in high purity aluminum. *JOM*, *4*(9), 965–971.

Shimizu, I. (1998). Stress and temperature dependence of recrystallized grain size: A subgrain misorientation model. *Geophysical research letters*, *25*(22), 4237–4240.

Shimizu, I. (2008, July). Theories and applicability of grain size piezometers: The role of dynamic recrystallization mechanisms. *J. Struct. Geol.*, *30*(7), 899–917.

Sibson, R. H. (1977). Fault rocks and fault mechanisms. *J. Geol. Soc. London*.

Sibson, R. H. (1982, February). Fault zone models, heat flow, and the depth distribution of earthquakes in the continental crust of the united states. *Bull. Seismol. Soc. Am.*, *72*(1), 151–163.

Siemes, H., Rybacki, E., Klingenberg, B., & Rosiere, C. A. (2011, June). Development of a recrystallized grain size piezometer for hematite based on high-temperature torsion experiments. *Eur. J. Mineral.*, *23*(3), 293–302.

Singh, A. K., Balasingh, C., Mao, H.-K., Hemley, R. J., & Shu, J. (1998, June). Analysis of lattice strains measured under nonhydrostatic pressure. *J. Appl. Phys.*, *83*(12), 7567–7575.

Skemer, P., Katayama, I., Jiang, Z., & Karato, S.-I. (2005). *The misorientation index: Development of a new method for calculating the strength of lattice-preferred orientation* (Vol. 411) (No. 1-4).

Skemer, P., Warren, J. M., Hansen, L. N., Hirth, G., & Kelemen, P. B. (2013, August). The influence of water and LPO on the initiation and evolution of mantle shear zones. *Earth Planet. Sci. Lett.*, *375*, 222–233.

Skemer, P., Warren, J. M., Kelemen, P. B., & Hirth, G. (2010, January). Microstructural and rheological evolution of a mantle shear zone. *J. Petrol.*, *51*(1-2), 43–53.

Smith, C. S. (1948). Zener pinning. *Trans. Met. Soc. AIME*, *175*, 15–51.

Smyth, J. R. (1974, April). Experimental study on the polymorphism of enstatite. *Am. Mineral.*, *59*(3-4), 345–352.

Soleymani, H., Kidder, S., Hirth, G., & Garapić, G. (2020, June). The effect of cooling

during deformation on recrystallized grain-size piezometry. *Geology*, *48*(6), 531–535.

Spear, F. S., & Florence, F. P. (1992, March). Thermobarometry in granulites: pitfalls and new approaches. *Precambrian Res.*, *55*(1), 209–241.

Speciale, P. A., & Behr, W. M. (2014, December). A Naturally-Constrained orthopyroxene piezometer. In (Vol. 2014, pp. T31A–4577).

Speckbacher, R., Behrmann, J. H., Nagel, T. J., Stipp, M., & Devey, C. W. (2011, July). Splitting a continent: Insights from submarine high-resolution mapping of the moresby seamount detachment, offshore papua new guinea. *Geology*, *39*(7), 651–654.

Stipp, M., Stünitz, H., Heilbronner, R., & others. (2002). Dynamic recrystallization of quartz: correlation between natural and experimental conditions. *Geological Society*.

Stipp, M., Stünitz, H., Heilbronner, R., & Schmid, S. M. (2002, December). The eastern tonale fault zone: a 'natural laboratory' for crystal plastic deformation of quartz over a temperature range from 250 to 700°c. *J. Struct. Geol.*, *24*(12), 1861–1884.

Stipp, M., & Tullis, J. (2003, November). The recrystallized grain size piezometer for quartz. *Geophys. Res. Lett.*, *30*(21), 2088.

Stipp, M., Tullis, J., Scherwath, M., & Behrmann, J. H. (2010, August). A new perspective on paleopiezometry: Dynamically recrystallized grain size distributions indicate mechanism changes. *Geology*, *38*(8), 759–762.

Sundberg, M., & Cooper, R. F. (2008, December). Crystallographic preferred orientation produced by diffusional creep of harzburgite: Effects of chemical interactions among phases during plastic flow. *J. Geophys. Res.*, *113*(B12).

Tasaka, M., Hiraga, T., & Zimmerman, M. E. (2013). *Influence of mineral fraction on the rheological properties of forsterite enstatite during grain-size-sensitive creep: 2. deformation experiments* (Vol. 118) (No. 8).

Tasaka, M., Zimmerman, M. E., & Kohlstedt, D. L. (2016, January). Evolution of the rheological and microstructural properties of olivine aggregates during dislocation creep under hydrous conditions. *J. Geophys. Res.*, *121*(1), 92–113.

Tasaka, M., Zimmerman, M. E., & Kohlstedt, D. L. (2017, October). Rheological weakening of olivine + orthopyroxene aggregates due to phase mixing: 1. mechanical behavior. *J. Geophys. Res. [Solid Earth]*, *122*, 7584–7596.

Tasaka, M., Zimmerman, M. E., & Kohlstedt, D. L. (2020, September). Rheological weakening of olivine + orthopyroxene aggregates due to phase mixing: Effects of orthopyroxene

volume fraction. *J. Geophys. Res. [Solid Earth]*, *125*(9).

Tasaka, M., Zimmerman, M. E., Kohlstedt, D. L., Stünitz, H., & Heilbronner, R. (2017). Rheological weakening of olivine+ orthopyroxene aggregates due to phase mixing: Part 2. microstructural development. *J. Geophys. Res. [Solid Earth]*, *122*, 7597–7612.

Taylor, G. I. (1934, July). The mechanism of plastic deformation of crystals. part I.—Theoretical. *Proceedings of the Royal Society of London. Series A, Containing Papers of a Mathematical and Physical Character*, *145*(855), 362–387.

Ter Heege, J. H., De Bresser, J. H. P., & Spiers, C. J. (2005, February). Dynamic recrystallization of wet synthetic polycrystalline halite: dependence of grain size distribution on flow stress, temperature and strain. *Tectonophysics*, *396*(1), 35–57.

Thomas, J. B., Watson, E. B., Spear, F. S., Shemella, P. T., Nayak, S. K., & Lanzirotti, A. (2010). TitaniQ under pressure: the effect of pressure and temperature on the solubility of ti in quartz. *Contrib. Mineral. Petrol.*, *160*(5), 743–759.

Tokle, L., & Hirth, G. (2019, December). Watt's going on with the quartz recrystallized grain size?? application of the wattmeter for predicting quartz recrystallized grain size. In (Vol. 2019, pp. MR43A–05).

Toriumi, M. (1979, February). Relation between dislocation density and subgrain size of naturally deformed olivine in peridotites. *Contrib. Mineral. Petrol.*, *68*(2), 181–186.

Tovish, A., Schubert, G., & Luyendyk, B. P. (1978, December). Mantle flow pressure and the angle of subduction: Non-Newtonian corner flows. *J. Geophys. Res.*, *83*(B12), 5892–5898.

Trepmann, C. A., & Seybold, L. (2018). *Deformation at low and high stress-loading rates* (Vol. 10) (No. 1).

Trimby, P., Day, A., Mehnert, K., & Schmidt, N. H. (2002, March). Is fast mapping good mapping? a review of the benefits of high-speed orientation mapping using electron backscatter diffraction. *J. Microsc.*, *205*(Pt 3), 259–269.

Trimby, P., Prior, D., & Wheeler, J. (1998, July). Grain boundary hierarchy development in a quartz mylonite. *J. Struct. Geol.*, *20*(7), 917–935.

Tullis, J. (1972). Preferred orientations in experimentally deformed quartzites.

Tullis, J. (1979). High temperature deformation of rocks and minerals. *Rev. Geophys.*, *17*(6), 1137.

Tullis, J., Christie, J. M., & Griggs, D. T. (1973, January). Microstructures and preferred

orientations of experimentally deformed quartzites. *GSA Bulletin*, *84*(1), 297–314.

Tullis, T. E., Horowitz, F. G., & Tullis, J. (1991). Flow laws of polyphase aggregates from end-member flow laws. *J. Geophys. Res. [Solid Earth]*, *96*(B5), 8081–8096.

Türkoğlu, E., Zulauf, G., Linckens, J., & Ustaömer, T. (2016, October). Dextral strike-slip along the kapıdağ shear zone (NW turkey): evidence for eocene westward translation of the anatolian plate. *Geol. Rundsch.*, *105*(7), 2061–2073.

Twiss, R. J. (1977). Theory and applicability of a recrystallized grain size paleopiezometer. In *Stress in the earth* (pp. 227–244). Birkhäuser, Basel.

Twiss, R. J. (1986). Variable sensitivity piezometric equations for dislocation density and subgrain diameter and their relevance to olivine and quartz. In B. E. Hobbs & H. C. Heard (Eds.), *Mineral and rock deformation:laboratory studies:the paterson volume.* Washington, D.C: American Geophysical Union.

Underwood, E. E. (1970). *Quantitative stereology.* Addison-Wesley Pub. Co.

Urai, J. L., Means, W. D., & Lister, G. S. (1986). Dynamic recrystallization of minerals. In *Mineral and rock deformation: laboratory studies* (Vol. 36, pp. 161–199). AGU Washington, DC.

Valcke, S. L. A. (2008). *EBSD analysis of heterogeneous microstructures in experimentally deformed calcite: development of core and mantle subgrains, grain boundary bulges and recrystallised grains. geologica ultraiectina (289)* (Unpublished doctoral dissertation). University Utrecht.

Valcke, S. L. A., De Bresser, J. H. P., & others. (2015). Influence of deformation conditions on the development of heterogeneous recrystallization microstructures in experimentally deformed carrara marble. *Geological Society*.

Valcke, S. L. A., Drury, M. R., de Bresser, J. H. P., & Pennock, G. M. (2007). *Quantifying heterogeneous microstructures: Core and mantle subgrains in deformed calcite.*

Valcke, S. L. A., Pennock, G. M., Drury, M. R., & De Bresser, J. H. P. (2006, December). Electron backscattered diffraction as a tool to quantify subgrains in deformed calcite. *J. Microsc.*, *224*(3), 264–276.

van den Berg, A. P., van Keken, P. E., & Yuen, D. A. (1993, October). The effects of a composite non-newtonian and newtonian rheology on mantle convection. *Geophys. J. Int.*, *115*(1), 62–78.

Van der Wal, D., Chopra, P., Drury, M., & Gerald, J. F. (1993, July). Relationships between

dynamically recrystallized grain size and deformation conditions in experimentally deformed olivine rocks. *Geophys. Res. Lett.*, *20*(14), 1479–1482.

van der Werf, T., Chatzaras, V., Kriegsman, L. M., Kronenberg, A., Tikoff, B., & Drury, M. R. (2017, December). Constraints on the rheology of the lower crust in a strike-slip plate boundary: evidence from the san quintín xenoliths, baja california, mexico. *Solid Earth*, *8*(6), 1211–1239.

Voigt, W. (1928). *Lehrbuch der kristallphysik* (Vol. 962). Teubner Leipzig.

Wallis, D., Hansen, L., Britton, T., & Wilkinson, A. (2019). High-angular resolution electron backscatter diffraction as a new tool for mapping lattice distortion in geological minerals. *Journal of Geophysical Research: Solid Earth*, *124*(7), 6337—6358.

Wallis, D., Hansen, L. N., Britton, T. B., & Wilkinson, A. J. (2016, September). Geometrically necessary dislocation densities in olivine obtained using high-angular resolution electron backscatter diffraction. *Ultramicroscopy*, *168*, 34–45.

Wallis, D., Hansen, L. N., Kumamoto, K. M., Thom, C. A., Plümper, O., Ohl, M., ... Wilkinson, A. J. (2020, August). Dislocation interactions during low-temperature plasticity of olivine and their impact on the evolution of lithospheric strength. *Earth Planet. Sci. Lett.*, *543*, 116349.

Wallis, D., Lloyd, G. E., Phillips, R. J., Parsons, A. J., & Walshaw, R. D. (2015, August). Low effective fault strength due to frictional-viscous flow in phyllonites, karakoram fault zone, NW india. *J. Struct. Geol.*, *77*(Supplement C), 45–61.

Wallis, D., Parsons, A., & Hansen, L. (2019). Quantifying geometrically necessary dislocations in quartz using hr-ebsd:application to chessboard subgrain boundaries. *Journal of Structural Geology*, *125*, 235—247.

Wallis, D., Phillips, R. J., & Lloyd, G. E. (2014, June). Evolution of the eastern karakoram metamorphic complex, ladakh, NW india, and its relationship to magmatism and regional tectonics. *Tectonophysics*, *626*, 41–52.

Wang, J., Mao, Z., Jiang, F., & Duffy, T. S. (2015). *Elasticity of single-crystal quartz to 10 GPa* (Vol. 42) (No. 3).

Wang, Y., Durham, W., Getting, I., & Weidner, D. (2003, May). The deformation-DIA: A new apparatus for high temperature triaxial deformation to pressures up to 15 GPa. *Rev. Sci. Instrum.*, *74*(6), 3002–3011.

Wang, Y., Hilairet, N., Nishiyama, N., Yahata, N., Tsuchiya, T., Morard, G., & Fiquet,

G. (2013). *High-pressure, high-temperature deformation of CaGeO3(perovskite)±MgO aggregates: Implications for multiphase rheology of the lower mantle* (Vol. 14) (No. 9).

Wark, D. A., & Watson, B. E. (2006). *TitaniQ: a titanium-in-quartz geothermometer* (Vol. 152) (No. 6).

Warren, J. M., & Hirth, G. (2006, August). Grain size sensitive deformation mechanisms in naturally deformed peridotites. *Earth Planet. Sci. Lett.*, *248*(1), 438–450.

Weathers, M. S., Bird, J. M., Cooper, R. F., & Kohlstedt, D. L. (1979). Differential stress determined from deformation-induced microstructures of the moine thrust zone. *J. Geophys. Res. [Solid Earth]*, *84*(B13), 7495–7509.

Wegner, M. W., & Christie, J. M. (1983, February). Chemical etching of deformation sub-structures in quartz. *Phys. Chem. Miner.*, *9*(2), 67–78.

Weidner, D. J., Vaughan, M. T., Wang, L., Long, H., Li, L., Dixon, N. A., & Durham, W. B. (2010). *Precise stress measurements with white synchrotron x rays* (Vol. 81) (No. 1).

Wex, S., Mancktelow, N. S., Camacho, A., & Pennacchioni, G. (2019). *Interplay between seismic fracture and aseismic creep in the woodroffe thrust, central australia – inferences for the rheology of relatively dry continental mid-crustal levels* (Vol. 758).

Wheeler, J. (1992). Importance of pressure solution and coble creep in the deformation of polymineralic rocks. *J. Geophys. Res.*, *97*(B4), 4579.

White, S. (1979, September). Grain and sub-grain size variations across a mylonite zone. *Contrib. Mineral. Petrol.*, *70*(2), 193–202.

White, S., Drury, M., Ion, S., & Humphreys, F. J. (1985). *Large strain deformation studies using polycrystalline magnesium as a rock analogue. part i: grain size paleopiezometry in mylonite zones* (Vol. 40) (No. 3).

Wiesman, H. S., Zimmerman, M. E., & Kohlstedt, D. L. (2018). Laboratory investigation of mechanisms for phase mixing in olivine+ ferropericlase aggregates. *Philosophical Transactions of the Royal Society A: Mathematical, Physical and Engineering Sciences*, *376*(2132), 20170417.

Wilkinson, A. J. (1996, March). Measurement of elastic strains and small lattice rotations using electron back scatter diffraction. *Ultramicroscopy*, *62*(4), 237–247.

Wilkinson, A. J., Meaden, G., & Dingley, D. J. (2006, March). High-resolution elastic strain measurement from electron backscatter diffraction patterns: new levels of sensitivity. *Ultramicroscopy*, *106*(4-5), 307–313.

Wilkinson, A. J., & Randman, D. (2010, March). Determination of elastic strain fields and geometrically necessary dislocation distributions near nanoindents using electron back scatter diffraction. *Philos. Mag.*, *90*(9), 1159–1177.

Yabe, K., Sueyoshi, K., & Hiraga, T. (2020). Grain-Boundary diffusion creep of olivine: 1. experiments at 1 atm. *J. Geophys. Res.*.

Zhang, G., Mei, S., & Song, M. (2020, March). Effect of water on the dislocation creep of enstatite aggregates at 300 MPa. *Geophys. Res. Lett.*, *47*(5).

Zhang, G., Mei, S., Song, M., & Kohlstedt, D. L. (2017, October). Diffusion creep of enstatite at high pressures under hydrous conditions. *J. Geophys. Res. [Solid Earth]*, *122*(10), 7718–7728.

Zhao, N., Hirth, G., Cooper, R. F., Kruckenberg, S. C., & Cukjati, J. (2019, July). Low viscosity of mantle rocks linked to phase boundary sliding. *Earth Planet. Sci. Lett.*, *517*, 83–94.

Zoback, M. D., Apel, R., Baumgärtner, J., Brudy, M., & others. (1993). Upper-crustal strength inferred from stress measurements to 6 km depth in the KTB borehole. *Nature*.

Zoback, M. D., & Harjes, H.-P. (1997, August). Injection-induced earthquakes and crustal stress at 9 km depth at the KTB deep drilling site, germany. *J. Geophys. Res.*, *102*(B8), 18477–18491.

Zoback, M. D., & Zoback, M. L. (2002). Stress in the earth's lithosphere. *Encyclopedia of physical science and technology*, *16*, 143–154.